# Study of natural convection in a vertical channel for the development of innovative solar building envelopes

Ramez Raja

UNIVERSITÉ SAVOIE MONT BLANC

# THÈSE

Pour obtenir le grade de

## DOCTEUR DE L'UNIVERSITÉ SAVOIE MONT BLANC

Spécialité : **Energétique et Génie des procédés**

Arrêté ministériel : 25 Mai 2016

Présentée par


## « Ramez RAJA »


Thèse dirigée par **« Christophe MENEZO »** et
Codirigée par **« Mickael PAILHA »**

Préparée au sein du **Laboratoire procédés énergie bâtiment**
Dans **l'École Doctorale Sciences, Ingénierie, Environnement**

# STUDY OF NATURAL CONVECTION IN A VERTICAL CHANNEL FOR THE DEVELOPMENT OF INNOVATIVE SOLAR BUILDING ENVELOPES

Thèse soutenue publiquement le **« 03-07-2024 »**
devant le jury composé de :

**Professeur, Stéphanie, Giroux-Julien**
Fonction et lieu de la fonction, rôle (Rapporteur)
**Professeur, Chengwang, Lei**
Fonction et lieu de la fonction, rôle (Rapporteur)
**Professeur, Steven, Armfield**
Fonction et lieu de la fonction, rôle ( Examinateur)
**Professeur, Marco, Fossa**
Fonction et lieu de la fonction, rôle (Président du jury)
**Professeur, Victoria, Timchenko**
Fonction et lieu de la fonction, rôle (Examinateur)
**Chercheur, Martin, Thebault**
Fonction et lieu de la fonction, rôle (Examinateur)

## *ABSTRACT*

Rapid population growth and industrialization have led to a significant increase in global energy demand, although there was a 1% decrease in 2020 due to the COVID-19 pandemic. Despite advances in renewable energy, fossil fuels remain predominant. The building sector, which ranks third in terms of energy consumption, contributes significantly to $CO_2$ emissions, with air conditioning systems (heating, cooling, and ventilation) alone accounting for 40 to 45% of total energy consumption. The integration of photovoltaic (PV) technology into buildings via BIPV (Building Integrated Photovoltaics) or BAPV (Building Applied Photovoltaics) offers a promising solution to partially meet this energy demand and address $CO_2$ emission reduction challenges. However, the efficiency of photovoltaic cells is sensitive to their temperature, necessitating integration methods that promote their passive cooling, such as natural convection, particularly in BIPV systems, to maintain their performance and longevity. Passive solar-assisted technologies, such as double-skin facades, Trombe walls, and solar chimneys, utilize solar energy to enhance natural ventilation in buildings. Among these, solar wall chimneys provide effective cooling and ventilation. Building upon the NAMICO project (a Franco-Australian CNRS joint venture), a small-scale vertical solar chimney model under controlled conditions was developed at LOCIE to gain new insights and collect reliable data on BIPV systems integrated into a double-skin facade connected by a horizontal inlet to the living space.

In this doctoral research, experimental protocols and quasi-steady-state criteria for the experimental bench are first established. Experiments are then conducted to study the impact of the room air inlet position on the performance of the solar chimney and room

ventilation. These experiments are performed with a fixed aspect ratio (height/thickness of the air gap) of 8 for the chimney, a chimney wall surface emissivity of 0.08, and an electrical flux of 110 $W/m^2$ and 235 $W/m^2$ from the inlet-forming wall of the chimney. Additionally, experiments investigate the effects of varying the chimney wall surface emissivity from 0.08 to 0.96 under the same electrical heat flux conditions on the performance of the chimney. The thermal and kinematic performance of the L-shaped vertical channel was evaluated by measuring the chimney wall temperatures and performing PIV (Particle Image Velocimetry) measurements at the central plane of the chimney once the test bench reached a quasi-steady thermal state. Natural convection flows are characterized in 2D (mean velocity fields) across the entire height of the channel. The impact of the room air inlet position is evaluated by measuring the room air temperature, observing flow patterns using a smoke generator inside the reduced scale model of the room, and measuring the measuring the 2D mean velocity field across the entire height of the chimney. Finally, a simplified 1D model, the Steady Heat Balance Model (SHBM), is developed for the experimental test bench and compared with experiments.

It was found that the room air inlet position does not visibly impact the performance of the chimney but influences the temperature distribution in the room. Additionally, the horizontal inlet geometry of the vertical channel affects the evolution of the thermal field of the walls and natural convection. Increasing the heat flux strengthens the thermal field of the walls and the flow field inside the chimney on both low- and high-emissivity walls of the channel. Higher surface emissivity improves wall-to-wall radiative heat transfer, modifying the wall thermal profiles and flow patterns by altering the thermal conditions from one-wall to asymmetrical heating of the channel. Consequently, the temperature of the heated wall decreases significantly, while the temperature of the radiated wall

increases proportionally. The air volumetric flow rate from the chimney is higher on high-emissivity walls compared to low-emissivity walls for the same injected wall heat flux. No reverse flow phenomenon is observed along the unheated wall on both low- and high-emissivity chimney walls. However, the horizontal air inlet of the vertical channel creates recirculation zones; the size of these structures is affected by the injected heat flux and wall emissivity. Finally, the SHBM modelling approach helps predict ventilation rate of solar chimney but tends to overestimate chimney wall temperatures, requiring further analysis to ensure its robustness.

**Keywords:** BIPV double façade, solar chimney, L-shaped vertical channel, natural convection, wall-to-wall radiation, room inlet position, one-wall uniform heating, surface emissivity, PIV measurements, flow field analysis, wall thermal fields, reverse flow, recirculation zones, SHBM modelling.

# *RÉSUMÉ*

La croissance rapide de la population mondiale et de l'industrialisation ont conduit à une augmentation significative de la demande énergétique à l'échelle mondiale, bien qu'une baisse de 1% se soit produite en 2020 en raison de la pandémie de COVID-19. Malgré les progrès réalisés dans le domaine des énergies renouvelables, les combustibles fossiles restent prédominants. Le secteur du bâtiment, qui se classe au troisième rang en termes de consommation d'énergie, contribue fortement aux émissions de $CO_2$, les systèmes de conditionnement d'air (chauffage, rafraichissement, ventilation) représentant à eux seuls 40 à 45% de la consommation énergétique totale. L'intégration de la technologie photovoltaïque (PV) dans les bâtiments via le BIPV (intégration) ou le BAPV (surimposition) offre une solution prometteuse pour répondre partiellement à cette demande énergétique et aux enjeux de la réduction des émissions de $CO_2$. Cependant, l'efficacité des cellules photovoltaïques est sensible à leur niveau de, nécessitant des méthodes d'intégration favorisant leur rafraichissement passif comme par convection naturelle, notamment dans les systèmes BIPV, pour maintenir leur performance et leur longévité. Les technologies passives assistées par l'énergie solaire, telles que les façades double-peau, les murs Trombe et les cheminées solaires, utilisent l'énergie solaire pour améliorer la ventilation naturelle des bâtiments. Parmi celles-ci, les cheminées solaires murales offrent un refroidissement et une ventilation efficaces. En s'appuyant sur le projet NAMICO (Exploratoire CNRS Franco-Australien), un modèle à échelle réduite de cheminée solaire verticale à échelle réduite et en conditions contrôlées a été fabriquée au LOCIE afin d'apporter de nouvelles connaissances et collecter des données fiables sur les systèmes BIPV intégrés sur une façade à double peau connectée par une ouverture d'entrée horizontale avec l'espace habitable.

Dans cette recherche doctorale, les protocoles expérimentaux et les critères de quasi-état stationnaire pour le banc d'essais sont d'abord établis. Des expériences sont ensuite menées pour étudier l'impact de la position de l'entrée d'air de la pièce sur les écoulements de convection naturelle et les transferts de chaleur associés pilotant la performance de la cheminée solaire et de la ventilation de la pièce. Ces expériences sont réalisées avec un rapport de forme (hauteur/épaisseur de la lame d'air) fixe de la cheminée de 8, une émissivité de surface des parois de la cheminée de 0,08, et un flux électrique de 110 W/m² et 235 W/m² provenant du mur formant l'entrée de la cheminée. De plus, des expériences investiguent les effets de la variation de l'émissivité de surface des parois de la cheminée de 0,08 à 0,96 sous les mêmes conditions de flux de chaleur électrique sur la performance de la cheminée. La performance thermique et cinématique du canal vertical en forme de L a été évaluée en mesurant les températures des parois de la cheminée et en réalisant des mesures PIV au niveau du plan central de la cheminée une fois que le banc d'essai a atteint l'état quasi-stationnaire thermique. Les écoulements de convection naturelle sont caractérisés en 2D (champs de vitesse moyennés) sur dans l'ensemble de la hauteur du canal. L'impact du positionnement de l'entrée d'air de la pièce en amont du canal, sur les écoulements est évalué en mesurant la température de l'air de la pièce et en observant les schémas d'écoulement à l'aide d'un générateur de fumée. Enfin, un modèle simplifié unidimensionnel, le Modèle de Bilan Thermique Stationnaire (SHBM), est développé pour le banc d'essai expérimental et confronté aux expérimentations.

Il a été constaté que la position de l'entrée d'air de la pièce n'impacte pas visiblement la performance de la cheminée, mais influence la distribution de la température dans la pièce. De plus, la géométrie de l'entrée de la cheminée en forme de L'affecte l'évolution du champ thermique des parois et de convection naturelle dans le canal vertical. L'augmentation du flux de chaleur renforce le champ thermique des parois et le champ

d'écoulement à l'intérieur de la cheminée sur les parois à faible et haute émissivité du canal. Une émissivité de surface plus élevée améliore le transfert de chaleur radiatif de paroi à paroi, modifiant les profils thermiques des parois et les schémas d'écoulement en modifiant les conditions thermiques du chauffage d'une paroi à un chauffage asymétrique du canal. En conséquence, la température de la paroi chauffée diminue notablement tandis que la température de la paroi recevant le rayonnement augmente proportionnellement. Le débit volumique d'air provenant de la cheminée est plus élevé sur les parois à haute émissivité par rapport aux parois à faible émissivité, pour le même flux de chaleur injecté en paroi. Aucun phénomène d'écoulement inverse n'est observé le long de la paroi non chauffée sur les parois à faible et haute émissivité de la cheminée. Les angles droits de l'entrée d'air dans le canal créent, des zones de recirculation ; la taille de ces structures est affectée par le flux de chaleur injecté ainsi que par l'émissivité des parois. Enfin, l'approche de modélisation SHBM aide à prédire la ventilation mais a tendance à surestimer les températures des parois de la cheminée, nécessitant une analyse plus approfondie pour garantir sa robustesse.

**Mots-clés :** double façade BIPV, cheminée solaire, canal vertical en forme de L, convection naturelle, radiation de paroi à paroi, position de l'entrée de la pièce, chauffage uniforme d'une paroi, émissivité de surface, mesures PIV, analyse du champ de vitesse d'écoulement, champs de température aux parois, zones de recirculation, modélisation SHBM.

## *ACKNOWLEDGEMENTS*

I wish to express sincere gratitude to individuals who have offered assistance and motivation during my academic Endeavor, contributing to the attainment of this significant milestone. Foremost, I am deeply grateful to my supervisor, Professor Christophe Menezo, whose invaluable guidance, and oversight have been instrumental throughout my candidacy. It is with sincere acknowledgment that I recognize his indispensable role, without which reaching this milestone would not have been possible. Additionally, I owe profound gratitude to my co-supervisor, Assistant Professor Mickael Pailha, for his exceptional support and proactive involvement during the entirety of the research process, particularly in the fabrication and experimental phases.

I am immensely thankful to Mr. David Cloet for his comprehensive technical assistance. His support spanned various aspects, including aiding in the design and implementation of experimental setups, the development of LabVIEW programs for data acquisition, and furnishing an Arduino-operated heating plate for conducting experiments on surface emissivity measurement. His contributions significantly contributed to the successful execution of experiments. Acknowledgment is also due to my fellow PhD colleagues and professors affiliated with the LOCIE Laboratory for their timely technical assistance when urgently required.

I also would like to gratefully thank Hadi Ahmadi Moghaddam, a fellow PhD student at UNSW, Sydney for his fruitful collaboration during the PIV experimentation Phase of the Project.

The administrative staff of LOCIE deserve commendation for fostering an enabling research environment, which allowed me to concentrate on my studies without undue administrative burden.

I also want to express my appreciation to the Higher Education Commission of Pakistan and Campus France for their financial assistance throughout my candidacy, without which pursuing a PhD abroad would have been unattainable.

Lastly, I would like to extend special thanks to my family members in Pakistan for their unconditional love, unwavering understanding, and encouragement, which alleviated my worries and contributed to my overall well-being during this academic journey.

## *DECLARATION*

I affirm that this dissertation represents solely my own efforts. To the fullest extent of my understanding, the material contained herein is original, except for citations acknowledging the contributions of other scholars. I wish to clarify that the research presented in chapters 4 and 5 was conducted in collaboration with Hadi Ahmadi Moghaddam, a fellow PhD student at UNSW, Sydney. This collaboration occurred during his Nicolas Baudin Internship at LOCIE in France, where he contributed to joint efforts involving PIV experimental design, experimental execution, and processing of the results. I stress that the design of the experimental setup, as well as the analysis and interpretation of both theoretical and experimental findings presented in this dissertation, are my own work. I confirm that no part of this dissertation has been previously submitted for any academic qualification at this or any other institution.

# *NOMENCLATURE*

**List of Symbols**

| | |
|---|---|
| g | gravitational constant [9.81 $m/s^2$] |
| K | thermal conductivity [W/m K] |
| $C_f$ | specific heat of air at constant pressure [J /kg K] |
| q” | heat flux [W/m2] |
| D | gape between walls of the chimney [m] |
| W | width of chimney [m] |
| L | height [m] |
| Y | height [m] |
| A | cross-sectional area of chimney [$m^2$] |
| $C_d$ | coefficient of discharge of air in chimney |
| X | thickness [m] |
| P | electrical power [W] |
| U | overall conductive heat transfer coefficient [$W/m^2$ K] |
| T | mean temperature [K] |
| h | heat transfer coefficient [$W/m^2$ K] |
| I | air exchange rate [1/h] |
| $\dot{m}$ | mass flow rate [kg/s] |
| $\dot{v}$ | volumetric air flow rate [$m^3/s$] |
| V | volume of the room attached to chimney |
| ACH | air change per hour [] |

**List of Greek Symbols**

| | |
|---|---|
| $\epsilon$ | surface emissivity [-] |

| | |
|---|---|
| $\mu_f$ | dynamic viscosity of air [kg/m s] |
| $\nu_f$ | kinematic viscosity of air [$m^2/s$] |
| $\rho_f$ | density of air at [$kg/m^3$] |
| $\sigma$ | Stefan–Boltzmann constant [ $5.67\times10-8$ $W/m^2$ $K^4$] |
| $\beta$ | thermal expansion coefficient [1/K] |

**List of Dimensionless Terms**

| | |
|---|---|
| Nu | Nusselt number [ $Nu = \frac{h\,L}{\kappa_f}$ ] |
| Gr | Grashof number [ $Gr_A = \frac{g\beta\,\Delta T\,L^3}{\nu_{f1}{}^2}$ ] |
| Pr | Prandtl number [ $Pr = \frac{c_f \mu_f}{K_f}$ ] |
| Ra | Rayleigh number [ $Ra = \frac{g\,\boldsymbol{\beta}\,q''_{in}\,Y^4}{VK\boldsymbol{\alpha}}$ , $Ra = \frac{g\,\boldsymbol{\beta}\,\Delta T\,L^4}{VK\boldsymbol{\alpha}}$ ] |
| $Ra^*$ | modified Rayleigh number [ $Ra^* = \frac{g\,\boldsymbol{\beta}\,q''_{in}\,D^5}{VK\,\boldsymbol{\alpha}\,Y_H}$ ] |
| X/W | non-dimensional width of the chimney |
| Y/H | non-dimensional height of the chimney |
| Z/D | non-dimensional air cavity gap |

**List of Subscripts**

| | |
|---|---|
| A | active wall of the chimney |
| P | passive wall of the chimney |
| H | heater in the active of the chimney |
| a | ambient air |
| f | fluid inside the chimney |
| r | air in the room |
| i | glass wool insulation |
| inlet | inlet of the chimney |

| | |
|---|---|
| out | outlet of the chimney |
| wall | active and passive wall of the chimney |
| loss | loss of thermal flux from the back side of the heater |
| elec | electrical flux from the heater |
| in | thermal flux reaching the fluid in contact with active wall |
| film | flim |
| avg | average |
| st | stack height of the chimney |
| adia | adiabatic top section of the chimney |
| w | plexiglass wall of the room attached to the chimney |
| B | gypsum board on the passive wall |

**List of Superscripts**

| | |
|---|---|
| conv | convection heat transfer |
| rad | radiative heat transfer |

**List of Abbreviations**

| | |
|---|---|
| AW | All window |
| BAPV | Building attached photovoltaic |
| BES | Building energy simulation |
| BIPV | Building integrated photovoltaic |
| BOS | Background oriented Schlieren |
| BW | Bottom window |
| CFD | Computational fluid dynamics |
| COVID-19 | Coronavirus disease of 2019 |
| GEB | Global energy balance |
| GSCW | Glazed solar chimney wall |
| GUI | Graphical user interface |
| HH | High emissivity |

| | |
|---|---|
| HPC | High performance computing |
| HVAC | Heating, ventilation, and air conditioning |
| IA | Interrogation area |
| IPWSC | Inclined passive wall solar chimney |
| IR | Infrared radiation |
| LDA | Laser Doppler anemometry |
| LL | Low emissivity |
| LOCIE | Laboratoire procédés énergie bâtiment |
| MW | Middle window |
| MSW | Metallic solar wall |
| MTW | Modified Trombe wall |
| NZE | Net Zero Emissions |
| PCB | Printed circuit board |
| PIV | Particle image velocimetry |
| PVC | Polyvinyl chloride |
| RB | Radiant barrier |
| RTD | Resistance temperature detector |
| RSC | Roof solar chimney |
| SC | Solar chimney |
| SHBM | Steady heat balance model |
| THBM | Transient heat balance model |
| TI | Thermal imager |
| TW | Top window |
| UHF | Uniform heat flux |
| UWT | Uniform wall temperature |

## *LIST OF TABLES*

## *LIST OF FIGURES*

# *TABLE OF CONTENTS*

# CHAPTER 1: INTRODUCTION

## 1.1 Motivation

Buildings, not only significant energy consumers but also contributors to greenhouse gas emissions [1,2], stand at the crossroads of global energy demand and climate change mitigation efforts. Balancing the reduction of energy consumption in the expanding building sector while maintaining thermal comfort is a formidable research challenge [3]. Hence, it becomes crucial to meet the energy needs of our built environment with passive technologies. Over the 19th and 20th centuries, industrialization spurred innovations in natural ventilation strategies [4]. Several passive ventilation strategies [5–11] have been devised to improve indoor thermal comfort, among which the solar chimney stands out for its energy-saving potential, versatility, and retrofitting ease into existing building architecture. The double-skin façade, Trombe wall, and solar chimney are examples of open-ended vertical solar-heated buoyancy-driven ventilation technologies that operate on the same principle. These technologies have been extensively used to enhance passive cooling of living spaces [12–18] and building-integrated photovoltaics [19–23] by utilizing the stack effect. The solar chimney harnesses buoyancy effects resulting from the absorption of solar heat to enhance natural ventilation [12,24]. It comprises a solar collector that absorbs and retains solar heat along its absorber wall, thereby warming the air within the channel [13]. This thermal buoyancy creates a natural updraft, drawing ambient room air into the chimney channel to offset the pressure drop caused by the upward airflow [25]. Through minor adjustments, a wall-mounted solar chimney affixed to a building's facade can be adapted to operate in heating, cooling, and thermal insulation modes as dictated by seasonal requirements [26,27].

For a solar-heated vertical channel, the inlet or outlet opening can be either horizontal or vertical. A horizontal inlet opening on a vertical wall attached to the facade of the building typically facilitates natural ventilation [15,28–30]. Conversely, a vertical inlet opening at the bottom of the channel on a vertical wall attached to the facade represents the operation of ventilation cooling in a double façade [26,27]. Similarly, a vertical inlet opening at the bottom of the cavity on a vertical wall attached to the ceiling is also linked to natural ventilation [14,31–34]. Additionally, the top of a solar chimney can have an open vertical outlet [14,15,31], or be covered with a rain guard for horizontal outlets, enabling airflow in any direction [22,35–37] .

Several indoor experimental rigs, both standalone and wall-mounted, have been devised with varying wall heating strategies and chimney configurations. Numerous studies have explored standalone setups [18,33,35,38–43], while fewer have focused on wall-mounted solar chimneys with attached room test rigs [16,44–46]. The studies with the attached room model have employed different heating conditions for chimney walls. For instance, [44,45] utilized a symmetric UWT heating strategy, [46] employed an adiabatic wall for the chimney inlet and a UHF wall for the opposite side, and [16] utilized a UHF wall for the chimney inlet and an adiabatic wall opposite. The author [16] also contends that these modelling approaches better simulate real-world scenarios where solar radiation passing through glass walls is absorbed by the absorber wall.

None of the mentioned experimental studies have comprehensively measured the detailed thermal fields on the chimney walls for conjugate heat transfer analysis. Nor have they quantitatively assessed the time-averaged velocity field throughout the chimney's height or investigated the development of accompanying flow structures. Additionally, there has been no effort to establish a correlation between wall thermal fields and the kinematic

field resulting from natural convection air flow inside the chimney, mainly due to experimental constraints. Consequently, CFD computational studies have predominantly focused on either a standalone numerical model of L-shaped solar ventilation channels [17,20,21,27,47] or computational domain models with attached rooms [48–50] to examine heat transfer and airflow in one-wall heated L-shaped vertical channels.

Numerical studies [49,50] reveal that standalone numerical models of wall-mounted solar chimneys display higher velocity profiles compared to attached room models. They also show reduced turbulent kinetic energy production and a smaller region of reverse flow influence at the horizontal inlet. Consequently, the standalone wall-mounted chimney model tends to over-predict the mass flow rate. Additionally, studies by [20,47,48] indicate that heat transfer and airflow in single-wall heated solar ventilation channels are influenced by factors including heat distribution on channel walls due to wall-to-wall radiative heat transfer resulting from increased surface emissivity of chimney walls, total heat input, and the flow resistance at the inlet and outlet of the chimney.

Several experimental investigations, including references [16,44,51], [17,20,47,49,52], have highlighted a reverse flow phenomenon at the chimney outlet across different Rayleigh numbers. Conversely, studies such as [15,46,53] have not observed this phenomenon experimentally. Flow structures and development in the L-shaped vertical channel have been numerically computed by multiple studies [20,47,48,50,52], which require further experimental investigations. Additionally, [44,46] conducted experimental studies on wall chimneys, with [44] investigating a full-scale model attached to a room, while [46] focused on a reduced-scale model. They observed airflow movement from the window into the chimney inlet, with contrasting claims regarding the airflow pattern within the room. Meanwhile, [54] developed a full-scale numerical model

to examine the influence of window placement on chimney performance. The results suggested a minimal impact of room dimensions and window placement on the airflow rate out of the chimney. Addressing these identified gaps necessitates further experimental investigation.

## 1.2 Aims and Objectives

An indoor wall-mounted solar chimney, along with a scaled-down room model featuring three room inlet positions, will be fabricated. The chimney incorporates UHF one-wall heating similar to that described [16] on the inlet-forming wall. Unlike previous indoor experimental solar chimney studies, both walls will be made from the same opaque material to maintain adiabatic conditions on the non-heated wall of the chimney and minimize conduction heat losses from the heated wall. To manipulate the surface emissivity of the chimney walls, the inner surfaces of the heated and non-heated walls will be wrapped with aluminium tape. Additionally, an adiabatic chimney top will be added at the trailing edge of the heated wall to maintain adiabatic conditions and increase the stack height of the wall chimney.

The thesis concentrates on the following pivotal research inquiries:

- The present study aims to offer experimental insights into the development of natural convection flows and the associated thermal fields along the walls that arise at quasi-steady state within a one-wall heated L-shaped vertical channel connected to a small-scale model of a room.
- The study aims to investigate the impact of variations in input heat flux, modified Rayleigh number and wall emissivity on a one-wall heated L-shaped vertical channel. This will be done by analysing the operational wall temperature

evolution and the streamwise time-averaged velocity field, considering both low and high emissive walls of the chimney.

- The study aims to investigate the impact of changing the surface emissivity of chimney walls from low to high, as well as increasing heat input fluxes and modifying Rayleigh numbers, on the volume of air flowing out of the L-shaped vertical channel.
- The study aims to explore the effect of room inlet position on the thermal and kinematical performance of a wall-mounted solar chimney, as well as on the air temperature distribution and airflow patterns within a scaled-down room model connected to the chimney.
- A one-dimensional steady heat balance model will be developed for the experimental bench, building upon the approach pioneered by [12,55], and subsequently utilized by multiple authors [15,28,30,48,56–59] to predict the performance of outdoor solar chimneys under diverse climatic conditions.
- The steady heat balance model simulation will be compared with experimental data from the bench to evaluate its reliability in predicting chimney wall volume flow rate and mean temperature under varying input heat fluxes and emissive wall conditions.

## 1.3 Significance and Contributions

The results from this experimental bench will serve to optimizing the design and performance of L-shaped solar-heated natural ventilation cavities and solar building facades attached to living spaces via horizontal inlet air openings. Moreover, the findings of study will contribute to optimize the efficiency of building-integrated photovoltaics

(BIPV) by lowering the operating temperature of PV cells attached to wall-mounted solar chimney structures and L-shaped solar building facades.

This research work presents the first experimental investigation into natural convection flows within a one-wall heated L-shaped vertical channel connected to a living space. The research employs experimental fluid dynamics techniques such as particle image velocimetry (PIV) to explore the effects of varying heat flux, modified Rayleigh number, and changes in chimney wall surface emissivity on the development of natural convection flows. Additionally, the study provides experimental insights into the impact of the size and placement of room air inlets on the thermal and kinematic performance of a wall-mounted solar chimney. The study also investigates effect of position of room air inlet on room ventilation by measuring air temperature distribution and visualizing airflow patterns within a scaled-down model of a room connected to an L-shaped solar-ventilated vertical channel.

The research aims to produce precise and comprehensive data to deepen our understanding of L-shaped solar ventilated vertical channels and their integration with living spaces, as well as wall-mounted solar chimney structures. This new data will build upon existing computational fluid dynamics (CFD) studies, refining and advancing our knowledge in this area. By exploring the performance of these systems, the information gleaned from these experiments is intended to enhance the effectiveness and efficiency of solar-driven vertical ventilation channels. Ultimately, this research aims to improve indoor air quality, increase energy efficiency in buildings, and mitigate environmental impacts.

## 1.4 Thesis Structure

The thesis comprises seven separate chapters, each with its own distinct focus, outlined as follows:

**Chapter 1** offers a concise overview of the motivation of the study and background, outlining its objectives and the structure of the thesis.

**Chapter 2** provides an extensive overview of the latest research on solar chimneys, including the methodologies used and the parameters examined. It offers a synopsis of the literature, highlights research gaps, and clarifies the aim of addressing some of the gaps in the current study.

**Chapter 3** details the fabrication of the experimental bench, including its instrumentation and operation. This covers the installation, functioning, and specifications of thermocouples, PIV systems, heat flux injection systems, omnidirectional anemometers, and data logger switch units used to generate the experimental data.

**Chapter 4** describes the modification of the laboratory duct ventilation system for conducting natural convection experiments with the fabricated experimental bench. It discusses the evolution of air temperature near the rig with and without a heating source in the laboratory room, dynamic analysis of the experimental bench to establish the thermal quasi-steady state of the test rig and assesses repeatability in the operational wall temperature fields, and criteria for particle image velocity (PIV) tests, including a repeatability analysis on vertical velocity profiles.

**Chapter 5** offers an in-depth experimental analysis of the fabricated indoor model of a wall-mounted solar chimney integrated into a scaled-down room model. It explores the influence of position and size of room air inlet on the performance of solar chimneys and

room ventilation. Additionally, it also investigates the impact of varying surface emissivity on both active and passive chimney walls, as well as single-wall uniform heating on wall temperature and velocity fields within the L-shaped vertical channel, featuring an adiabatic extension at the outlet.

**Chapter 6** introduces a simplified theoretical model for an indoor vertical wall solar chimney featuring an adiabatic chimney top. The study thoroughly assesses the thermal and kinematic performance of the developed model with experimental results from the test rig. Furthermore, the impact of changes in wall surface emissivity and chimney air gap on the performance of the theoretical model has been discussed, along with recommendations for improvements.

**Chapter 7** summarizes the key conclusions and offers recommendations for future research pertaining to this project. It outlines the major findings and suggests avenues for further study.

**Appendix A** presents the measurement technique for finding the value of bulk emissivity of aluminium scotch tape and of the matte black paint layer on the aluminium scotch tape.

## 1.5 References

[1] The GlobalABC releases 2022 Global Status Report for Buildings and Construction | Globalabc, (n.d.). https://globalabc.org/news/globalabc-releases-2022-global-status-report-buildings-and-construction (accessed September 1, 2023).

[2] M. González-Torres, L. Pérez-Lombard, J.F. Coronel, I.R. Maestre, D. Yan, A review on buildings energy information: Trends, end-uses, fuels and drivers, Energy Reports 8 (2022) 626–637. https://doi.org/10.1016/j.egyr.2021.11.280.

[3] AR5 Climate Change 2014: Mitigation of Climate Change — IPCC, (n.d.). https://www.ipcc.ch/report/ar5/wg3/ (accessed September 18, 2023).

[4] A.Y.K. Tan, N.H. Wong, Parameterization Studies of Solar Chimneys in the Tropics, Energies 6 (2013) 145–163. https://doi.org/10.3390/en6010145.

[5] Net Zero by 2050 - A Roadmap for the Global Energy Sector, (n.d.).

[6] L. Moosavi, M. Zandi, M. Bidi, E. Behroozizade, I. Kazemi, New design for solar chimney with integrated windcatcher for space cooling and ventilation, Building and Environment 181 (2020) 106785. https://doi.org/10.1016/j.buildenv.2020.106785.

[7] Z. Hu, W. He, J. Ji, S. Zhang, A review on the application of Trombe wall system in buildings, Renewable and Sustainable Energy Reviews 70 (2017) 976–987. https://doi.org/10.1016/j.rser.2016.12.003.

[8] F. Manzano-Agugliaro, F.G. Montoya, A. Sabio-Ortega, A. García-Cruz, Review of bioclimatic architecture strategies for achieving thermal comfort, Renewable and Sustainable Energy Reviews 49 (2015) 736–755. https://doi.org/10.1016/j.rser.2015.04.095.

[9] C.-M. Lai, S. Hokoi, Solar façades: A review, Building and Environment 91 (2015) 152–165. https://doi.org/10.1016/j.buildenv.2015.01.007.

[10] N. Monghasemi, A. Vadiee, A review of solar chimney integrated systems for space heating and cooling application, Renewable and Sustainable Energy Reviews 81 (2018) 2714–2730. https://doi.org/10.1016/j.rser.2017.06.078.

[11] H. Omrany, A. Ghaffarianhoseini, A. Ghaffarianhoseini, K. Raahemifar, J. Tookey, Application of passive wall systems for improving the energy efficiency in buildings: A comprehensive review, Renewable and Sustainable Energy Reviews 62 (2016) 1252–1269. https://doi.org/10.1016/j.rser.2016.04.010.

[12] N.K. Bansal, J. Mathur, S. Mathur, M. Jain, Modeling of window-sized solar chimneys for ventilation, Building and Environment 40 (2005) 1302–1308. https://doi.org/10.1016/j.buildenv.2004.10.011.

[13] N.K. Bansal, R. Mathur, M.S. Bhandari, Solar chimney for enhanced stack ventilation, Building and Environment 28 (1993) 373–377. https://doi.org/10.1016/0360-1323(93)90042-2.

[14] C. Afonso, A. Oliveira, Solar chimneys: simulation and experiment, (2000) 9.

[15] K.S. Ong, C.C. Chow, Performance of a solar chimney, Solar Energy (2003) 17.

[16] R. Khanal, C. Lei, An experimental investigation of an inclined passive wall solar chimney for natural ventilation, Solar Energy 107 (2014) 461–474. https://doi.org/10.1016/j.solener.2014.05.032.

[17] R. Khanal, C. Lei, Numerical investigation of the ventilation performance of a solar chimney, ANZIAM Journal 52 (2010) C899–C913. https://doi.org/10.21914/anziamj.v52i0.3947.

[18] Z.D. Chen, P. Bandopadhayay, J. Halldorsson, C. Byrjalsen, P. Heiselberg, Y. Li, An experimental investigation of a solar chimney model with uniform wall heat flux, Building and Environment 38 (2003) 893–906. https://doi.org/10.1016/S0360-1323(03)00057-X.

[19] S. M, Cooling of building integrated photovoltaics by ventilation air., (1999). https://www.aivc.org/resource/cooling-building-integrated-photovoltaics-ventilation-air (accessed October 5, 2023).

[20] G. Gan, Prediction of heat transfer and air flow in solar heated ventilation cavities, Computational Fluid Dynamics: Theory, Analysis and Applications (2013) 137–178.

[21] B. Moshfegh, M. Sandberg, Flow and heat transfer in the air gap behind photovoltaic panels, Renewable and Sustainable Energy Reviews 2 (1998) 287–301. https://doi.org/10.1016/S1364-0321(98)00005-7.

[22] B. Moshfegh, M. Sandberg, Investigation of fluid flow and heat transfer in a vertical channel heated from one side by PV elements, part I - Numerical Study, Renewable Energy 8 (1996) 248–253. https://doi.org/10.1016/0960-1481(96)88856-2.

[23] M. Sandberg, B. Moshfegh, Investigation of fluid flow and heat transfer in a vertical channel heated from one side by PV elements, part II - Experimental study, Renewable Energy 8 (1996) 254–258. https://doi.org/10.1016/0960-1481(96)88857-4.

[24] W.F.M. Yusoff, E. Salleh, N.M. Adam, A.R. Sapian, M. Yusof Sulaiman, Enhancement of stack ventilation in hot and humid climate using a combination of roof solar collector and vertical stack, Building and Environment 45 (2010) 2296–2308. https://doi.org/10.1016/j.buildenv.2010.04.018.

[25] V. Siva Reddy, M. Premalatha, K.R. Ranjan, Experimental studies on solar chimney for enhanced ventilation, International Journal of Sustainable Energy 31 (2012) 35–42. https://doi.org/10.1080/1478646X.2010.534554.

[26] T. Miyazaki, A. Akisawa, T. Kashiwagi, The effects of solar chimneys on thermal load mitigation of office buildings under the Japanese climate, Renewable Energy 31 (2006) 987–1010. https://doi.org/10.1016/j.renene.2005.05.003.

[27] T. Zhang, H. Yang, Flow and heat transfer characteristics of natural convection in vertical air channels of double-skin solar façades, Applied Energy 242 (2019) 107–120. https://doi.org/10.1016/j.apenergy.2019.03.072.

[28] J. Hirunlabh, W. Kongduang, P. Namprakai, J. Khedari, Study of natural ventilation of houses by a metallic solar wall under tropical climate, Renewable Energy 18 (1999) 109–119. https://doi.org/10.1016/S0960-1481(98)00783-6.

[29] W. Rattanongphisat, P. Imkong, S. Khunkong, An Experimental Investigation on the Square Steel Solar Chimney for Building Ventilation Application, Energy Procedia 138 (2017) 1165–1170. https://doi.org/10.1016/j.egypro.2017.10.226.

[30] J. Arce, M.J. Jiménez, J.D. Guzmán, M.R. Heras, G. Alvarez, J. Xamán, Experimental study for natural ventilation on a solar chimney, Renewable Energy 34 (2009) 2928–2934. https://doi.org/10.1016/j.renene.2009.04.026.

[31] A. Lechowska, N. Szczepanik-Ścisło, J. Schnotale, M. Stelmach, T. Pyszczek, CFD modelling of transient thermal performance of solar chimney used for passive ventilation in a building, IOP Conf. Ser.: Mater. Sci. Eng. 415 (2018) 012049. https://doi.org/10.1088/1757-899X/415/1/012049.

[32] A. Abdeen, A.A. Serageldin, M.G.E. Ibrahim, A. El-Zafarany, S. Ookawara, R. Murata, Solar chimney optimization for enhancing thermal comfort in Egypt: An experimental and numerical study, Solar Energy 180 (2019) 524–536. https://doi.org/10.1016/j.solener.2019.01.063.

[33] W. Ding, Y. Hasemi, T. Yamada, Natural ventilation performance of a double-skin façade with a solar chimney, Energy and Buildings 37 (2005) 411–418. https://doi.org/10.1016/j.enbuild.2004.08.002.

[34] W. Liping, L. Angui, A numerical study of vertical solar chimney for enhancing stack ventilation in buildings, in: 2004. https://www.semanticscholar.org/paper/A-numerical-study-of-vertical-solar-chimney-for-in-Liping-Angui/6b893c56f67c0ec342826d0e7ce324c4ab50a5bb (accessed November 9, 2023).

[35] A. La Pica, G. Rodonò, R. Volpes, An experimental investigation on natural convection of air in a vertical channel, International Journal of Heat and Mass Transfer 36 (1993) 611–616. https://doi.org/10.1016/0017-9310(93)80036-T.

[36] A. Li, P. Jones, P. Zhao, L. Wang, Heat Transfer and Natural Ventilation Airflow Rates from Single-sided Heated Solar Chimney for Buildings, Journal of Asian Architecture and Building Engineering 3 (2004) 233–238. https://doi.org/10.3130/jaabe.3.233.

[37] W. Liping, L. Angui, A numerical Study of Trombe Wall for Enhancing Stack Ventilation in Buildings, (2006) 7.

[38] S.A.M. Burek, A. Habeb, Air flow and thermal efficiency characteristics in solar chimneys and Trombe Walls, Energy and Buildings 39 (2007) 128–135. https://doi.org/10.1016/j.enbuild.2006.04.015.

[39] D. Ryan, S.A.M. Burek, Experimental study of the influence of collector height on the steady state performance of a passive solar air heater, Solar Energy 84 (2010) 1676–1684. https://doi.org/10.1016/j.solener.2010.05.018.

[40] A. Dimoudi, Investigation of the flow and heat transfer in a solar chimney, The University of Bath's Research Portal (n.d.). https://researchportal.bath.ac.uk/en/studentTheses/investigation-of-the-flow-and-heat-transfer-in-a-solar-chimney (accessed October 3, 2023).

[41] H. Jing, Z. Chen, A. Li, Experimental study of the prediction of the ventilation flow rate through solar chimney with large gap-to-height ratios, Building and Environment 89 (2015) 150–159. https://doi.org/10.1016/j.buildenv.2015.02.018.

[42] J. Kong, C. Lei, J. Niu, Experimental and Numerical Investigations of Roof-top Solar Chimney for Building Ventilation, (n.d.).

[43] Y. Hou, H. Li, A. Li, Experimental and theoretical study of solar chimneys in buildings with uniform wall heat flux, Solar Energy 193 (2019) 244–252. https://doi.org/10.1016/j.solener.2019.09.061.

[44] A. Bouch

air, Solar chimney for promoting cooling ventilation in southern Algeria, (n.d.).

[45] A. Bouchair, Solar induced ventilation in the Algerian and similar climates, phd, University of Leeds, 1989. https://etheses.whiterose.ac.uk/616/ (accessed October 11, 2023).

[46] S. Spencer, An experimental investigation of a solar chimney natural ventilation system, masters, Concordia University, 2001. https://spectrum.library.concordia.ca/id/eprint/1378/ (accessed September 26, 2023).

[47] G. Gan, General expressions for the calculation of air flow and heat transfer rates in tall ventilation cavities, Building and Environment 46 (2011) 2069–2080. https://doi.org/10.1016/j.buildenv.2011.04.014.

[48] R. Bassiouny, N.S.A. Koura, An analytical and numerical study of solar chimney use for room natural ventilation, Energy and Buildings 40 (2008) 865–873. https://doi.org/10.1016/j.enbuild.2007.06.005.

[49] R. Khanal, C. Lei, A numerical investigation of buoyancy induced turbulent air flow in an inclined passive wall solar chimney for natural ventilation, Energy and Buildings 93 (2015) 217–226. https://doi.org/10.1016/j.enbuild.2015.02.019.

[50] T.N. Huynh, Y.Q. Nguyen, Numerical simulation of a solar chimney for natural ventilation of a building: Comparison of different computational domains, IOP Conf. Ser.: Mater. Sci. Eng. 1109 (2021) 012014. https://doi.org/10.1088/1757-899X/1109/1/012014.

[51] R. Khanal, C. Lei, Flow reversal effects on buoyancy induced air flow in a solar chimney, Solar Energy 86 (2012) 2783–2794. https://doi.org/10.1016/j.solener.2012.06.015.

[52] B. Zamora, A.S. Kaiser, Optimum wall-to-wall spacing in solar chimney shaped channels in natural convection by numerical investigation, Applied Thermal Engineering 29 (2009) 762–769. https://doi.org/10.1016/j.applthermaleng.2008.04.010.

[53] L.P. Chung, M.H. Ahmad, D.R. Ossen, M. Hamid, Effective Solar Chimney Cross Section Ventilation Performance in Malaysia Terraced House, Procedia - Social and Behavioral Sciences 179 (2015) 276–289. https://doi.org/10.1016/j.sbspro.2015.02.431.

[54] L. Shi, G. Zhang, An empirical model to predict the performance of typical solar chimneys considering both room and cavity configurations, Building and Environment 103 (2016) 250–261. https://doi.org/10.1016/j.buildenv.2016.04.024.

[55] K.S. Ong, A mathematical model of a solar chimney, Renewable Energy (2003) 14.

[56] H.H. Al-Kayiem, S. K.V., S.I.U.-H. Gilani, Mathematical analysis of the influence of the chimney height and collector area on the performance of a roof top solar chimney, Energy and Buildings 68 (2014) 305–311. https://doi.org/10.1016/j.enbuild.2013.09.021.

[57] R. Vargas-López, J. Xamán, I. Hernández-Pérez, J. Arce, I. Zavala-Guillén, M.J. Jiménez, M.R. Heras, Mathematical models of solar chimneys with a phase change material for ventilation of buildings: A review using global energy balance, Energy 170 (2019) 683–708. https://doi.org/10.1016/j.energy.2018.12.148.

[58] M.A. Hosien, S.M. Selim, Effects of the geometrical and operational parameters and alternative outer cover materials on the performance of solar chimney used for natural ventilation, Energy and Buildings 138 (2017) 355–367. https://doi.org/10.1016/j.enbuild.2016.12.041.

[59] C. Jiménez-Xamán, J. Xamán, N.O. Moraga, I. Hernández-Pérez, I. Zavala-Guillén, J. Arce, M.J. Jiménez, Solar chimneys with a phase change material for buildings: An overview using CFD and global energy balance, Energy and Buildings 186 (2019) 384–404. https://doi.org/10.1016/j.enbuild.2019.01.014.

# CHAPTER 2: STATE OF THE ART REVIEW

## 2.1 Introduction

Buildings, which are not only substantial consumers of energy but also contributors to greenhouse gas emissions, The intersection of worldwide energy demand, efforts to combat climate change, and a and a reduction in consumption of energy within the growing building sector without compromising on the pursuit of thermal comfort represents one of the most challenging areas of research. As the world deals with the aftermath of climate change, it is imperative to address the energy needs of our built environment with passive technologies. In this section, an overview of the current global energy demand, the state of climate change, and the role buildings play in the energy sector is provided. Moreover, the discussion covers the escalating energy consumption and the growing demand for heating and cooling within the built environment. It provides a global perspective, with a specific emphasis on Europe.

## 2.2 Bioclimatic Architecture

The purpose of architecture has traditionally been to provide protection to humans from external environmental factors. In the realm of bioclimatic architecture, the goal is to attain human thermal comfort through proactive engagement with the ambient climatic conditions, such as solar exposure, prevailing winds, and temperature fluctuations, to minimize the requirement for heating, cooling, and artificial lighting. Throughout history, in diverse geographical regions and climates, architectural advancements have evolved through a process of trial and error rather than being designed by professional architects with the common goal of optimizing indoor thermal comfort, a phenomenon commonly referred to as vernacular architecture, which offers notable case studies in countries such

as India [1], Pakistan [2], China [3], and Iran [4]. Since the Industrial Revolution, the extensive utilization of non-renewable energy for building climate control has defined 20$^{th}$ century buildings, relegating the concept of thermal comfort in modern buildings to reliance on continuously energy-consuming devices with severe environmental impacts [5]. The pursuit of meeting the Net Zero Emissions (NZE) target by 2050, as defined in the report [6], to mitigate the carbon footprint of the buildings has sparked a renewed interest in bioclimatic architecture.

### 2.2.1 Strategies for Bioclimatic Design

The Givoni bioclimatic chart, illustrated in Figure 2.1, is utilized to integrate bioclimatic strategies into architectural design, customized for various climate zones, with the aim of maximizing human comfort [7]. There are 14 distinct zones outlined in the chart. Among these, zones 1 and 2 represent the desired comfort areas. Therefore, the goal is to plan climatic conditions and corresponding architectural methods to transition the built environment into these comfort zones. Whenever feasible, passive strategies will be employed since they do not consume any energy. In cases where passive strategies are not solely viable, passive strategies are integrated with active energy devices to minimize energy consumption.

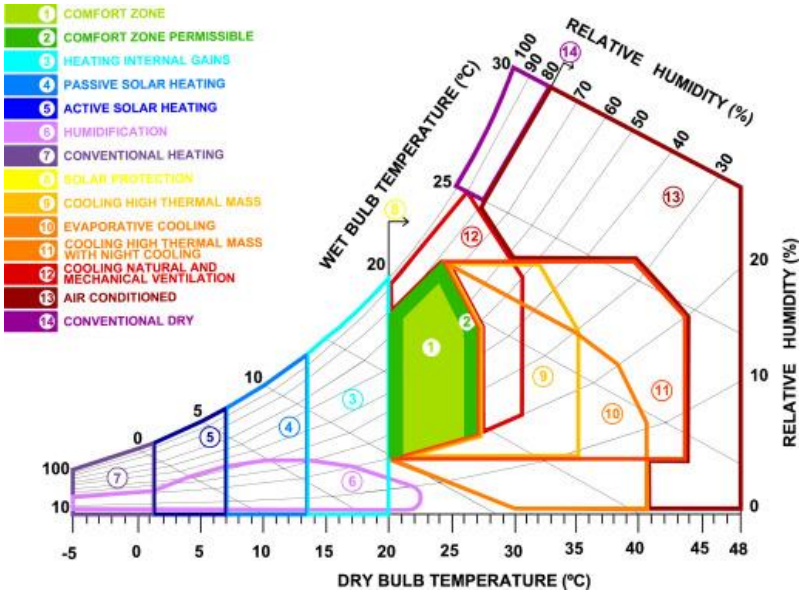


Figure 2.1: Psychrometric chart adapted from Givoni [8]

No bioclimatic strategies are needed for Zone 1, which covers temperatures ranging from 21 to 26 °C and relative humidity levels between 20% and 70%. This zone comfortably accommodates 70% of dwellers with minimal energy expenditure [8]. Whereas Zone 2, which covers temperatures ranging from 20 to 27 °C and relative humidity between 20% and 80%, offers acceptable comfort for 80% of individuals, though some minimal adaptation may be needed based on factors like sex, metabolism, size, and activity level [8].

### 2.2.2 Passive Ventilation Strategies

A passive ventilation strategy can effectively achieve the desired thermal comfort within a built environment when the external climatic conditions surrounding the home align with Zone 12 as defined in the Givoni bioclimatic chart, as illustrated in Figure 2.1. Zone 12 encompasses temperature values ranging from 20°C to 31.5°C and relative humidities ranging from 95% to 20%. Passive ventilation enhances thermal comfort by facilitating natural air circulation within the built environment, achieved through either buoyancy-driven ventilation, wind-driven ventilation, or a combination of both. This can lead to a

more comfortable indoor temperature and serves as a method for passive air purification. Figure 2.2 displays some passive strategies mentioned in [8] that can be integrated with the building's architecture.

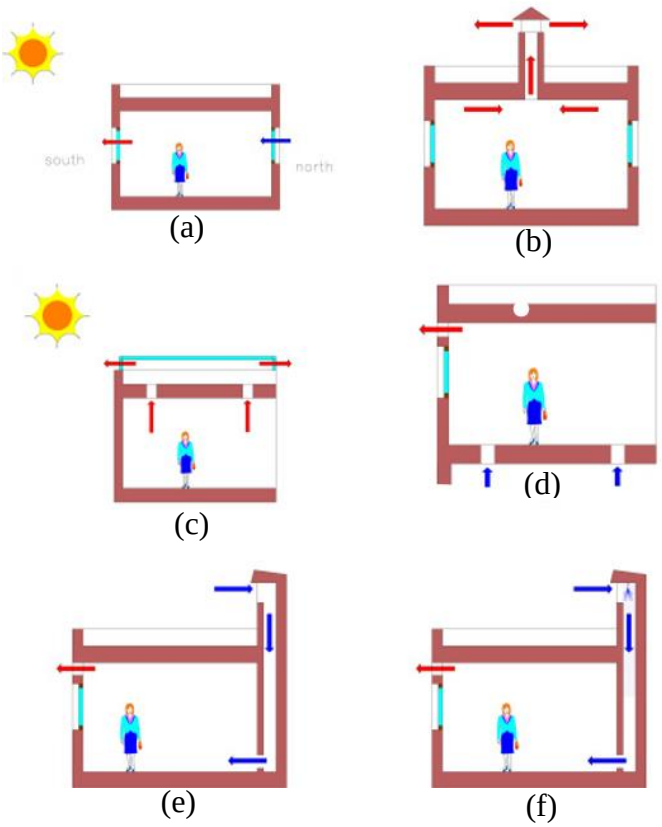


Figure 2.2: Natural ventilation and cooling strategies: (a) cross-ventilation; (b) stack effect; (c) solar-assisted chimney effect; (d) underground ventilation; (e) wind tower (f) evaporative cooling tower [8]

### 2.2.3 Natural Ventilation of Built Environment

Ventilation of the built environment can be achieved either naturally through Bioclimatic architectural designs or mechanically using devices like ceiling and exhaust fans. Natural ventilation in the built environment can be accomplished by utilizing wind and thermal forces. Wind-induced ventilation is generated by pressure differences induced by wind around building architecture, enabling air to pass through openings in the building. This pressure gradient prompts air to flow from high-pressure areas (like room openings and windward sides of windcatchers) to low-pressure regions (such as room openings and

leeward sides of windcatchers). Ventilation caused by wind can be categorized as cross-ventilation when openings are situated on two or more facades or as single-sided ventilation when the opening is only on one façade [9]. Buoyancy-driven ventilation, also called stack ventilation, occurs due to temperature differences between the interior and exterior of a building. These temperature differences between indoor and outdoor environments create varying air densities, establishing a vertical pressure gradient along the walls of the building. Elevated indoor temperatures result in higher pressure at the upper portions of the building and lower pressure at the lower levels. Openings in these areas enable the movement of air, allowing intake at lower openings and exhaust through upper openings [9] .

## 2.3 Solar Chimney: A Concept for Natural Ventilation

In response to environmental challenges like global warming and energy scarcity, building design is shifting away from traditional air conditioning. Instead, designers are embracing innovative technologies and bioclimatic principles, such as the solar chimney, to explore more sustainable solutions for natural ventilation and cooling in the built environment [10]. Natural ventilation, a sustainable approach to building design, has been recognized by humans for centuries [11]. The utilization of natural ventilation can be traced back to vernacular architecture. Instances of this include the application of Badgir, a wind tower used in the Middle East since 900 AD, and the use of stack chimneys during the Roman era. Throughout the 19th and 20th centuries, industrialization led to innovations in natural ventilation strategies, such as the Trombe-Michel wall, solar roof collectors, and solar chimneys, which enhanced the effectiveness of solar stack ventilation [12]. The solar chimney is increasingly recognized for its role in enabling natural ventilation in residential buildings and reducing heat gain in the built

environment. A solar chimney offers the potential benefits of cost savings, lowering energy consumption, and reducing carbon emissions [13] . In hot humid climates, hot summer days, and in hot days without wind of the year When the temperature variation between the interior and exterior of the building is minimal. Buoyancy-driven ventilation induced by conventional chimneys is insufficient because of the insignificant temperature difference between the inside and outside of the building. Therefore, utilizing solar-induced ventilation presents a viable option for improving stack ventilation [14,15]. The double-skin façade, Trombe wall, and solar chimney are all open-ended cavities that capture solar energy and enhance air circulation via the stack effect. A double-skin façade comprised of double-glazed walls and an air cavity gap in between primarily offers heating but also provides ventilation, daylighting, and sound protection. The Trombe wall, with its south-facing storage wall, glazing, and air cavity gap, is used for heating and can also be adapted for ventilation and cooling. And the solar chimney is a structural feature that can be affixed to either the façade, like a Trombe wall, or the rooftop. It is linked to the interior of the building through an aperture, facilitating ventilation and cooling.

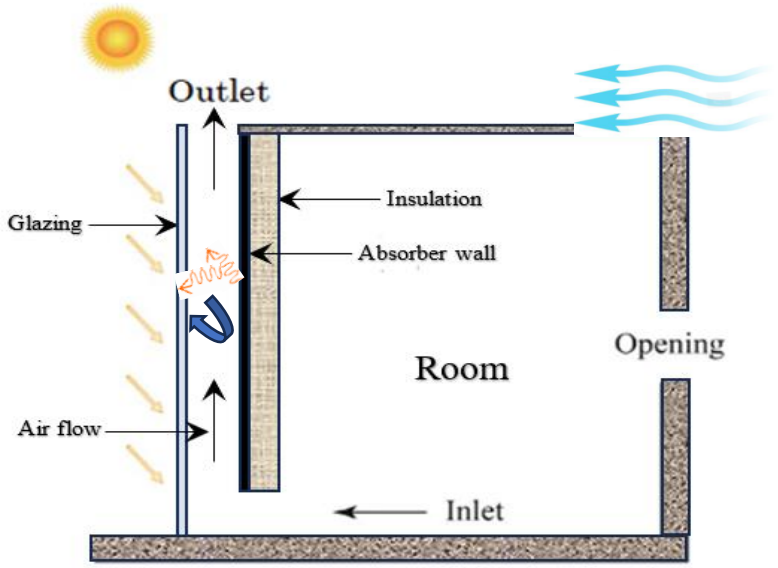


Figure 2.3: Schematic of vertical wall solar chimney

Air within the chimney is heated through convection and radiative heat transfer from the absorber wall due to the absorption of solar energy penetrating glazing, as illustrated in the Figure 2.3. As a result, the air temperature within the solar chimney rises considerably in comparison to the surrounding ambient temperature. This temperature difference causes a reduction in air density within the chimney, promoting noticeable air circulation and, consequently, improving ventilation. This results in an upward flow of air from the outlet of the solar chimney. Hence, an equivalent volume of air is sucked in from the inlet of the chimney connected to the room. The rate at which fresh air is sucked into the room through the windows is determined by factors such as the buoyancy force, the airflow resistance inside the chimney, and the resistance to the flow of fresh air into the room [16]. In actual climatic conditions, the solar chimney effect, which promotes natural ventilation, is a synergy of solar-induced stack and wind-driven natural ventilation, as indicated in various studies [14,17–19]. The solar-assisted stack effect functions as a pulling force for air movement within the solar chimney system, and it is further enhanced by the pushing effect of ambient winds [12].

### 2.3.1 Operation Modes of wall Solar Chimney

A solar chimney is a versatile technology traditionally employed to enhance air circulation within a building by harnessing solar energy to facilitate natural ventilation [9,15,18,20], but can also be used for cooling PV panels [21] and crop drying [22]. The combination of a solar chimney with additional technologies, like evaporative cooling [23–27], wind towers [28,29], and underground wet channel cooling [25], is efficient in enhancing the indoor thermal comfort of the built environment. Citations [30,31] provided overviews of the integrated solar chimney system technologies for space heating and cooling. According to the paper [32], as depicted in Figure 2.4, with little adjustments,

a wall solar chimney attached to the building facade can be operated in three distinct operation modes, each of which is suitable for a specific season.

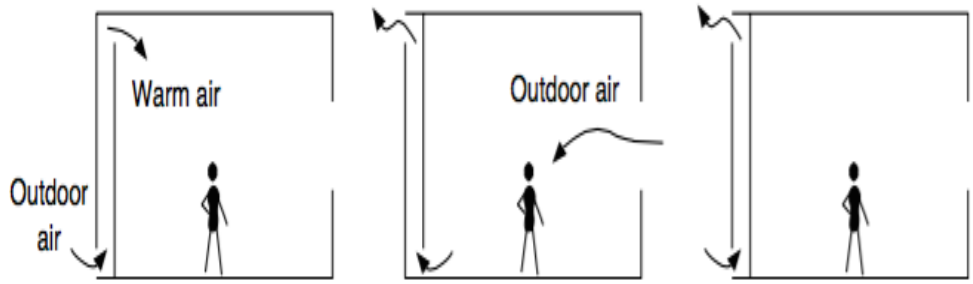


Figure 2.4: Modes of operation of wall solar chimney: (a) heating mode (b) cooling mode (c) Thermal insulation mode [32]

In passive heating mode, the wall-mounted solar chimney functions similarly to a Trombe wall, where it uses absorbed solar energy to heat outdoor air and thereby lessens the heating demand by delivering warm air into the room. In passive cooling mode, when the need for cooling is high and the outside temperature is lower than the indoor air temperature, In this mode, absorbed solar energy is utilized to create a stack effect inside the chimney, which reduces the cooling demand by delivering fresh air into the room. In thermal insulation mode, when the cooling load is predominant and the outdoor temperature exceeds the room temperature, The inlet aperture of the chimney is closed, and outdoor air is introduced into the chimney through the lower opening in the glazing and expelled through the upper opening. This operation reduces heat gain from the solar chimney into the room.

### 2.3.2 Geometrical Configurations of Solar Chimney

A solar chimney can serve both nighttime and daytime ventilation purposes. For daytime ventilation design, a lightweight structure configuration is suitable, transferring heat directly to the air in the chimney. In contrast, a heavyweight structure configuration is employed for thermal storage for optimal nighttime use [33]. Figure 2.5 illustrates various

geometric designs for solar chimneys that can be incorporated into walls, roofs, and windows. As cited in reference [34], the geometrical configurations of solar chimneys attached to single-story buildings can be broadly categorized into three types: (1) wall-mounted solar chimneys; (2) roof solar chimney; and (3) combined wall and roof solar chimney.

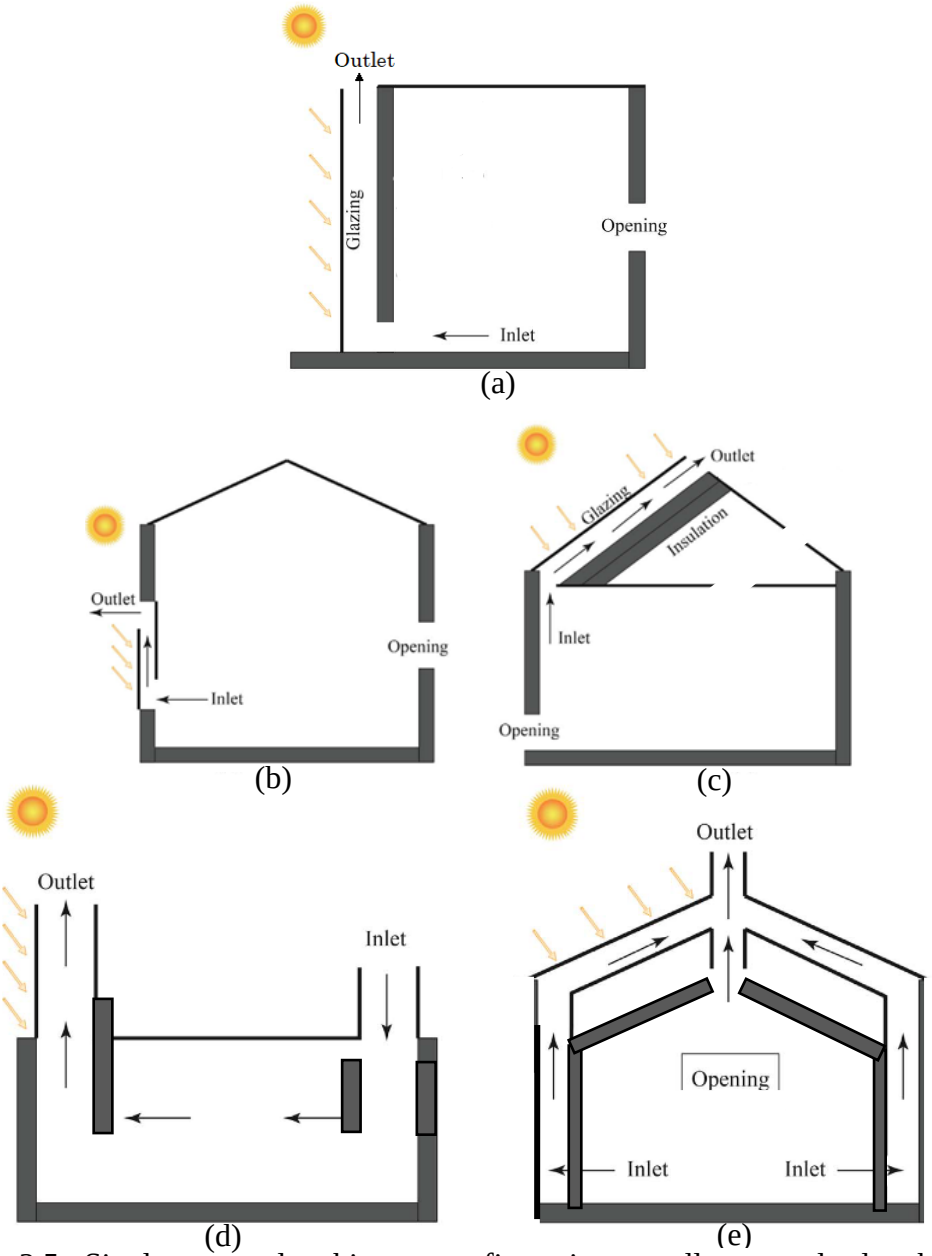


Figure 2.5: Single-story solar chimney configurations: wall-mounted solar chimney comprising (a) and (b); roof solar chimney comprising (c) and (d); combined wall and roof solar chimney (e) [34]

Figure 2.5(a) shows a vertical-walled solar chimney with external glazing and an absorber wall for capturing solar radiation. Sunlight enters the chimney, heating the air, which rises and exits through the top opening. The window opening in the room brings in fresh outdoor air, while a bottom chimney opening promotes indoor air exchange. During the winter, the upper opening of a vertical wall chimney can be sealed, while a new opening is created at the upper section of the absorber wall, like the Trombe wall. This modification enables the warm, rising air within the chimney to circulate back into the room. In Figure 2.5(b), the window-sized vertical wall solar chimney, also known as a glazed wall solar chimney, is depicted. It comprises double glass panels, each matching the size of a typical room window with an air cavity gap, and features openings located at both the bottom and the top.

A roof solar chimney can be inclined (Figure 2.5(c)) or vertical (Figure 2.5(d)). Figure 2.8(c) depicts a typical roof solar chimney. A solar air collector on the roof is employed to enhance the temperature difference between inside and outside air by absorption of solar radiation in the air cavity. In Figure 2.5(d), a vertical roof-top solar chimney is depicted, accompanied by a traditional vertical chimney designed for air inlet. The solar chimney depicted in Figure 2.5(e) is a composite system that comprises rooftop solar chimneys and roof chimneys connected to vertical wall solar chimneys. The air within the room can be expelled directly to the outside through the top vertical air solar collector, while an opening on one side of the wall allows fresh air to be drawn in from the exterior.

### 2.3.3 Performance Indicator of Solar Chimney

Parametric studies on solar chimneys have explored the impact of different design factors on ventilation performance, often measured in mass flow rate, volume flow rate, or air changes per hour (ACH) [12,15,18,18,20,35,36]. However, for practical applications in

both commercial and residential buildings, the air ventilation rate in the solar chimney is typically measured using ACH. The air exchange rate (I) also serves as a performance indicator for solar chimneys, linking the volume flow rate to the ventilated space volume. It is calculated as follows:

$$I = \frac{\dot{V}}{V} \quad (1)$$

where ($\dot{V}$) represents the volume flow rate into a space in $m^3/s$, and (V) stands for the interior volume of the space in $m^3$. The air exchange rate (I) is expressed as a unit of one per time. When (I) is measured for a period of one hours, it is defined as ACH.

$$ACH = \frac{3600\,\dot{V}}{V} \quad (2)$$

The review paper discussed in citation [37] outlines various variables that influence the ACH achieved by the solar chimney. These include the external environment, materials used, installation conditions, chimney and room geometrical parameters, and occupant behaviour, as mentioned in Figure 2.6.

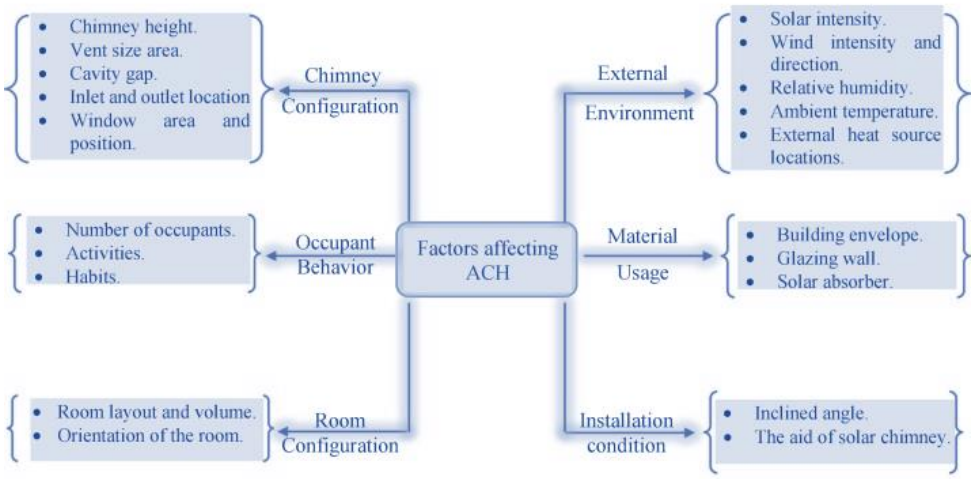


Figure 2.6: variables affecting ACH [37]

Furthermore, [27] provides a presentation of the necessary ACH values for ensuring efficient ventilation in a variety of residential and non-residential settings for proper sizing of solar chimney installations. Refer to Table 2.1 for specific ACH requirements for different types of workspaces within residential and non-residential structures.

Table 2.1: ACH for various workplaces

| **Workplace** | **ACH** | **Workplace** | **ACH** |
|---|---|---|---|
| Banks | 4–8 | Bakeries | 20–30 |
| Bathrooms | 6–10 | Battery charging rooms | 6–8 |
| Bedrooms | 2–4 | Dairies | 8–10 |
| Domestic kitchens | 6–8 | Dye workshop | 20–30 |
| Cafes | 10–12 | Electroplating store | 10–12 |
| Canteens | 8–12 | Foundries | 15–30 |
| Churches | 1–3 | Garages | 6–8 |
| Dance halls | 8–12 | Launderettes | 15–20 |
| Domestic kitchens | 15–20 | Paint shops | 10–20 |
| Corridors and entrance halls | 3–5 | X-ray rooms | 10–15 |
| Gathering halls | 4–8 | Showers | 15–20 |
| Hairdressing salons | 10–15 | Swimming pools | 10–15 |
| Hospitals – sterilizing | 15–25 | Toilets | 6–10 |
| Hospitals – wings | 6–8 | Workshops and factories | 8–10 |
| Laboratories | 6–15 | Living rooms | 3–6 |
| Lecture hall | 5–8 | Showrooms and shops | 8–12 |
| Offices | 6–10 | Restaurants | 8–12 |
| Libraries | 3–5 | Theatres and cinemas | 10–15 |

## 2.4 Scientific Investigation on Solar Chimney

The prevalence of forced ventilation systems and advancements in living conditions during the 20$^{th}$ century rendered solar-powered and wind-driven ventilation systems obsolete. Consequently, research on solar chimneys was scarce before the 1980s [38]. Over the past few decades, the renewed focus on the solar chimney has been motivated by the imperative to cut greenhouse gas emissions, decrease building energy usage, and enhance indoor air quality. Therefore, since the 1990s, experts in the field of construction have thoroughly examined the effectiveness of solar chimneys in minimizing heat accumulation and promoting natural cooling [39]. Numerous studies in the literature have examined solar chimneys in different environments. They range from outdoor assessments in natural conditions to indoor evaluations in controlled settings. Researchers have used various methods, including computational fluid dynamics (CFD), global energy balance (GEB) modelling approaches, and developing analytical models to predict the ventilation performance of the solar chimney.

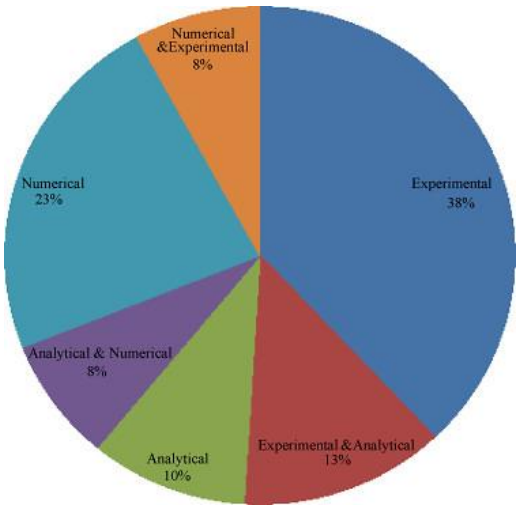


Figure 2.7: Distribution of study approaches in solar chimney investigations [11]

According to the review paper cited in reference [11], experimental research is the primary methodology employed in solar chimney studies. Most of the reviewed publications rely on pure experimentation or integration with analytical and numerical modelling. The distribution of these study approaches is illustrated in Figure 2.7. Recently, researchers are increasingly favouring numerical methods, with approximately 23% of reviewed studies relying on techniques like CFD due to their flexible geometry modelling capabilities. However, high-quality experimental data remains essential to validating CFD results.

### 2.4.1 Experimental Investigations

Multiple research studies have extensively examined various configurations of solar chimneys, which can be classified into two types of models: open-ended channel (vertical and inclined) models and room-attached solar chimney models. These configurations have been evaluated with different construction approaches, including opaque external and internal surfaces, transparent external with opaque internal surfaces, and glass external and internal surfaces. The experimental investigations of solar chimneys can also be broadly categorized into two groups based on the testing environment and the size of the test rig: small-scale or full-scale outdoor models and small-scale or full-scale indoor models. These diverse test rig designs aid researchers in exploring options for more efficient and sustainable solar chimney design for building integration.

#### 2.4.1.1 Experiments Based on Outdoor Environment

Outdoor models undergo testing in actual weather conditions, enabling the collection of real-world data using instruments such as thermocouples, anemometers, fluxmeters, and pyranometers. Nevertheless, conducting extensive outdoor experiments is costly, and

maintaining precise testing conditions proves challenging. Some examples of both full-scale and small-scale experimental work conducted in outdoor climates found in the literature are presented below.

In the study [39], as shown in Figure 2.8, a reduced-scale outdoor mode of solar chimney was made in a dry and hot climatic zone of India, featuring a 1 $m^3$ wooden room with a vertically sliding shutter on one side, covered with a 1 mm thick and 1 $m^2$ aluminium sheet painted black. This sheet absorbed solar radiation. Experiments were done with the chamber facing south, exploring parameters like inlet height (0.1 to 0.3 m), stack height (0.85 to 0.95 m), and cavity depth (0.1 to 0.3 m).

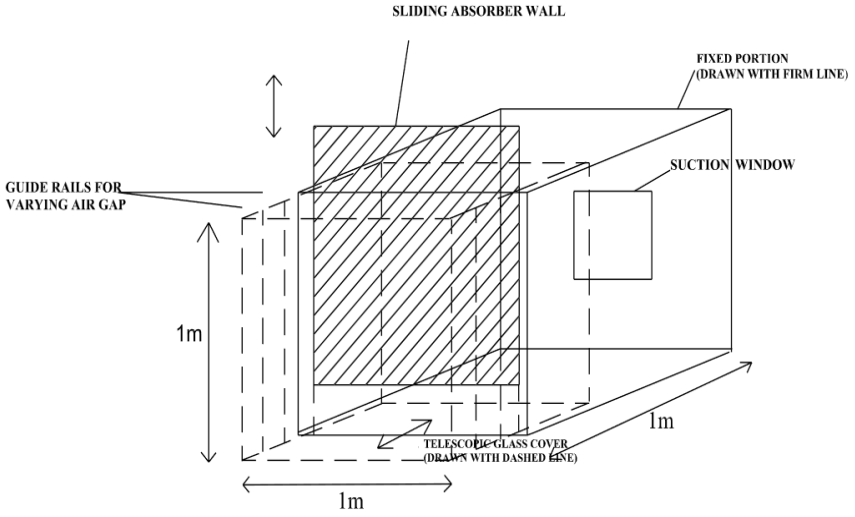


Figure 2.8: Isometric view of experimental set-up [39]

The experiments confirmed that increasing the absorber height-to-gap ratio led to higher ventilation rates, consistent with the global energy balance (GEB) model. This study investigated the impact of aspect ratio on ventilation using nine absorber height and air gap combinations in a small solar chimney. Ventilation rates increased with aspect ratio, and while no single ideal aspect ratio was identified, the maximum ventilation rate of 5.6 ACH in a 27 $m^3$ room was achieved with an aspect ratio of 2.83, 700 $W/m^2$ solar intensity, and absorber heights ranging from 0.7 m to 0.9 m for a 1 m high chimney.

The authors in [15] conducted an experiment exploring the use of a window as a solar chimney in hot and dry conditions in India, similar to study described in [39]. They employed a 1 mm thick, black-painted aluminium sheet as an absorber and placed it in a 1 $m^3$ wooden box with glazing facing south on roof of the building. Three different combinations of the cavity gap and the size of the inlet opening were tested. The maximum flow velocity reached 0.24 m/s with a 0.13 m air gap and a 0.13 m height of the inlet opening. A simplified GEB model showed a 2% lower glass temperature and a 4% lower air temperature in the chimney, while the absorber temperature was higher by 6%.

The paper [40] comprises a comprehensive parametric analytical study that involves the utilization of a spreadsheet computer program as well as an accompanying experimental investigation. This study focuses on an inclined rooftop solar chimney integrated with a wind cavity. A detailed description and sizing of this system, attached to a two-story residential building in the hot-arid city of Al-Ain, UAE, is provided in Figure 2.9.

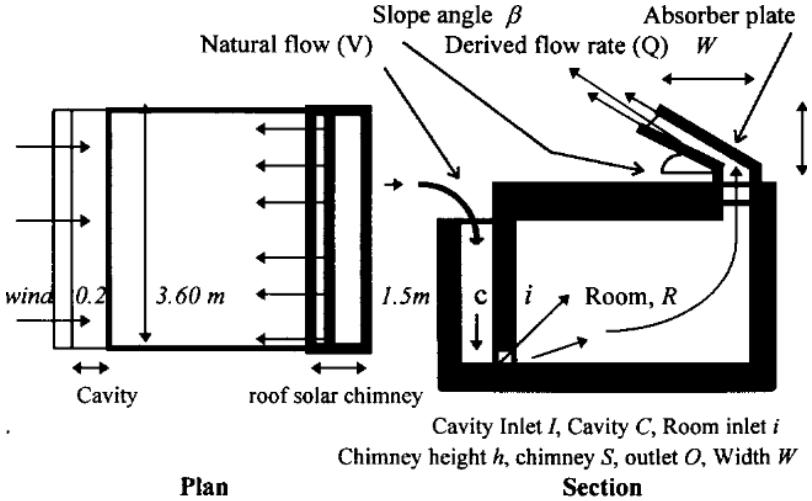


Figure 2.9: Roof solar chimney assisted by wind cavity for a residential building, AI-Ain -UAE [40].

For optimal cooling performance, it is recommended to have an air cavity gap of 0.2 meters and a ratio of inlet to outlet chimney area of 2.5. An air gap of less than 0.10 meters

is not advisable. The most efficient performance of a roof solar chimney is achieved with a slope angle of 35°. The parametric study indicates that the maximum volume flow rate is 0.81 m³/s under an average solar radiation of 850 W/m².

Theoretical parametric analysis, using a spreadsheet program, and experimental investigations conducted by [35] explored the implementation of a combined wall and inclined rooftop solar chimney to enhance nighttime ventilation in a two-story house located in Al-Ain, UAE, as depicted in Figure 2.10. A spreadsheet program was employed to optimize the chimney configuration. The results indicate a threefold increase in airflow compared to a standalone inclined rooftop solar chimney cited in [40].

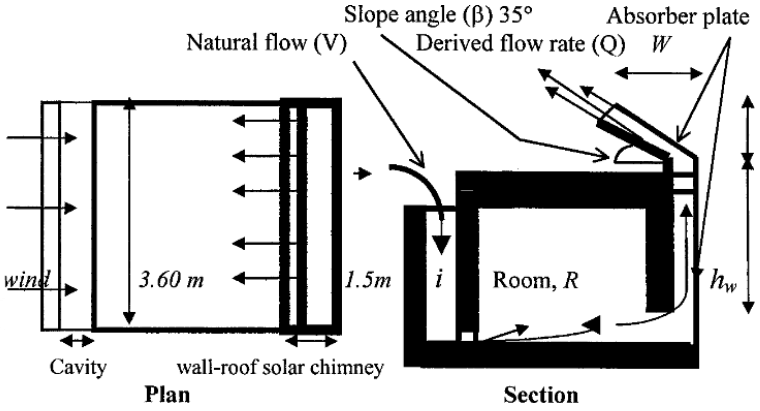


Figure 2.10: Combined wall-roof solar chimney attached to a residential building in Al-Ain, UAE [35]

With an average incident solar radiation of 850 W/m$^2$, 25° inclined chimney plates spaced 0.25 m apart, and an optimum wall chimney height of 3.45 m (inlet height 0.15 m and total chimney height 3.60 m), a maximum air velocity of 1.1 m/s is induced, resulting in a high air flow rate of nearly 2.3 m$^3$/s. This achieves an ACH number of up to 26, which effectively addresses the high cooling load of buildings in hot climates within a flat volume of 321 m$^3$.

In this study [18], the impact of solar chimneys on building ventilation was evaluated. Two vertical chimneys were constructed on the rooftop of a test cell in Porto, Portugal:

one solar chimney and one conventional chimney, as shown in Figure 2.11. Both chimneys have an internal cross-section area of 0.2 x 1 m and a stack height of 2 m. The walls consist of 10 cm thick bricks with an additional 5 cm insulation layer on the backside of the absorber wall. Both chimneys feature inlet and outlet apertures through the roof. This installation entailed dividing the test cell, which has an area of 12 $m^2$, into two equal compartments. The test cell itself is constructed with concrete walls, a ceiling, and insulated outer surfaces.

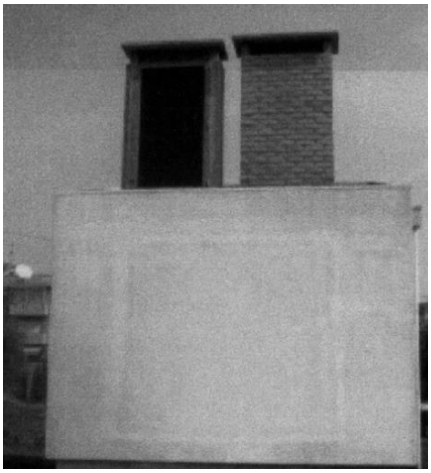

Figure 2.11: Solar and conventional chimneys installed on a test room [18]

The tracer gas technique was employed to measure real-time airflow rates induced by both chimneys. An analytical model was also developed to predict the air flow induced by buoyancy-driven forces developed in the chimney and to take into account the influence of wind. The results of the model were found to satisfactorily predict the experimental results. It was concluded that the solar chimney outperformed the conventional chimney.

A small-scale solar wall chimney outdoor experiment was conducted in Malaysia by [20]. As illustrated in Figure 2.12, featuring a 2 m tall and 0.45 m wide chimney with glazed external surfaces and a black opaque internal wall. The chimney, with varying air gap depths of 0.1, 0.2, and 0.3 m, was connected to a 2 m high, 0.48 m wide, 1.02 m deep

rectangular box made of rigid polyurethane sheets with steel sheet cladding. Additionally, a 50mm thick polystyrene sheet was added to the heat-absorbing wall for insulation. The inlet to the room was located 0.1 m above the ground.

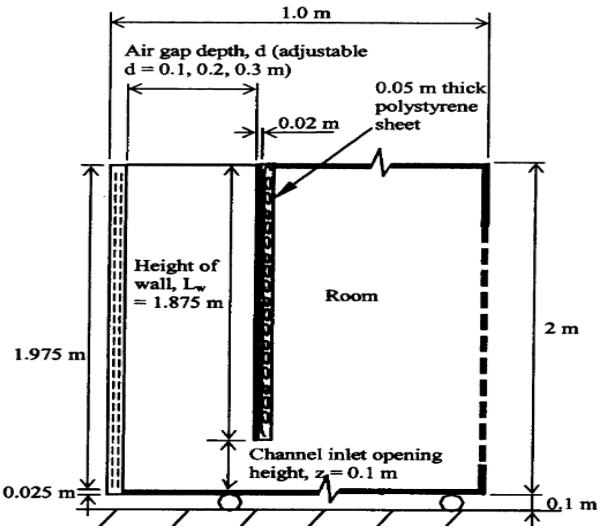


Figure 2.12: The cross-sectional view of wall-type solar chimney [20]

It was observed that air velocities increased with the air gap, ranging from 0.25 to 0.39 m/s at air gaps between 0.1 and 0.3 m for a radiation intensity of 650 W/m$^2$. A 0.3 m air gap provided 56% more ventilation than a 0.1 m air gap in a solar chimney. No reverse air flow was observed up to a 0.3 m air gap. These results verified a steady-state model for a wall-type solar chimney developed by the same author [41].

Researchers in study [42] conducted experimental and theoretical investigations using the GEB approach to assess the feasibility of integrating a metallic solar wall (MSW) on the southern wall of a 2.68 m high, 3.35 m x 3.45 m room in Bangkok, Thailand, as depicted in Figure 2.13. The MSW, with dimensions of 1 m x 2 m, featured an absorber wall made of 0.7mm zinc plate microfiber and 25mm plywood, painted matte black, and covered with 5mm commercial glass. The MSW design allowed for variable height (1-2 m) and air gap (10-14.5 cm) and included pairs of vents, 25 cm x 5 cm, at both the bottom and top. Experimental tests demonstrated that a 1 m height and a 14.5 cm gap in the MSW

result in optimal natural ventilation, effectively reducing heat gain in the house and enhancing thermal comfort through improved air circulation.

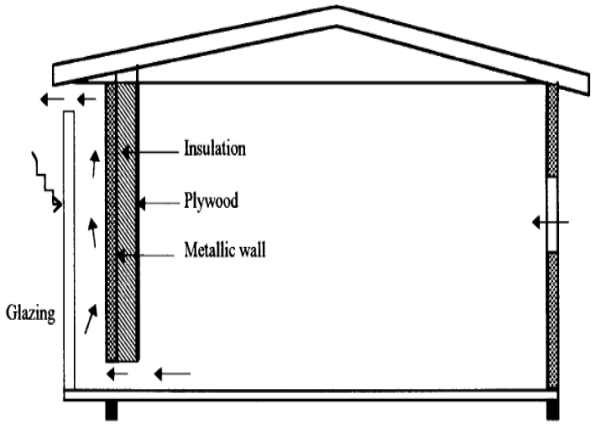


Figure 2.13: Schematics of metallic solar wall attached to a single room house [42]

In citation [43], researchers conducted experiments to evaluate the potential of integrating a modified Trombe wall (MTW) on the southern wall of a 25 $m^3$ single-room solar house in tropical climate of Thailand. The MTW includes a masonry wall (100 x 200 x 0.9 cm), an air gap (10 to 14 cm), and a gypsum wall (100 x 200 x 0.9 cm), as depicted in Figure 2.14.

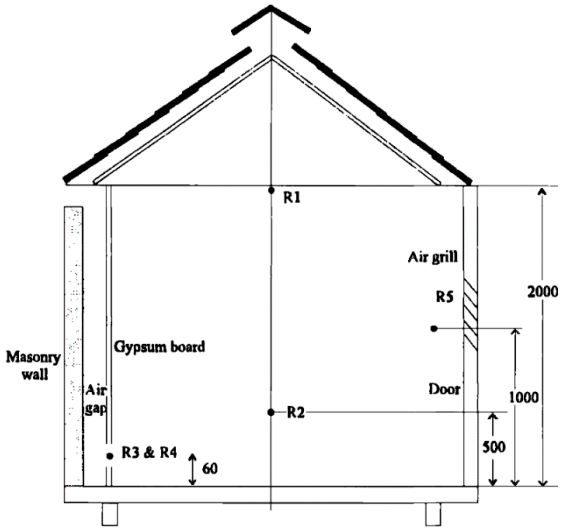


Figure 2.14: Schematics Modified Trombe Wall attached to a single room house [43]

The study found that a 2 $m^2$ dark-coloured MTW with a 14 cm air gap induced the highest natural ventilation rate (20–90 $m^3/h$), while even a light-coloured wall provided

significant ventilation. However, relying solely on natural ventilation for thermal comfort seems challenging. Still, the recommended MTW configuration offers excellent insulation properties for new house construction.

The research [44] aimed to experimentally test the effectiveness of solar chimneys in reducing heat in Thai residential buildings. Four different solar chimney configurations, as shown in Figure 2.15, were built with various materials, including two roof solar collectors (1.5 $m^2$ each), one modified Trombe wall, one Trombe wall, and one metallic solar wall (2 $m^2$ each). Two different inlet opening heights, 0.04 meters and 1 meter above the floor, were examined for wall chimneys.

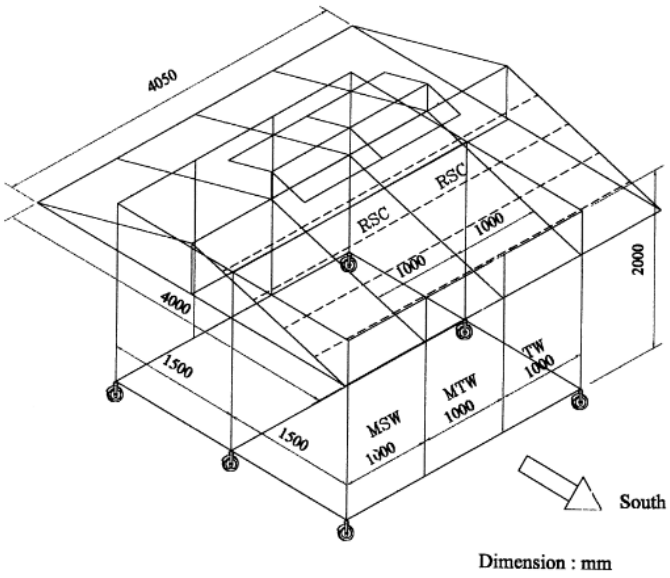


Figure 2.15: Schematics of solar chimneys installed in the single-room solar house [44]

Solar chimneys integrated into the southern wall of a single-room school solar house, with a volume of about 25 $m^3$, serve a dual purpose. They act as excellent insulation materials to reduce solar heat absorption and promote natural ventilation, enhancing thermal comfort. However, they provide an average of 1.6 to 2.5 air changes per hour (ACH) between 12 PM and 2 PM, which may not fully meet occupant ventilation needs,

as an ACH value above 20 is typically required for houses without mechanical cooling systems.

The authors in study [45] examined the Glazed Solar Chimney Wall (GSCW) concept experimentally and numerically by developing a 2D GEB dynamic model. The study focused on a reduced-scale single-room house in tropical Thailand, measuring 1.4 m × 1.4 m at the base and 2 m in height. The GSCW system was attached to the house, with dimensions of 0.74 m in height, 0.50 m in width, a 0.10 m air gap, and 0.006 m glass thickness. The inlet and outlet openings were 0.05 m × 0.5 m² in size, as depicted in Figure 2.16.

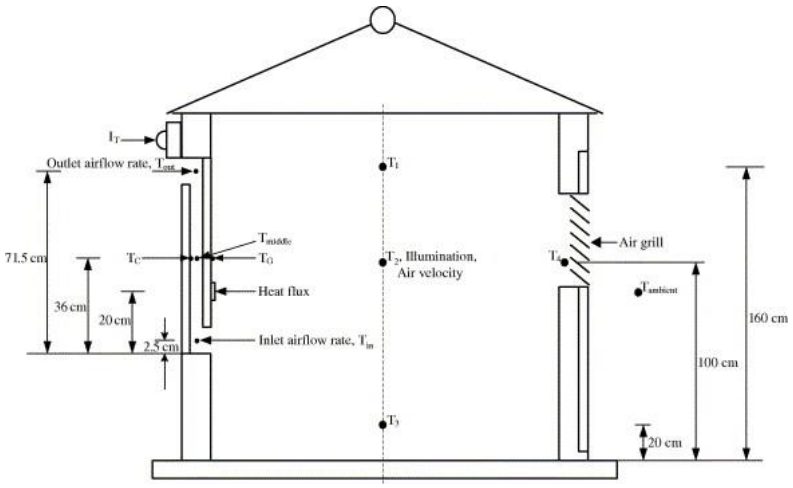


Figure 2.16: Schematic view of the GSCW attached to a test room [45]

It was found that the difference in temperature between room and ambient was smaller with double glass layers compared to a single clear glass window chimney. Daylight reduction from the double glass layer was minimal. Experimental results matched well with the results of the GEB model solved by using finite-difference and Gauss Seidel iterative methods.

In Thailand, researchers [46] conducted an experimental and numerical study on the use of solar chimneys in high-rise buildings. Two small-scale, three-story building models

were constructed, each measuring 1.2 m x 2 m x 1 m per floor. Solar chimneys were incorporated into the south-facing wall, as depicted in Figure 2.17. Two configurations were investigated: the first (a Combined solar chimney) had a single outlet opening on the third floor with individual inlet openings on each floor, while the second (a Separated solar chimney) featured separate inlet and outlet openings on every floor.

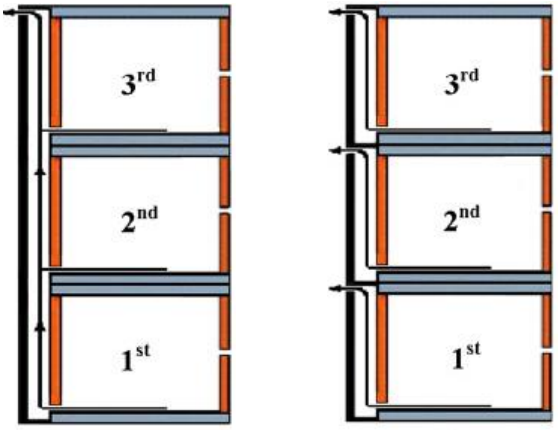


(a) (b)

Figure 2.17: Multi-story solar chimney configurations: (a) Combined solar chimney (b) Separated solar chimney [46]

The study found a strong agreement between experimental data and simulations of 2D dynamic mathematical models. It demonstrated superior performance for a solar chimney with the given configuration, suggesting that multi-story solar chimneys could serve as an energy-efficient and environmentally friendly alternative for mechanical ventilation in tall buildings in hot climates.

In this study, the author [16] conducted experiments on a scaled-down rooftop solar chimney, as shown in Figure 2.18, and developed a GEB model to predict its performance and tilt angle. A wooden room measuring 100 cm × 40 cm × 80 cm was built for the study, featuring a solar chimney with an adjustable inclination angle between 30° and 90° relative to the horizontal plane in the upper section.

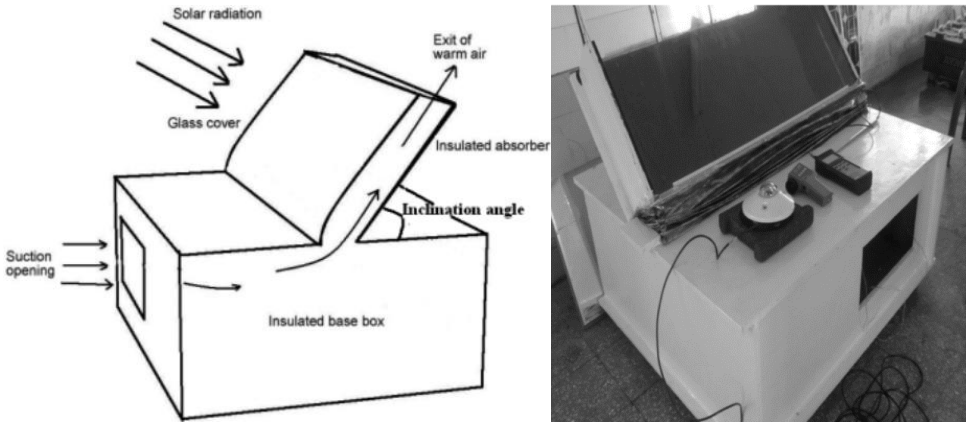


Figure 2.18: Schematic of a solar chimney with photograph of a solar chimney [16]

The chimney component was made of a 2 mm thick aluminium sheet, 40 cm tall and 100 cm wide, coated with black paint to absorb solar radiation. A 5mm thick glass cover with an air gap of 5 to 10 cm was placed over the absorber sheet. The chimney outlet matched the inlet. To reduce heat transfer, the base chamber and rear side of the absorber were insulated with 2.5 cm thick plywood sheets. The room had a 20 × 40 $cm^2$ opening on one wall. The study found that a south-facing solar chimney in Tiruchirappalli, India (78°69′E, 10°81′N) with a 50° inclination angle and a black-coated aluminium surface was more efficient than a vertical chimney.

The authors conducted a study [47] in the climatic conditions of Malaysia, investigating a roof solar chimney attached to a circular cross-section chimney. They explored various collector areas (15, 150, and 600 $m^2$) and different chimney heights (5, 10, and 15 m). The authors validated a GEB model using experimental data obtained from a circular chimney with a diameter of 0.15 m and a height of 5 m, positioned on top of the cover. This chimney featured two inclined collectors, each measuring 7.5 $m^2$, as depicted in Figure 2.19.

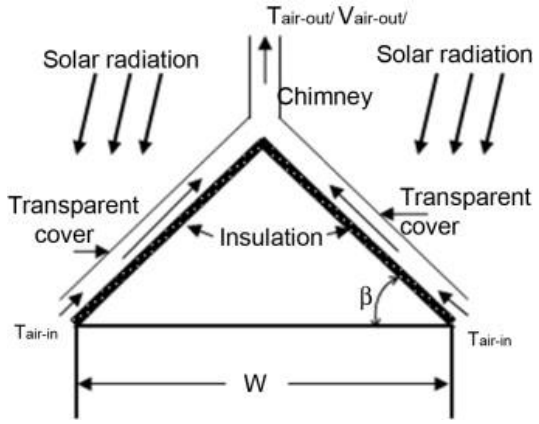


Figure 2.19: Schematic view of roof top solar chimney [47]

The results of the simulations indicated that solar intensity is the key factor affecting solar chimney performance. Even with a large collector area of up to 600 $m^2$, the system is not feasible when solar intensity falls below 400 $W/m^2$ in Malaysia and similar weather conditions.

A global energy balance model was developed in study [48] for a vertical rooftop solar chimney, as shown in Figure 2.20, on a bioclimatic office in southeastern Spain. The chimney measures 1.95 m in height, 1.70 m in width, and 0.24 m in cavity gap, with a solar-absorbing metallic plate on the backside.

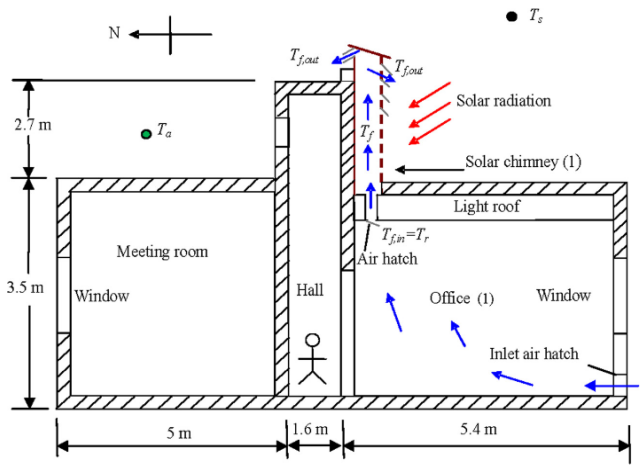


Figure 2.20: Schematic view of a building with a solar chimney [48]

It's connected to a 0.2 m thick concrete wall for storage and insulation, and a glass cover minimizes heat loss. The chimney has an inlet area of 0.05 m² and an outlet area of 0.7

m². The theoretical model was first validated with GEB models developed by [20,42]. It was determined that as solar flux increases from 100 to 700 W/m$^2$, the maximum instantaneous efficiency of the solar chimney rises from 28% to 37%, while the volumetric flow rate rises from 61 to 147 m$^3$/h.

In this study, the author [14] conducted experiments on a reduced-scale model of a roof solar collector combined with a vertical stack solar chimney, as shown in Figure 2.21, and developed a steady-state mathematical model (GEB) to study the effectiveness of solar-induced ventilation in a hot and humid climate in Selangor, Malaysia.

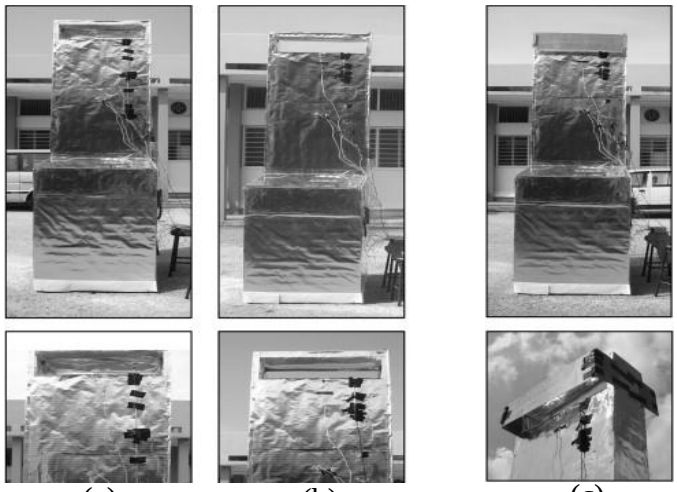

(a) (b) (c)

Figure 2.21: Models A, B and C with different vertical stack outlet design [14]

To study the impact of wind, three prototype devices were developed with identical configurations but different vertical stack outlet designs. The study utilized a 1 m$^3$ cubic room constructed with 0.003 m thick plywood, insulated with 0.05 m thick rockwool, and covered with aluminium foil on both sides. The room included a solar collector on the roof (1 m x 1 m x 0.2 m) and a vertical stack (1 m x 1.95 m x 0.2 m), both with specific inlet and outlet dimensions (0.9 m x 0.175 m). The roof solar collector had a clear glass cover (0.005 m thick) and featured a black-painted aluminium foil absorber on top of 0.1 m rockwool and 0.003 m plywood. Similarly, the vertical stack was insulated with

rockwool and covered in aluminium foil both inside and outside. The results were presented as two performance variables: air temperature and air velocity. The findings suggest that the strategy improves stack ventilation under various sky conditions, aligning well with theoretical predictions for glass, air, and absorber temperatures. It was found that the outside wind significantly influences the induced air velocity inside the chimney.

The authors in study [17] conducted experiments in the Desert of Tabernas, Spain, using a large-scale standalone vertical solar chimney model as shown in Figure 2.22. They enhanced solar absorption by coating a 4.5 m high, 1.0 m wide, and 0.15 m thick south-facing concrete wall with black paint and covering it with 0.004 m thick glass. The chimney had a 0.3 m air gap, and its inlet and outlet cross-areas remained constant at 0.07 m². They insulated the side walls and back surface of the absorber wall with plywood to reduce heat loss. The chimney had a bottom air inlet and a top outlet, with a wind-driven protection system to prevent reverse airflow and turbulence due to wind.

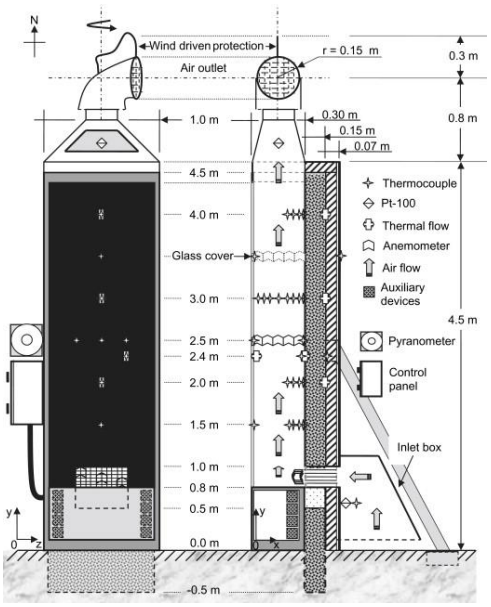


Figure 2.22: Schematic view of solar chimney [17]

It was observed that the airflow rate in the solar chimney is affected by a pressure difference between the inlet and outlet, which is generated by the thermal gradient and

wind speed. Through experiments, a discharge coefficient ($C_d$) of 0.52 was determined, and it can be applied in theoretical models of solar chimneys to calculate the mass flow rate.

In this study [49], a 3D quasi-steady CFD model, utilizing the RNG k-ε turbulence model, was created to predict buoyant airflow. Experimental tests with an inclined rooftop solar chimney attached to a single room were conducted to validate the model. In Alexandria, Egypt (31.2°N, 29.91°E), as illustrated in Figure 2.23, a cubic wooden room with 8 $m^3$ of internal volume was constructed. On its roof, an inclined, south-facing solar chimney with an absorber wall (1.4 m tall, 0.6 m wide, made of 1 mm ductile steel sheet) was installed. This chimney draws fresh air through a 0.6 m × 0.6 m north-facing window with a 16% window-to-wall ratio. The south side of the chimney is covered with 4 mm float glass, separated by a 0.25 m air channel gap.

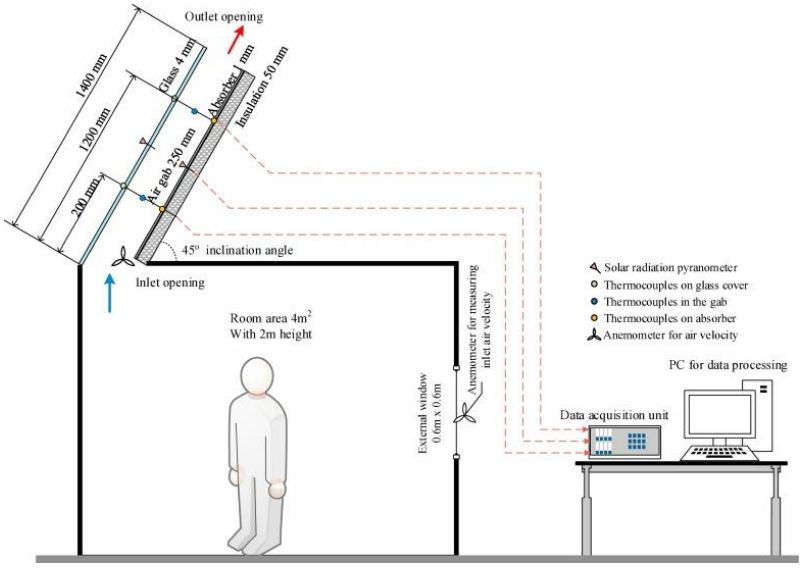


Figure 2.23: Instrumentation on outdoor experimental set-up of solar chimney [49]

The experimental results closely match CFD calculations, with a 5.14% deviation. The proposed solar chimney can induce natural air motion at speeds of 0.28, 0.47, and 0.52 m/s under solar radiation values of 500, 700, and 850 W/$m^2$, respectively. A sensitivity

analysis shows that chimney width is the most significant factor, followed by inclination angle and air gap, while chimney height has minimal impact.

Experimental research conducted in Phitsanulok, Thailand [50] assessed the impact of varying solar radiation levels throughout the day on a wide, standalone square solar chimney for a one-story building with and without wind conditions. The chimney featured a 1 mm thick steel plate absorber wall and three insulation material walls, as shown in Figure 2.24. It had a height of 3 m and an inlet and outlet area measuring 0.4 m by 0.4 m. The absorber wall, painted black, faced the southwest direction, and the outlet of the chimney was positioned toward a tall building wall to minimize wind interference. To further control wind influence, a plastic board covered the inlet cross-sectional area.

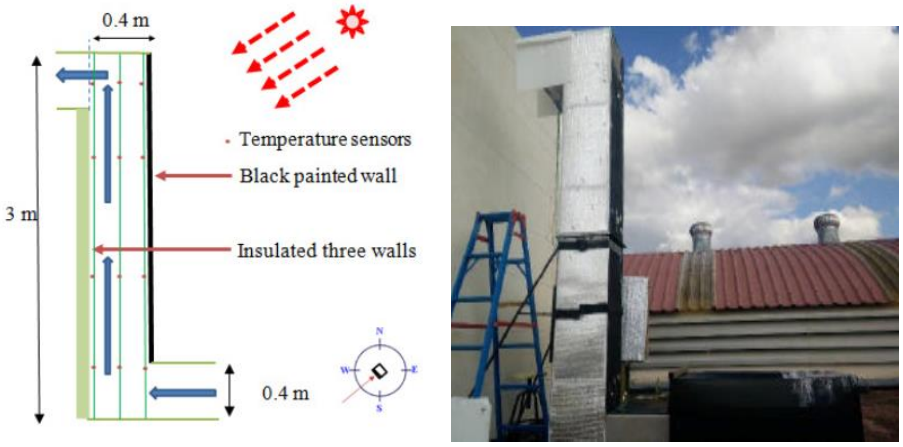


Figure 2.24: Schematic of outdoor square solar chimney (left); the test rig (right)

It was concluded that the air temperature decreases from the black surface to the insulated wall, with a 7°C horizontal and 1.4°C vertical temperature difference. Wind slightly reduces the air temperature at the inlet of the chimney but enhances air velocity measured at the inlet and outlet of the chimney, leading to increased heat transfer rates compared to experiments without wind.

Some researchers [10] have argued that outdoor solar chimney models lack universal validity due to their dependence on local climate and experimental conditions. This raises

questions about the universal applicability of the experimental results. Utilizing building energy simulation software for modelling, instead of relying on the results of outdoor models, proves to be a valuable tool for accurately evaluating the performance of the system.

#### 2.4.1.2 Experiments Based on Controlled Indoor Environment

In order to establish a stable testing environment, controlled laboratory conditions are typically employed for small-scale indoor experiments, making them more practical due to their relatively lower manufacturing costs. The primary factor that significantly impacts the overall results of solar chimney studies is the source of solar energy, which poses challenges in terms of prediction and control. Consequently, in indoor experimental models, the absorber and glass cover walls of the solar chimney are often simulated by heating only one or two walls with a uniform wall temperature (UWT) [51–53] or a uniform heat flux (UHF) [54–56]. This simulation is achieved using methods such as electrical plates [51,53,54,57], hot oil, or a solar simulator [58,59]. The walls of the experimental setup are well insulated to minimize conduction heat losses. Thermocouples, anemometers, and fluxmeters are used to collect air and surface temperature data, measure heat flux from the heating plate, and assess air flow. Moreover, the controllable experimental conditions and use of transparent Perspex walls of the indoor test rig also allow the implementation of advanced optical methods for flow visualization. For example, flow visualization can be achieved using a fog generator to visualize reverse flow phenomena [60,61], and incense sticks to determine the direction of flow [51–54]. Shadowgraph and Schlieren visualization techniques can be used to visualize and quantify the thermal field and development of the thermal boundary layer at the outlet of the chimney [60,62], while particle image velocimetry (PIV) techniques

can be employed to visualize the flow field, velocity boundary layer, and flow development [63,64]. Below are some examples of reduced-scale and full-scale experimental work conducted in indoor climates, as available in the literature.

The authors in [55] conducted an investigation of a solar chimney configuration using an open-ended rectangular channel in controlled conditions. The test rig, as depicted in Figure 2.25, featured a vertical channel measuring 1 m in height and 0.925 m in width. It had an open top and bottom, with one side covered in transparent material (glass plate) and the other side consisting of a matte, black-painted aluminium (absorber plate). The channel depth ranged from 0.02 to 0.11 m. Solar intensity was provided by an electric heating mat with adjustable heat input ranging from 200 to 1000 W/m$^2$.

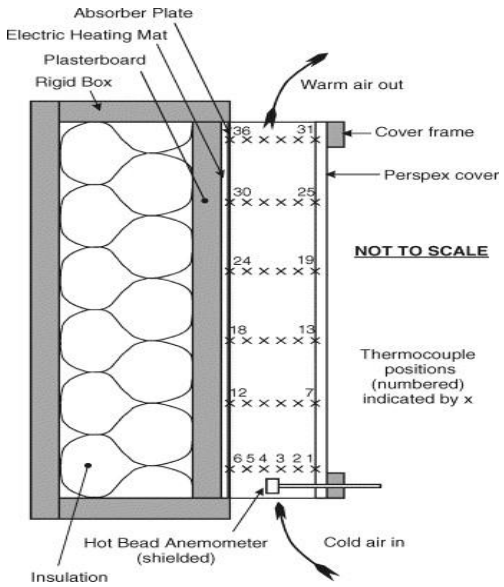


Figure 2.25: Schematic view of the indoor test rig [55]

Additionally, the same author in 2010 [56] developed three similar test rigs with heights of 0.5, 1.0, and 2.0 m, adjustable channel depths (0.02–0.15 mm), and heat inputs of up to 1000 W/m$^2$. The investigation included measurements of air, plate, and cover temperatures, as well as air velocities. The results are presented as dimensionless

correlations, showing that thermal efficiency depends on heat input and system height but not channel depth, while mass flow is influenced by all three parameters.

A laboratory investigation [58] explored the impact of varying the channel depth (0.1 m to 0.5 m) and inlet opening height (0.1 m to 0.2 m) on the performance of a rectangular chimney made from mild steel plates with black-painted external surfaces. As shown in Figure 2.26, the chimney had a height of 2 m and a length of 1 m, with an inlet at the bottom back surface and an exit at the top. Rigid polystyrene board formed the side walls. A solar simulator, consisting of three 1000 W halogen heat lamps in parabolic reflectors, was used to irradiate uniformly on the surface of the chimney. The experimental results were validated with the developed transient GEB model of the system. It was found that the mass flow rate per unit area was highest for the narrower channel (d = 0.10 m) and decreased with increasing channel depth.

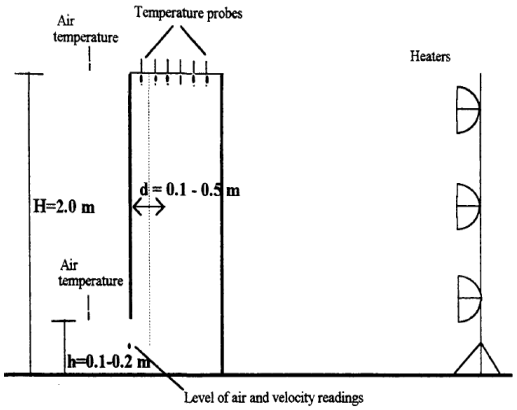


Figure 2.26: Section through the experimental rig [58]

The authors in [65] experimented with a small-scale solar chimney model made of Perspex, as depicted in Figure 2.27. They placed this model in a large tank filled with saltwater. By passing current through a copper wire cathode along the outer wall of the chimney, they created a plume of hydrogen bubbles, simulating the buoyancy effect caused by solar radiation. These bubbles represented the density difference between the

plume and the surrounding fluid, which mimicked temperature variations due to solar radiation. A solar chimney with two adjustable heights and varying chimney channel gaps (5–30 mm for the 200 mm chimney and 8–50 mm for the 400 mm chimney) was connected to a room measuring 200 mm in width, 100 mm in depth, and 200 m in height. Velocity measurements were taken at the inlet of the room under different chimney air gap conditions, heights, and different inlet geometries while varying parameters like solar radiation and buoyancy fluxes (ranging from 122 to 489 $cm^4/s^3$).

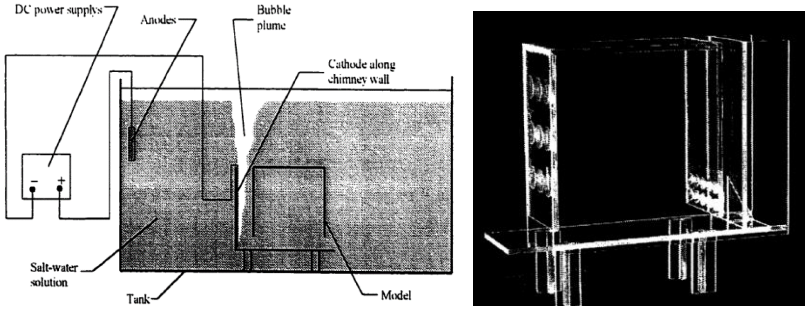


Figure 2.27: Schematic view of the experimental model. Photograph of small-scale model inside the saltwater tank [65]

Results indicated that the optimal air gap depended on building geometry and inlet size, irrespective of solar radiation intensity, but was positively correlated with inlet size and stack height.

In this study [51], an indoor full-scale solar chimney model was experimentally examined, and a dynamic model of the system was developed using a finite difference technique to evaluate the performance under various conditions. As depicted in Figure 2.28, the room model had dimensions of 1.8 m x 1.8 m in plan area and a height of 2 m. It featured an aluminium chimney measuring 1.9 m in height and 1.5 m in width. The air inlet of the cavity maintained a constant size of 0.1 m in height and 1.40 m in width, while the cavity gap varied from 0.1 m to 0.5 m.

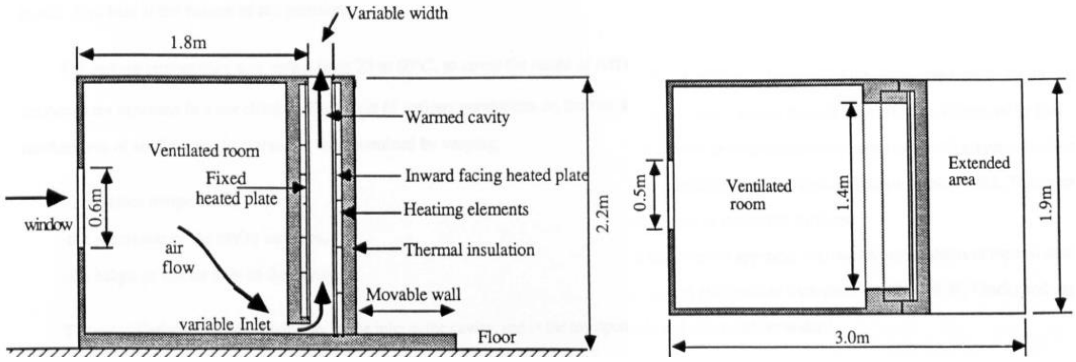


Figure 2.28: Schematic drawing of indoor solar chimney attached with room [51]

Two walls of the solar chimney were maintained at uniform wall temperature (UWT) boundary conditions by installed electric heaters. Mass flow rate measurements were taken at various surface temperatures, chimney depths, and inlet heights, revealing that temperature differences between the chimney walls and ambient air influenced flow rate. The study identified the cavity gap and air inlet area as crucial performance parameters for the solar chimney. Moreover, anemometers were employed to observe air flow patterns in both the room and the cavity. Smoke, generated from hydrochloric acid fumes using smoke tubes, aided in assessing the direction of flow within the cavity and the thickness of the velocity boundary layer for optimizing the cavity gap.

The authors in [54] performed experiments, as depicted in Figure 2.29, on a solar chimney that was configured as a rectangular channel with uniform heat flux applied to one of its walls. The chimney featured a variable air gap (ranging from 10 to 60 cm), various heat flux values (ranging from 200 to 600 $W/m^2$), and inclination angles (ranging from 15º to 60º relative to the vertical orientation). The channel had internal dimensions of 1.5 m in height, 0.62 m in width, and an adjustable air gap ranging from 0.1 to 0.6 m. It was built with insulated Plexiglass on three walls and a heated stainless-steel surface. The study involved measuring air temperature and velocity at various points within the channel. Air flow patterns were visualized using a Drager smoke tube.

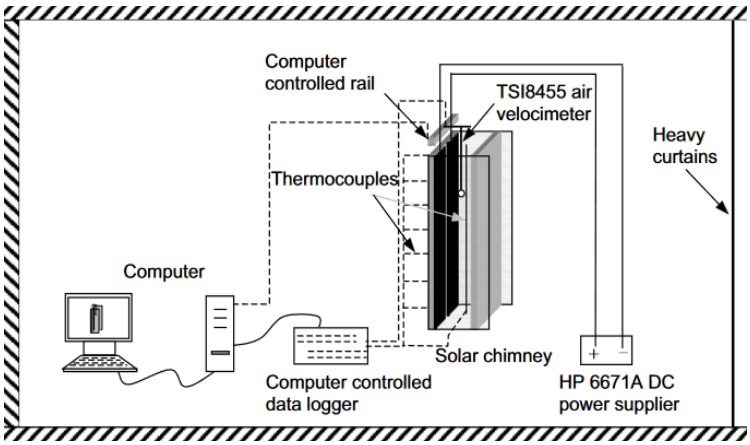


Figure 2.29: Schematic view of the experimental system [54]

The results revealed the following findings:

- Air flow increased with chimney gap size, but no optimal gap width was identified.
- Reverse flow occurred at the chimney outlet for gaps starting at 30 cm, extending into the chimney channel with larger gaps.
- Maximum air flow was achieved at a 45° inclination angle for a 20 cm gap and a 1.5 m high chimney, 45% higher than for a vertical chimney.
- Vertical chimney with large gaps had non-uniform air temperature and velocity, with the velocity peak near the heated wall. This could lead to over-predictions of air flow in similar chimney configurations, especially for large-gap vertical chimney, due to an underestimation of pressure losses at the outlet.
- Air temperature generally increased with chimney height, but not linearly, and dropped above the mid-height of the chimney.

Experiments were conducted in study [59] on a reduced-scale model of a solar chimney attached to a room to investigate natural ventilation and smoke exhaust during fire conditions. As illustrated in Figure 2.30, the room had dimensions of 1.5 m x 1.5 m x 0.9 m and included a window measuring 0.33 m × 0.33 m, positioned 0.28 m above the floor

on the right wall. The experiments explored various design parameters of the chimney, including inlet height (ranging from 0.2 to 0.8 m), cavity depth (ranging from 0.025 to 0.175 m), solar radiation (ranging from 400 to 1200 W/m$^2$), fire size (ranging from 6.8 to 15.8 kW), and a chimney with a width of 1.5 m. Solar radiation was simulated using a solar simulator, and temperature and air velocity were measured using thermocouples and an anemometer, respectively.

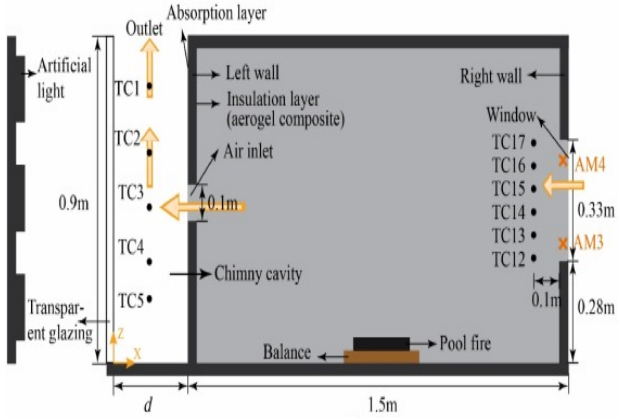


Figure 2.30: schematic of the experimental test rig [59]

The study found that a chimney configuration with a 0.5 m high air inlet and a 12.5 cm cavity depth was optimal for natural ventilation and smoke exhaustion. External radiation improved natural ventilation but had a limited impact on smoke exhaustion. Additionally, an empirical model was created to predict flow rates in normal and fire conditions.

A prototype building is proposed in reference [53], designed to be a 1/25 scale model of a full-scale eight-story office building with an atrium on the north side. The south facade of the building features a double-skin facade attached to a vertical rooftop solar chimney channel, as shown in Figure 2.31. Experimental and CFD analyses were conducted in this research to assess the natural ventilation performance of the prototype building. Panel heaters were employed to simulate temperature increases in the blinds of double-skin facade blinds and the absorber wall of roof-top solar chimney due to solar absorption.

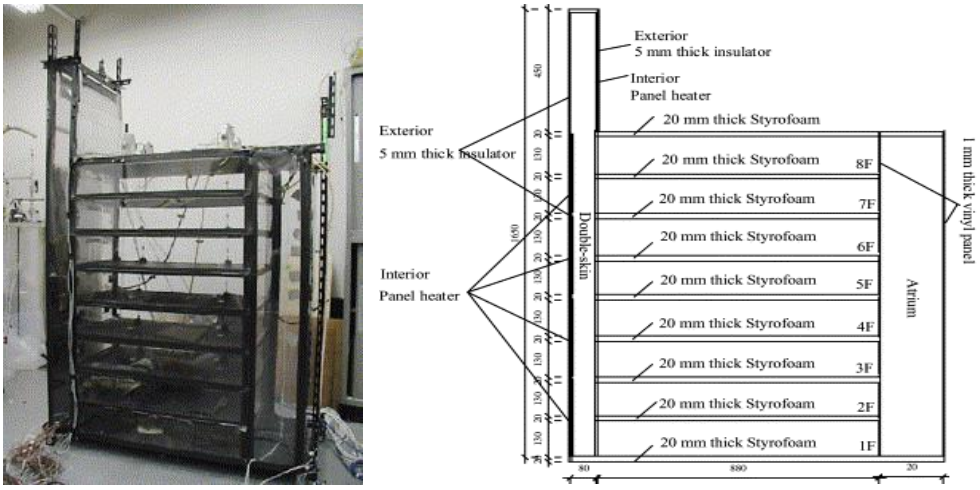


Figure 2.31: View of the test rig and schematic of the experimental model [53]

Temperature and pressure differences were measured to assess airflow conditions once the system reached a steady state. Incense sticks were used to the determine of airflow direction near openings. The outer facade blinds and chimney absorber wall were maintained at temperatures 10°C and 20°C higher than the outside. It was found that increasing the solar chimney height enhances the pressure difference between the atrium and double-skin space, improving air circulation on each floor. To maintain an effective pressure difference, the solar chimney should be taller than two floors.

In a study conducted by [57], an open-ended inclined rectangular channel with an emissivity of 0.02 radiant barrier (RB) was used, as depicted in Figure 2.32. The RB was applied to the lower plate, and the upper plate received a constant heat flux. The channel dimensions were 0.7 m in width and 1.5 m in length, with an adjustable air gap ranging from 3 to 11 cm. The channel had a fixed 30° slope from the horizontal plane. The study examined four heat flux values (190.5, 285.7, 380.9, and 476.2 $W/m^2$) and five air gap spacings (3, 5, 7, 9, and 11 cm). The surface temperature was measured using thermocouples, while a hot wire anemometer measured air velocity at nine different positions in the channel inlet.

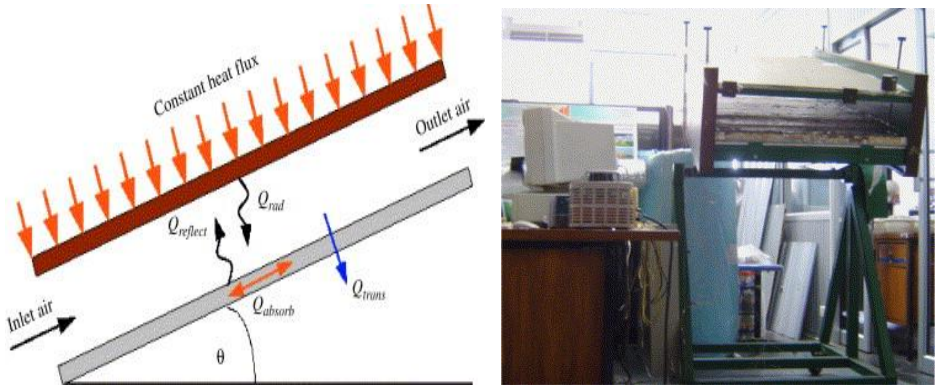


Figure 2.32: Schematic of experimental bench and real image of the inclined rectangular channel [57]

An empirical relationship was established for heat transfer in an inclined, open-ended rectangular channel with a top heating element and a reflective barrier (RB) on the lower plate. Comparing it to a standard solar roof configuration with gypsum board, the RB enhanced convection heat transfer and airflow by 40–50%, resulting in a 50% increase in heat transfer through the lower plate.

In this study [60], experiments were conducted using a reduced scale model of an inclined passive wall solar chimney (IPWSC) attached to a room under steady-state conditions. The model, shown in Figure 2.33, consists of a transparent glazing on one side and a heating plate on the opposite side to simulate the absorber wall, with an air channel in between. The chimney has a width of 0.5 m, an absorber wall height of 0.7 m, an inlet aperture size of 0.1 m, and a fixed air gap width of 0.1 m. Temperature and air flow rates were investigated for three Rayleigh numbers ($8.05 \times 10^{10}$, $2.76 \times 10^{11}$, and $4.19 \times 10^{11}$) at various inclination angles of the passive wall, ranging from 0° to 6°, while keeping the base air gap width constant. The smoke visualization technique was employed to observe reverse flow, while the shadowgraph visualization technique quantified the thermal field and thermal boundary layer near the absorber wall.

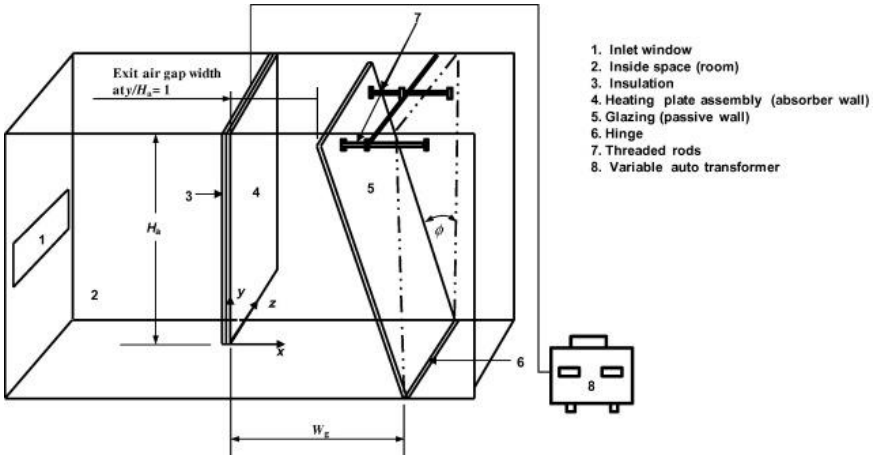


Figure 2.33: Schematics of IPWSC experimental model [60]

Experimental evidence shows that tilting the passive wall of a solar chimney, while keeping other factors constant, boosts airflow as the inclination angle increases up to a certain point. After that point, airflow decreases. This effect is due to the reduction of reverse airflow near the chimney exit.

In a study by [61], experiments and analytical analyses were conducted to investigate buoyancy-driven convection air flow in a solar chimney for airflow rate prediction improvement. The experimental solar chimney (Figure 2.34) was 2.0 m tall and 1.0 m wide, with a cavity gap varying from 0.2 to 1.0 m in 0.2 m increments.

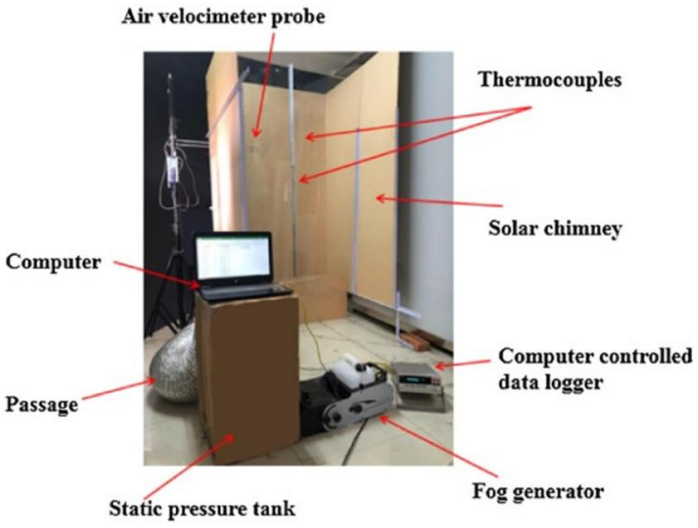


Figure 2.34: Picture showing the experimental test rig [61]

It featured three insulated walls, heat flux ranging from 100 to 600 W/m$^2$ at 100 W/m$^2$ intervals, and an observation glass plate. Thermocouples measured wall and air temperatures, while an anemometer recorded air velocity. Smoke was generated using a fog generator and stored in a static pressure tank. It was subsequently drawn into the solar chimney via natural convection, and the airflow was recorded with a CCD camera to observe the reverse flow in the channel. The air flow prediction method applied to the chimney under investigation showed good agreement with experimental results, with and without reverse flow.

### 2.4.2 Analytical Investigations

Analytical studies are conducted using the principles and fundamental equations of heat transfer and fluid dynamics, which encompass mass, momentum, and energy conservation principles. Mathematical models have been employed to predict the airflow rate within the chimney. These models are derived through mathematical deduction or correlations based on experimental or numerical findings. Analytical methods for analysing solar chimneys often rely on simple assumptions, like laminar flows and a uniform air temperature along the chimney height. These methods are effective for predicting thermal performance in chimneys with a small aspect ratio, typically less than or close to 10:1. However, in wider chimneys, the assumption of uniform temperature distribution may become invalid, and reverse flows near the chimney outlets can render theoretical predictions inadequate. In the realm of solar chimney analysis, the single zone model and plume model are commonly utilized techniques.

### 2.4.2.1 Single Zone Model Approach

The single zone model treats the entire chimney channel as one single zone in terms of density and temperature. This model formulates the mass flow rate as an explicit function of the density difference between the channel and the ambient [66]. Assuming that the heat input to the chimney, as depicted in Figure 2.35, is entirely utilized to alter the air temperature, the energy balance can be applied to demonstrate that the pressure difference at the two openings of the channel is offset by various pressure losses and changes in potential energy.

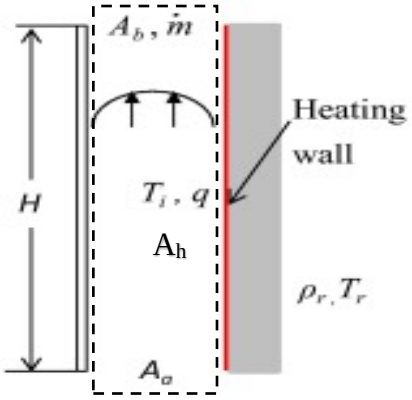


Figure 2.35: Solar chimney representations in single zone model

By utilizing the ideal gas law and disregarding the influence of pressure changes on density, focusing instead on the impact of temperature differences (according to the Boussinesq approximation), the mass flow rate can be obtained for a chimney with a uniform vertical inlet and outlet as below:

$$\dot{m} = C_d \rho_i A_a \sqrt{\frac{2gH(T_i - T_r)}{T_r}} \quad (3)$$

$$C_d = \left( k_a + + k_b \frac{A_a^2}{A_b^2} + \frac{fH}{2d_h} \frac{A_a^2}{A_h^2} \right)^{-\frac{1}{2}} \quad (4)$$

To determine the discharge coefficient ($C_d$) and the pressure loss coefficients ($k_a$) at the inlet and ($k_b$) at the outlet, a commonly employed method involves utilizing existing data associated with forced flows in a rectangular channel where both ends are open and one wall is heated [67]. In earlier investigations, the air temperature at the chimney exit was used to compute the density difference [9,68]. In more recent studies, a weighted average of the inlet and outlet temperatures was employed to enhance model predictions [20,39,41,42,48,69]. The choice of the weighting factor and the discharge coefficient, which relate to flow resistance, was somewhat arbitrary. These parameters could potentially be determined by fitting experimental data. Even when using a similar weighting factor, three studies produced different discharge coefficients, ranging from 0.52 to 0.8, despite having similar solar chimney configurations [17,41,42]. Since the accuracy of the model predictions is highly dependent on the discharge coefficient, this wide range renders the single-zone model unsuitable for general applications. Single-zone models were further classified into four types based on their modelling input variables, as suggested by [34]. The first type of model exhibits a power-law relationship between mass flow rate and an individual parameter. Below, some examples of this type of modelling approach as documented in the literature are presented.

Empirical formulas were derived by [55] through multivariate regression analysis using data from controlled experiments. These experiments involved heating a rectangular indoor channel uniformly from one wall in the range of 200 to 1000 $W/m^2$. The dimensions of the channel were 102.5 cm in height and 92.5 cm in width, and its depth varied from 20 to 110 mm. The study found that the mass flow rate within the channel was directly proportional to both the heat input power and the channel depth.

The empirical formula was derived by [56] through regression analysis based on data from experiments involving indoor rectangular channels heated uniformly from one wall, with power ranging from 200 to 1000 W/m$^2$. This study examined 90 combinations of channel depth, channel height, and heat input using three test rigs with varying channel dimensions. The channel depth ranged from 20 mm to 150 mm, and the mass flow rate within the channel was found to be related to the heat input and the height of the absorber wall.

The second type of model predicts mass flow rate using cavity air temperature and ambient air temperature, inlet and outlet areas, cavity height, and inclination angle (for roof solar chimneys). Some documented examples of this modelling approach are mentioned below.

First, Andersen, in his work [70], developed an analytical model for predicting natural ventilation through small openings in a room using the pressure model based on thermal buoyancy. Subsequently, in references [9,28,58], analytical formulas were derived for predicting airflow rates in the case of a solar chimney with varying opening sizes and inclination angles. These formulas assumed that the pressure head inside a chimney entirely counterbalanced the pressure drop caused by wall friction and inlet and outlet pressure losses. Additionally, references [18,35,40] adopted a similar approach to predict flow rates induced by a solar chimney with a uniform wall temperature.

The third model utilizes density-based predictions, employing air densities within and outside the chimney cavity as input variables, like the second model, which substitutes air temperature with air density. One example of this modelling approach is mentioned below.

the authors in study [71] developed an analytical formula to estimate the average air flow rate within a tilted chimney. They assumed that the pressure head in the chimney offsets pressure losses from wall friction and inlet and outlet pressure, especially when the chimney has similar cross-sectional areas at both ends and experiences minimal density variations.

The fourth type of model is heat flux-based prediction in the chimney channel. The model shows a power law relationship between airflow rate and injected heat flux. Some examples of this type of modelling approach in the literature are presented below.

Considering heat balance and opposing forces like friction and end pressure losses, the authors in their research work [21] developed a power law expression for airflow rate of the rectangular channel with a uniform wall heat flux. The study confirmed the close agreement between the predicted airflow rate and experimental results for a rectangular channel with one heated wall and a 28:1 height-to-gap ratio.

Similarly, the study [54] demonstrated that the air flow rate correlation they developed aligned well with experimental results for rectangular channels with one wall uniformly heated, having aspect ratios ranging from 15:1 to 5:2. However, this analytical correlation tends to significantly overestimate air flow rates in specific chimney configurations, particularly in wide vertical chimneys.

A power-law relationship was determined for the average air exit velocity and solar energy intensity through a study of a vertical wall chimney attached to a room, based on numerical and analytical analysis conducted by [72].

All four analytical models discussed for predicting mass flow rate primarily focused on cavity configuration, neglecting room layout. To address this issue, the study [73]

introduced a full-scale numerical model considering both room and chimney configurations. They utilized the Fire Dynamic Simulator (FDS) to simulate a solar chimney attached to a room, validating it with previous experimental data [52]. Subsequently, they developed an empirical model for airflow prediction, incorporating room configuration and introducing a coefficient to account for room and chimney characteristics. The study demonstrated that room size and opening placement have a limited impact on performance.

#### 2.4.2.2 Plume Model Approach

To achieve more accurate modelling, it's essential to account for the non-uniform density distribution due to thermal boundary layers. Numerical methods offer detailed insights into complex phenomena, like reverse flow [74–78], but their time-consuming iterations are impractical in certain applications. For instance, building energy simulations (BES) with a solar chimney design require a quicker flow rate solution. An alternative option is to model the thermal boundary.

A plume model was introduced by [79] based on thermal boundary layer and energy balance theory to predict mass flow rate in solar chimneys, accounting for density variations in both horizontal and vertical directions within the chimney. In this model, as shown in Figure 2.36, not all parts of the chimney channel contribute to the stack flow, particularly when it has not yet fully developed. Flow and stack pressure primarily manifest within the plume, with the width of the plume being directly related to the thermal boundary thickness at the top of the channel.

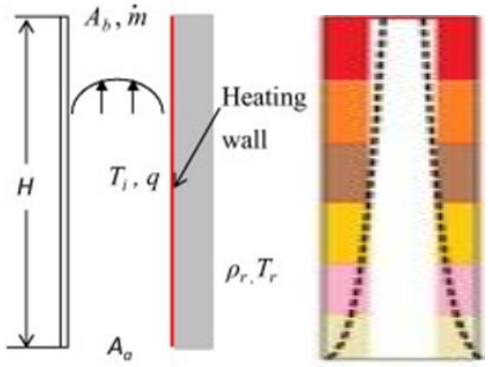


Figure 2.36: Representation of solar chimney in plume model

The model was iteratively solved and validated using six experimental data sets [39,54,55,80–82], representing various inlet and outlet designs for the solar chimney. In conclusion, the model performed well in predicting air flow rates, and further improvement was suggested by considering a turbulent boundary layer for high-velocity conditions. The authors of study [79] have enhanced their plume model for predicting flow rates in vertical solar chimneys linked to multiple ducts or pipes connected to the chimney in their study [66]. Validation of this improved model was carried out using field data gathered from a full-scale solar chimney attached to a test house on a university campus in Hangzhou, China, during the fall and winter seasons [83]. Wind interference was mitigated by employing a windproof net at the chimney outlet. The primary contributors to stack flow were solar radiation and the temperature differential between the interior and exterior. The field data confirmed the accuracy of the improved plume model, accurately predicting all the data points.

### 2.4.3 Computational Investigations

This section of the text presents computational studies pertaining to numerical thermal modelling of diverse solar chimney types. The primary focus within this section centres on two distinct research domains: Computational fluid dynamics (CFD) and simulations grounded in the global energy balance (GEB) framework for solar chimney analysis. CFD

is a potent tool for studying solar chimney heat transfer and flow topology, but few transient state CFD models exist due to excessive computational time. High performance computing (HPC) is needed for CFD. In contrast, GEB models quickly predict solar chimney system behaviour and can be integrated into building energy simulation (BES) programs with ease.

#### 2.4.3.1 Global Heat Energy Balance Approach

Most of the analyses reported in the literature [15,20,38,39,41,42,47,48,69,72] adopted the global heat energy balance (GEB) model approach for computational studies on solar chimneys. This approach is employed to quickly assess the thermal performance of solar chimneys by applying global heat energy balance approach. This widely adopted method involves treating the working fluid and various components of the studied solar chimney as distinct nodes within a thermal network. Under certain assumptions, energy conservation equations are then applied to these nodes, with a focus on predicting their temperatures. In addition, flow rate in the solar chimney can be predicted by integrating the single zone model equation proposed by [9,70] with the GEB model of the solar chimney. The GEB model offers a rapid assessment of the thermal efficiency of a solar chimney with significantly reduced computational costs. Hence, GEB models are a very valuable tool for engineers to predict the dynamic behaviour of a system in relatively short time and one can integrate them into Building Energy Simulation (BES) tools like EnergyPlus, DOE-2, TRNSYS, and other software [10,84,85]. Some significant contributions from the literature in the field of GEB modelling concerning the solar chimney are given below.

The study [9] used a GEB steady-state model for a solar chimney, reportedly the pioneering work that appeared in the literature. The solar chimney proposed by [9] is a

solar air collector roof connected to a conventional vertical chimney for natural ventilation. Since then, the GEB steady state model approach has been employed under different climatic conditions and for different configurations of conventional solar chimneys by scores of authors [14,15,19,20,28,32,39,41,42,47,48,72,86,87]. It was found that the seminal work of [42], [41], [20], [39], [86] has paved the way for other researchers to adopt the GEB modelling approach for novel configurations of solar chimney design. The authors have introduced various steady-state GEB models for distinct solar chimney configurations operating in different climatic zones. The mathematical models were validated with outdoor experimental data generated from the physical models. Satisfactory theoretical predictions and experimental findings have been obtained with respect to air flow rate, the increase in mean air temperature, mean absorber temperature, and glass wall temperature. Moreover, scientific publications on transient heat balance models (THBM) for solar chimneys are available but less abundant than steady-state GEB models. THBM models have been developed for various indoor and outdoor solar chimney configurations using the finite difference technique [45,46,51,58,69,88]. A review of the literature on solar chimney models, as cited in reference [84], reveals four distinct mathematical models related to solar chimney, which are illustrated in Figure 2.37.

Model-1 comprises three nodes for conducting the global energy balance. The energy balance of the absorber plate is calculated for the node positioned at the surface in contact with the fluid, while the other two nodes are situated: one in the centre of the glass cover and the other in the centre of the channel. Model-2, on the other hand, utilizes four nodes for energy balance, taking into account two nodes each for the inner and outer surfaces of the absorber wall, along with nodes at the centre of the glass cover and the channel.

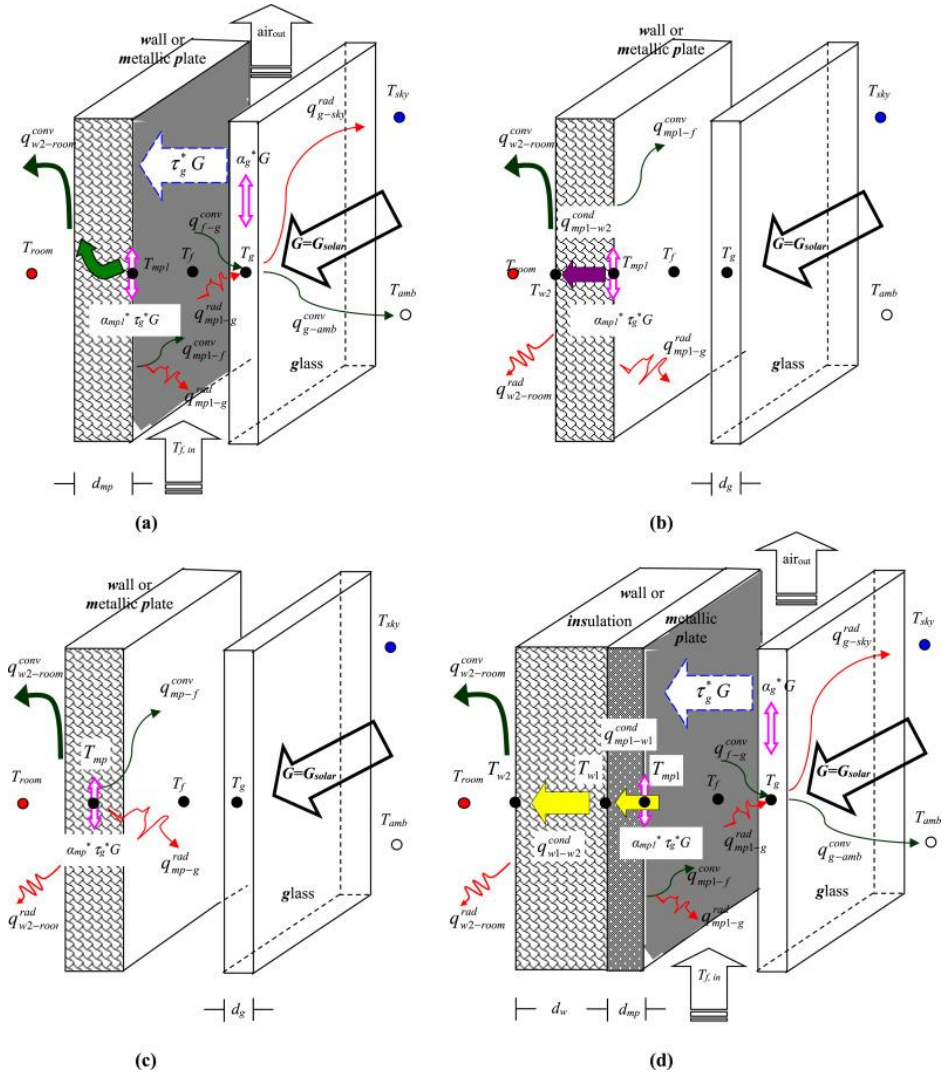


Figure 2.37: Physical models of solar chimney: (a) Model-1 (b) Model-2 (c) Model-3 and (d) Model-4 [84]

In Model-3, three nodes are employed for energy balance, positioned at the centre of absorber plate, glass cover, and air channel. Model-4 integrates five nodes: at the centre of the glazing and air channel, the inner and outer surface of the metallic plate, and the outer cover of the insulation layer, for energy balance calculations.

### 2.4.3.2 Computational Fluid Dynamic Approach

Computational fluid dynamics (CFD), initially introduced in the 1970s for building ventilation, has gained significant popularity over the years. The number of peer-reviewed articles has surged from less than 10 annually in the 1990s to 60–70 per year

[89]. The use of CFD in solar chimney analysis has been facilitated by fast numerical schemes. CFD offers comprehensive flow and thermal data for the whole field of interest. The CFD technique can capture flow phenomena like reverse flow and complex flow development at the inlet and outlet of the chimney, in contrast to the GEB modelling approach. Laminar flow codes were used before commercial CFD software became available. According to study [30], CFD k-epsilon models closely match experimental results, offering more accurate velocity and temperature predictions. This is attributed to the fact that turbulent flow better reflects conditions in solar chimneys. As can be seen in Figure 2.38, 2.41, 66% of authors have adopted k-epsilon models as the primary research method for solar chimney investigations.

However, it is still challenging to define proper boundary conditions in CFD. The majority of solar chimney modelling using CFD has primarily concentrated on steady-state simulations, as exemplified by references [38,49,72,74–76,87,90–94]. Fewer investigations, such as those presented in references [36,95] , have delved into transient CFD simulations, primarily owing to their substantially greater computational load and time constraints.

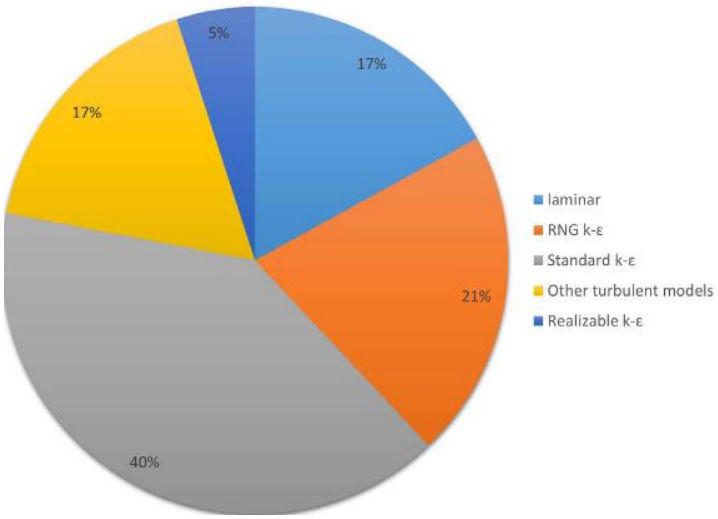


Figure 2.38: CFD techniques used in solar chimney investigations [30]

Numerous CFD studies have examined different chimney configurations and conducted parametric studies to optimize solar chimney designs and identify critical geometric variables affecting performance. However, this section will focus on CFD studies of thermal and kinematic flow fields in solar chimneys and how the computational domain affects performance prediction. In this regard, some significant contributions from the literature are given below.

The authors in study [72] Conducted steady-state computational fluid dynamics (CFD) and analytical analysis on a vertical-wall solar chimney attached to a room, as shown in Figure 2.39. The research investigated variables including chimney inlet size and cavity gap. It was observed that the chimney cavity gap has a greater influence on the air changes per hour (ACH) compared to the chimney inlet size. Moreover, the flow pattern in the chimney was examined to identify and prevent flow separation. It was noticed that flow separation occurred at the leading edge of the absorber wall of the chimney due to the sudden contraction at the inlet opening, known as the vena-contracta effect.

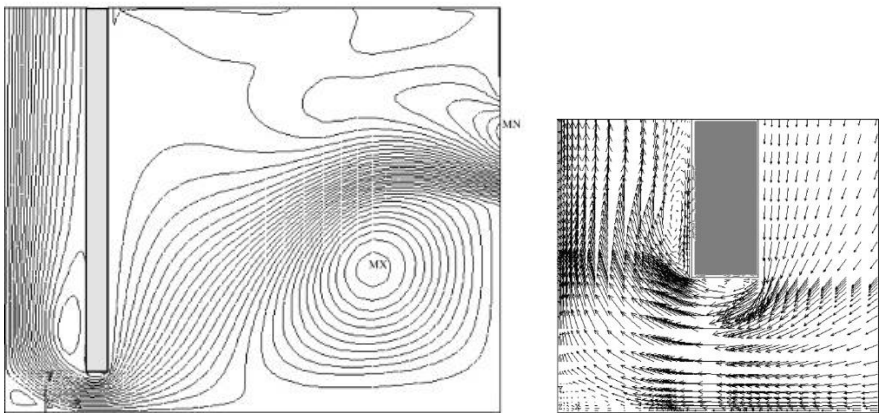


(a) (b)

Figure 2.39: (a) Streamline plot through a 0.2 m chimney width under 300 W/m$^2$ solar intensity (b) Velocity field in the expanded portion beneath the absorber wall. [72]

This separation resulted in the dissipation of mechanical energy and increased resistance in the upward flow, reducing the exit velocity and mass flow rate. To prevent flow separation, it was recommended to chamfer the inlet sharp edge of the absorber wall.

A validated CFD model, as reported by [76], was utilized to predict buoyancy-induced airflow and heat transfer in open-ended vertical cavities. These cavities featured various combinations of heat distribution on two vertical walls, ranging from symmetrical to fully asymmetrical heating, and included different types of inlet and outlet openings. The paper by the same author, referenced as [96], contains detailed information regarding the various models of vertical cavities and their corresponding equations. In the simulations, the computational domain was expanded up to 10 times the channel width around all four sides of the channel to accurately predict the flow topology within the channel, as described in study [77]. Figure 2.40 depicts predicted airflow patterns near the inlet and outlet under specified boundary conditions. Velocity vectors were plotted at the top and bottom of the channel. In the cavity with a horizontal inlet, air flowed from the inlet, turning from horizontal to vertical, creating a large recirculation zone near the unheated bottom wall and a smaller zone above the inlet. In horizontal inlet cavities, reverse flow occurred near the top of a shiny, unheated mirror wall.

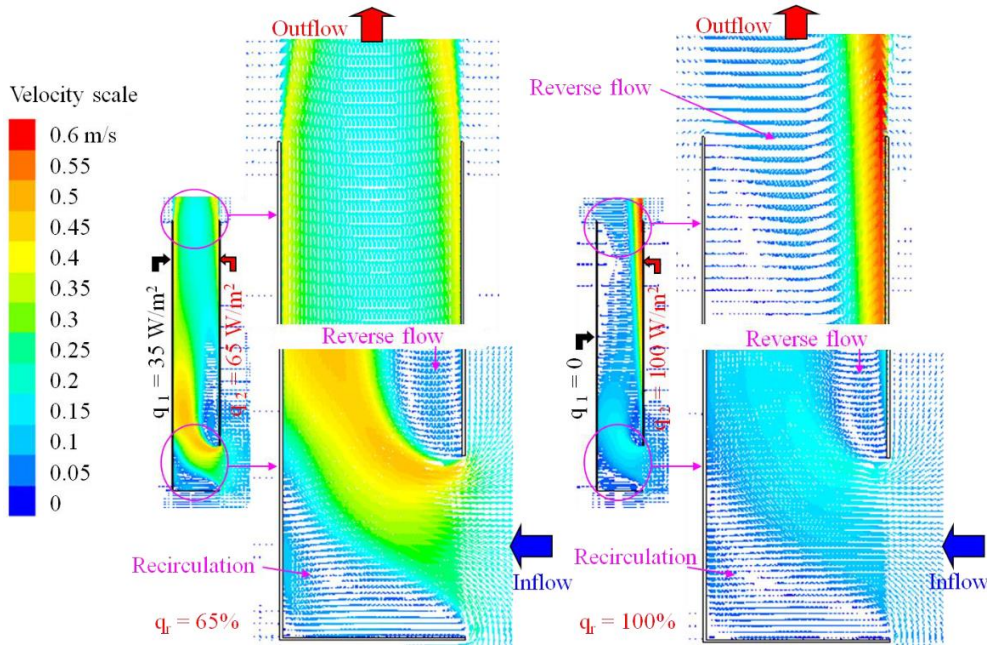


Figure 2.40: velocity vectors near the inlet and outlet of 3 m tall and 0.6 m cavity gap with 65% and 100% heat distribution ratio[96].

It was concluded that in the case of cavities like those found in solar chimneys or room ventilation double façades, horizontal inlet cavities exhibit lower flow rates compared to cavities with vertical inlets at the bottom. Remarkably, cavities with horizontal inlets typically have higher heat transfer rates than those with vertical inlets.

A study [97] investigates the influence of computational domain selection on the accuracy of CFD simulations for a vertical wall solar chimney attached to a building as illustrated in Figure 2.41. Four domain configurations were evaluated, including the chimney and room, the chimney and inlet length, chimney with a horizontal inlet, and the air channel. The CFD model employed RANS equations with an RNG $k-\epsilon$ turbulence model and a surface-to-surface (S2S) model for radiative heat transfer, validated against experimental data [55]. The study examined four computational domains at different absorber heights (1.0 m, 2.0 m, and 3.0 m) and heat flux levels (200 to 1000 W/m$^2$) on the left or right air channel wall, while keeping the air gap and inlet height constant at 0.1 m.

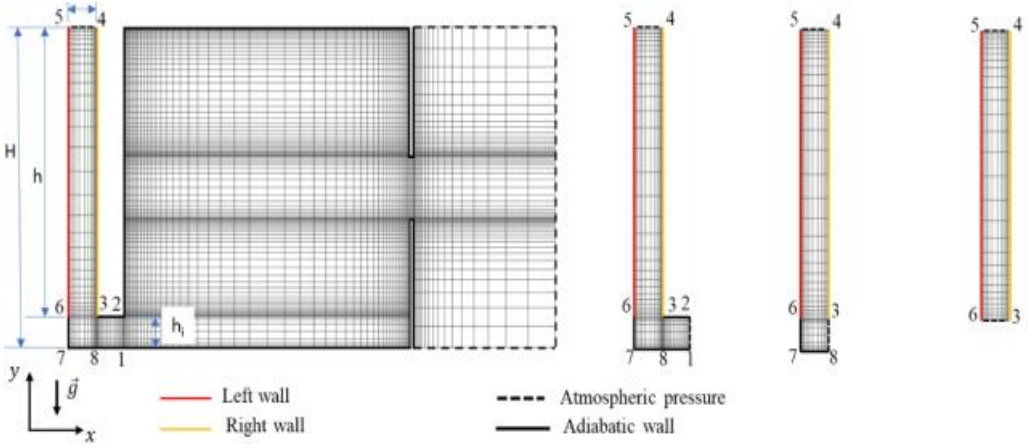


Figure 2.41: Computational domain for simulations: (a) Solar chimney with room, (b) chimney and the inlet length, (c) chimney and horizontal inlet (d) chimney only [97]

It was found that the selection of the computational domain should match the desired solution accuracy. For accurate evaluations of building energy and thermal performance, using the full computational domain is advised for accurate results.

The authors in [75] investigate turbulent air flow inside the inclined passive wall solar chimney (IPWSC) for room ventilation under varying conditions. A standard $k - \varepsilon$ turbulence model has been adopted to model air turbulence in the IPWSC system. Simulations cover a wide range of Rayleigh numbers ($1.36 \times 10^{13} \leq Ra \leq 1.36 \times 10^{16}$) with specific geometric parameters, including aspect ratio 6.25, room-to-absorber wall height ratio 1.2, absorber-to-window height ratio 2.5, room-to-absorber wall thickness ratio 12.5, and passive wall inclination angle ($0° \leq {}^{\theta} \leq 6°$). Moreover, Simulation compared a standalone vertical wall solar chimney configuration to a room-attached vertical wall solar chimney configuration.

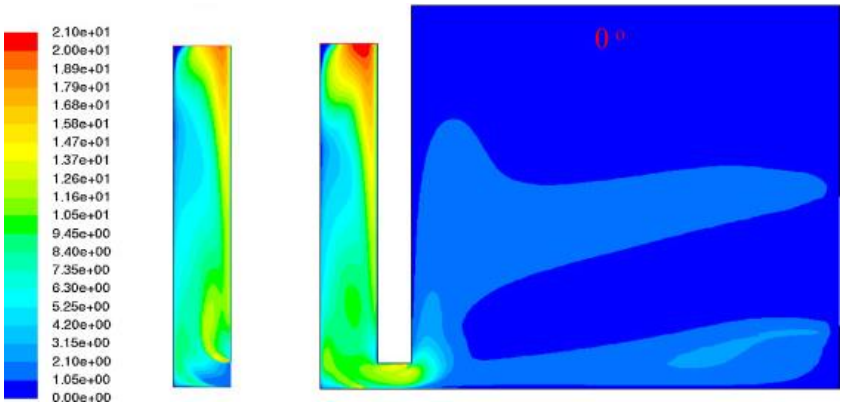


Figure 2.42: Contour plots of the turbulent intensity for Ra = 1.36 × $10^{14}$(a) standalone chimney model and (b) an attached room model [75]

In Figure 2.42, the turbulent intensity distributions inside the solar chimney are similar for both configurations, particularly in the upper part of the vertical channel. However, the turbulence intensity is significantly higher in the attached room model, especially near the exit and at the inlet section. Furthermore, the room attached model exhibits local flow circulation beneath the absorber wall in the inlet section, while the standalone model lacks this circulatory pattern. The flow patterns near the chimney entrance are also explained in references [72,76]. The standalone model exhibits higher velocity profiles than the attached model, along with reduced turbulent kinetic energy production and a smaller region of reverse flow influence. Consequently, the standalone chimney model over-predicts the mass flow rate by 10% at a Rayleigh number of Ra = 1.36 × $10^{14}$.

The study [74] conducted a 2D steady-state CFD simulation to investigate the impact of surface emissivity on the thermal and flow characteristics of a wall solar chimney. The study focused on laminar airflow within an asymmetrically heated absorber, with flux ranging from 20 to 100 W/$m^2$, a fixed absorber height of 0.7m, and varying air cavity gap (0.1 –0.4 m) and inlet aperture (0.1–0.5 m) heights. The presence of surface emissivity distinctly alters the thermal and flow field topologies, as evident in Figure 2.43.

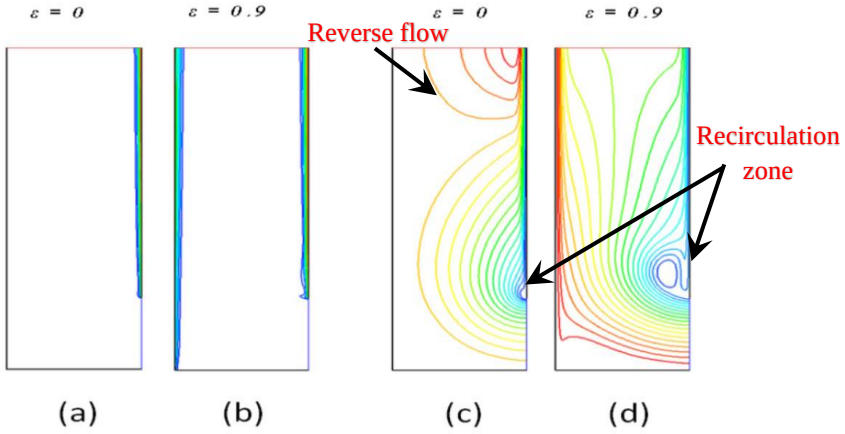


Figure 2.43: Contours of static temperature (a) and (b) and streamline plots (c) and (d) at cavity gap 0.3 m, inlet opening height 0.2 m, absorber wall 0.7 m and Ra = 8.36 × $10^{10}$ [74]

A minor circulation is seen near the front of the thermal boundary layer, just above the inlet aperture on the heated wall, caused by inlet flow separation, which is more significant when considering radiation effects. Numerical findings show that mass flow rates rise with higher surface emissivity and input heat flux. 0.9 surface emissivity leads to a 59% greater mass flow rate than 0.0 emissivity. Furthermore, the performance of chimney was found to be more affected by changes in the air cavity gap than by changes in the inlet opening height.

## 2.5 Design Parameters of Solar Chimney System

Numerous studies conducted by researchers have aimed to pinpoint the essential factors influencing ventilation rates. In their research [34,98], the authors have consolidated these factors into four categories, encompassing a total of thirteen parameters that impact the performance of solar chimneys. These categories comprise solar chimney and building configurations, installation methods, material properties, and external environmental conditions. In Figure 2.44, 13 influencing parameters affecting the performance of solar chimneys are presented. This literature review specifically delves into the impact of eight of these parameters on solar chimney performance.

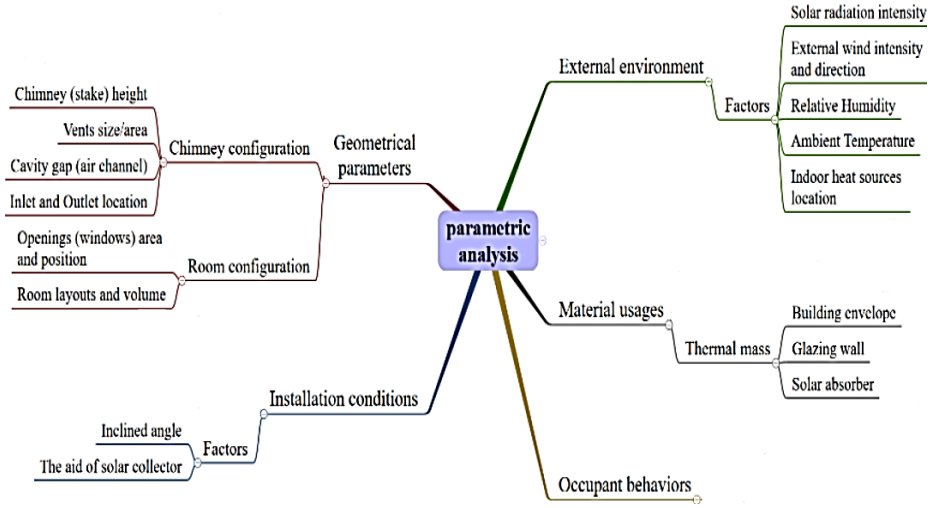


Figure 2.44: Factors affecting solar chimney performance [98]

It places particular emphasis on the influence of geometrical factors such as air cavity width, absorber height, aspect ratio, and vent location on the solar chimney. Additionally, it explores the role of attached rooms and their openings and examines the effects of external wind on the performance of solar chimneys.

### 2.5.1 Effect of Chimney Absorber Height

Chimney height, sometimes called stack height in solar chimney literature, plays a crucial the ventilation performance of the chimney. It impacts temperature and pressure differentials, influencing the stack effect. Some of the studies highlighting the effect of stack height are given below.

Experiments using metallic solar walls of different heights, 1 and 2 m, was conducted by [42]. The findings indicated that a 2 m high absorber wall with a 0.145 m air cavity gap and a surface area of 2 $m^2$ can generate a mass flow rate ranging from 0.01 to 0.02 kg/s.

Solar chimney integrated into the walls and roof to improve ventilation in low-rise buildings located in hot and arid regions was studied by [35]. The height of the chimney wall varied from 1.95 m to 3.45 m. They discovered that by optimizing the chimney wall

height to 3.45 m and setting the inlet aperture height at 0.15m, it was possible to achieve an air flow rate of 2.3 $m^3$/s. Furthermore, their model could achieve an Air Changes per Hour (ACH) of up to 26 for a flat with a volume of 321 $m^3$, effectively addressing the high cooling requirements of a building in a hot climate.

A 1-D GEB model was used by [47] to study how stack height affects the ventilation performance of a double-sided roof-top solar chimney in Malaysia's climate and similar conditions. Simulations were conducted with chimney heights of 5m, 10m, and 15m, and experiments were performed to validate the results. The analysis closely matched the experimental findings, showing that as chimney height increased, the airflow velocity also increased. A 15 m high chimney achieved a maximum velocity of 4.5 m/s, which was 23% higher than the 5 m high chimney.

An empirical equation was derived by analysing simulations of a full-scale numerical study on a solar chimney attached to a room, as referenced in [73]. This equation establishes a relationship between air flow rate and different design factors, such as the absorber height of the solar chimney.

The study [10] examined how chimney height impacts a solar chimney's ventilation using EnergyPlus simulations. In all tested climates, increasing chimney height enhanced ventilation due to the extended convection heat transfer path between the absorber wall and the air. The results indicated that raising the chimney height from 3.5 m to 9.5 m led to an average 74% increase in ventilation rate.

The author of the study [53] conducted experiments and used computational fluid dynamics to investigate a 1/25 scale model of an eight-story office building with an atrium. This building had a double-skin facade on the south side and a solar chimney

above it. The height of this solar chimney influenced the absorption of solar radiation by the thermal storage wall and created a stack effect, leading to increased air exchange rates.

An analytical study, as reported by [19], investigated the height of a vertical wall chimney connected to a room, ranging from 2 to 8 meters. The research determined that the impact of chimney height was minimal, resulting in a mere 18% increase in mass flow rate when doubling the height of the chimney.

In the CFD study referenced in [12], the authors examined how chimney height affects the ventilation performance of combined wall and roof solar chimneys. The stack heights in their investigation ranged from 7 m to 21 m, with 3.5 m intervals. Their findings demonstrated that with a smaller width of the solar chimney (1.0 m), increasing the stack height resulted in a slight increase in the induced air change rate. However, with a larger width (7.0 m), the increase in the induced air change rate became much more significant as the stack height increased.

### 2.5.2 Effect of Chimney Cavity Gap

The air gap, or cavity gap or width, which is the space between the glazing and the absorber wall of a solar chimney, significantly influences heat transfer in the system. Researchers have extensively studied the relationship between the cavity gap and the ventilation performance of solar chimneys to better comprehend its effects. Some relevant research findings on cavity gap in vertical and inclined chimneys are mentioned below.

An indoor experimental study was conducted by [51] on a full-scale wall solar chimney attached to a room to examine the impact of varying an air gap. The solar chimney was 1.95 m in height and 1.5 m wide, with air cavity gap ranging from 0.1 m to 0.5 m. The inlet aperture was 0.1 m high and located at the base of the wall. The study considered a

range of UWT boundary conditions with temperature differences between the heated wall and the ambient from 0 to 30 K. It was observed that the optimum flow rate induced by the solar chimney was 0.2 m air gap.

An indoor experimental study on a model of solar chimney similar to a rectangular open-ended channel, was conducted by [54]. The height and width of the channel were 1.5 m and 0.62 m, respectively. The air cavity gap and inclination angle were adjusted, with the height-to-gap ratio ranging from 15:1 to 5:2. To assess the impact of the air gap, it was varied from 100 mm to 600 mm. One wall of the model was uniformly heated (200 $W/m^2$ to 600 $W/m^2$) to simulate a solar chimney's absorber wall. The results showed that an increase in air cavity gap led to higher ventilated airflow, but no optimal air gap was identified, as also referenced in [39].

The study [20] also reported similar findings in relation to the air cavity gap and air flow rate in their study. They developed a GEB model to predict how solar radiation intensity and air gap affect the performance of solar chimney, validating their results with experimental data. They discovered that, within the range of solar flux considered, increasing the air cavity gap resulted in higher airflow rates through the solar chimney. Their calculations showed that a solar chimney with a 0.3 m air gap width at a solar flux of 650 $W/m^2$ resulted in a 56% higher airflow velocity compared to a 0.1 m air gap. Moreover, widening the air cavity gap reduced the mean temperatures of air, glazing, and the heated wall.

Indoor experiments were conducted by [55] on a vertical channel to simulate the operation of a standalone solar chimney. In these experiments, a black-painted wall served as the absorber, and a transparent cover acted as the glazing wall. The air cavity gap ranged from 20 to 110 mm, and it was reported that the mass flow rate increased as the air gap

width widened. Moreover, their analysis revealed that the mass flow rate can be expressed as a power-law relationship between the heat input and the channel depth, independently.

In their full-scale outdoor study [99], the authors examined the impact of the air cavity gap on the ventilation rate of a 1.5 m long roof solar chimney (RSC). They considered two air gap widths, 80 mm and 140 mm, and measured temperatures and air velocities, respectively. The results revealed that a larger air gap width resulted in higher airflow rates, suggesting that increasing the air gap width can enhance RSC ventilation performance, with differences of up to 20 $m^3$/hr between various configurations.

The literature also contains reports of optimal air gap for maximizing solar chimney performance, with details of the research work provided below.

In this study [65], the authors used experimental and analytical approaches to investigate the impact of the air cavity gap on a small-scale solar chimney model attached to a room. Their findings highlighted the presence of an optimal air gap, which was unrelated to solar radiation intensity but exhibited a positive relationship with inlet aperture size and stack height. The ideal air cavity gap is 1/12 of the chimney height and is also dependent on the inlet aperture geometry and dimensions.

The study [52] found that in a full-scale study of a wall solar chimney attached to a room in southern Algeria, an optimum air cavity gap of 0.2 m to 0.3 m led to maximum induced airflow regardless of the wall temperature, with inlet aperture heights of 0.1 m and 0.4 m. For a 0.2 m air gap, 0.1 m inlet aperture height, and a 5K temperature difference, the induced mass flow rate could reach 0.043 kg/s.

### 2.5.3 Effect of Chimney Aspect Ratio

Aspect ratio typically pertains to the ratio between the height of the absorber and the depth for a wall solar chimney, or alternatively, the ratio between the length of the cavity and the depth for a roof solar chimney. Researchers conducted systematic studies to optimize the aspect ratio of the solar chimney design for improved ventilation performance. Some of the research findings on chimney aspect ratios are mentioned below.

The authors in study [54] developed a 1.5 m tall and 0.62 m wide experimental model of a solar chimney resembling a rectangular open-ended channel to estimate airflow rates. They varied the air gap from 100 mm to 600 mm and used an electric heating system to simulate solar radiation (200 $W/m^2$ to 600 $W/m^2$) on one chimney wall. The aspect ratio was altered from 15:1 to 5:2 to study its impact on airflow, reaching a maximum rate of 0.035 $m^3/s$ at an aspect ratio of 7.5:1. However, no specific optimal aspect ratio was determined.

A study conducted by [15] involved outdoor experiments to study the impact of aspect ratio on the performance of solar chimney. They used various combinations of absorber height and air gap widths of a wall chimney attached to a small wooden room (1 m × 1 m × 1 m) with a solar chimney. The absorber wall was made of black-painted aluminium, and a glass panel (1 m×1 m) represented a typical window in hot regions. For a 1 m high solar chimney with an aspect ratio of 2.83, a ventilation rate equivalent to 5.6 ACH in a 27 $m^3$ room under 700 $W/m^2$ solar radiation could be achieved. However, the optimal aspect ratio was not determined.

Researchers have identified the optimal aspect ratio for a vertical wall chimney to maximize ventilation rates. This ratio was found to be closely linked to the proportion of

the inlet opening to chimney height. Various studies, mentioned below, have documented the optimum height-to-gap ratios.

A parametric study [51] was conducted on a full-scale indoor model of a vertical wall chimney attached to a room. The study investigated the aspect ratio for various UWT symmetrical heat flux boundary conditions and air cavity gaps. It was observed that, for a 2 m high chimney wall and an inlet height of 0.1 m, the optimal cavity gap was approximately 0.2 m. Consequently, the aspect ratio was found to be 10:1 under various UWT symmetrical heat flux boundary conditions.

A study by [65] found that for a reduced-scale model of a solar chimney attached to a room, maintaining a constant aspect ratio of 12:1 (chimney height to optimal air cavity gap) yields the highest ventilation rate, regardless of chimney height. Specifically, the authors determined that with a buoyancy flux of 489 $cm^4/s^3$, a solar chimney with a 400 mm height requires a 24 mm air gap width, while a 200 mm chimney height needs a 12 mm air cavity gap to achieve maximum ventilation.

A parametric study [92] simulated a solar chimney with horizontal inlet and outlet openings, which were asymmetrically heated at UHF. Simulations were aimed at predicting the mass flow rate, temperature, and velocity under steady-state conditions. The results indicated that, for an optimal wall solar chimney design, the recommended ratios should be 10:1 for height to air cavity gap and 3:20 for inlet chimney height.

In the study [100], experiments were conducted using a 2 m high and 1 m wide vertical wall model of a solar chimney. The chimney air gap ranged from 0.4 m to 1.2 m in width. The model featured vertically positioned inlet and outlet openings and was uniformly heated asymmetrically at a range of 200–400 $W/m^2$, with aspect ratios between 5:1 and

3:5. Results indicated that an optimal aspect ratio of around 2:1 maximized the airflow rate in the chimney. The optimal chimney air cavity gap was determined to be 1 m.

To comprehend the impact of air moisture content in hot and humid regions on the aspect ratio of the solar chimney and, consequently, its ventilation rate, the findings of the study in the literature review mentioned below are essential.

The paper presented by [101] investigated the optimal aspect ratio by varying the cavity gap in the range of 0.005–0.5 m and the height of the heated walls of the channel in the range of 1.5–5 m. low-Reynolds k–ω turbulence numerical simulations were performed to analyse flow patterns in an L-shaped channel that resembles a wall solar chimney configuration. The findings indicate that under uniform wall temperature (UWT) heating conditions, the optimum aspect ratio for maximizing the generated airflow initially rises as Ra approaches $10^8$ but subsequently decreases as Ra continues to increase. A reverse flow region at the outlet of the channel appears when Ra is around $10^8$. But when the heating condition of the wall was changed to UHF, the authors presented three main observations: first, the shift from a laminar to turbulent flow regime happened at Ra ≈ $10^{13}$; second, there was no identified optimal air cavity gap and aspect ratio of the chimney.

### 2.5.4 Effect of chimney Apertures

The inlet and outlet areas play a crucial role in regulating air flow in solar chimneys. In the case of roof solar chimneys and wall solar chimneys with vertically oriented inlet and outlet areas, most of the test rigs are designed with equal inlet and outlet areas, as demonstrated in references [46,54,55]. In such configurations, the impact of the inlet and outlet areas on performance can be assessed by considering the air cavity area. However,

it's important to note that this trend does not consistently apply to rooftop and wall solar chimneys with horizontal inlet or horizontal outlet configurations, as seen in references [9,15,17,39,42,94,102].

The paper presented by [65] studied experimentally the impact of the inlet opening on the ventilation rate of the solar chimney on their small-sized indoor model. Two types of inlet opening configurations were examined. The initial design featured a rectangular aperture with an area of 1500 $mm^2$. In the second design, 10 circular openings were incorporated into the rectangular aperture from the first design, resulting in a combined inlet aperture size of 3000 $mm^2$. The data from the experiment demonstrated that a larger opening size resulted in higher airflow. Additionally, the study indicated that the ventilation performance of the solar chimney was more responsive to variations in the size of the chimney inlet opening than to alterations in the shape of the inlet opening or changes in the size of the window opening of the room.

In the experimental study [51], the impact of the inlet opening height on the performance of a full-scale indoor solar chimney model was investigated. Two specific inlet opening heights, namely 0.1 m and 0.4 m, were taken into consideration. The experiments were carried out across various air cavity gaps, including 0.1 m, 0.2 m, 0.3 m, and 0.5 m. For each air cavity gap, the air flow rate was determined at both 0.1 m and 0.4 m inlet opening heights. It was concluded that, for a 0.1 m air cavity gap, variations in inlet opening height had a negligible impact on the ventilation performance of the solar chimney. Nevertheless, as the air cavity gap widened, differences in air flow rates at varying inlet heights became more pronounced, revealing that higher inlet heights resulted in increased air flow rates.

### 2.5.5 Effect of Room and Window Placement

The literature review lacks enough numerical and experimental studies regarding the impact of room configuration on air inlet flow patterns and the role of window size and location in influencing flow inside the room and in the solar chimney. Some of the key findings from the available studies are mentioned below.

To visualize the flow pattern in the (3 m x 3 m x 3 m) room attached to the wall solar chimney, smoke tubes were employed by [51] to generate dense white smoke. The smoke was introduced into the air streams through the large window opening, and photographs of the resulting smoke traces were captured, as depicted in Figure 2.45.

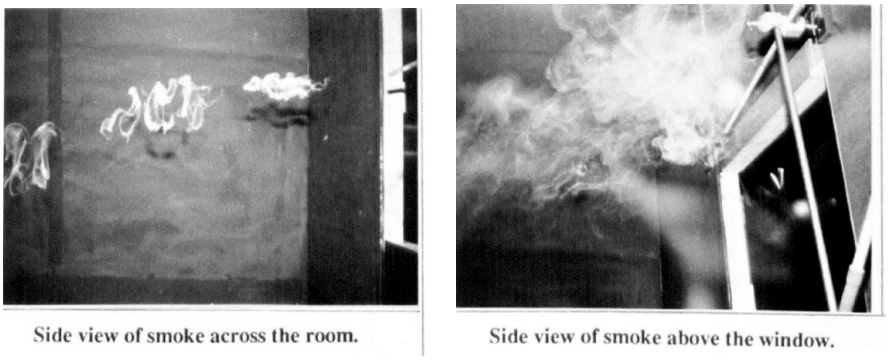


Figure 2.45: Air flow patterns in the room [51]

The smoke test revealed that air flows in streamlines from the window into the inlet of the chimney and then into the heated cavity without any reverse flow. Stagnant smoke traces below and above the window indicate that the airflow did not fill the entire room. This suggests that window placement should be carefully considered to ensure effective ventilation throughout the internal space.

An experimental study was conducted by [65] using the particle tracking method on a reduced-scale Perspex model of a wall solar chimney attached to a room (0.2 m x 0.1 m x 0.2 m). The model was submerged in a large glass tank filled with a saltwater solution.

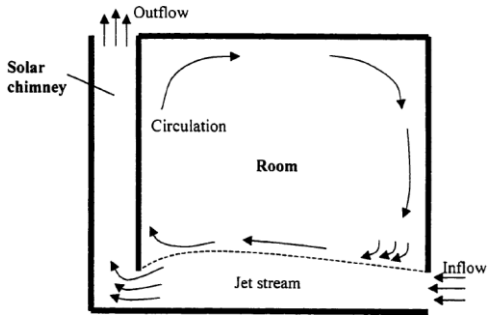


Figure 2.46: Schematic of the observed circulation within the room [65]

Figure 2.46 shows particle traces, indicating that the initial flow path from the room inlet to the chimney inlet is in a straight line. Some particles deviated near the chimney inlet, circulating within the room before rejoining the flow. The capacity of the chimney inlet to handle this added flow was insufficient, causing fluid to peel off and create room circulation. Higher fluid velocities intensified this effect, unlike Reference [51], which did not observe circulation in the room due to possible insufficient airflow velocities in their solar chimney experimental model.

In study [73], a full-scale model in Fire Dynamic Simulator (FDS) software was developed to simulate a wall solar chimney integrated with a room. The simulations were validated by using previous experimental data presented in [52]. The study found that room dimensions and window placement have minimal impact on air inlet flow, suggesting the entire room can be treated as a single control volume for analytical studies. However, enlarging the window opening initially leads to an exponential increase in airflow rate, but then the rate of increase slows down.

## 2.6 Combined Surface Radiation in Solar Chimney and Vertical Channel

Vertical channels play a vital role in a wide range of applications, including the cooling of electronic devices that produce heat, the optimization of solar panels to improve their efficiency, the operation of solar chimneys, and the construction of Trombe walls and

double-skin facades to enhance thermal comfort. Extensive research has been conducted on this topic since the pioneering work of [103], introducing the modified Rayleigh number for the study of natural convection in vertical channels, leading to numerous theoretical, numerical, and experimental studies. Although surface radiation plays a crucial role in altering the thermal and flow dynamics in vertical channels, there is a scarcity of experimental research on the combined effects of surface radiation and natural convection. In recent decades, numerous numerical studies have emerged, utilizing various radiation models for simulating conjugate heat transfer phenomena. Therefore, there is a pressing need for new experimental studies to enhance the accuracy of thermal and flow predictions in CFD simulations.

In addition to the geometric aspects of a solar chimney, a comprehensive understanding of the heat transfer mechanisms within a solar chimney is essential for optimizing its design and efficiently harnessing solar power. This entails taking into account all three heat transfer modes: conduction, convection, and radiation. However, many researchers have focused primarily on conduction and convection, neglecting the effects of radiation due to the complexity of modelling. This omission is often justified by assuming mirror-like walls in the chimney, as exemplified in references [55,56,90,101,104,105]. As a result, there is a scarcity of research studies addressing the impact of combined surface radiation, particularly on solar chimney applications, as evident in references [74,78,91,101,101,106–111]. Furthermore, it should be noted that the surface emissivity of many practical materials used in the construction of solar chimneys falls within the range of 0.7–0.9. Hence, radiative heat transfer cannot be considered negligible in solar chimney systems and must not be ignored when accurately predicting and improving the performance of solar chimneys. Some of the research findings related to solar chimneys are mentioned below.

A numerical study conducted by [106] investigated the conjugate heat transfer in solar chimney systems for residential heating and ventilation. They employed a finite difference-control volume numerical method to solve the conservation equations. The study considered Rayleigh numbers ranging from $5 \times 10^8$ to $10^{11}$ and chimney aspect ratios between 6 and 15. The study found that surface radiation impacted flow and temperature fields, enhancing the velocity gradient on the active wall. Moreover, higher Rayleigh numbers, surface emissivity, and chimney aspect ratios increased the volume flow rate, while greater wall thickness and chimney inlet size decreased it.

In their numerical simulations, [74] found that radiation significantly impacts heat transfer in solar chimneys. They assumed diffuse gray walls and observed that the mass flow rate inside the chimney increased with higher surface emissivity and input heat flux. When the walls had an emissivity of 0.9, the mass flow rate increased by up to 59%. Additionally, they noted the formation of a thermal boundary layer near the absorber wall and another one near the passive wall, which mitigated reverse flow and improved ventilation rates.

The study [54] reported an instance of the radiation effect on their indoor test rig. They found that the temperature of the unheated wall was slightly higher than the air in the channel, and an increase in air speed near the unheated wall suggested the development of thermal boundary layer due to radiation heat exchange from the heated wall. Their experiments showed that less than 10% of total heat transfer occurred through radiation.

Another observation of the radiation effect on the test rig was made by [61]. They reported that the air temperature distribution in the cavity gap of the chimney was highly non-uniform. It was highest near the heated wall. The temperature of the air decreased gradually as one moved away from the heated wall. It is worth mentioning that there was

a minor temperature rise in the vicinity of the movable glass plate, attributed to the radiation emitted by the heated wall.

Similar to the findings of studies on solar chimneys, studies on asymmetrically heated rectangular channels have also documented the heating of unheated walls due to radiation transfer. Here are some key findings from the literature.

Experiments were conducted by [110] to investigate heat transfer in an inclined channel with asymmetric heating using natural convection and radiation exchange. The study examined heat flux ranging from 50 to 400 W/m² with a channel composed of two 2.4 m long and 0.34 m wide plates separated by air cavity gaps ranging from 0.01 to 0.04 m. The experiments considered inclination angles between 18° and 30° and wall surface emissivity values between 0.29 and 0.95. Correlations were established to relate Nusselt numbers to the modified channel Rayleigh number, particularly for inclination angles of 18° and emissivity values of 0.95 in the range of $10 < Ra^* < 5.6\times104$. It was determined that increasing surface emissivity enhanced radiation exchange and reduced the temperature on the heated wall. With a surface emissivity of 0.95, roughly 45% of the heat flux was transferred to the unheated wall through radiation.

In a study by [78], both coupled and uncoupled numerical methods were used to investigate the impact of surface radiation on laminar airflow resulting from natural convection in vertically oriented, asymmetrically heated channels with adiabatic extensions at the inlet and outlet. Computations were validated using the experimental design and data presented in [112]. The coupled simulations ($\varepsilon \neq 0$) showed that even minimal surface radiation (0.1) can eliminate pocket-like recirculation near the outlet, lower temperatures on the heated wall, and raise temperatures on the opposite wall. However, flow reversal only occurred in the uncoupled solutions ($\varepsilon = 0$). The isothermal

and streamline patterns for different ε values (0, 0.1, and 1) and changes in the cavity gap demonstrated significant alterations in the flow morphology.

## 2.7 Adiabatic Extension Effect on Channel-Chimney System

Several new techniques have been proposed in the literature to enhance heat transfer in vertical heated channels. Among these techniques, the channel-chimney system stands out as a promising solution. This system consists of a heated vertical parallel plate (channel), followed by an unheated downstream region (chimney). Placing adiabatic extensions downstream of the channel increases flow rate via the chimney effect. This higher flow rate, in turn, boosts heat transfer efficiency and prevents reverse flow at the chimney outlet when the exit is unheated.

A numerical study [112] investigated the influence of adiabatic entry and exit sections on air flow and convection heat transfer in vertical parallel plate channels, considering uniform heat flux (UHF) and uniform wall temperature (UWT) boundary conditions. The study found that unheated entry or exit sections have a notable impact on heat transfer characteristics, especially in the case of UHF with an unheated exit at low Rayleigh numbers.

The study [113] analysed the impact of adiabatic extensions downstream of a vertically heated channel with symmetrical UHF in the range of 100–450 W/m$^2$. It determined optimal configurations based on wall temperature profiles, considering extension and expansion ratios (length of chimney/length of channel and cavity gap of chimney/cavity of channel). Both the channel and chimney were 475 mm wide, with the channel height at 100 mm and the chimney height ranging from 0 to 300 mm. The gap between the channel and chimney varied from 10 to 40 mm, and the chimney cavity gap ranged from

10 to 200 mm. This resulted in channel aspect ratios between 2.5 and 20 and expansion ratios from 1.0 to 8.0. The study concluded that adding an extension ratio of 3 and an expansion ratio of approximately 2.0 improved heat transfer rates and significantly reduced maximum wall temperatures.

## 2.8 Discussion of Literature Review

The solar chimney, a promising passive ventilation method, has garnered substantial research interest in recent years for its energy-saving potential. Hence, various geometric configurations [9,14,18,20,43,45,46,60,99] for single- and multi-story buildings and with newer designs of solar chimneys have also been proposed for enhancing the performance of solar chimney systems. However, there are research gaps based on this extensive literature review that need to be further investigated for optimizing the solar chimney design.

The impact of geometrical features has not been thoroughly understood thus far.

- Researchers have not reached a consensus on the optimal aspect ratio for wall chimneys in their studies. While some findings [51,92] suggest an optimum aspect ratio of 10:1 regardless of heat flux, others propose ratios such as 12:1 [65], 2:1 [100,114], and 5:2 [61]. Conversely, some studies failed to identify any optimum ratio at all [20,39,54–56]. Additionally, certain researchers [101] argue that the optimal aspect ratio is influenced by the Rayleigh number and the inlet aperture height of the chimney. A separate study [115] suggests a 14:1 height-to-gap ratio for optimizing ventilation and minimizing reverse flow in solar chimneys with moist air.

- Researchers disagree on the optimal air gap for wall chimney design, with conflicting findings in different studies. One study [51] identified 0.2 m as the optimal air gap for inducing the highest flow rate in solar chimneys. However, other studies [20,39,55] reported inconclusive results, with variations attributed to diverse geometric designs and climatic conditions. Additionally, researchers [51,60,92,100,114] found that beyond a certain cavity gap extension, mass flow diminishes due to the occurrence of reverse flow phenomena, leading to the downflow of cold air through the chimney outlet.
- An increase in the height of the wall chimney has been reported by [41,56,65] to drastically increase the ventilation rate of the performance, but some authors suggest it is the least important parameter after chimney air gap width, inclination angle, and width of the solar chimney [12,49]. These contradictory findings warrant further investigation.

Research is required to integrate the Analytical Plume Model into the Thermal Nodal Network computational method for the solar chimney. Additionally, more investigation is needed to empirically confirm the solar chimney model, which takes into account both room and window openings.

- The GEB modelling approach, based on the single-zone model by [9,70], has been utilized to study various solar chimney configurations in both steady-state and dynamic simulations [14,19,20,41,45–48]. However, for larger chimneys, the assumption of a uniform temperature distribution may not be valid, leading to potential inaccuracies due to reverse flows near chimney outlets. To address this, the modified analytical plume model by [66] should be integrated with the GEB modelling approach to assess its suitability in such scenarios.

- The authors in study [98] introduced a new empirical model to estimate the airflow in a solar chimney. This model considers the configuration of the attached room and the size of the window openings, relying on readily available input parameters. Consequently, the need for experimental validation of this research arises, along with the potential for improving this analytical modelling approach.

The performance of a solar chimney relies on two critical factors: the thermal boundary layer and the velocity boundary layer. However, there is a lack of comprehensive experimental understanding of the detailed flow morphology and air thermal field within the solar chimney.

- Thermal field data have been gathered from indoor and outdoor solar chimney test rigs [20,54,58,61,80,100] resembling rectangular channels with either vertical or horizontal inlet and outlet openings. Thin wire T-type or K-type thermocouples were positioned inside the chimney. The thermocouples were moved within the channel to capture sparse thermal field data of air across its height and the cavity air gap. Some researchers [55,56] have inserted thermocouples into radiation shields, specifically designed for minimal flow disturbance and a reduced impact of radiation heat transfer on thermal data collection. Researchers have also utilized non-disturbing methods such as optical techniques like Shadowgraph and Schlieren visualization (referenced as [60,62]) to quantitatively measure the thermal boundary layer near the chimney outlet. Additionally, due to experimental constraints in visualizing the entire 2D detailed thermal flow field without disturbing the flow, numerical studies (e.g., [22,74,75,78,93,94,97]) have been employed in the literature.

- In solar chimney research, the velocity profile is measured around 1 m above the chimney inlet using an anemometer. This height was chosen based on a numerical study by [114]. At this height, minimal disturbance is assumed from inlet and outlet reverse flow. Hence, in studies such as [54,61,100], velocity readings were taken approximately 1 m above the channel inlet, with samples collected regularly across the chimney air gap. In contrast, studies like [20,51,55,56,59] collected data samples at regular intervals only at the inlet of the channel. However, in solar chimneys attached to rooms, velocity readings were also taken at the room window in studies like [44,59]. Additionally, some studies, including [39,43], measured the air velocity at the chimney outlet.
- Researchers utilized Drager tubes, incense sticks, and fog generators for qualitative analysis of airflow patterns inside chimney channels, as referenced in [51,53,54,60–62,94]. However, to achieve a detailed 2D velocity flow field inside a solar chimney test rig without disrupting the flow, numerical studies were employed due to experimental constraints, as seen in [24,72,74,76,78,87,91,96].

No experimental study has measured the whole 2D instantaneous velocity field developed within a solar chimney heated asymmetrically with a uniform flux, either with or without an attached room model.

- Most of the indoor models of solar chimneys are developed as rectangular channels, either in an inclined or vertical configuration, heated symmetrically and asymmetrically under uniform heat flux [54–57,61,62,80,81,100,110], or at uniform wall temperature [103,116]. Some researchers have developed an indoor reduced-scale model of a vertical wall chimney with an attached room heated

asymmetrically at UHF [59,60,65] and some symmetrically and asymmetrically heated at UWT [51,53,117].

- Moreover, numerical analysis [75,76,96,97] of standalone and room-attached vertical wall solar chimney model shows the attached models exhibit lower velocity profiles inside the chimney and increased turbulent kinetic energy production at the inlet and outlet compared to standalone models. However, a comprehensive experimental study is lacking to improve the CFD modelling.

The influence of surface radiation on the intricate flow topology and the air temperature field in wall chimneys and rectangular channel configurations has not been experimentally investigated.

- References [54,61,81] discuss the impact of emissivity on thermal and momentum boundary layer evolution near an unheated wall in vertical channels under asymmetric heating. [118] compared the experimental results of a full-scale outdoor wall chimney prototype and found the DO radiation model to be superior in CFD simulation. While the majority of studies [74,76,91,96,106] focus exclusively on numerical analyses of wall chimney configurations to investigate air temperature and airflow topology, few experimental studies have been conducted on rectangular open-ended vertical and inclined channels [57,110,111] to study the effect of radiation on the wall thermal field and on the average air temperature rise inside the channel. However, due to experimental limitations, numerical studies [78,96,108] were employed to quantitatively visualize the effects of emissivity on the thermal and flow morphology of air.

Quantitative experimental investigation is needed to study the reverse flow phenomenon occurring at the outlet of L-shaped vertical channels, as well as the formation of flow

circulations and separation at the inlet. Additionally, understanding flow reattachment is crucial in this context.

- Some experimental investigations, such as those documented in references [51,54,60,94], identified a reverse flow phenomenon at the exit of a vertically oriented rectangular channel, considering various air cavity gaps and Rayleigh numbers. In contrast, studies like [20,65,119] failed to detect the presence of reverse flow at the chimney outlet. Conversely, a number of numerical analyses [74–76,96,101] anticipated the occurrence of reverse flow at the channel outlet. However, a numerical examination [78] focused on an asymmetrically heated channel with adiabatic extensions at the inlet and outlet indicated that setting ε to 0.1 for the unheated wall eliminated pocket-like recirculation near the outlet. Flow reversal occurred solely at the channel outlet when ε was set to 0 for the unheated wall.
- The intricate flow patterns occurring at the horizontally oriented inlet of the vertical channel and at the leading edge of the absorber wall have been extensively examined through numerical investigations by various studies [72,76,96,97,101]. However, there is not any quantitative experimental study to validate these numerical findings.

The effect of the attached room model and the positioning of the room window on the ventilation performance of a solar chimney is not experimentally well understood.

- In study [51], a full-scale experimental study on a wall chimney attached to a room, revealed a streamlined airflow from the window to the inlet of the chimney and then into the heated cavity without any reverse flow observed at the inlet of the chimney. In contrast, the authors in [65] conducted an experimental study on

a reduced-scale model of a wall solar chimney attached to a room, indicating a straight initial flow path from the room inlet to the chimney inlet. However, particle traces showed deviations near the chimney inlet, with some particles circulating within the room before rejoining the flow.

- In study [73], a numerical model of a wall chimney was developed to study the impact of window placement. Their findings indicate that room dimensions and window placement minimally affect air inlet flow. However, a comprehensive experimental study for validation is lacking based on the literature review.

The contradictory results discussed in this literature review suggest that there is still much to learn about the solar chimney as a passive ventilation method. This underscores the importance of further research to improve its effectiveness, which is the main motivation for this study.

## 2.9 Objective of the Present Study

The literature review indicates number of indoor experimental models of wall solar chimney attached to room, with various wall heating conditions. For instance, the study [51] employed a symmetric UWT heating method for chimney walls, while in study [65] used an adiabatic wall as the inlet of the chimney and a UHF opposite wall. Meanwhile, in study [60] utilized a strategy where a UHF wall formed the inlet of the chimney and an adiabatic opposite wall. This latter modelling approach has also been employed to construct indoor vertical channels mimicking different configurations of standalone solar chimneys [54–56,62,80,100].

- The first objective of this study is to fabricate a reduced-scale model of a wall solar chimney with an attached room, incorporating UHF conditions similar to

previous studies mentioned in the literature [54–56,60,62,80,100]. Unlike prior models using glazing for the unheated wall, this study opts for an opaque and well-insulated unheated wall to maintain adiabatic conditions and minimize conduction heat loss. Additionally, the test rig design will incorporate a novel feature, an adiabatic chimney top, to boost the stack height of the wall chimney. This addition aims to achieve adiabatic conditions at the trailing edge of the heated wall and simultaneously minimize radiation losses from the heated channel to the surrounding environment, as indicated in the cited references [63,64,120].

- The objective is to examine how placement of room air inlet affects the ventilation performance of a solar chimney. This will be achieved by observing airflow patterns from the room air inlet to the chimney inlet, analysing air temperature distribution within the room, and measuring parameters such as volumetric flow rate and the thermal field of the chimney walls.
- The study seeks to employ particle image velocimetry (PIV) to measure the entire 2D time-averaged velocity field within the central plane of an L-shaped vertical channel. Additionally, it will measure the temperature distribution on the chimney walls for heat transfer analysis in a quasi-steady state of experimental bench.
- The research will quantitatively study the time-averaged air flow field and flow structures developed in an L-shaped vertical channel. Additionally, it will examine how changing chimney wall surface emissivity affects flow morphology, wall thermal fields, and chimney performance.
- Finally, a 1-D GEB model will be developed for this novel experimental setup. The simulations of the model will be compared with the experimental results obtained from the setup.

## 2.10 References

[1] A. Garg, 5 Vernacular Architecture styles in India, RTF | Rethinking The Future (2020). https://www.re-thinkingthefuture.com/rtf-fresh-perspectives/a1242-5-vernacular-architecture-styles-in-india/ (accessed October 25, 2023).

[2] Traditional forms of rural habitat in Pakistan - UNESCO Digital Library, (n.d.). https://unesdoc.unesco.org/ark:/48223/pf0000043702 (accessed October 25, 2023).

[3] F. Sun, Chinese Climate and Vernacular Dwellings, Buildings 3 (2013) 143–172. https://doi.org/10.3390/buildings3010143.

[4] A.G. Kazemi, A.H. Shirvani, An Overview of Some Vernacular Techniques in Iranian Sustainable Architecture in Reference to Cisterns and Ice Houses, JSD 4 (2011) p264. https://doi.org/10.5539/jsd.v4n1p264.

[5] C. Ganem, A. Esteves, H. Roura, Traditional climate-adapted typologies as a base for a new contemporary architectural approach, (2006) 6–8.

[6] Net Zero by 2050 - A Roadmap for the Global Energy Sector, (n.d.).

[7] Comfort, climate analysis and building design guidelines, Energy and Buildings 18 (1992) 11–23. https://doi.org/10.1016/0378-7788(92)90047-K.

[8] F. Manzano-Agugliaro, F.G. Montoya, A. Sabio-Ortega, A. García-Cruz, Review of bioclimatic architecture strategies for achieving thermal comfort, Renewable and Sustainable Energy Reviews 49 (2015) 736–755. https://doi.org/10.1016/j.rser.2015.04.095.

[9] N.K. Bansal, R. Mathur, M.S. Bhandari, Solar chimney for enhanced stack ventilation, Building and Environment 28 (1993) 373–377. https://doi.org/10.1016/0360-1323(93)90042-2.

[10] K.H. Lee, R.K. Strand, Enhancement of natural ventilation in buildings using a thermal chimney, Energy and Buildings 41 (2009) 615–621. https://doi.org/10.1016/j.enbuild.2008.12.006.

[11] R. Khanal, C. Lei, Solar chimney—A passive strategy for natural ventilation, Energy and Buildings 43 (2011) 1811–1819. https://doi.org/10.1016/j.enbuild.2011.03.035.

[12] A.Y.K. Tan, N.H. Wong, Parameterization Studies of Solar Chimneys in the Tropics, Energies 6 (2013) 145–163. https://doi.org/10.3390/en6010145.

[13] X.Q. Zhai, Z.P. Song, R.Z. Wang, A review for the applications of solar chimneys in buildings, Renewable and Sustainable Energy Reviews 15 (2011) 3757–3767. https://doi.org/10.1016/j.rser.2011.07.013.

[14] W.F.M. Yusoff, E. Salleh, N.M. Adam, A.R. Sapian, M. Yusof Sulaiman, Enhancement of stack ventilation in hot and humid climate using a combination of roof solar collector and vertical stack, Building and Environment 45 (2010) 2296–2308. https://doi.org/10.1016/j.buildenv.2010.04.018.

[15] N.K. Bansal, J. Mathur, S. Mathur, M. Jain, Modeling of window-sized solar chimneys for ventilation, Building and Environment 40 (2005) 1302–1308. https://doi.org/10.1016/j.buildenv.2004.10.011.

[16] V. Siva Reddy, M. Premalatha, K.R. Ranjan, Experimental studies on solar chimney for enhanced ventilation, International Journal of Sustainable Energy 31 (2012) 35–42. https://doi.org/10.1080/1478646X.2010.534554.

[17] J. Arce, M.J. Jiménez, J.D. Guzmán, M.R. Heras, G. Alvarez, J. Xamán, Experimental study for natural ventilation on a solar chimney, Renewable Energy 34 (2009) 2928–2934. https://doi.org/10.1016/j.renene.2009.04.026.

[18] C. Afonso, A. Oliveira, Solar chimneys: simulation and experiment, (2000) 9.

[19] M.A. Hosien, S.M. Selim, Effects of the geometrical and operational parameters and alternative outer cover materials on the performance of solar chimney used for natural ventilation, Energy and Buildings 138 (2017) 355–367. https://doi.org/10.1016/j.enbuild.2016.12.041.

[20] K.S. Ong, C.C. Chow, Performance of a solar chimney, Solar Energy (2003) 17.

[21] S. M, Cooling of building integrated photovoltaics by ventilation air., (1999). https://www.aivc.org/resource/cooling-building-integrated-photovoltaics-ventilation-air (accessed October 5, 2023).

[22] S. Khaldi, A.N. Korti, S. Abboudi, Applying CFD for Studying the Dynamic and Thermal Behavior of Solar Chimney Drying System with Reversed Absorber, International Journal of Food Engineering 13 (2017). https://doi.org/10.1515/ijfe-2017-0081.

[23] T. Miyazaki, A. Akisawa, I. Nikai, The cooling performance of a building integrated evaporative cooling system driven by solar energy, Energy and Buildings 43 (2011) 2211–2218. https://doi.org/10.1016/j.enbuild.2011.05.004.

[24] M. Maerefat, A.P. Haghighi, Natural cooling of stand-alone houses using solar chimney and evaporative cooling cavity, Renewable Energy 35 (2010) 2040–2052. https://doi.org/10.1016/j.renene.2010.02.005.

[25] M. Rabani, Performance analysis of a passive cooling system equipped with a new designed solar chimney and a water spraying system in an underground channel, Sustainable Energy Technologies and Assessments 35 (2019) 204–219. https://doi.org/10.1016/j.seta.2019.07.005.

[26] M. Rabani, V. Kalantar, M. Rabani, Passive cooling performance of a test room equipped with normal and new designed Trombe walls: A numerical approach, Sustainable Energy Technologies and Assessments 33 (2019) 69–82. https://doi.org/10.1016/j.seta.2019.03.005.

[27] M. Rabani, V. Kalantar, A.A. Dehghan, A.K. Faghih, Empirical investigation of the cooling performance of a new designed Trombe wall in combination with solar chimney and water spraying system, Energy and Buildings 102 (2015) 45–57. https://doi.org/10.1016/j.enbuild.2015.05.010.

[28] N.K. Bansal, R. Mathur, M.S. Bhandari, A study of solar chimney assisted wind tower system for natural ventilation in buildings, Building and Environment 29 (1994) 495–500. https://doi.org/10.1016/0360-1323(94)90008-6.

[29] L. Moosavi, M. Zandi, M. Bidi, E. Behroozizade, I. Kazemi, New design for solar chimney with integrated windcatcher for space cooling and ventilation, Building and Environment 181 (2020) 106785. https://doi.org/10.1016/j.buildenv.2020.106785.

[30] N. Monghasemi, A. Vadiee, A review of solar chimney integrated systems for space heating and cooling application, Renewable and Sustainable Energy Reviews 81 (2018) 2714–2730. https://doi.org/10.1016/j.rser.2017.06.078.

[31] Z. Hu, W. He, J. Ji, S. Zhang, A review on the application of Trombe wall system in buildings, Renewable and Sustainable Energy Reviews 70 (2017) 976–987. https://doi.org/10.1016/j.rser.2016.12.003.

[32] T. Miyazaki, A. Akisawa, T. Kashiwagi, The effects of solar chimneys on thermal load mitigation of office buildings under the Japanese climate, Renewable Energy 31 (2006) 987–1010. https://doi.org/10.1016/j.renene.2005.05.003.

[33] A. Dimoudi, Solar Chimneys in Buildings—The State of the Art, Advances in Building Energy Research 3 (2009) 21–44. https://doi.org/10.3763/aber.2009.0302.

[34] L. Shi, G. Zhang, W. Yang, D. Huang, X. Cheng, S. Setunge, Determining the influencing factors on the performance of solar chimney in buildings, Renewable and Sustainable Energy Reviews 88 (2018) 223–238. https://doi.org/10.1016/j.rser.2018.02.033.

[35] M.M. AboulNaga, S.N. Abdrabboh, Improving night ventilation into low-rise buildings in hot-arid climates exploring a combined wall–roof solar chimney, Renewable Energy 19 (2000) 47–54. https://doi.org/10.1016/S0960-1481(99)00014-2.

[36] A. Lechowska, N. Szczepanik-Ścisło, J. Schnotale, M. Stelmach, T. Pyszczek, CFD modelling of transient thermal performance of solar chimney used for passive ventilation in a building, IOP Conf. Ser.: Mater. Sci. Eng. 415 (2018) 012049. https://doi.org/10.1088/1757-899X/415/1/012049.

[37] H.M. Maghrabie, M.A. Abdelkareem, K. Elsaid, E.T. Sayed, A. Radwan, H. Rezk, T. Wilberforce, A.G. Abo-Khalil, A.G. Olabi, A review of solar chimney for natural ventilation of residential and non-residential buildings, Sustainable Energy Technologies and Assessments 52 (2022) 102082. https://doi.org/10.1016/j.seta.2022.102082.

[38] D.J. Harris, N. Helwig, Solar chimney and building ventilation, Applied Energy 84 (2007) 135–146. https://doi.org/10.1016/j.apenergy.2006.07.001.

[39] J. Mathur, N.K. Bansal, S. Mathur, M. Jain, Anupma, Experimental investigations on solar chimney for room ventilation, Solar Energy 80 (2006) 927–935. https://doi.org/10.1016/j.solener.2005.08.008.

[40] M.M. Aboulnaga, A roof solar chimney assisted by cooling cavity for natural ventilation in buildings in hot arid climates: An energy conservation approach in Al-Ain city, Renewable Energy 14 (1998) 357–363. https://doi.org/10.1016/S0960-1481(98)00090-1.

[41] K.S. Ong, A mathematical model of a solar chimney, Renewable Energy (2003) 14.

[42] J. Hirunlabh, W. Kongduang, P. Namprakai, J. Khedari, Study of natural ventilation of houses by a metallic solar wall under tropical climate, Renewable Energy 18 (1999) 109–119. https://doi.org/10.1016/S0960-1481(98)00783-6.

[43] J. Khedari, C. Lertsatitthanakorn, N. Pratinthong, J. Hirunlabh, The Modified Trombe Wall: A simple ventilation means and an efficient insulating material, International Journal of Ambient Energy 19 (1998) 104–110. https://doi.org/10.1080/01430750.1998.9675299.

[44] J. Khedari, B. Boonsri, J. Hirunlabh, Ventilation impact of a solar chimney on indoor temperature fluctuation and air change in a school building, (2000) 5.

[45] P. Chantawong, J. Hirunlabh, B. Zeghmati, J. Khedari, S. Teekasap, M.M. Win, Investigation on thermal performance of glazed solar chimney walls, Solar Energy 80 (2006) 288–297. https://doi.org/10.1016/j.solener.2005.02.015.

[46] S. Punyasompun, J. Hirunlabh, J. Khedari, B. Zeghmati, Investigation on the application of solar chimney for multi-storey buildings, Renewable Energy 34 (2009) 2545–2561. https://doi.org/10.1016/j.renene.2009.03.032.

[47] H.H. Al-Kayiem, S. K.V., S.I.U.-H. Gilani, Mathematical analysis of the influence of the chimney height and collector area on the performance of a roof top solar chimney, Energy and Buildings 68 (2014) 305–311. https://doi.org/10.1016/j.enbuild.2013.09.021.

[48] J. Arce, J.P. Xamán, G. Álvarez, M.J. Jiménez, R. Enríquez, M.R. Heras, A Simulation of the Thermal Performance of a Small Solar Chimney Already Installed in a Building, Journal of Solar Energy Engineering 135 (2013) 011005. https://doi.org/10.1115/1.4007088.

[49] A. Abdeen, A.A. Serageldin, M.G.E. Ibrahim, A. El-Zafarany, S. Ookawara, R. Murata, Solar chimney optimization for enhancing thermal comfort in Egypt: An experimental and numerical study, Solar Energy 180 (2019) 524–536. https://doi.org/10.1016/j.solener.2019.01.063.

[50] W. Rattanongphisat, P. Imkong, S. Khunkong, An Experimental Investigation on the Square Steel Solar Chimney for Building Ventilation Application, Energy Procedia 138 (2017) 1165–1170. https://doi.org/10.1016/j.egypro.2017.10.226.

[51] A. Bouchair, Solar chimney for promoting cooling ventilation in southern Algeria, (n.d.).

[52] A. Bouchair, Solar induced ventilation in the Algerian and similar climates, phd, University of Leeds, 1989. https://etheses.whiterose.ac.uk/616/ (accessed October 11, 2023).

[53] W. Ding, Y. Hasemi, T. Yamada, Natural ventilation performance of a double-skin façade with a solar chimney, Energy and Buildings 37 (2005) 411–418. https://doi.org/10.1016/j.enbuild.2004.08.002.

[54] Z.D. Chen, P. Bandopadhayay, J. Halldorsson, C. Byrjalsen, P. Heiselberg, Y. Li, An experimental investigation of a solar chimney model with uniform wall heat flux, Building and Environment 38 (2003) 893–906. https://doi.org/10.1016/S0360-1323(03)00057-X.

[55] S.A.M. Burek, A. Habeb, Air flow and thermal efficiency characteristics in solar chimneys and Trombe Walls, Energy and Buildings 39 (2007) 128–135. https://doi.org/10.1016/j.enbuild.2006.04.015.

[56] D. Ryan, S.A.M. Burek, Experimental study of the influence of collector height on the steady state performance of a passive solar air heater, Solar Energy 84 (2010) 1676–1684. https://doi.org/10.1016/j.solener.2010.05.018.

[57] W. Puangsombut, J. Hirunlabh, J. Khedari, B. Zeghmati, M.M. Win, Enhancement of natural ventilation rate and attic heat gain reduction of roof solar collector using radiant barrier, Building and Environment 42 (2007) 2218–2226. https://doi.org/10.1016/j.buildenv.2005.09.028.

[58] A. Dimoudi, Investigation of the flow and heat transfer in a solar chimney, The University of Bath's Research Portal (n.d.). https://researchportal.bath.ac.uk/en/studentTheses/investigation-of-the-flow-and-heat-transfer-in-a-solar-chimney (accessed October 3, 2023).

[59] X. Cheng, L. Shi, P. Dai, G. Zhang, H. Yang, J. Li, Study on optimizing design of solar chimney for natural ventilation and smoke exhaustion, Energy and Buildings 170 (2018) 145–156. https://doi.org/10.1016/j.enbuild.2018.04.016.

[60] R. Khanal, C. Lei, An experimental investigation of an inclined passive wall solar chimney for natural ventilation, Solar Energy 107 (2014) 461–474. https://doi.org/10.1016/j.solener.2014.05.032.

[61] Y. Hou, H. Li, A. Li, Experimental and theoretical study of solar chimneys in buildings with uniform wall heat flux, Solar Energy 193 (2019) 244–252. https://doi.org/10.1016/j.solener.2019.09.061.

[62] J. Kong, C. Lei, J. Niu, Experimental and Numerical Investigations of Roof-top Solar Chimney for Building Ventilation, (n.d.).

[63] S.Q. Estibaliz, Experimental investigation of thermal and fluid dynamical behavior of flows in open-ended channels. Application to Building Integrated Photovoltaic (BiPV) Systems, (n.d.).

[64] O.A. Tkachenko, V. Timchenko, S. Giroux-Julien, C. Ménézo, G.H. Yeoh, J.A. Reizes, E. Sanvicente, M. Fossa, Numerical and experimental investigation of unsteady natural convection in a non-uniformly heated vertical open-ended channel, International Journal of Thermal Sciences 99 (2016) 9–25. https://doi.org/10.1016/j.ijthermalsci.2015.07.029.

[65] S. Spencer, An experimental investigation of a solar chimney natural ventilation system, masters, Concordia University, 2001. https://spectrum.library.concordia.ca/id/eprint/1378/ (accessed September 26, 2023).

[66] G. He, A general model for predicting the airflow rates of a vertically installed solar chimney with connecting ducts, Energy and Buildings 229 (2020) 110481. https://doi.org/10.1016/j.enbuild.2020.110481.

[67] M. Sandberg, B. Moshfegh, Ventilated-solar roof air flow and heat transfer investigation, Renewable Energy 15 (1998) 287–292. https://doi.org/10.1016/S0960-1481(98)00175-X.

[68] H.B. Awbi, Design considerations for naturally ventilated buildings, Renewable Energy 5 (1994) 1081–1090. https://doi.org/10.1016/0960-1481(94)90135-X.

[69] J. Martı´-Herrero, M.R. Heras-Celemin, Dynamic physical model for a solar chimney, Solar Energy 81 (2007) 614–622. https://doi.org/10.1016/j.solener.2006.09.003.

[70] K.T. Andersen, DESIGN OF NATURAL VENTILATION BY THERMAL BUOYANCY WITH TEMPERATURE STRATIFICATION, (n.d.) 8.

[71] E.P. Sakonidou, T.D. Karapantsios, A.I. Balouktsis, D. Chassapis, Modeling of the optimum tilt of a solar chimney for maximum air flow, Solar Energy 82 (2008) 80–94. https://doi.org/10.1016/j.solener.2007.03.001.

[72] R. Bassiouny, N.S.A. Koura, An analytical and numerical study of solar chimney use for room natural ventilation, Energy and Buildings 40 (2008) 865–873. https://doi.org/10.1016/j.enbuild.2007.06.005.

[73] L. Shi, G. Zhang, An empirical model to predict the performance of typical solar chimneys considering both room and cavity configurations, Building and Environment 103 (2016) 250–261. https://doi.org/10.1016/j.buildenv.2016.04.024.

[74] R. Khanal, C. Lei, Numerical investigation of the ventilation performance of a solar chimney, ANZIAM Journal 52 (2010) C899–C913. https://doi.org/10.21914/anziamj.v52i0.3947.

[75] R. Khanal, C. Lei, A numerical investigation of buoyancy induced turbulent air flow in an inclined passive wall solar chimney for natural ventilation, Energy and Buildings 93 (2015) 217–226. https://doi.org/10.1016/j.enbuild.2015.02.019.

[76] G. Gan, General expressions for the calculation of air flow and heat transfer rates in tall ventilation cavities, Building and Environment 46 (2011) 2069–2080. https://doi.org/10.1016/j.buildenv.2011.04.014.

[77] G. Gan, Impact of computational domain on the prediction of buoyancy-driven ventilation cooling, Building and Environment 45 (2010) 1173–1183. https://doi.org/10.1016/j.buildenv.2009.10.023.

[78] R. Li, M. Bousetta, E. Chénier, G. Lauriat, Effect of surface radiation on natural convective flows and onset of flow reversal in asymmetrically heated vertical channels, International Journal of Thermal Sciences 65 (2013) 9–27. https://doi.org/10.1016/j.ijthermalsci.2012.10.023.

[79] G. He, J. Zhang, S. Hong, A new analytical model for airflow in solar chimneys based on thermal boundary layers, Solar Energy 136 (2016) 614–621. https://doi.org/10.1016/j.solener.2016.07.041.

[80] A. La Pica, G. Rodonò, R. Volpes, An experimental investigation on natural convection of air in a vertical channel, International Journal of Heat and Mass Transfer 36 (1993) 611–616. https://doi.org/10.1016/0017-9310(93)80036-T.

[81] B. Moshfegh, M. Sandberg, Investigation of fluid flow and heat transfer in a vertical channel heated from one side by PV elements, part I - Numerical Study, Renewable Energy 8 (1996) 248–253. https://doi.org/10.1016/0960-1481(96)88856-2.

[82] B. Liu, X. Ma, X. Wang, C. Dang, Q. Wang, R. Bennacer, Experimental study of the chimney effect in a solar hybrid double wall, Solar Energy 115 (2015) 1–9. https://doi.org/10.1016/j.solener.2015.02.012.

[83] G. He, Q. Wu, Z. Li, W. Ge, D. Lv, L. Cong, Ventilation performance of solar chimney in a test house: Field measurement and validation of plume model, Building and Environment 193 (2021) 107648. https://doi.org/10.1016/j.buildenv.2021.107648.

[84] R. Vargas-López, J. Xamán, I. Hernández-Pérez, J. Arce, I. Zavala-Guillén, M.J. Jiménez, M.R. Heras, Mathematical models of solar chimneys with a phase change material for ventilation of buildings: A review using global energy balance, Energy 170 (2019) 683–708. https://doi.org/10.1016/j.energy.2018.12.148.

[85] C. Jiménez-Xamán, J. Xamán, N.O. Moraga, I. Hernández-Pérez, I. Zavala-Guillén, J. Arce, M.J. Jiménez, Solar chimneys with a phase change material for buildings: An overview using CFD and global energy balance, Energy and Buildings 186 (2019) 384–404. https://doi.org/10.1016/j.enbuild.2019.01.014.

[86] J. Mathur, S. Mathur, Anupma, Summer-performance of inclined roof solar chimney for natural ventilation, Energy and Buildings 38 (2006) 1156–1163. https://doi.org/10.1016/j.enbuild.2006.01.006.

[87] R. Bassiouny, N.S.A. Korah, Effect of solar chimney inclination angle on space flow pattern and ventilation rate, Energy and Buildings 41 (2009) 190–196. https://doi.org/10.1016/j.enbuild.2008.08.009.

[88] H. Wang, C. Lei, Theoretical modeling of combined solar chimney and water wall for buildings, Energy and Buildings 187 (2019) 186–200. https://doi.org/10.1016/j.enbuild.2019.01.025.

[89] P.V. Nielsen, Fifty years of CFD for room air distribution, Building and Environment 91 (2015) 78–90. https://doi.org/10.1016/j.buildenv.2015.02.035.

[90] G. Gan, A parametric study of Trombe walls for passive cooling of buildings, Energy and Buildings 27 (1998) 37–43. https://doi.org/10.1016/S0378-7788(97)00024-8.

[91] B. Moshfegh, M. Sandberg, Flow and heat transfer in the air gap behind photovoltaic panels, Renewable and Sustainable Energy Reviews 2 (1998) 287–301. https://doi.org/10.1016/S1364-0321(98)00005-7.

[92] W. Liping, L. Angui, A numerical Study of Trombe Wall for Enhancing Stack Ventilation in Buildings, (2006) 7.

[93] A.P. Haghighi, M. Maerefat, Solar ventilation and heating of buildings in sunny winter days using solar chimney, Sustainable Cities and Society 10 (2014) 72–79. https://doi.org/10.1016/j.scs.2013.05.003.

[94] R. Khanal, C. Lei, Flow reversal effects on buoyancy induced air flow in a solar chimney, Solar Energy 86 (2012) 2783–2794. https://doi.org/10.1016/j.solener.2012.06.015.

[95] J. Xamán, R. Vargas-López, M. Gijón-Rivera, I. Zavala-Guillén, M.J. Jiménez, J. Arce, Transient thermal analysis of a solar chimney for buildings with three different types of absorbing materials: Copper plate/PCM/concrete wall, Renewable Energy 136 (2019) 139–158. https://doi.org/10.1016/j.renene.2018.12.106.

[96] G. Gan, Prediction of heat transfer and air flow in solar heated ventilation cavities, Computational Fluid Dynamics: Theory, Analysis and Applications (2013) 137–178.

[97] T.N. Huynh, Y.Q. Nguyen, Numerical simulation of a solar chimney for natural ventilation of a building: Comparison of different computational domains, IOP Conf. Ser.: Mater. Sci. Eng. 1109 (2021) 012014. https://doi.org/10.1088/1757-899X/1109/1/012014.

[98] H. Zhang, Y. Tao, L. Shi, Solar Chimney Applications in Buildings, Encyclopedia 1 (2021) 409–422. https://doi.org/10.3390/encyclopedia1020034.

[99] J. Khedari, W. Mansirisub, S. Chaima, N. Pratinthong, J. Hirunlabh, Field measurements of performance of roof solar collector, Energy and Buildings 31 (2000) 171–178. https://doi.org/10.1016/S0378-7788(99)00003-1.

[100] H. Jing, Z. Chen, A. Li, Experimental study of the prediction of the ventilation flow rate through solar chimney with large gap-to-height ratios, Building and Environment 89 (2015) 150–159. https://doi.org/10.1016/j.buildenv.2015.02.018.

[101] B. Zamora, A.S. Kaiser, Optimum wall-to-wall spacing in solar chimney shaped channels in natural convection by numerical investigation, Applied Thermal Engineering 29 (2009) 762–769. https://doi.org/10.1016/j.applthermaleng.2008.04.010.

[102] A. Li, P. Jones, P. Zhao, L. Wang, Heat Transfer and Natural Ventilation Airflow Rates from Single-sided Heated Solar Chimney for Buildings, Journal of Asian Architecture and Building Engineering 3 (2004) 233–238. https://doi.org/10.3130/jaabe.3.233.

[103] W. Elenbaas, Heat dissipation of parallel plates by free convection, Physica 9 (1942) 1–28. https://doi.org/10.1016/S0031-8914(42)90053-3.

[104] B. Zamora, A.S. Kaiser, Numerical study on mixed buoyancy-wind driving induced flow in a solar chimney for building ventilation, Renewable Energy 35 (2010) 2080–2088. https://doi.org/10.1016/j.renene.2010.02.009.

[105] E. Bacharoudis, M.Gr. Vrachopoulos, M.K. Koukou, D. Margaris, A.E. Filios, S.A. Mavrommatis, Study of the natural convection phenomena inside a wall solar chimney with one wall adiabatic and one wall under a heat flux, Applied Thermal Engineering 27 (2007) 2266–2275. https://doi.org/10.1016/j.applthermaleng.2007.01.021.

[106] H.F. Nouanégué, E. Bilgen, Heat transfer by convection, conduction and radiation in solar chimney systems for ventilation of dwellings, International Journal of Heat and Fluid Flow 30 (2009) 150–157. https://doi.org/10.1016/j.ijheatfluidflow.2008.08.006.

[107] S. Tkachenko, V. Timchenko, G. Yeoh, J. Reizes, Effects of radiation on turbulent natural convection in channel flows, International Journal of Heat and Fluid Flow 77 (2019) 122–133. https://doi.org/10.1016/j.ijheatfluidflow.2019.03.009.

[108] S. Hussain, Numerical study of natural convection and radiation exchange in an asymmetrically heated inclined channel, 1 (2016) 11.

[109] Z. Nasri, Y. Derouich, A.H. Laatar, J. Balti, Effect of surface radiation on natural convection in an asymmetrically heated channel-chimney system, Heat and Mass Transfer 54 (2018) 1511–1529. https://doi.org/10.1007/s00231-017-2246-6.

[110] Q. Lin, S.J. Harrison, Experimental Study on Natural Convection in an Asymmetrically Heated Inclined Channel With Radiation Exchange, in: Heat Transfer: Volume 1, ASME, Las Vegas, Nevada, USA, 2003: pp. 41–45. https://doi.org/10.1115/HT2003-47202.

[111] X. Cheng, U. Müller, Turbulent natural convection coupled with thermal radiation in large vertical channels with asymmetric heating, International Journal of Heat and Mass Transfer 41 (1998) 1681–1692. https://doi.org/10.1016/S0017-9310(97)00303-7.

[112] K.-T. Lee, NATURAL CONVECTION IN VERTICAL PARALLEL PLATES WITH AN UNHEATED ENTRY OR UN HEATED EXIT, Numerical Heat Transfer, Part A: Applications 25 (1994) 477–493. https://doi.org/10.1080/10407789408955961.

[113] A. Auletta, O. Manca, B. Morrone, V. Naso, Heat transfer enhancement by the chimney effect in a vertical isoflux channel, International Journal of Heat and Mass Transfer 44 (2001) 4345–4357. https://doi.org/10.1016/S0017-9310(01)00064-3.

[114] W. Liping, L. Angui, A numerical study of vertical solar chimney for enhancing stack ventilation in buildings, in: 2004. https://www.semanticscholar.org/paper/A-numerical-study-of-vertical-solar-chimney-for-in-Liping-Angui/6b893c56f67c0ec342826d0e7ce324c4ab50a5bb (accessed November 9, 2023).

[115] S. Sudprasert, C. Chinsorranant, P. Rattanadecho, Numerical study of vertical solar chimneys with moist air in a hot and humid climate, International Journal of Heat

and Mass Transfer 102 (2016) 645–656. https://doi.org/10.1016/j.ijheatmasstransfer.2016.06.054.

[116] A. Bar-Cohen, W.M. Rohsenow, Thermally Optimum Spacing of Vertical, Natural Convection Cooled, Parallel Plates, Journal of Heat Transfer 106 (1984) 116–123. https://doi.org/10.1115/1.3246622.

[117] A. Auletta, O. Manca, M. Musto, S. Nardini, Thermal design of symmetrically and asymmetrically heated channel–chimney systems in natural convection, Applied Thermal Engineering 23 (2003) 605–621. https://doi.org/10.1016/S1359-4311(02)00241-7.

[118] P. Yuan, Z. Fang, W. Wang, Y. Chen, K. Li, Numerical Simulation Analysis and Full-Scale Experimental Validation of a Lower Wall-Mounted Solar Chimney with Different Radiation Models, Sustainability 15 (2023) 11974. https://doi.org/10.3390/su151511974.

[119] L.P. Chung, M.H. Ahmad, D.R. Ossen, M. Hamid, Effective Solar Chimney Cross Section Ventilation Performance in Malaysia Terraced House, Procedia - Social and Behavioral Sciences 179 (2015) 276–289. https://doi.org/10.1016/j.sbspro.2015.02.431.

[120] M. Fossa, C. Ménézo, E. Leonardi, Experimental natural convection on vertical surfaces for building integrated photovoltaic (BIPV) applications, Experimental Thermal and Fluid Science 32 (2008) 980–990. https://doi.org/10.1016/j.expthermflusci.2007.11.004.

# CHAPTER 3: APPARATUS DESIGN

## 3.1 Objective of The Experimental Set Up

The primary objective of fabricating this indoor experimental setup is to determine, through experimentation, the effects of low and high surface emissivity on natural convection and radiative heat transfer phenomena in the L-shaped vertical channel walls. The channel walls are designed to study of one-wall uniform heat flux (UHF) heating from the inlet forming wall of the chimney at a fixed aspect ratio. This heating approach has been employed as it best mimics the real-world heating conditions encountered by solar chimneys and L-shaped solar-ventilated building façades. Furthermore, to establish realistic boundary conditions, particularly emphasizing applications associated with double-skin façades for cooling and natural ventilation in residential spaces, the horizontally oriented inlet of the L-shaped vertical channel is attached to a scaled-down model of the room constructed from plexiglass. This adaptation transforms the design of the vertical L-shaped channel into an innovative indoor wall-mounted solar chimney experimental bench. Additionally, to ensure adiabatic conditions at the trailing edge of the heated walls, the vertical channel is extended with a non-heated section. Three evenly spaced rectangular slots are carved into the room wall opposite the chimney inlet to assess the impact of room air inlet on the performance of a wall-mounted solar chimney and the air ventilation of the attached room. Figure 3.1(a) shows the 3D schematic view of the experimental bench with the exact dimensions. Figure 3.1(b) shows the 2D schematic view of the L-shaped vertical channel with exact dimensions.

The thermal and kinematic data collected from the experimental setup include the air temperature at the inlet and outlet of the chimney, the 2D time-averaged velocity flow field inside the entire vertical channel along its centre plane, detailed wall surface

temperature distribution on the centre plane of the chimney walls, surface temperature measurements on the insulating layers of the chimney walls, air temperature distribution, and the collection of airflow patterns in the reduced scale model of the room.

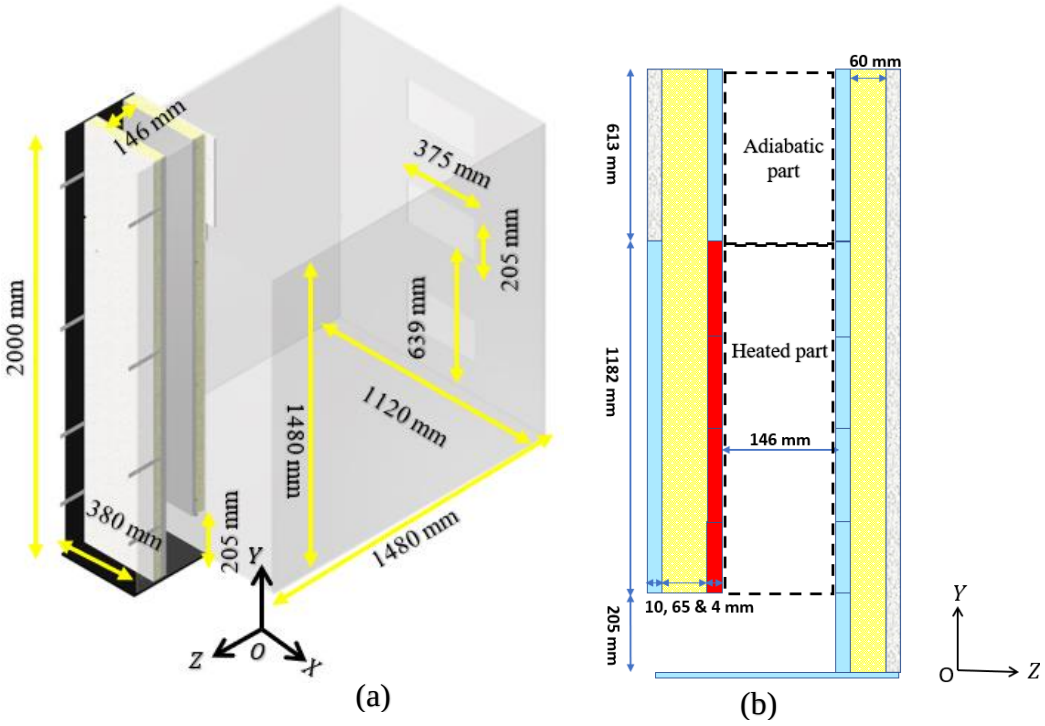


Figure 3.1: (a) 3D schematic view of indoor wall-mounted solar chimney (b) 2D view of the L-shaped vertical channel

Data obtained from the experiments, including average surface wall temperature and volume flow rate calculations, will be utilized to verify a 1D steady-state thermal network model developed in this doctoral thesis. Furthermore, detailed thermal field data from chimney walls and 2D time-averaged kinematical field data inside the chimney, along with airflow patterns and room air temperature distribution in a scaled-down model at the quasi-steady state of the experimental bench.

## 3.2 Configurations of the Studies

A number of tests will be conducted by varying the parameters as depicted in the schematics diagram of the test rig in Figure 3.2. (A) Room air inlet configurations were

tested, including: (1) top window (TW), (2) middle window (MW), (3) bottom window (BW), and (4) all window (AW) open configurations. (B) The bulk surface emissivity (ε) of both active and passive walls of the chimney at (1) LL = 0.08 and (2) HH = 0.96. (C) The electrical flux injected ($q''_{elec}$) from the heated part of the active wall of the chimney ranged from (1) 110 W/m$^2$ to (2) 235 W/m$^2$.

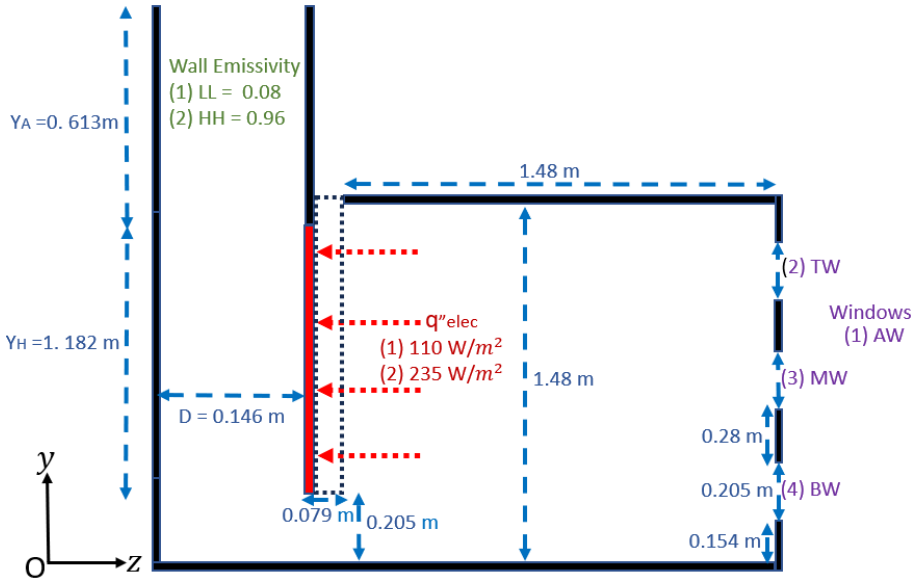


Figure 3.2: Schematic view of the tested configuration.

Electrical flux ($q''_{elec}$) is injected via an electric heater with a height of 1.182 m from the active wall of the chimney. The chimney has a fixed air cavity gap of 0.146 m between its active and passive walls, with insulated outer surfaces. It connects to a room measuring 1.48 m x 1.48 m x 1.12 m via the active wall. The room has three rectangular air inlet openings (0.205 m x 0.375 m) on the wall opposite the chimney inlet opening (0.205 m x 0.38 m). The horizontal inlet duct of the chimney, connecting to the room, is 0.079 m long. The spanwise width of the chimney along the X-axis is 0.38 m. Additionally, an adiabatic chimney top (0.613 m) is included to provide adiabatic boundary conditions at the trailing edge of the heater and to increase the overall stack height of the vertical wall chimney design.

For all the experiments, the aspect ratio of chimney ($Y_H/D$) is kept at 8, and the extension ratio of the adiabatic chimney top ($Y_A/Y_H$) is maintained at 0.52. To evaluate the effect of changing the surface emissivity of the active and passive walls from 0.08 to 0.96 on the performance of the L-shaped vertical channel, electrical fluxes of 110 W/m² and 235 W/m² were applied from the inlet-forming wall of the chimney. The room air inlet (TW) was kept open, while all other air inlets on the room wall were closed.

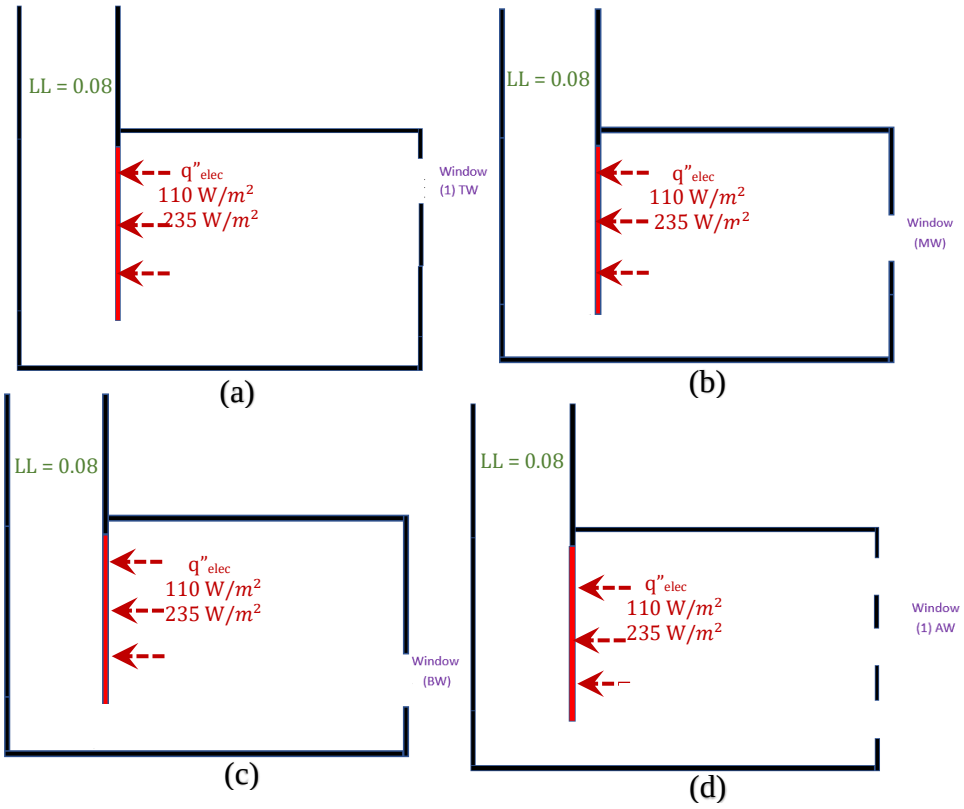


Figure 3.3: Schematic view of room air inlet tested configurations: (a) Top window (TW) open (b) middle window (MW) open (c) bottom window (BW) open (d) and all window (AW) open.

To study the effect of position of room air inlet on the performance of a wall-mounted solar chimney and room air ventilation, as shown in Figure 3.3, tests were conducted for four room air inlet configurations (TW, MW, BW, and AW) once the test rig reached a quasi-steady state. Each configuration was tested under 110 W/m$^2$ and 235 W/m² ohmic heat fluxes, with chimney wall surface emissivity at $\varepsilon = 0.08$.

## 3.3 Experimental Model Design

A comprehensive 3D model of the experimental bench was developed using Autodesk Inventor Pro 2021®, as depicted in Figure 3.4. This 3D model was crucial for obtaining precise information on the list of materials, mechanical components, and manufacturing methods necessary to develop the reduced-scale model of the wall-mounted solar chimney in accordance with the project requirements without causing excessive delays or changes to the plan during the fabrication stage.

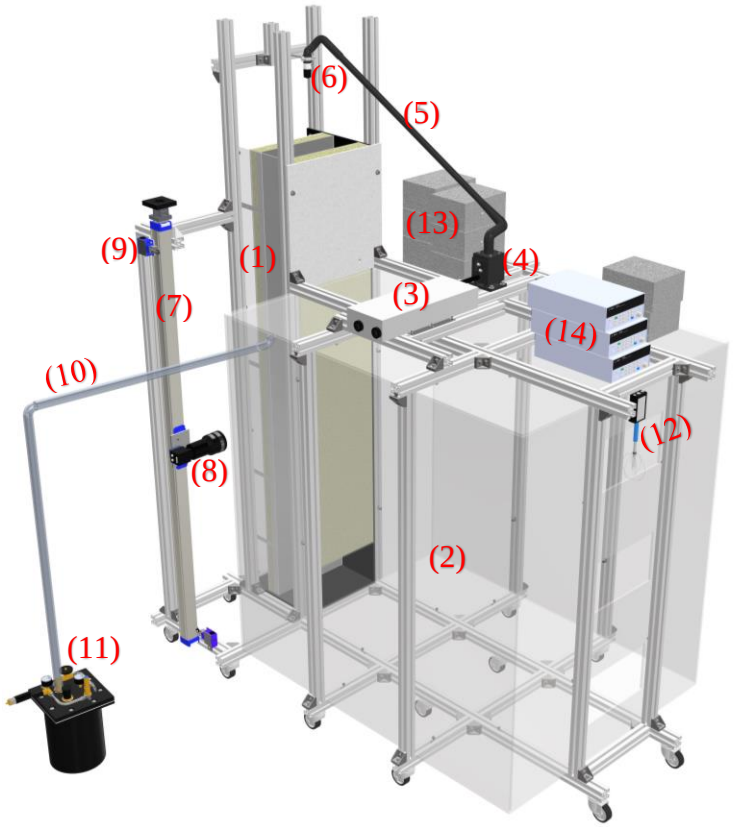


(1) Chimney (2) Room (3) Laser head unit (4) Base unit (5) Light guide arm (6) Laser optics (7) Linear motion unit (8) Camera with lens (9) Limiting switches (10) Reinforced PVC hose (11) Seeder (12) Anemometer (13) Compensation boxes (14) Data acquisition units

Figure 3.4: 3D model of the experimental bench with all Instruments mounted

The 3D model accurately depicts the sizes and placements of auxiliary fasteners and rollers necessary for assembling, securing, and supporting the chimney and room. It also illustrates the design strategies implemented for changing the air cavity gap of the

chimney, the passage for thermocouple wires and electric heater cables out of the channel, and details regarding the construction of aluminium frames with different combinations of fasteners to secure heaters tightly within the chimney walls. The 3D model not only provides accurate dimensions and positions of aluminium frames and auxiliary fasteners needed to mount the Dantec Dynamics PIV system and the customized Thomson linear motion traverse system onto the experimental bench but also ensures precise installation and integration, facilitating the desired PIV experimentation on the test rig. It is designed not only to rigidly support the equipment in place but also to provide flexibility of movement during the calibration process of the PIV experiment.

### 3.3.1 Fabrication of Chimney

Figure 3.5(a) illustrates the all the components required for fabrication of the indoor model of solar chimney. The chimney consists of 10 mm thick plexiglass plates constituting the bottom, front, and rear walls of the chimney, 65 mm thick glass wool insulation sheets with a 10 mm thick piece of gypsum board at the right sidewall of the chimney, and 55 mm thick glass wool insulation sheets with a 10 mm thick gypsum board cover over the left sidewall of the chimney. The left and right sidewalls of the chimney consist of 4 mm thick glass heaters and glasses plates covered with 0.5 mm thick layer aluminium scotch tape. Finally, Figure 3.5(a) depicts special aluminium frames used to secure the heaters and glass plates together. These frames are fabricated from unequal aluminium angle profiles with cross-sectional dimensions of 30 mm x 3 mm x 1.6 mm.

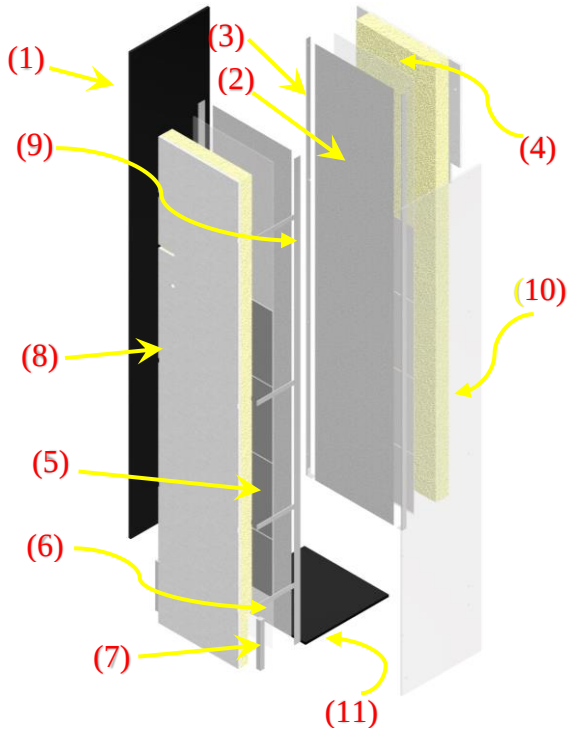


(1) Rear wall (2) Aluminum scotch layer (3) Frame for right sidewall (4) Glass plates (5) Heaters (6) Glass plate for left sidewall (7) Aluminium profiles For left sidewall (8) Glass wool sheet & gypsum board (9) Frame for left sidewall (10) Front wall (11) Bottom plate

(a)

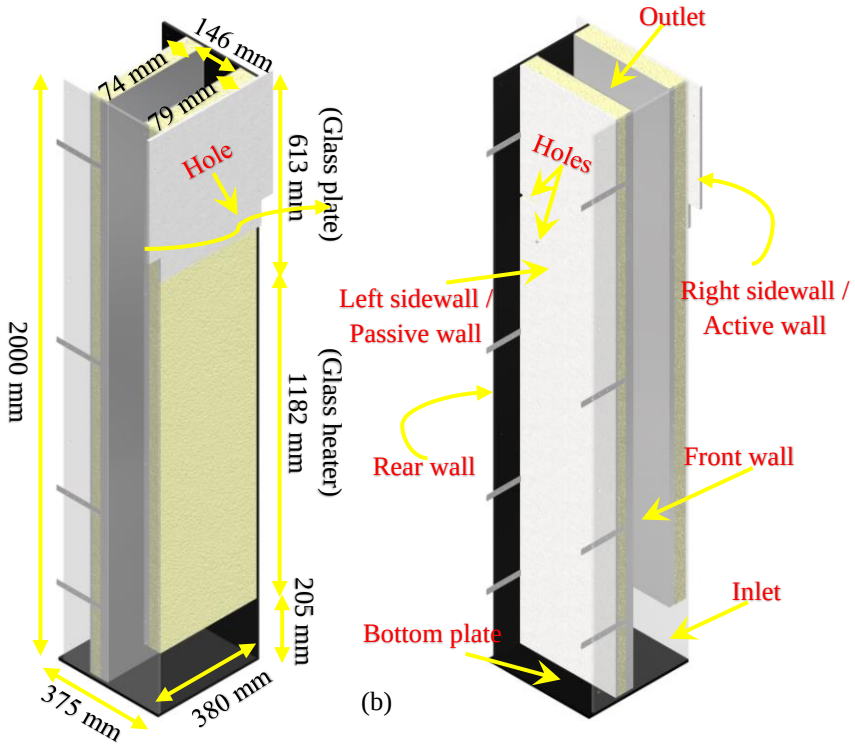


(b)

Figure 3.5: Solar chimney Fabrication: (a) View of components of chimney (b) Dimensions and parts of chimney.

As can be seen in Figure 3.5(a), Special frames were fabricated for the construction of the left and right sidewalls of the chimney using aluminium unequal angle profiles. These frames were designed to hold the heaters and glass plates in their designated locations on the respective walls of the chimney. The aluminium frame designed for the right sidewall of the chimney has been installed securely at a height of 205 mm from the bottom plate and positioned 69 mm from the left corner of both the rear and front walls to accommodate the installation of a glass wool insulation sheet. This placement allows for the design of a horizontal air inlet. The frame was securely fastened using screws along the chimney walls, and the heater and glass plate were then firmly attached within the frame. Finally, a glass wool insulation sheet was positioned behind the frame to complete the construction of the active chimney wall. The left sidewall frame was fabricated to facilitate easy chimney access for painting, air cavity gap adjustment, and cleaning of olive oil residue from the front wall for PIV tests. Hence, a dedicated aluminium frame was fabricated from non-uniform angle profiles, with four aluminium handles welded evenly spaced on each of the two sides of the frame. The frame was positioned within the chimney at a distance of 0.146 m from the right sidewall. The glass plates and heater were securely fixed within the frame. Additionally, two small-sized aluminium profiles were glued behind the glass plate at the bottom of the frame to enhance its overall stability while supporting the load of the heater and glass plates. Finally, a glass wool insulation sheet with an attached gypsum board was placed behind the frame to complete the formation of the passive wall of the chimney. Finally, to minimize background noise within the PIV data, the rear wall and bottom plate of the chimney were painted black, while the front wall was kept transparent for PIV measurements of the channel.

To pass the thermocouple wires from the left sidewall of the chimney, as can be observed in Figure 3.5(b), it was necessary to drill a hole of 15 mm diameter in the left corner of

the gypsum board, located 1.54 m away from the bottom plate. Additionally, a second hole of 8 mm was drilled in the left sidewall wall of the chimney, approximately 1.418 m from the bottom plate, to allow for the passage of electric cables soldered to the heating elements of the glass heater. The heater and the glass surfaces were both wrapped with 0.5 mm thick aluminium scotch tape to create a low-emissive surface on the left sidewall of the chimney. Similarly, to ensure that all the necessary thermocouple wires were crossed through the right sidewall of the chimney, a hole was created in the left corner of the gypsum board, located 1.55 m from the bottom plate. Additionally, a separate hole was drilled from the left corner of the rear wall in contact with the with the right sidewall at 1.42 m above the bottom plate to accommodate the passage of electric cables soldered to the heating elements of the glass heater. The heater and the glass plate surfaces were both wrapped with 0.5 mm thick aluminium scotch tape on the right sidewall of the chimney.

### 3.3.2 Fabrication of Reduced-scale Room Model

Contrary to from prior studies [1–4], which utilized vertical channels for analysing the performance of building integrated photovoltaic (BIPV) ventilated façades. In this research work, a L-shaped vertical channel, akin to a wall-mounted solar chimney, was constructed with a reduced-scale model of a room, simulating double-skin building façade attached to living space. Hence, a reduced-scale model of the room was constructed from six 10 mm thick plexiglass plates and were attached to the right sidewall of the solar chimney. Figure 3.6 illustrates all the internal dimensions and important features of the room. To study the effect of room air inlet position on the ventilation performance of the chimney, three room air inlet openings are made on the room wall opposite the chimney

inlet. During the experiments, only the necessary windows were left open, while the others were covered with transparent Scotch tape.

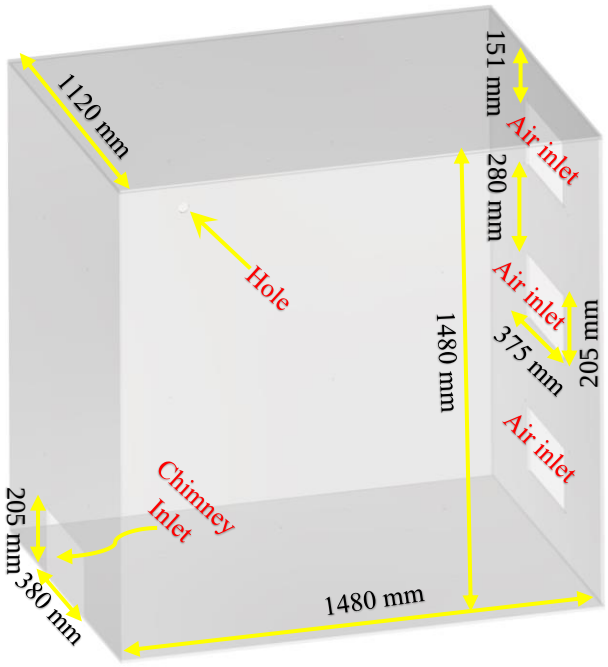


Figure 3.6: 3D Scale model of the attached room of solar chimney

To facilitate the injection of seeding particles into the chimney via the room during PIV tests, a 34 mm diameter hole was drilled in the front wall of the room, matching the diameter of the reinforced PVC tube connected to the particle generator. Additionally, two 6 mm diameter holes were drilled in the back face of the room wall to accommodate the cables of the thermocouples mounted inside the room.

### 3.3.3 Aluminium Framing for Experimental Bench

To facilitate the assembly of the chimney and room as a single unit, an aluminium frame was constructed, as depicted in Figure 3.7(a). This involved cutting T-slot aluminium bars to the required lengths and securing them together with angle brackets. To ensure both manoeuvrability and adequate support for the experimental bench, ten swivel castors were attached along the base of the aluminium frame to distribute the load evenly. The built

structure perfectly aligned the outlet of the room with the inlet of the chimney and provided an airtight air passage from the air inlet of the room to the outlet of the chimney.

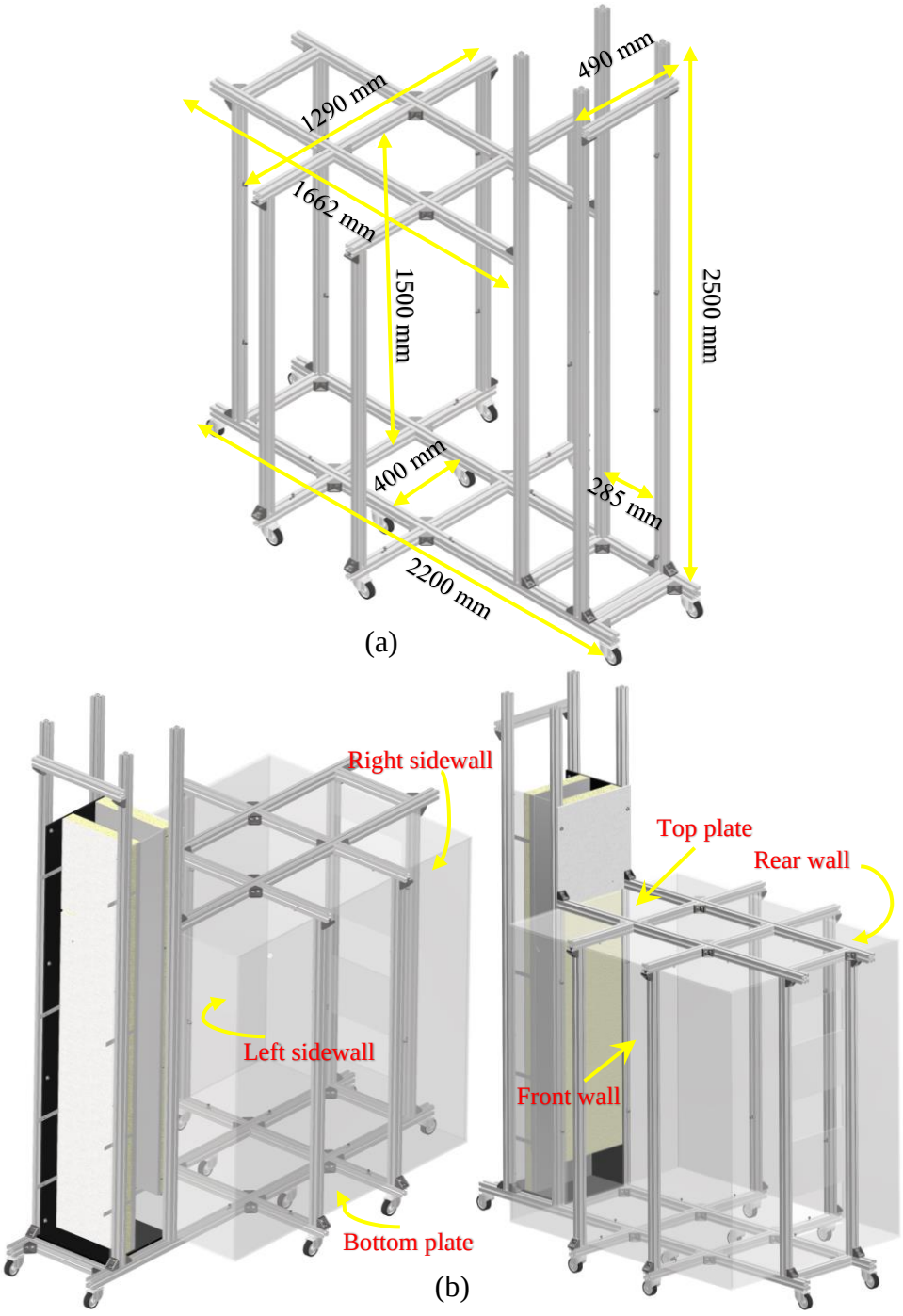


Figure 3.7: Mounting of Experimental bench on T-slot Extrusion Aluminium frame: (a) Aluminium frame design (b) Chimney and room inside the frame.

As depicted in Figure 3.7(b), to construct the chimney within the frame, the process began by positioning the bottom plate in its designated spot. Following this, the front and rear Plexiglass walls were placed atop the bottom plate. Subsequently, four 8 mm diameter holes were drilled into both the front and rear walls of the chimney to fasten them with sets of sliding blocks, washers, and screws to the aluminium framing. To attach the right sidewall of the chimney to the aluminium framing, a customized L-section aluminium frame designed for fabrication of the right sidewall of the chimney was fastened using ten 2 mm diameter holes drilled into the frame and in both the front and rear walls. T-bolt screws and nuts were used to secure the frame tightly. Once the heater and glass plates were placed into the frame, glass wool insulation was inserted from behind the wall. To maintain good contact with the insulation, a piece of gypsum board was fastened by drilling two 8 mm diameter holes in the gypsum board and using sliding blocks, washers, and screw assemblies to fasten it with profiles. After the left sidewall of the chimney was fabricated, it was slid onto the bottom plate using handles and positioned correctly in the chimney. To prevent air leakage and securely hold the left sidewall in place, a piece of horizontally oriented aluminium profile was also fastened with angle brackets at the top of T-slot bar on left sidewall of the chimney. In order to construct the room shown in Figure 3.7(b) inside the frame of the experimental bench, eight 6 mm holes were drilled into the plexiglass plates forming the floor and ceiling. Additionally, four 6 mm holes were drilled into each of the remaining plexiglass plates, forming the walls. All the plates making up the room were then firmly attached using sliding blocks, washers, and screws to the aluminium frame. To ensure airtightness, lastly, transparent Scotch tape was used to seal all the edges of the room.

### 3.3.4 Aluminium Framework for PIV Equipment

The aluminium framework was created to house the laser sheet unit, PIV camera, and traverse system on the experimental bench for analysing the natural convection air flow field at the central plane of the entire chimney using 2D PIV technique.

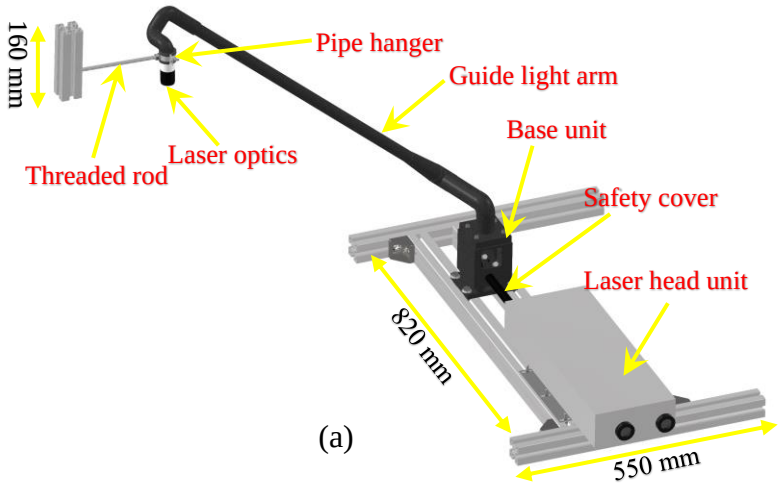


(a)

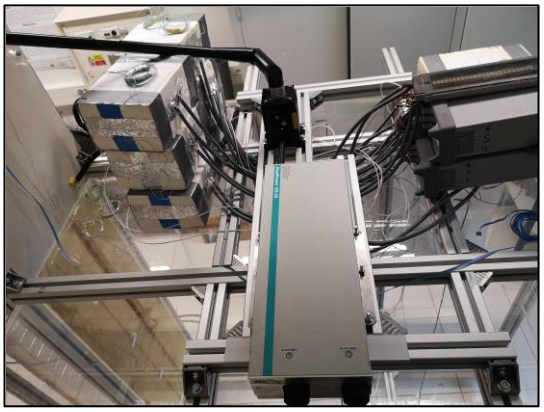

(b)

Figure 3.8: Aluminium framing for laser sheet system: (a) Scale model of laser sheet system (b) View of Laser sheet system installed on the ceiling of the room.

As shown in Figure 3.8(a) and (b), the installation process for the laser sheet system on the experimental bench involved several steps. Initially, five aluminium profile bars were cut to the required length and then securely fastened together using angle brackets to create a rigid frame. This frame served as the base on which the Dantec Dynamics laser head unit, safety cover, and base unit were mounted. The frame itself was then affixed to the aluminium frame on the roof of the attached room of the solar chimney. The base unit

was linked to the light guiding arm and light sheet optics. To support the weight of the light guiding arm and suspend the light sheet optics at the top of the chimney, a split-ring pipe hanger was used. One end of a threaded rod was attached to the split-ring pipe hanger. Additionally, a piece of T-slot profile was cut and drilled, then fastened with an angle bracket on the top of the left sidewall of the chimney, midway across its width. The other end of the threaded rod was inserted into the hole of the T-slot profile. Once the light sheet optics were positioned at the centroidal axis of the chimney, the threaded rod was tightened using nuts and washers, securing it to the T-slot profile. This design of the aluminium frame for the laser sheet system allows for easy manoeuvring and adjustment of the light sheet optics during the calibration of PIV experiments.

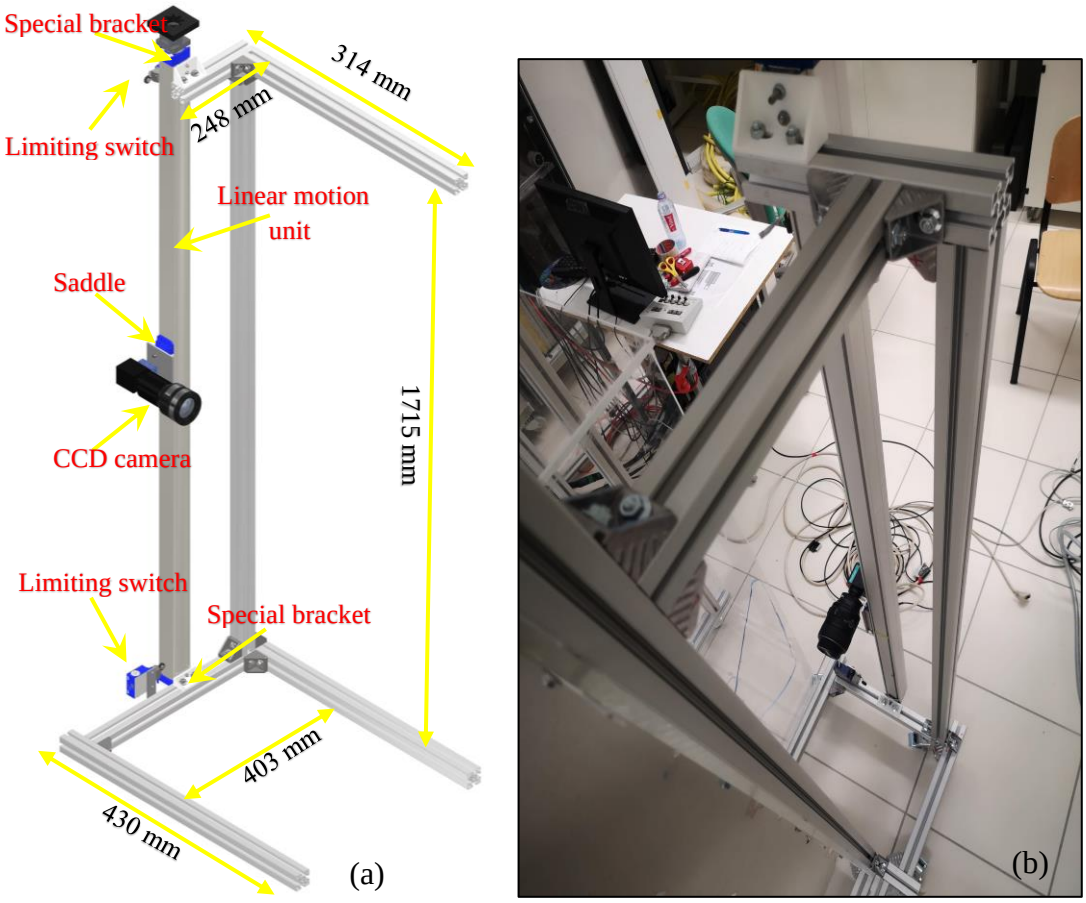


Figure 3.9: Aluminium framing for PIV camera & traverse system: (a) Scale model of traverse system (b) View of traverse system installed on the front wall of the chimney.

Figure 3.9(a) and (b) depict the fabrication of aluminium frame used to vertically support the Thomson linear motion traverse system, CCD camera, and limiting switches in front of the transparent plexiglass wall of the chimney. The frame was assembled by cutting T-slot bars to the required lengths and connecting them with angle brackets. It was then attached to the aluminium frame of the front wall of the chimney. The aluminium frame design for the laser sheet system facilitates smooth movement of the linear motion unit during the calibration process of PIV experiments. This ensures that the CCD camera remains at the midpoint of the cavity gap, maintaining a focal length distance of about 535 mm from the mid-width of the chimney. Specially designed brackets, produced using a 3D printer available at LOCIE, were used to attach the linear motion unit to the aluminium frame. Roller arm limiting switches were installed at both the top and bottom ends of the saddle to automatically control the camera movement on the linear motion unit. To evenly support the load of the traversing system and aluminium frame, three swivel castors were attached along the base of the frame.

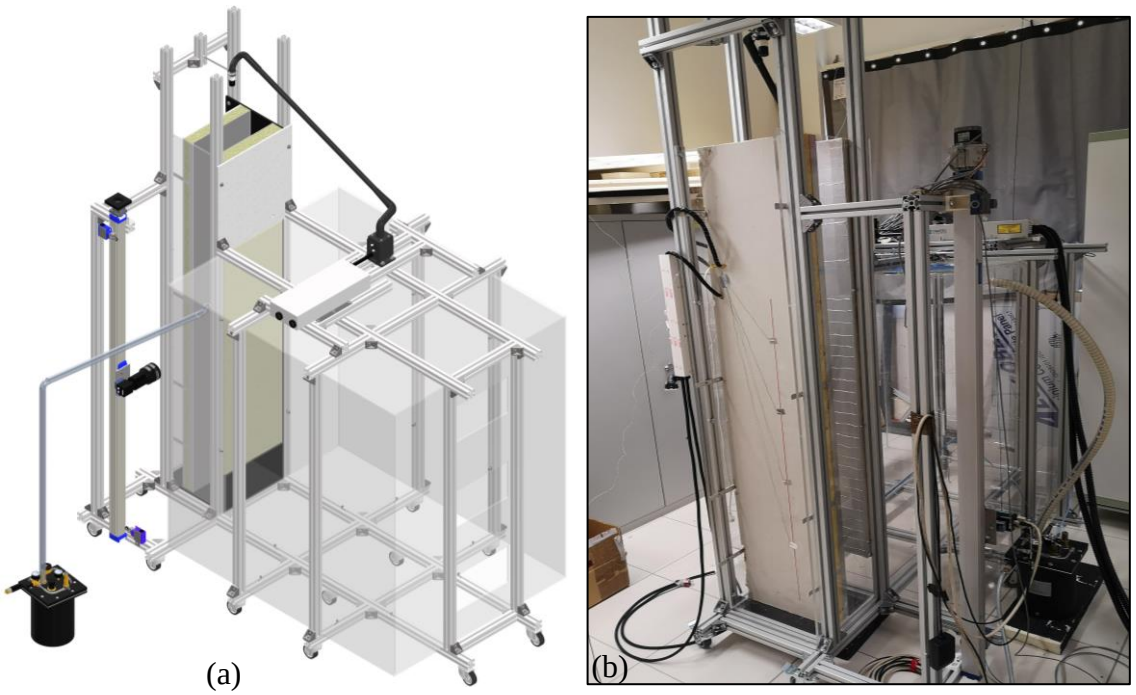


Figure 3.10: PIV system installed on the experimental bench: (a) Scale model of traverse system (b) View of experimental apparatus equipped with PIV apparatus.

Figures 3.10(a) and (b) depict both the 3D scale model and the actual experimental setup equipped with all PIV equipment. To facilitate the seeding of air inside the chimney for PIV experiments, a reinforced polyvinyl chloride (PVC) hose was inserted from the outlet of the particle generator into the room by drilling a hole in the front wall.

## 3.4 Instrumentation of Experimental Bench

In this study, considerable attention has been placed on selecting the appropriate tools and procedures for examining the thermal fields on the walls of the chimney and the 2D kinematic flow field throughout the entire chimney. When it comes to measuring temperature, K-type thermocouples have been employed. These sensors are widely recognized in the field for their reliability and accuracy in capturing temperature data. By utilizing these sensors, precise measurements of the thermal conditions during the experiments were obtained. In addition to temperature measurements, 2D velocity flow fields were studied within the entire flow domain of the chimney. To accomplish this, the particle image velocimetry (PIV) technique was employed, which utilizes particles in a fluid or gas medium to track their movement and deduce velocity information.

## 3.5 Temperature Measurement Technique

To gauge the temperature of both surfaces and air within the experimental bench test setup, K-type thermocouples were chosen for their cost-effectiveness, durability, rapid response time, broad temperature range spanning from 0 to 1000 °C, and sensitivity of around 41 μV /°C [5]. Consequently, a K-type Class 1 PFA thermocouple cable reel with a diameter of 0.2 mm was purchased, and 126 thermocouple beads were manufactured, as can be seen in Figure 3.11(a) to (c), by welding positive chromel wire with negative alumel wire using a hot spot welder. A continuity test was conducted using a Fluke 117

digital multimeter to ensure the functionality of the manufactured thermocouples. Each thermocouple was then labelled with specific names using a labelling machine and affixed to the cable for easy identification.

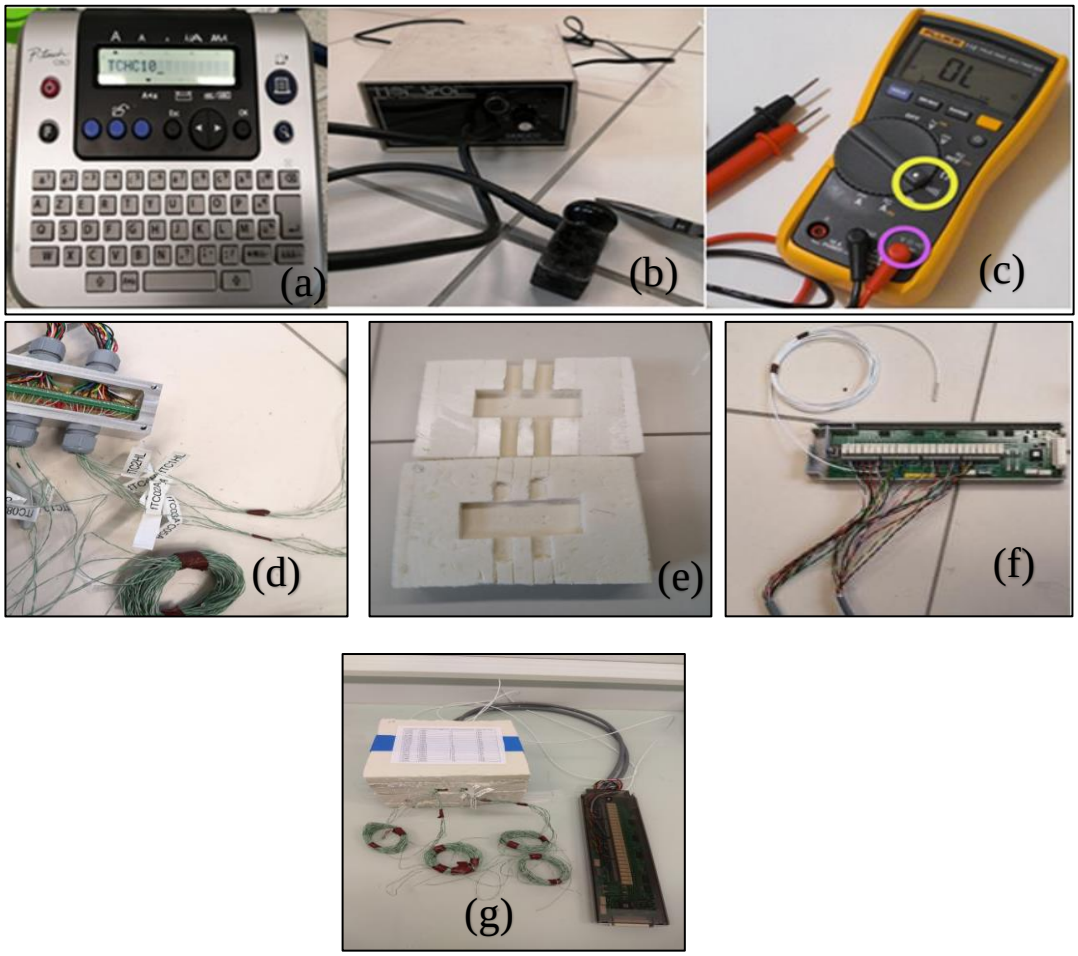


Figure 3.11: Temperature measurement with K-type thermocouples: (a) Labelling machine (b) Hot spot welder (c) Fluke 117 digital Multimeter (d) Isothermal block (e) Insulation box (f) 34901A multiplexer module (g) Thermocouples ready for the calibration process

To accurately measure the temperature at the hot junction, it was essential to reference both thermocouple leads and copper leads at the cold/reference junction. This prevents the development of thermal electromotive force (emf) at the data logger terminal, which could compromise temperature measurement accuracy. Figure 3.11(d)-(g) illustrates the utilization of the cold/reference junction compensation technique to ensure precise

temperature measurement at the thermocouple bead. To create the reference junction/compensation box for thermocouples, 18 pairs of thermocouple wires were connected to a printed circuit board (PCB) strip grid using electrical wire connectors. Twisted-pair copper cable wires were linked to each pair of thermocouple wires at the PCB, and then both cable wires and wire connectors were soldered together. To prevent electrical contact between the isothermal block and PCB, a mica sheet strip was placed inside the cavity of the isothermal block to hinder electrical conduction. For uniformly maintaining the temperature of the isothermal box from changes in ambient temperature, the isothermal box was covered inside the insulation box. To measure the reference temperature of the isothermal box, a PT100 resistance temperature detector (RTD) was placed inside a dedicated hole of the isothermal box along with electrolube heat transfer compound paste. Finally, the twisted copper cable and PT100 sensor wires were securely attached to the designated terminals on the detachable 34901A data logger module. Seven sets of compensation boxes and 34901A data logger modules were connected to collect thermal data from all the thermocouples mounted on the experimental bench.

To calibrate thermocouples, the hot bath technique was employed using the Thermo Scientific HAAKE A25 heating and cooling system, depicted in Figure 3.12. Eighteen thermocouples, accompanied by protective PT100 sensors, were placed inside a perforated copper cylinder and submerged in the bath tank of the HAAKE A25 filled with a mixture of ethylene glycol and distilled water. A polystyrene sheet was utilized to cover the top of the tank to minimize heat loss. The data logger module of the calibrated thermocouples was subsequently connected to the data acquisition unit, which in turn was connected to the laptop via USB cables. Once the temperature reading on the display screen of the HAAKE system reached the set temperature value, a 30-minute waiting period was observed to stabilize the temperature before recording the data for 3 minutes.

The calibration of thermocouples was conducted in the range of 15 to 80°C with intervals of 5°C. The LabVIEW program saved the recorded data in CSV file format. These files were then imported into the LabVIEW program, facilitating the calculation of polynomial coefficients for each thermocouple.

Figure 3.12: Hot bath technique for thermocouple calibration

All calibrated thermocouples underwent a verification test by immersing them again in the bath tank of the HAAKE system, and their accuracy was assessed at temperatures of 18, 47, and 72 °C. Once the temperature reached a steady state, the temperature data from the sensors was recorded for 3 minutes. The average temperature values for each thermocouple were then compared with the average temperature of the PT100 sensor. The accuracy of the calibration process was determined by subtracting the calculated average temperature of the thermocouples from the average temperature of the PT100 sensor. The accuracy of the calibrated thermocouples was measured to be approximately ± 0.1°C relative to the PT100.

### 3.5.1 Thermocouples Mounted in Chimney

Calibrated thermocouples were installed on the walls of the chimney to assess wall temperature evolution and calculate conductive losses from the walls of the chimney. Temperature measurements at the chimney walls were used to determine the local convection heat coefficient indirectly through the local energy balance at the air/chimney

wall interface. To ensure proper wall contact, the thermocouples were wrapped with 0.5-mm-thick aluminium foil against the wall surface. For measuring the air temperature at the inlet and outlet of the chimney, thermocouples with hot junctions were suspended in the air at the desired locations of the solar chimney. In Figure 3.13, schematics illustrate the placement of sensors on both the active and passive walls of the chimney, each labelled with a distinct identification name. To prevent potential flow disruption during PIV experiments along the centre plane of the chimney, thermocouples were positioned 50 mm to the left and right of the vertical symmetry line of the wall. 39 thermocouples were attached to the passive wall of the chimney, whereas the active wall had 38 thermocouples installed.

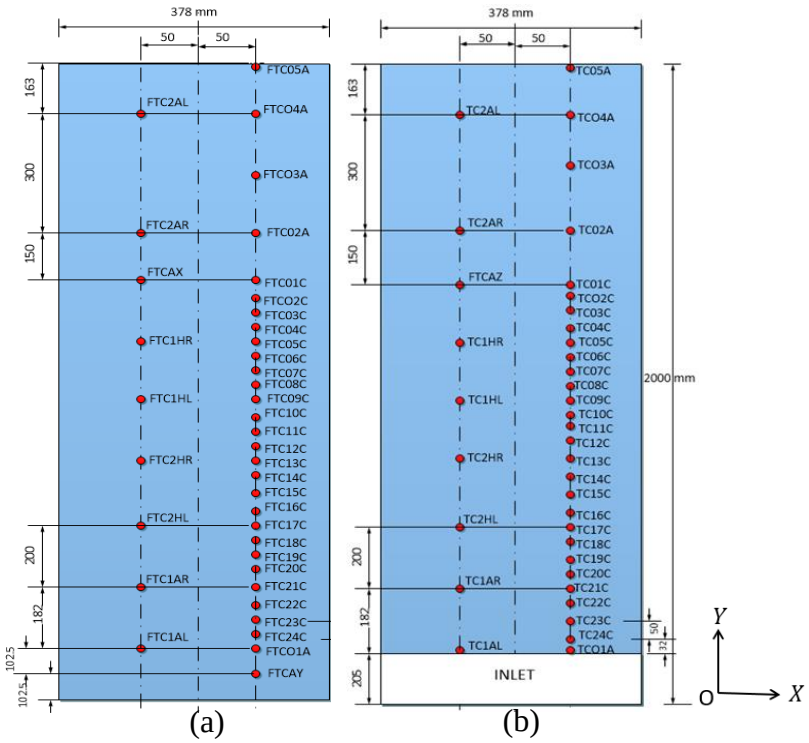


Figure 3.13: Thermocouples position layout on the wall of chimney: (a) Passive wall of the chimney (b) Active wall of the chimney

To install the thermocouples on the active and passive walls of the chimney according to the schematic diagrams in Figure 3.13, three small strips of aluminium tape were used to attach the thermocouple beads at specific locations (refer to Figure 3.14). These strips not

only secured the thermocouple beads in place but also straightened the wires on the heater and the glass plates of the chimney walls. Finally, aluminium tape was carefully wrapped around the heaters and glass plates to apply a low emissivity coating to the chimney walls.

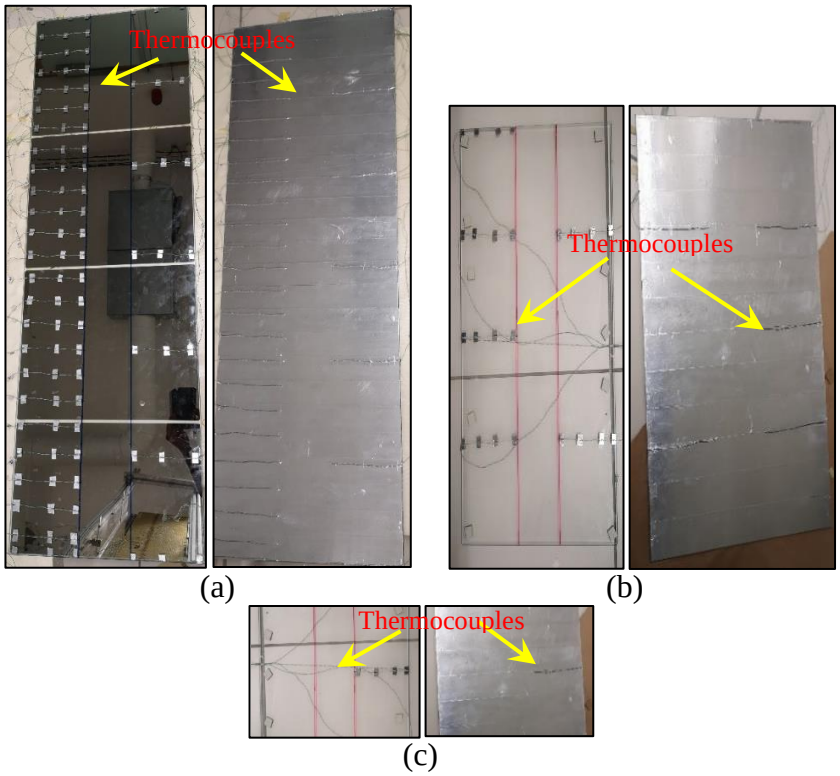


Figure 3.14: Thermocouples wrapped on the walls of the chimney: (a) Thermocouples wrapped on the heaters of active and passive walls (b) Thermocouples wrapped on glass plates of active and passive walls (c) Thermocouples wrapped on glass plates located at the bottom of the passive wall.

The schematic in Figure 3.15 illustrates the positioning of 16 thermocouples for measuring input heat flux and heat flux losses from the chimney walls. These thermocouples were placed behind the heaters on both the active and passive walls of the chimney. They were also placed behind glass wool insulation on the active wall and behind the surface of gypsum board on the passive wall. Furthermore, three thermocouples were positioned at the inlet and outlet of the chimney to record the average air temperature entering and leaving the chimney.

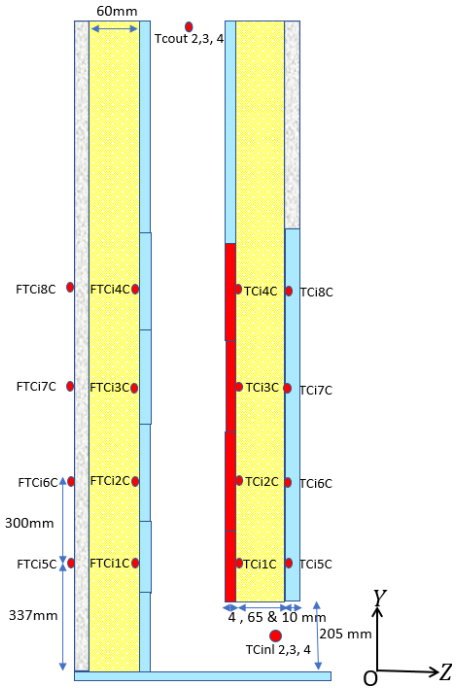


Figure 3.15: layout of thermocouples on the back side heaters, insulation cover of walls and inlet & outlet of the chimney.

Thermocouples were mounted on the backside of heaters for both active and passive chimney walls (refer to Figure 3.16). The process involved encasing the thermocouples within mica sheets for electrical insulation. Then, the thermocouples were affixed to the heater surfaces using aluminium. Additionally, thermocouples were also placed behind the glass wool insulation and gypsum board at designated locations using the same aluminium scotch. Lastly, to install the thermocouples at the inlet and outlet of the chimney at specified positions, the cables were initially suspended to the desired lengths and then secured to the nearby walls using clear Scotch tape.

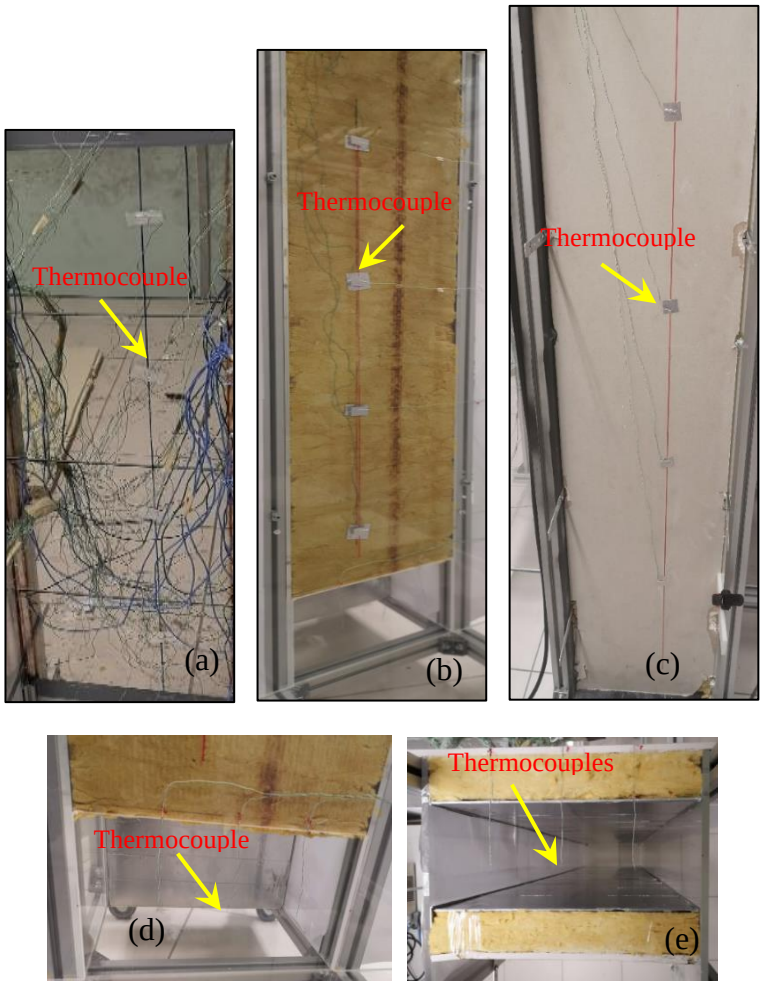


Figure 3.16: Thermocouples mounted behind the heaters, insulation cover and inlet & outlet of the chimney: (a) Thermocouples and heater cables on the backside of heaters on active and passive walls (b) Thermocouples on glass wool insulation cover on the active (c) Thermocouples on gypsum board cover on the passive wall (d) Thermocouples at the inlet of chimney (e) Thermocouples at the outlet of the chimney

### 3.5.2 Thermocouples Mounted in Room

To assess how the placement of room air inlet impacts ventilation performance wall-mounted solar chimney, the airflow and temperature distribution within the room were analysed. Thermocouples were strategically positioned from the window to the chimney inlet to gather thermal data for this purpose. The illustration in Figure 3.17 displays the names and positions of all 19 sensors within the room. 16 sensors were placed throughout the room and were affixed to the room wall adjacent to the active chimney wall to gauge heat transfer loss. Finally, three thermocouples were placed at equal intervals along one

of the rectangular room air inlet openings during experiments to gauge the temperature of the incoming air.

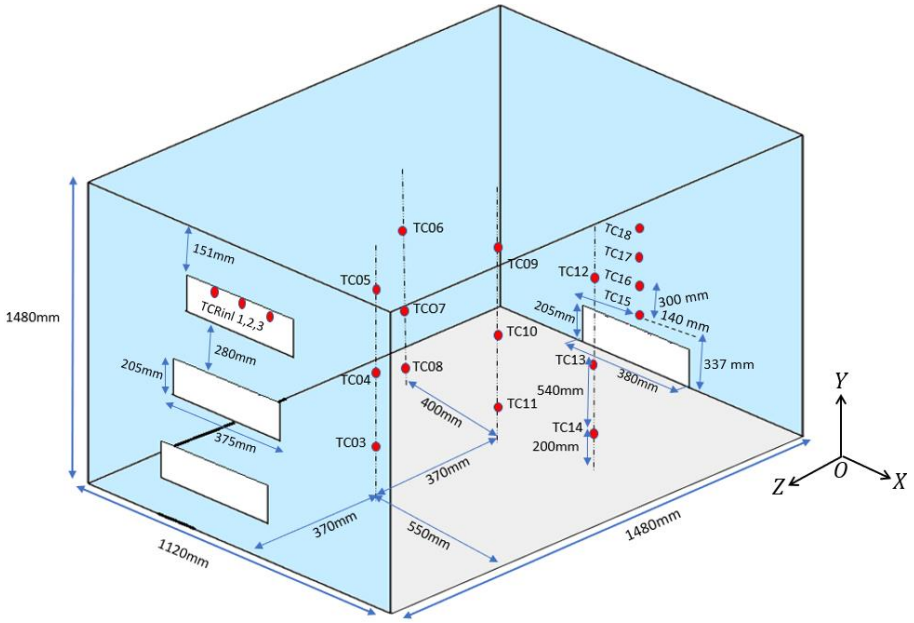


Figure 3.17: Layout of thermocouples inside the room & at the inlet opening of the chimney.

The thermocouples shown in Figure 3.18 were installed on four 3.5mm diameter cables, which were cut and attached from the floor to the ceiling of the room using scotch tape. The thermocouples were then fixed onto these cables in their designated positions using transparent tape. Additionally, thermocouples were affixed to the surface of the room walls near the chimney using aluminium tape. Finally, to secure the thermocouples at the room air inlet opening, their cables were suspended to the desired lengths before being taped to the adjacent walls with transparent Scotch tape.

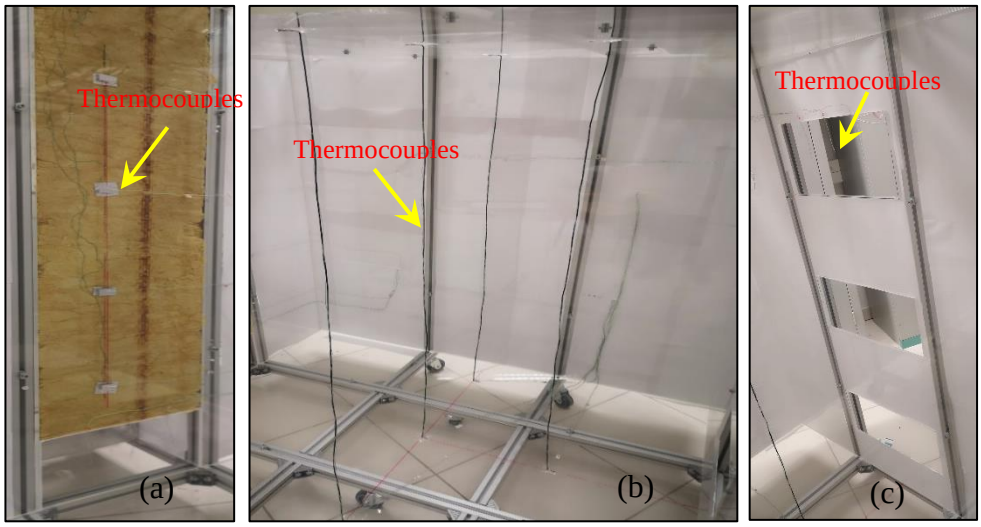


Figure 3.18: Thermocouples mounted on the wall, inside the room and at the inlet of the room: (a) thermocouples mounted on the wall of the room, (b) thermocouples attached on the cables inside the room, (c) Thermocouples suspended at the inlet of the room.

### 3.5.3 Thermocouples Mounted in The Laboratory Room

To understand how external environmental changes affect the internal conditions of the laboratory and to measure the temperature stratification outside the chimney, which is crucial for natural convection airflow and flow structures within the chimney as identified in previous studies [1–4,6], temperature variations were recorded in the laboratory room with and without a heating source. Three thermocouples were placed at different heights near the chimney, as depicted in Figure 3.19. Similarly, three thermocouples were positioned near the window-facing room wall, and one was placed midway between the chimney and the attached room of the test bench. All sensors were located in the mid-plane of the solar chimney test rig.

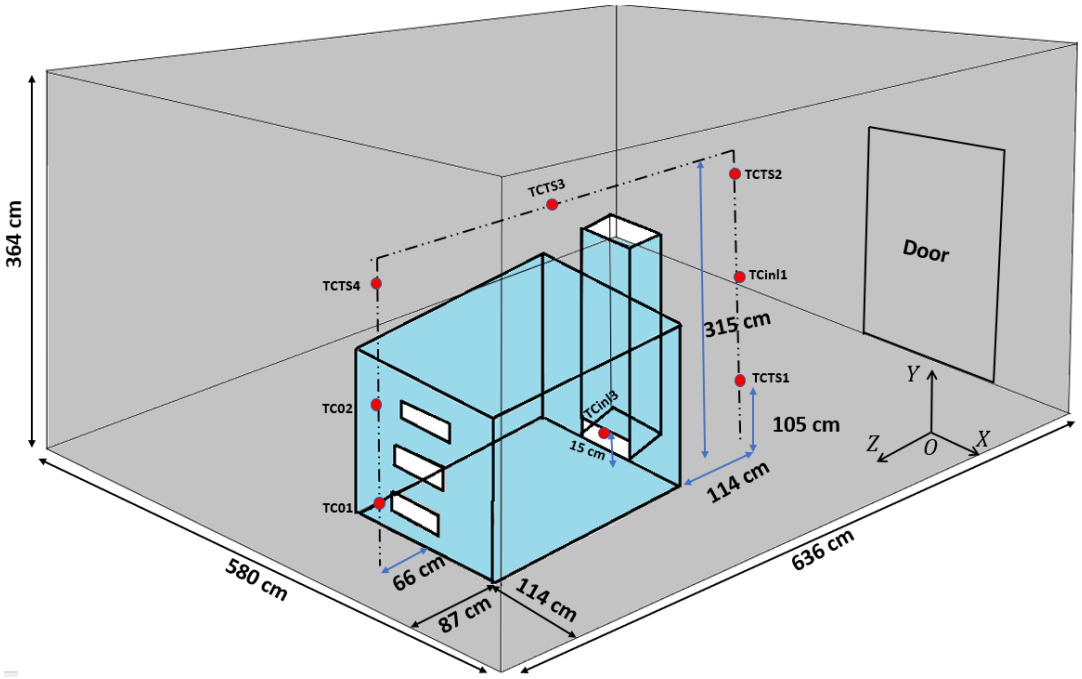


Figure 3.19: Layout of thermocouples in the laboratory room next to the experimental bench

The methods for installing the thermocouples in the laboratory are illustrated in Figure 3.20. First, three 3.5mm diameter cables were chosen and cut to the required length. These cables were secured to the upper ends of the curtain rod pipe and ventilation duct pipe in the laboratory. Their lower ends were then taped to the floor. The upper ends of the two vertical wires were horizontally tied together with an extra electric cable. Lastly, each thermocouple was meticulously affixed to the wires in its designated position using transparent scotch tape.

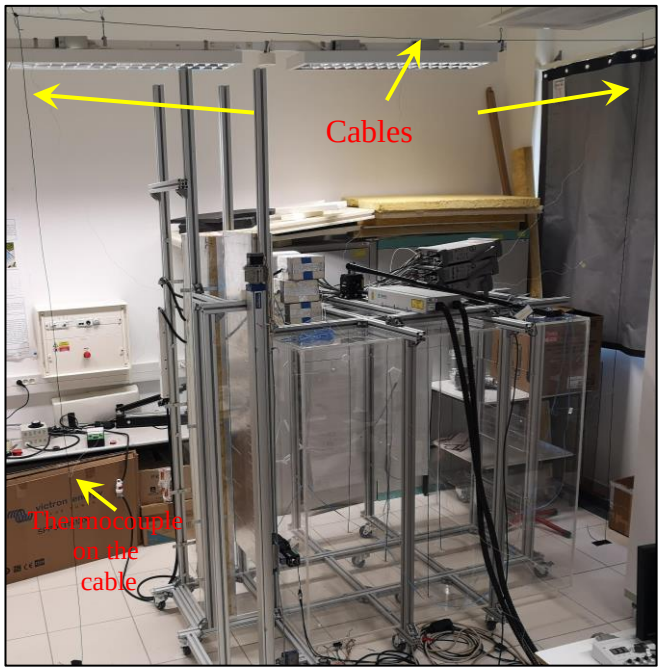


Figure 3.20: Thermocouples mounted in the laboratory room

## 3.6 Fluid Flow Velocity Measurements Technique

This experimental study primarily aims to investigate the behaviour of 2D time-averaged flow field and flow structures within the whole solar chimney under different uniform heat flux (UHF) boundary conditions. It also aims to analyse how the positioning of room air inlet and change in the wall surface emissivity affect the flow patterns within an L-shaped vertical channel. To achieve this, the experimental setup incorporates Particle Image Velocimetry (PIV) for its high spatial resolution.

PIV is a non-intrusive optical technique that provides instantaneous velocity vector maps of fluid flow without the need for physical probes. Intrusive approaches like Pitot-static tubes and hotwire anemometers, which could have potentially disturbed the flow field in the chimney, were ruled out for this experimental investigation in Favor of the non-intrusive PIV technique. In contrast to point-wise non-intrusive measurement techniques like Laser Doppler Anemometry (LDA), PIV is a whole-field global-wise technique that captures instantaneous velocity fields with high spatial resolution have been adopted

[7,8]. This enables the examination of spatial details in both large and small-scale structures, even in unsteady flow fields [8,9]. Unlike the LDA, the data acquisition rate in PIV is fixed and determined by the technical limitations of the devices employed. Consequently, the temporal resolution of PIV is generally much lower compared to LDA measurements. The attainable double frame rate typically ranges from 4 to 20 Hz, which may not be adequate for accurately capturing unsteady flow dynamics over time. However, the ability to detect the smallest possible length scale primarily depends on the spatial resolution of the camera capturing the images. These special and temporal limitations pose challenges in defining and taking measurements in the boundary sub-layer due to its low definition in the near-wall regions. Due to the complex nature of the flow in this sub-layer region, accurately measuring and visualising the flow properties becomes challenging. The flow near the wall can exhibit rapid changes and fluctuations, making it difficult to precisely define its boundaries and capture its detailed features. Factors such as the small scales of motion and the presence of turbulence contribute to the low definition in this region.

### 3.6.1 Operational Principal of PIV

The fundamental concept of PIV (refer to Figure 3.21) involves using a laser light sheet to illuminate the flow area, containing small particles that help visualize the flow being measured. A double-pulse YAG laser and a double-shutter camera are synchronized to capture two particle images with very short time difference.

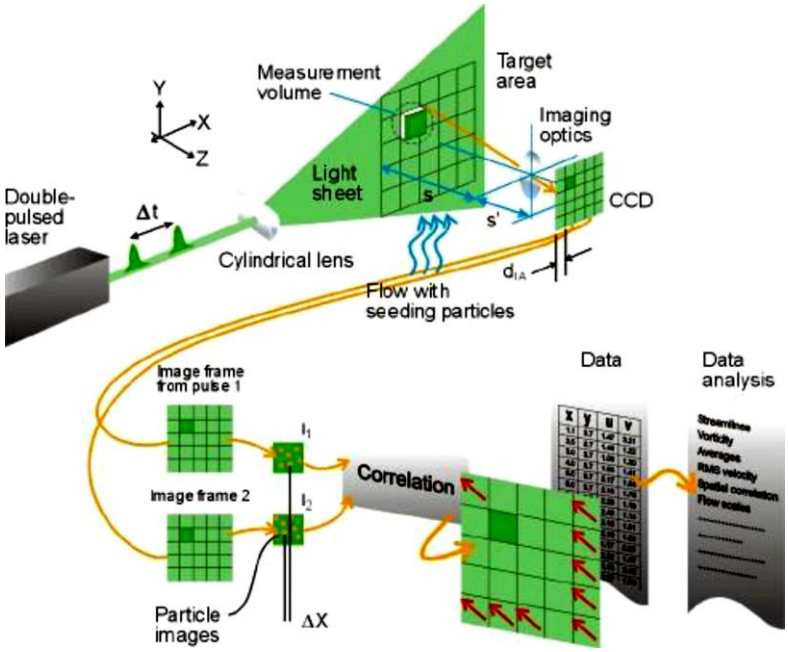


Figure 3.21: Measurement principle of the PIV technique[10]

PIV requires two particle images with a very short time separation, typically less than 100 microseconds. The frame straddling technique enables the recording of two images with a time separation of down to 100 nanoseconds. A double-pulse laser and a double-shutter camera are synchronised by the timing controller. Once the images are successfully recorded, the next step is the PIV analysis. The images are divided into small search areas called "interrogation areas" or "windows (IA). The interrogation windows from each image frame, 1 and 2, are cross correlated with each other, pixel by pixel, using specialised software. The location of the interrogation windows in both images remains constant (in the standard FFT cross-correlation, the interrogation windows are shifted in advanced algorithms). Peak detection in each interrogation window, after applying FFT algorithms to the images, reveals the dominant displacement in each window. Prior to capturing images of the flow field, the camera and the optical setup need to be calibrated. This involves determining the spatial and temporal calibration parameters, such as the pixel-to-distance ratio and the time interval between consecutive frames. Therefore, once the size of a pixel in flow and the time separation between two images are known, the

velocity can be calculated with sub-pixel interpolation. A velocity vector map over the whole target area is obtained by repeating the cross-correlation for each interrogation area over the two image frames captured by the camera.

### 3.6.2 PIV Data Recording Modes

There are two primary classifications for the PIV recording modes: (1) techniques that capture multiple images of illuminated particles onto a single frame over time; and (2) techniques that generate a single image of the particle distribution for each instance of illumination[11]. These branches are known as single-frame/double-exposure or single-frame/multi-exposure PIV (see Figure 3.22(a)) and double-frame/single-exposure or (see Figure 3.22(b)) multi-frame/single-exposure PIV.

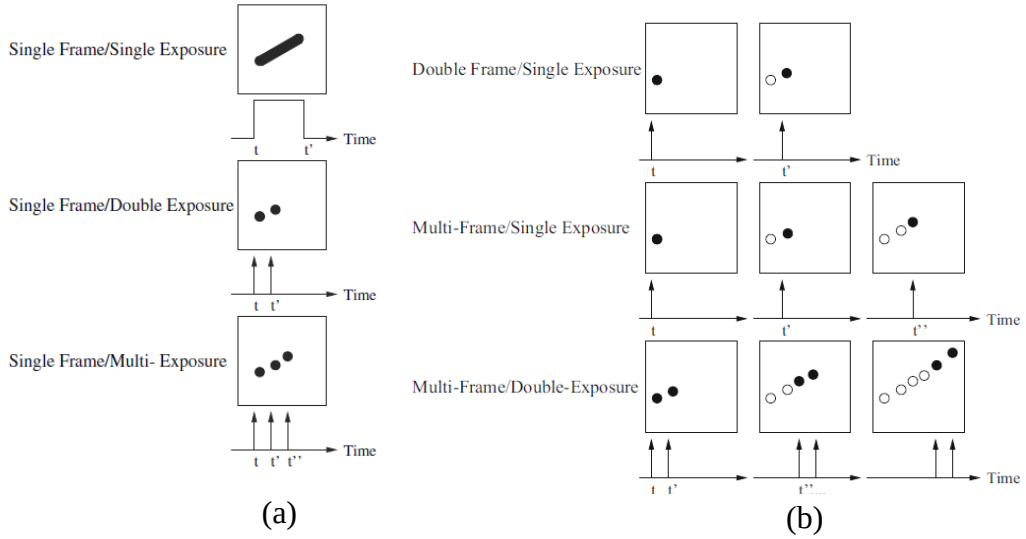


Figure 3.22: PIV recording techniques: (a) double-frame/single-exposure (b) multi-frame/single-exposure PIV

The double-frame single-exposure recording method offers several advantages over the single-frame double-exposure method. Additionally, with access to a CCD camera and a double-pulsed laser in the laboratory, this technique has been implemented in this research work. The double frame/single exposure PIV technique involves the acquisition

of two images of a fluid flow using a double-pulsed laser. This method necessitates a CCD camera equipped with two frames, one for each image, and precise control over the time delay between the frames. By employing cross-correlation techniques, the displacement of particles between the two frames can be measured, enabling the determination of the velocity and direction of the fluid flow. Typically, the evaluation of this recording mode involves cross-correlating between frame I and frame II, resulting in a single correlation peak that corresponds to the average displacement of particles within the interrogation window.

### 3.6.3 PIV Components and Measurement Procedure

This section provides a comprehensive description of the PIV apparatus and measurement techniques employed in this experimental study. Figure 3.23 illustrates the schematics of the PIV apparatus mounted on the solar chimney test rig. The PIV setup includes double-pulsed lasers, which produce two light pulses with an adjustable time interval. These light pulses are synchronized and pass through a laser sheet optic system, generating a flat sheet of light that illuminates the particles seeded in the flow. The CCD camera, positioned at a 90° angle to the laser sheet, captures the scattered light from the particles, ensuring alignment between the object plane and the illuminated fluid section. The CCD camera and laser unit synchronize with the timer box unit and are triggered externally by a specialized LabVIEW program. This LabVIEW program also controls the movement of the CCD camera, which is mounted on a linear motion unit to capture PIV images of the entire chimney during experiments. Additionally, limiting switches installed on the traverse system restrict camera movement. The flow images captured are then transferred to the computer for analysis using DynamicStudio software. Subsequently, the data is post-processed in Python by developing suitable codes.

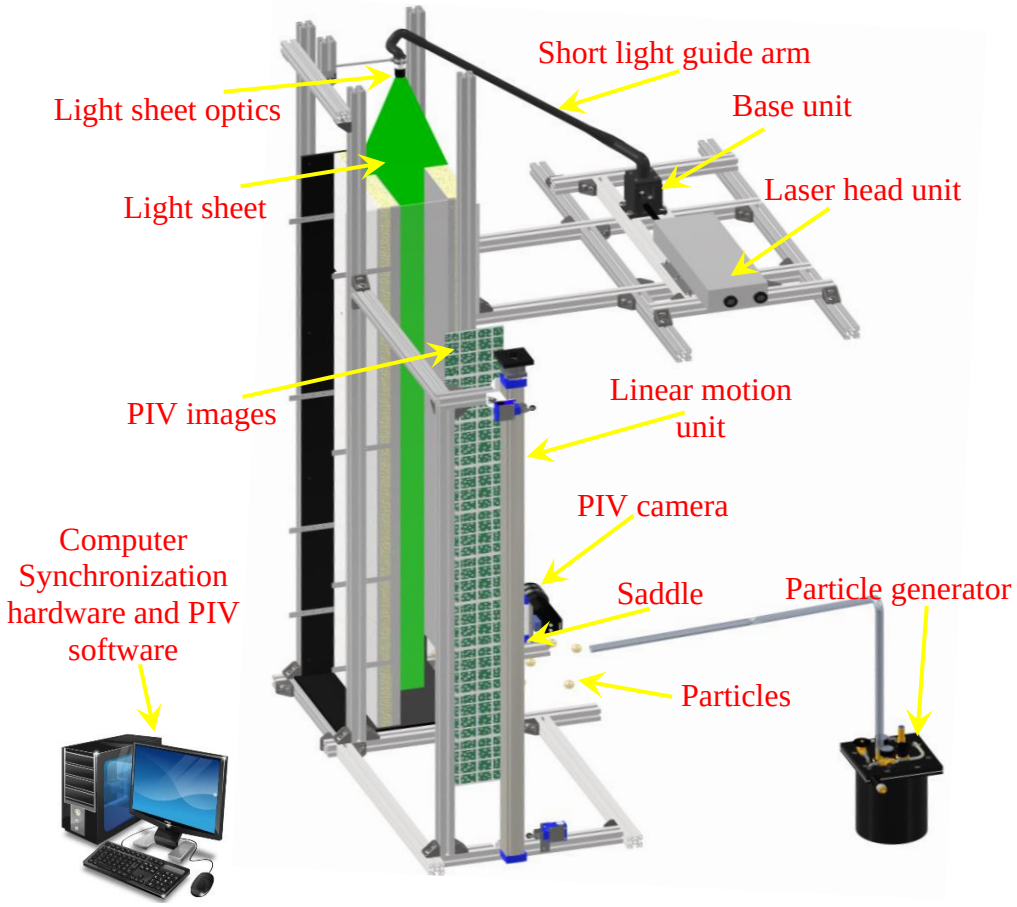


Figure 3.23: schematic of the 2D PIV set-up for the solar chimney.

3.6.3.1 Laser System

The laser system comprises three primary parts: the laser head, power supply unit, and laser remote controller, illustrated in Figure 3.24. For stability, the laser head is firmly attached to a specially crafted aluminium frame, then mounted on the roof of the attached room of the solar chimney. Using a light guiding arm and light sheet optics, the laser sheet is directed towards the central plane of the chimney being studied. The power supply unit has been placed in an open area to ensure adequate airflow for cooling. A laser remote control is on the table to manage and activate the power supply for the laser head unit of the system.

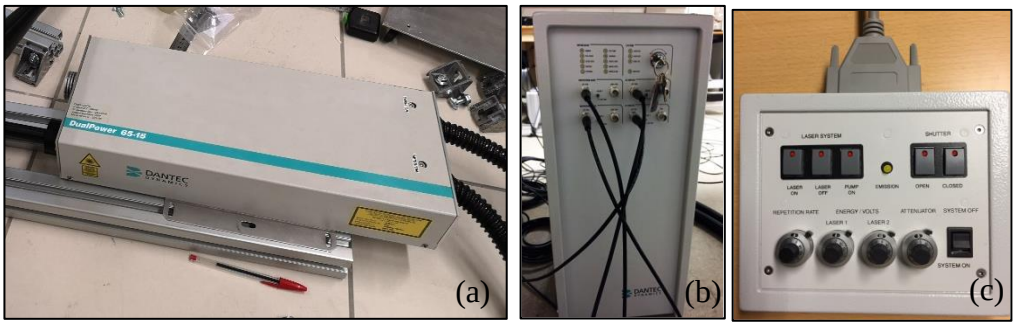


Figure 3.24: Laser system (a) Laser head (b) Power supply (c) Remote controller

The head unit contains a dual-cavity flash-pumped Nd:YAG (neodymium-doped Yttrium Aluminum Garnet). The key features of this laser are outlined in Table 3.1. The duration between consecutive pulses is set to be approximately 1000 µm, which is determined based on the flow velocities observed in the chimney during experiments. This time interval has been found to be adequate for effectively displacing the seeded particles in double-frame images.

Table 3.1: Details of the laser system

| Specifications | |
|---|---|
| Light generating system | Freq. doubled, Nd: YAG laser |
| Model | Dantec Dynamics dual power 65-15 |
| Wavelength | 532 nm |
| Pulse duration | 3-5 ns |
| Polarisation | Horizontal |
| Max. repetition rate | 15 Hz |
| Cooling | Water (external) |
| Pulse energies | 120 mJ |
| Time b/w pluses | 1000 µs |

It also helps in achieving a well-defined peak during the cross-correlation of PIV images. The repetition rate of the pulses is maintained at 4 Hz, and each pulse delivers an energy

of 120 mJ. It is important to note that pulse energy plays a crucial role in properly illuminating the cross-section of the flow domain, particularly when the seeded particles are smaller than 1 μm in diameter.

3.6.3.2 Design of Laser Sheet

For the solar chimney experimental setup, the laser beam is directed horizontally from the laser head unit installed on the roof of the attached room (see Figure 3.25) to the chimney outlet. Hence, the laser beam is first directed towards the base unit with the help of a safety cover. The base unit utilizes a mirror tilted at an angle of 45° to vertically align the laser beam. This mirror possesses a specialized coating that reflects over 99.8% of the incoming laser light. On the upper part of the base unit, a short light-guiding arm is installed, enabling the laser beam to be conveniently directed along the centre plane of the chimney outlet.

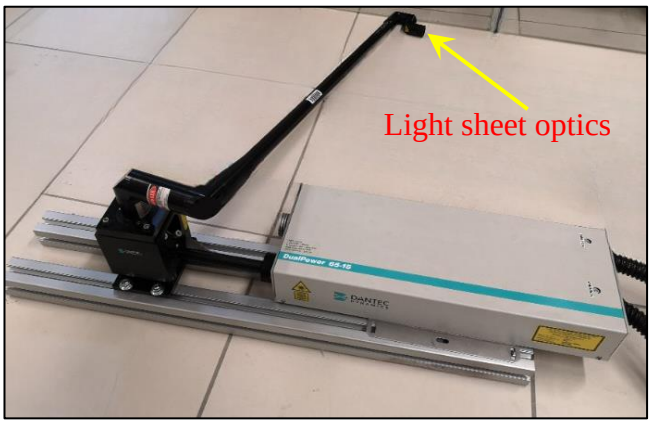


Figure 3.25: Laser head unit equipped with safety cover, base unit, light guiding arm & light sheet optics.

The generated light beams are aligned and directed through light sheet optics positioned at the end of a light guiding arm, as illustrated in Figure 3.23. This creates a thin light sheet, 2 mm thick at all measuring points, which illuminates the central plane of the flow in the chimney. The shaping optics combine a diverging and converging system of cylindrical lenses with variable space between lenses.

3.6.3.3 CCD Camera with Micro Lens

The PIV images were acquired using a Flow Sense EO 2M CCD camera paired with a Nikon Micro Nikkor 55 mm lens, as depicted in Figure 3.26(a). The short focal length of the lens enables precise focusing on small seeding particles in the flow domain.

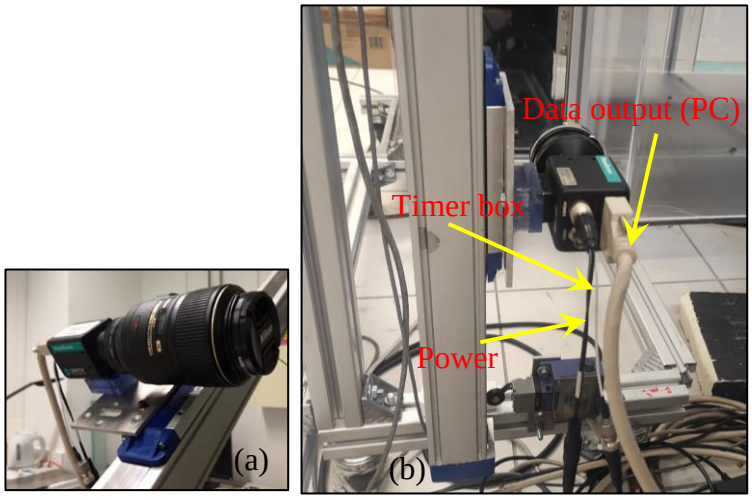


Figure 3.26: CCD camera mounted on traverse system (a) view of CCD camera on saddle (b) view of CCD camera and its connections

In Table 3.2 below, the key features of the camera and lenses employed are outlined. The CCD camera has three connections on its backside: power, synchronisation signal, and data output. The synchronisation signal cable is connected to the timer box; see Figure. 4.26(b) The data output cable connected to the PC, and power cable connected to the power supply.

Table 3.2: Details of the CCD camera and its attached lens

| Specifications | |
|---|---|
| PIV camera | Full frame interline transfer CCD |
| Model | Flow sense EO 4M |
| Resolution | 2 MP |
| Pixel size | 7.4 x 7.4 $\mu m^2$ |
| Max. frame rate (double frame/s) | 15 fps |
| Interframe time | 200 ns |
| Sensor resolution | 2015 x 2015 pixel |
| Lens system | Nikon Micro Nikkor 55 |
| Focal length | 55 mm |
| Maximum aperture | f/2.8 |
| Synchronisation system | External |

3.6.3.4 Traverse System and Control

An automatically controlled traverse system has been developed for the research apparatus, as depicted in Figure 3.27. This system accurately captures PIV images from the bottom to the top end positions of the linear motion unit, which is mounted beside the front wall of the chimney. This setup comprises a Thomson linear motion unit with a camera connected to its saddle, along with limit switches installed on the aluminum frame at each end of the linear motion unit to control the movement of the camera. The camera movement was managed using a specialized LabVIEW program that was developed and installed on the computer. The motor cables and limit switches of the linear motion system connect to the drivers. Additionally, LabVIEW software sends signals to the timer box to

synchronize the camera and laser, triggering the laser beam and coordinating with the frame rate of the CCD camera unit.

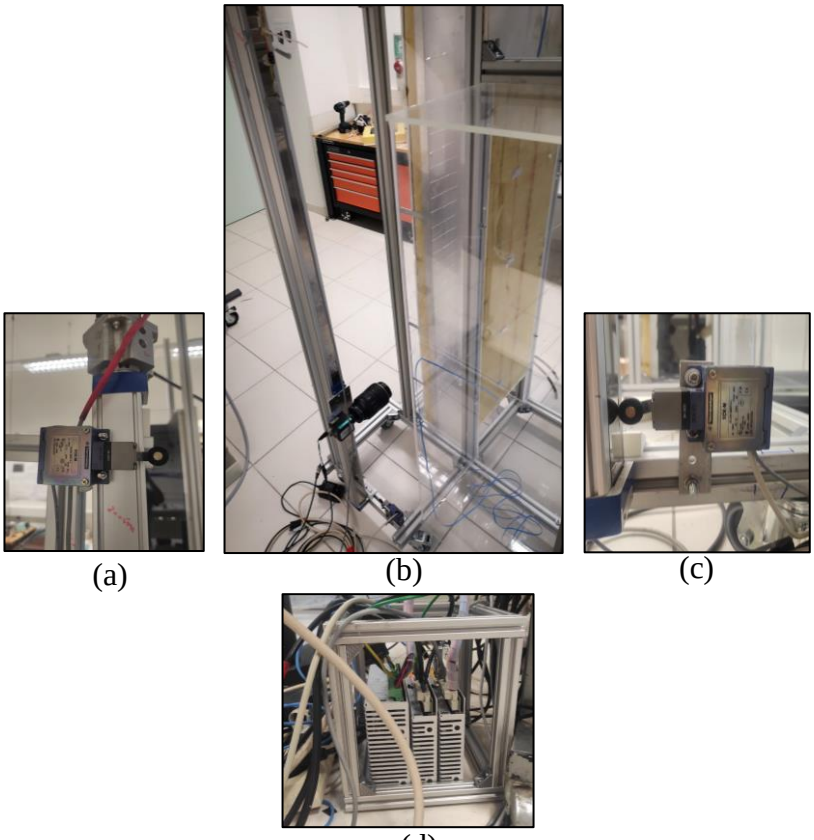


Figure 3.27: Traverse system and its control: (a) limiting switch at the top end position of the camera (b) PIV camera on linear motion unit (c) Limiting switch at the bottom end position of the camera (d) Motor drivers for linear motion unit.

Through the graphical user interface (GUI) of the LabVIEW program, you can define the vertical distance and the number of double-frame pairs of images for measuring the time-averaged velocity field inside the chimney. The GUI of the LabVIEW program made it easy to specify both the camera travel distance and the number of PIV image pairs to be recorded at the chosen spot on the chimney. To avoid overlap or gaps in chimney height within consecutive field-of-views (FOVs) of PIV images, the camera travel distance chosen on the LabVIEW interface is adjusted for each test. Despite thorough calibrations, there was an approximate 2 mm of uncertainty in the PIV images. This uncertainty is

likely due to vibrations generated by the motor of the linear motion unit when the camera begins or stops its movement.

3.6.3.5 Timer Box / Synchronizer

For PIV synchronization, the timer box is essential for coordinating the timing between the camera and laser. It simultaneously activates the camera exposure and regulates the laser firing to ensure precise particle picture capture for flow analysis and velocity measurements. The timer box enables accurate timing parameter adjustment and ensures precise synchronization in PIV experiments [12]. The connection of the timer to the laser head unit, CCD camera, and laser power unit is shown in Figure 3.28.

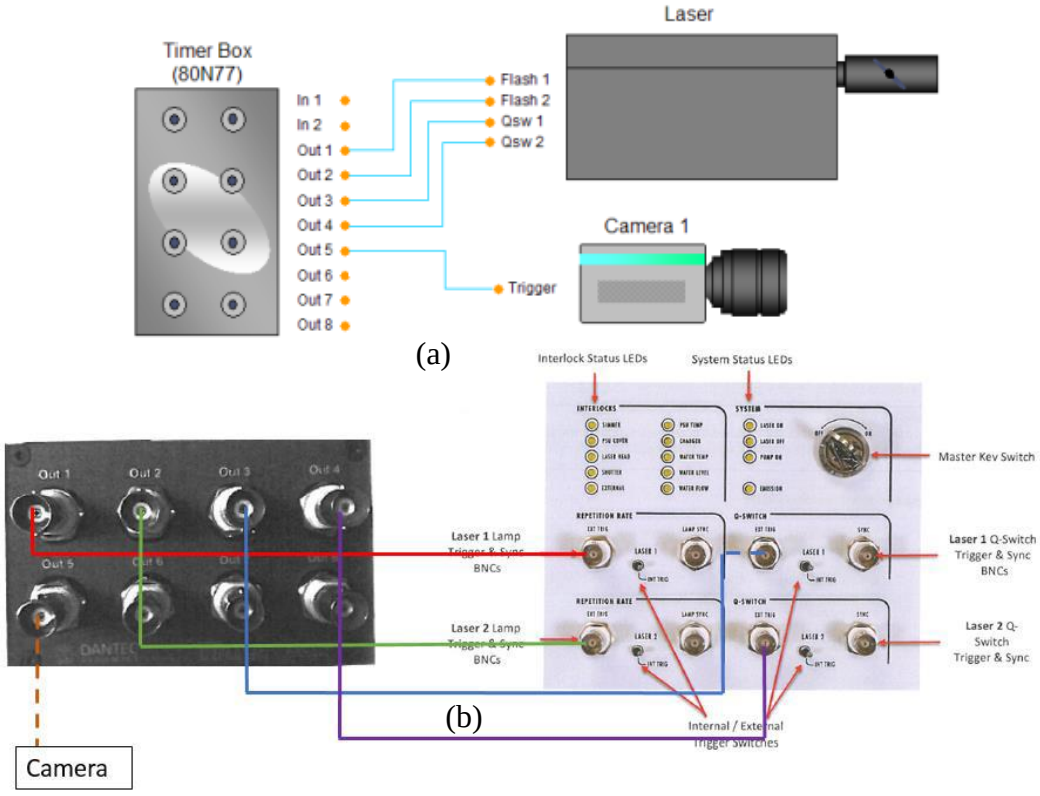


Figure 3.28: Synchronization of camera and laser [12]: (a) Connection of the timer box with laser and camera (b) Synchronizer output channels connected with laser power and camera.

To optimize the operation of this experimental setup, the timer box was integrated with DynamicStudio and a dedicated LabVIEW program. This integration allowed for efficient activation and synchronization of the camera and laser unit.

3.6.3.6 Particle Generator

PIV technique relies on tracking tracer particle velocity instead of fluid velocity, emphasizing the importance of precise particle seeding. Selecting the right particles and seeding methods is vital for enhancing measurement precision and minimizing uncertainty. This experiment uses a high-volume liquid droplet Seeding Generator (shown in Figure 3.29(b)) to generate tracer particles. Compressed air is passed through an inlet valve into a chamber filled with olive oil. The olive oil is atomized by the pressured air, producing the suspended oil droplets. As depicted in Figure 3.29(a), using a reinforced PVC hose, oil droplets suspended in pressurized air are directed from the discharge valve of the device to the hole in the front wall of the room. These droplets are then transported to the chimney through a hole in the attached room of the experimental bench. The air carries tiny oil droplets, ranging between 1 and 5 μm in size, to seed the fluid flow in the chimney. Ensuring a uniform dispersion of particles in the chimney. Following numerous attempts, a comprehensive seeding method has been established to meticulously capture the inherent natural convection airflow within the entire chimney at thermal quasi-steady state. It was found that a duration of 30 seconds was necessary to uniformly seed the solar chimney.

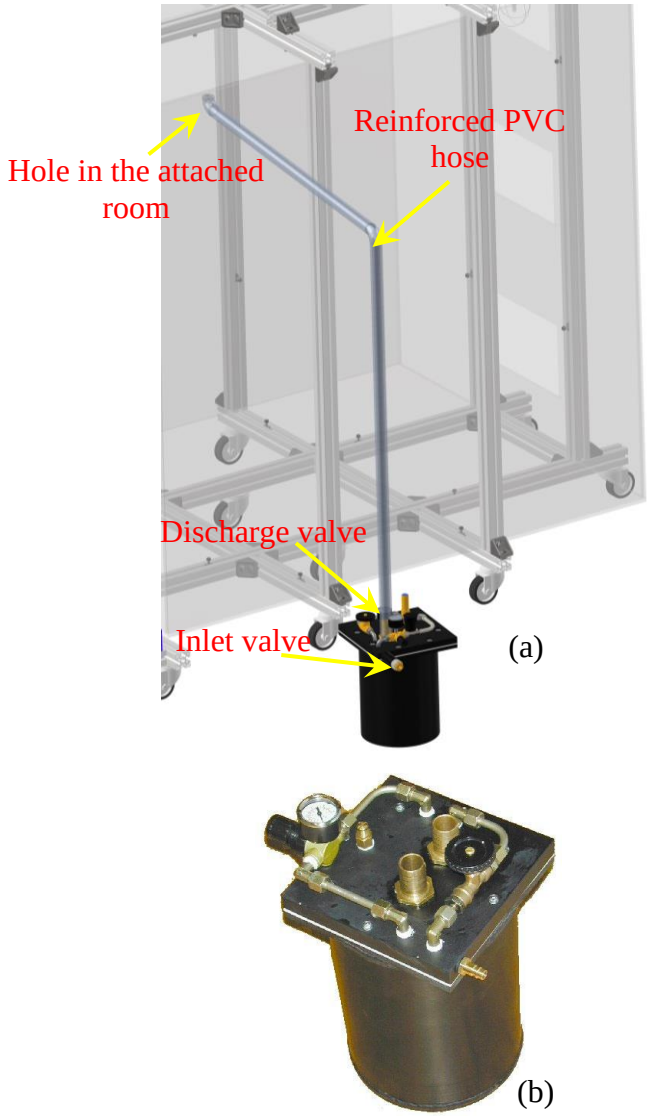


Figure 3.29: Particle generator & seeding of Experimental bench (a) Seeding of the experimental bench (b) 10F03 Seeding Generator

Subsequently, a 3 minute period was allocated for particle stabilization, allowing the fluid within the chimney to revert to its natural convection state. Following this, a series of 300 double-frame PIV images were captured at a trigger rate of 4 Hz. For each new position of the camera on the traversing unit, particles were reinjected after a 15 minute interval. This identical seeding process continued until the camera reached the topmost position on the linear motion unit. The main characteristics of the seeding material, seeding procedure, and seeding device are listed in Table 3.3.

Table 3.3: Details of particle generator and seeding procedure

| Specifications | |
|---|---|
| Seeding material | Olive oil |
| Diameter | 2µm to 4 µm |
| Density | 895 Kg/$m^3$ |
| Particle generator | 10F03 |
| Volume flow rate | approx. 43.5 l/min at 5 bar |
| Room attached with chimney | 2.45 $m^3$ |
| Laboratory room | 134 $m^3$ |
| Time for injection | 30 sec |
| Particle Stabilization time | 3 min |
| Number of images per location | 300 |
| Particle reinjection time break | 15 min |

### 3.6.4 PIV Image Acquisition Procedure

Ensuring accurate PIV results relies heavily on two factors: the size of the particle as it appears in the image and the average distance it moves between consecutive frames. In this experimental study, the PIV test showed that the particle size ranged from 2 to 4 pixels in the image, and the average particle displacement between double-frame photographs was approximately 6-7 pixels, indicating the reliability of the results. The interrogation window size in the image is divided into a grid of 64 by 64 pixels for cross-correlation analysis, typically accommodating around 10 particles per interrogation window.

Table 3.4: Details of the image acquisition procedure

| **Specifications** | **Low emissivity tests** ($\varepsilon \sim 0.08$) | **High emissivity tests** ($\varepsilon \sim 0.96$) |
|---|---|---|
| Flow geometry | Parallel to the laser sheet | Parallel to the laser sheet |
| Field of view | 161 x 161 $mm^2$ | 169 x 169 $mm^2$ |
| Interrogation volume | 64 x 64 x 2 $mm^3$ | 64 x 64 x 2 $mm^3$ |
| Observation distance | ≈ 0.535 m | ≈ 0.535 m |
| Recording method | Dual frame/single exposure | Dual frame/single exposure |
| Recording medium | Full frame interline transfer CCD | Full frame interline transfer CCD |
| Sensor resolution | (2015.5 x 2015.5 pixel) | (2015.5 x 2015.5 pixel) |
| Recording lens | f = 55 mm | f = 55 mm |
| scaling | 11.576 pixel/mm | 11.145 pixel/mm |
| Time b/w pulses ($\Delta t$) | 1000 µs | 1000 µs |
| Trigger rate | 4 Hz | 4 Hz |
| Particles injection time | 30 sec | 30 sec |
| stabilisation time | 3 min | 3 min |
| Images at each location | 300 | 300 |
| reinjection time break | 15 min | 15 min |

Table 3.4 provides a summary of the detailed parameters recorded during image acquisition for both low- and high-emissive tests. Due to technical limitations, the CCD camera cannot capture the entire airflow field in the chimney within a single field of view (FOV). The camera, mounted on a linear motion unit, is at a distance of 0.535 m from the illuminated central plane of the chimney. The distance travelled by the CCD camera for

capturing the PIV images between two successive locations on the linear motion unit varies depending on the vertical FOV of the PIV image during the experiment. Hence, in order to capture the time-averaged velocity field at each location of the chimney, 300 pairs of double-frame images are captured once the experimental bench reaches a quasi-steady thermal state. After several calibration trials, the time interval between two light pulses of the laser is adjusted to 1000 μs for double-frame images.

### 3.6.5 Image Evaluation Method and Post-Processing

The study uses DynamicStudio v3.12, a commercial software developed by Dantec Dynamics, to evaluate PIV images and extract valuable data. This software offers comprehensive features, including image preprocessing, PIV data analysis algorithms, and post-processing methods. Given the uniform illumination of the images, pre-processing techniques were unnecessary in this experiment. The cross-correlation method is employed to evaluate the PIV recordings, with post-processing conducted using both DynamicStudio v3.12 and by writing Python codes to interpret the results effectively.

#### 3.6.5.1 Image Processing

In the present investigation, the Dantec Dynamics PIV system was utilized to implement the double frame/single exposure recording technique, as illustrated in Figure 3.30(a). This technique involves capturing two successive frames of the flow field in a single exposure. Double-frame images were acquired within Ensemble in the DynamicStudio v3.12 software. Each Ensemble keeps together a double-frame 300 images for each location along the chimney. For all the images in ensembles, the cross-correlation function was computationally calculated using efficient Fast Fourier Transform (FFT) algorithms integrated within the software. Figure 3.30(b) demonstrates the determination

of correlation peak strength between two double-frame recordings from the experiments after the cross-correlation process.

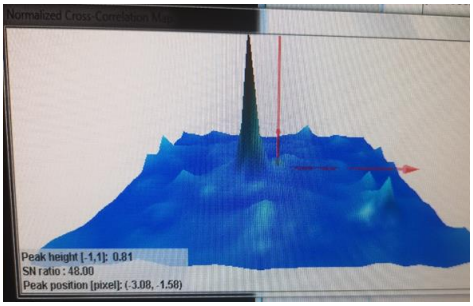


(b)

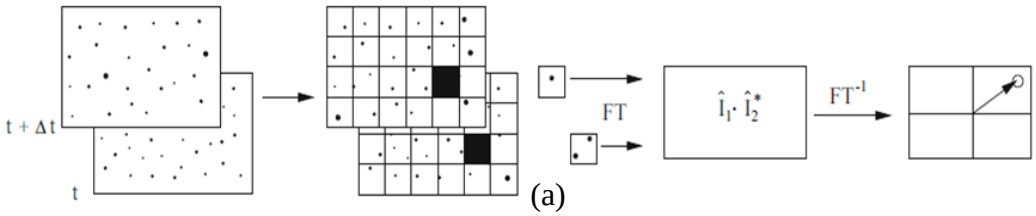


(a)

Figure 3.30: PIV image processing: (a) Example of a resulting cross-correlation field Analysis during the experimentation (b) Double frame/single exposure recordings: the digital cross-correlation method [11]

To improve the spatial resolution of the measurements, the multi-grid interrogation technique was used. The interrogation areas were set at 64 x 64 pixels with a 50% overlap. This choice was made to ensure that particle movement does not exceed a quarter of the size of the interrogation areas.

### 3.6.5.2 Post-Processing

Post-processing of the PIV images begins with the masking operation on each Ensemble. The main aim of using masking is to hide areas in the images that extend beyond and are close to the active and passive walls of the chimney. This is necessary due to the limited definition of fluid properties within the boundary sub-layer region near the walls, the sparse distribution of particles near the walls, and the presence of wall interference. After the masking procedure, an averaging operation is carried out on all ensembles. This averaging helps compute the time-averaged 2D velocity flow field for all sections of the

chimney. To present the results clearly and effectively, the CSV files containing the time-averaged velocity field data for each test were imported. Afterward, additional post-processing was carried out using Python scripts, and the results were plotted in this research work. Table 3.5 presents a summary of the parameters of the PIV cross-correlation image and the associated interrogation algorithm utilized within the study.

Table 3.5: Details of PIV cross-correlation and interrogation algorithm for solar chimney

| **Specifications** | |
|---|---|
| PIV Software | DynamicStudio v3.12 |
| size of the image after masking | 139 x 161 $mm^2$ ($\varepsilon \sim 0.08$), 135 x 169 $mm^2$ ($\varepsilon \sim 0.96$) |
| Interrogation window | 64 x 64 pixel |
| Number of refinement steps | 2 |
| Interrogation window overlapping | 50 % |
| Validation rate | 90 % |
| Number of valid vectors per image | 3528 |

It is important to note that in PIV, all information regarding the flow velocity field, except for the time delay between pulses and the calibration parameters of the camera, is stored during recording. This implies that the evaluation method and post-processing can be utilized for a transient flow field analysis in the chimney without the necessity of repeating the experiments.

## 3.7 Uniform Power Flux Injection Technique

To maintain the necessary heat flux range for the experimental bench and ensure uniform heat flux (UHF) boundary conditions on the walls of the chimney, the experimental bench

was fitted with an Electrical Power Flux Injection System. For this purpose, two heaters were procured from VERELEC. The choice of heaters was determined by the required heat flux range for experimentation and the geometric design of the chimney wall.

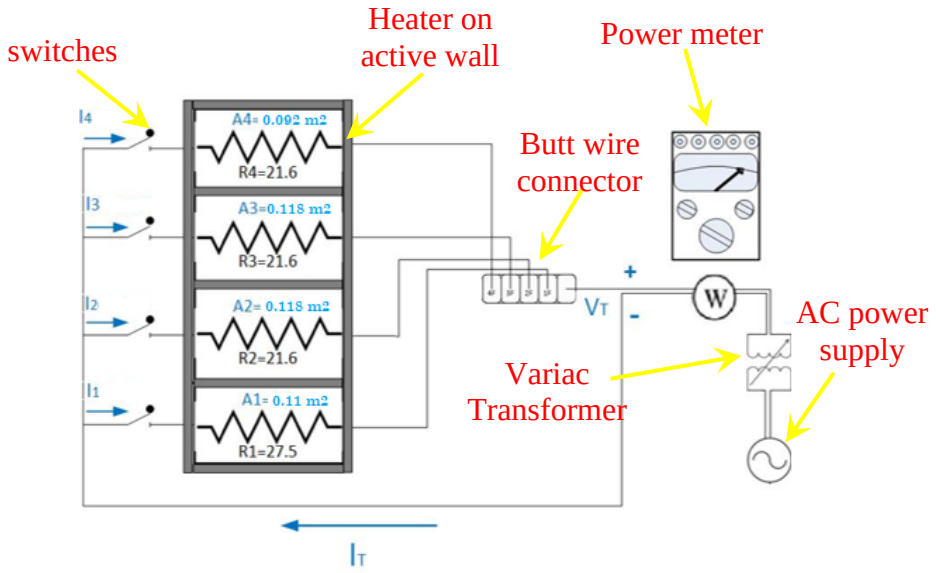


Figure 3.31: Schematic diagram for electrical power injection system on chimney active wall

The electrical block diagram depicted in Figure 3.31 outlines the layout and connection of essential electrical components, including the variac transformer, power meter, electrical cables, butt wire connectors, and switches, for uniform heating of the active wall of the chimney. The variac transformer and power meter were selected based on the AC single-phase power source in the laboratory room and the total resistance of the heating elements of the glass heater. The four heating elements of the heater were soldered to electrical wires, as shown in Figure 3.32(a). These wires were then passed through a hole drilled in the chimney wall, as depicted in Figure 3.32(c). Spiral cables were used to conceal the heater cables emerging from the hole. Additionally, cable trunking of suitable size was installed on the aluminium frame of the chimney to conceal the butt wire connectors and cables and to secure the switches on the top cover.

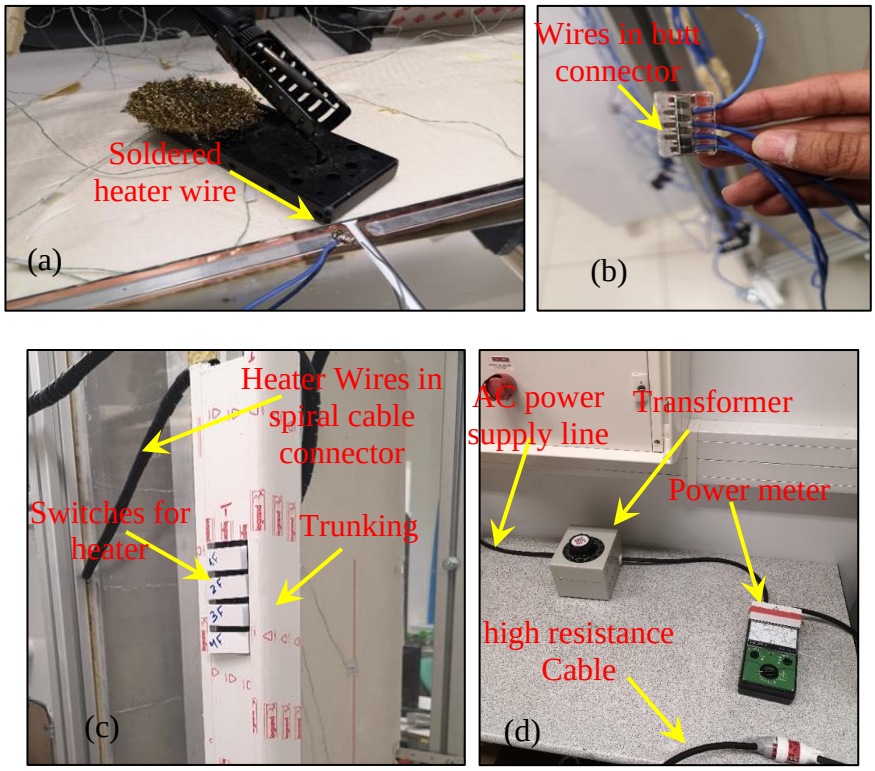


Figure 3.32: Electrification of the heater on Active wall: (a) Soldering of wire on the heating elements (b) Positive wires from the heaters into butt wire connector (c) Negative wires from the heater into the switches covered in cable trunking (d) Power meter & variac transformer connected cable of the heaters and AC power supply

The four slots in the butt wire connector (see Figure 3.32(b)) were used to secure the four cables constituting the negative terminals of the heater. The positive wires from the heating components were connected to the appropriate slots on the electrical switches. The negative end of the wire was then attached to the final slot of the butt wire connection, while the positive end of the high-heat resistive cable was linked to an available slot on the last electrical switch. The high-resistance wire from the cable trunking was connected to the MAVOWATT meter (see Figure 3.32(d)) using male and female connectors. The MAVOWATT meter was then connected to the Variac transformer with high-resistance cables, which in turn were connected to the power socket using a male connector during the experiment.

### 3.7.1 Heater

Glass heaters were installed on both the active and passive sides of the chimney wall to ensure consistent heating across the walls, meeting the specific experimental needs of the test setup.

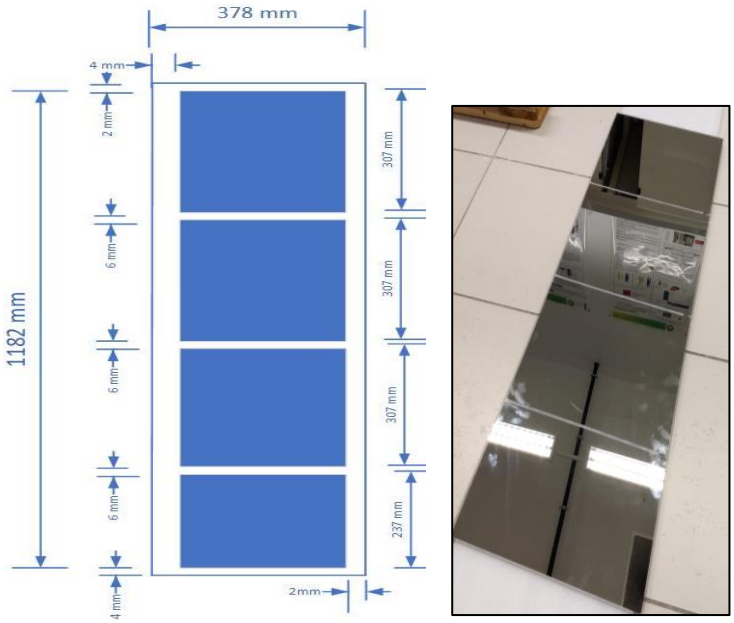


Figure 3.33: Schematic diagram of the heater with actual VERELEC Glass heater

The electric heater comprises tempered glass plates with four etched foil heating elements affixed on the backside. Figure 3.33 illustrates the dimensions of the heater and the dimensions of the coating on the heating element from its reverse side. The coating on heater consists of a nanolayer of chrome and nickel alloy applied through a plasma treatment process. This guarantees constant material resistance even with temperature fluctuations. Table 3.6 provides detailed technical specifications for further reference.

Table 3.6: VERELEC heater technical datasheet

| Specifications | |
|---|---|
| Dimensions | 1182 x 378 x 4 $mm^3$ |
| Power rating | 600 watts |
| Number of heating elements | 4 |
| Resistance of same-sized 3 elements | 21.4 Ω |
| Resistance of small-sized element | 27.5 Ω |
| Thermal conductivity | 1 W/mK |
| Specific Heat | 840 J/kg.K |
| density | 2500 $Kg/m^3$ |

### 3.7.2 Variac Transformer

To ensure consistent heating conditions during experiments, the power supply to the heater on the active wall of the chimney is regulated by adjusting voltage and current from a single-phase AC source using an RS Pro 1-phase 720 VA Variac transformer, as depicted in Figure 3.34. The variable transformer is connected to the electrical circuit of the experimental bench to maintain and regulate a uniform heat flux.

Figure 3.34: RS Pro 1-phase 720 VA Variac Transformer

Variac transformers are commonly utilized for their ability to provide adjustable AC voltage, ensuring a distortion-free output. This feature makes them invaluable in various applications where precise control of voltage is necessary. Table 3.7 outlines the key specifications of the Variac transformer.

Table 3.7: Variac Transformer technical datasheet

| Specifications | |
|---|---|
| Dimensions | 160 x 130 x 160 mm |
| Knob Rotation | Clockwise |
| Maximum Operating Frequency | 60 Hz |
| Number of Outputs | 1 |
| Number of Phases | 1 |
| Power Rating | 720 VA |
| Primary Current Rating | 3 A |
| Primary Voltage Rating | 240 $V_{ac}$ |
| Secondary Voltage Rating | 0 to 270 $V_{ac}$ |

### 3.7.3 Power Meter

The MAVOWATT 4 power meter (shown in Figure 3.35) was used to measure both the total current and the secondary voltage supplied to the heater, which allowed for the calculation of the heat flux injected into the chimney. For the experiment, the voltage and current settings on the power meter switches were adjusted to 50 V and 5 A, ensuring accurate measurement. Under these settings, the measurement error for voltage and current on the scale was within the range of 0.5V and 0.05A, respectively.


Figure 3.35: MAVOWATT 4 power meter

## 3.8 Omnidirectional Anemometer

The ThermoAir 64 omnidirectional anemometer (shown in Figure 3.36) is used to measure the speed of air generated by mechanical ventilation in the laboratory room and assess the airflow speed at room air inlet of the solar chimney. Following calibration, the anemometer was linked to a channel on the 34901A multiplexer module within the Keysight 34972A data logger for recording experimental data. The key specifications of the device are listed in Table 3.8 below.


Figure 3.36: ThermoAir 64 omnidirectional anemometer

Table 3.8: ThermoAir 64 technical data sheet

| Specifications | |
|---|---|
| Dimensions | 10 x 10 x 5 cm |
| Model | ThermoAir 64 omidir: |
| Operative range | 0.01 to 1 m/s |
| Precision at 22 Co air temp: | ± 1.0% to ± 1.5% |
| Humidity range | 0 to 40% |

## 3.9 Data Logger Switch Unit

The Keysight 34972A data logger switch unit was employed for gathering real-time raw data during the experiments. The data logger unit transmitted the raw electrical signals from the sensors to the LabVIEW program installed on the laboratory computer, where they were processed into meaningful outputs instantly. Additionally, this program saved the data in a CSV file for subsequent analysis. The data logger switch unit depicted in

Figure 3.37: Keysight 34972A data logger switch unit & 34901A multiplexer module

Figure 3.37 can accommodate three removable 34901A multiplexer modules, each capable of holding 18 sensor wires. To collect data from 125 thermocouples and an omnidirectional anemometer on the experimental bench, four sets of data logger switch units were used.

### 3.10 Reference:

[1] M. Thebault, Coherent structures and impact of the external thermal stratification in a transitional natural convection vertical channel, (n.d.).

[2] S.Q. Estibaliz, Experimental investigation of thermal and fluid dynamical behavior of flows in open-ended channels. Application to Building Integrated Photovoltaic (BiPV) Systems, (n.d.).

[3] M. Fossa, C. Ménézo, E. Leonardi, Experimental natural convection on vertical surfaces for building integrated photovoltaic (BIPV) applications, Exp. Therm. Fluid Sci. 32 (2008) 980–990. https://doi.org/10.1016/j.expthermflusci.2007.11.004.

[4] J. Vareilles, Étude des transferts de chaleur dans un canal vertical differentiellement chauffé: application aux enveloppes photovoltaïques thermiques, 2007.

[5] D. Michalski, K. Strąk, M. Piasecka, Comparison of two surface temperature measurement using thermocouples and infrared camera, EPJ Web Conf. 143 (2017) 02075. https://doi.org/10.1051/epjconf/201714302075.

[6] M. Thebault, S. Giroux-Julien, V. Timchenko, C. Ménézo, J. Reizes, Detailed flow development and indicators of transition in a natural convection flow in a vertical channel, Int. J. Heat Mass Transf. 143 (2019) 118502. https://doi.org/10.1016/j.ijheatmasstransfer.2019.118502.

[7] Y. Sun, Y. Zhang, An Overview of Room Air Motion Measurement: Technology and Application, HVACR Res. 13 (2007) 929–950. https://doi.org/10.1080/10789669.2007.10391463.

[8] X. Cao, J. Liu, N. Jiang, Q. Chen, Particle image velocimetry measurement of indoor airflow field: A review of the technologies and applications, Energy Build. 69 (2014) 367–380. https://doi.org/10.1016/j.enbuild.2013.11.012.

[9] S. Scharnowski, C.J. Kähler, Particle image velocimetry - Classical operating rules from today's perspective, Opt. Lasers Eng. 135 (2020) 106185. https://doi.org/10.1016/j.optlaseng.2020.106185.

[10] Measurement Principles of PIV - Dantec Dynamics, Dantec Dyn. Precis. Meas. Syst. Sens. (n.d.). https://www.dantecdynamics.com/solutions/fluid-mechanics/particle-image-velocimetry-piv/measurement-principles-of-piv/ (accessed August 7, 2023).

[11] M. Raffel, C.E. Willert, F. Scarano, C.J. Kähler, S.T. Wereley, J. Kompenhans, Particle Image Velocimetry: A Practical Guide, Springer International Publishing, Cham, 2018. https://doi.org/10.1007/978-3-319-68852-7.

[12] C. Zhang, S. Vasilevskis, B. Kozlowski, Particle Image Velocimetry - User Guide, (n.d.).

# CHAPTER 4: CHARACTERIZATION OF TEST BENCH

## 4.1 Purpose of Characterization of Experimental Bench

The experimental setup for studying natural convection in an L-shaped vertical channel, connected to a reduced-scale model of a room, underwent rigorous characterization to ensure the accuracy, reliability, and reproducibility of the results. This involved several procedural steps. Initially, measures were implemented to minimize the impact of mechanical ventilation in the test room, especially in the proximity of the experimental apparatus, creating an optimal environment for conducting experiments focused on exploring natural convection phenomena. Subsequently, a meticulous evaluation of the ambient conditions within the laboratory room was conducted, with a focus on temperature variations and stratification, both with and without a heating source, to precisely quantify the conditions during testing. After characterizing the laboratory room, a series of tests were conducted to establish the criteria for achieving a state of global thermal equilibrium for the experimental bench. This step was essential to ensuring reliable and repeatable results from the experiments. Once the criteria for thermal steady state were determined, repeatability tests were performed to validate the accuracy and consistency of the time-averaged temperature field measurements obtained during the experiments. Upon reaching global thermal equilibrium, particle image velocity (PIV) tests were undertaken to also define the criteria for acquiring a 2D time-averaged flow field at the central plane of the entire chimney. Lastly, repeatability tests were also conducted on the PIV measurements to ensure the reliability and consistency of the obtained time-averaged flow field data throughout the experimentation process. This comprehensive characterization process defined in this chapter ensures that the experimental setup operates under controlled and consistent conditions and that the data

obtained from the experiments is accurate, credible, and suitable for further academic analysis and interpretation.

## 4.2 Adaptation of Duct Ventilation System in the Laboratory Room

The entire experimental setup was assembled in the PIV experimental room at the LOCIE laboratory, which was already outfitted with a mechanical duct ventilation system. For accurate positioning of the test bench and placement of the thermal sensors installed in the PIV room, refer to Figure 3.17 in Chapter 3. As illustrated in Figure 4.1(a), the PIV room comprises two ducts for fresh air supply and one for return air.

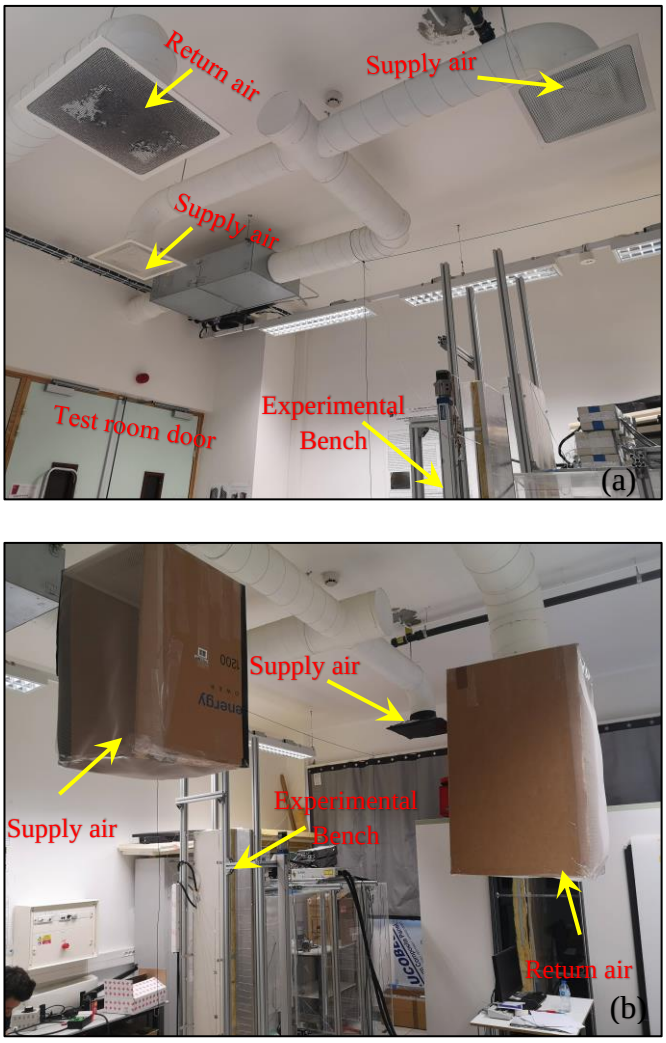


Figure 4.1:View of the PIV experimental test room (a) Mechanical duct ventilation system (b) Adaptation of duct ventilation system

To minimize the influence of mechanical ventilation and establish a quiescent state of air surrounding the experimental bench, as illustrated in Figure 4.1(b), one of the outlets of supply air ducts near the bench was completely covered with solid duct tape to block the air jet entirely. The other supply air duct was partially covered with cardboard on three sides. The remaining sides were covered with plastic mesh fabric, forming a hollow rectangular structure around the outlet of the supply air duct. This setup was intended to interrupt and reduce the airflow, redirecting it away from the experimental bench. Likewise, the return air duct outlet was covered with a rectangular hollow structure made of cardboard and plastic mesh to minimize the suction effect within the PIV room. Following the adjustments to the duct ventilation system in the PIV room, an omnidirectional anemometer was employed to gauge airflow at various points: the outlet, within the chimney cavity, and at the room air inlet of the adjacent experimental bench room, as depicted in Figure 4.2. Measurements were conducted for one hour at each designated spot, with a sampling frequency of 0.025 Hz.

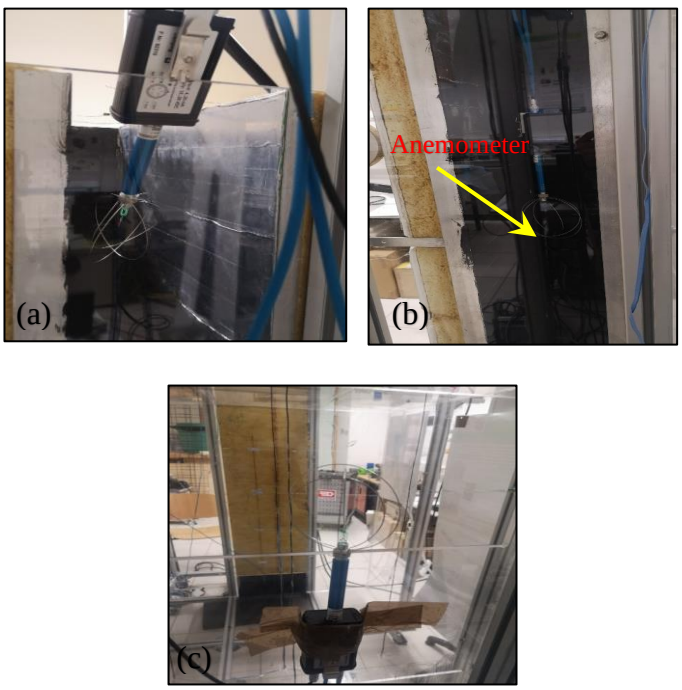


Figure 4.2: View of Omni-directional anemometer mounted on the test rig (a) Outlet of the chimney (b) Inside cavity of the chimney (c) Air inlet of the attached room

Figures 4.3(a), (b), and (c) show airspeed fluctuations and mean values at different location of the experimental bench: the chimney outlet, inside the chimney cavity, and at the attached room air inlet. The mean airspeed at the chimney outlet and inside the cavity is about 0.05 m/s, with fluctuations from 0.04 to 0.06 m/s at the outlet and 0.05 to 0.06 m/s inside. Meanwhile, the mean speed at the attached room window is 0.074 m/s, with fluctuations ranging from 0.071 to 0.076 m/s.

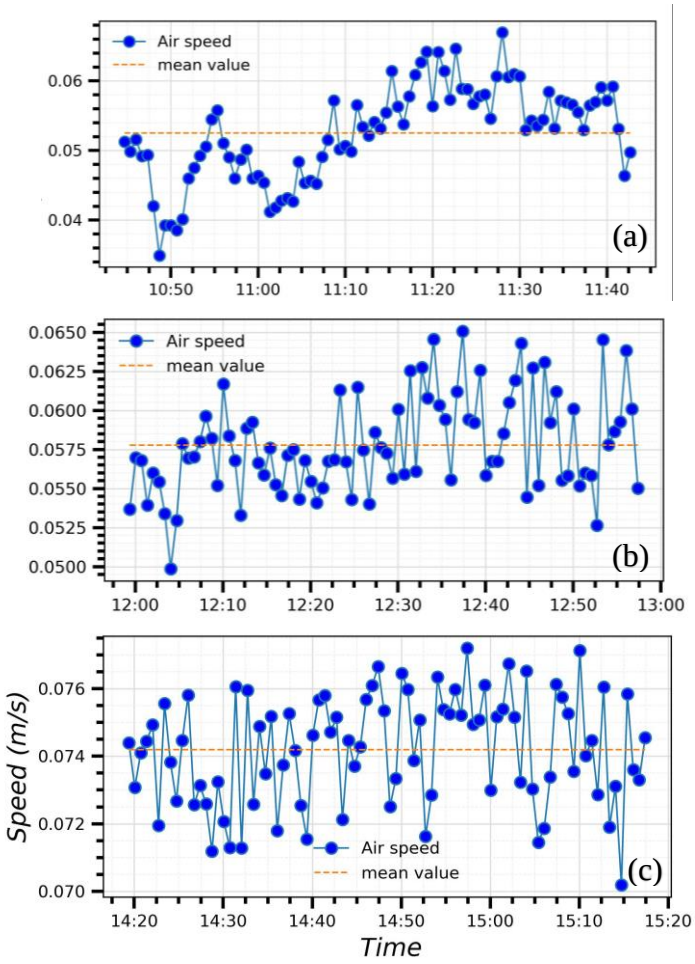


Figure 4.3: Measurement of Temporal movement of air (a) Outlet of the chimney (b) Inside the cavity of the chimney (c) Room air inlet of the attached room

Based on the magnitude of airflow in proximity to the experimental bench, it can be concluded that the modifications to the mechanical duct ventilation system in the PIV room have effectively reduced significant air currents around the experimental bench for conducting natural convection experiments.

## 4.3 Temperature Stratification in the Laboratory Room

As noted by various studies [1,2,3,4,5,6], thermal stratification outside the channel significantly affects natural convection airflow within the channel at low thermal power inputs. Therefore, tests were conducted to evaluate temperature evolution and stratification in both heated and unheated conditions to determine the ambient conditions for testing. Thermocouples were installed around the solar chimney test rig (see Figure 3.17 in Chapter 3 for exact locations) to measure temperature changes in the room. The PIV room, where the experiments took place, is considerably larger than the experimental bench, with a volume of approximately 134 $m^3$. The test room floor measures about 6.4 x 5.8 $m^2$, and the ceiling height is 3.64 m. Environmental conditions in the testing room varied daily and seasonally, with average room temperatures fluctuating by up to 10°C throughout the year, particularly at the entrance of the solar chimney. These fluctuations were recorded during experiments conducted from January to December. The current research findings indicate that the vertical thermal gradient remains consistent throughout all tests, with a negligible fluctuation of no more than 0.5 °C from the floor to the ceiling within the designated experimental timeframe. Additionally, the temperature variance between the height room corresponding to the channel inlet and the channel outlet does not surpass 1°C. Throughout the experiment duration, the temperature increase of the surrounding air at the chimney inlet is restricted to a maximum variation of 1 °C.

### 4.3.1 Temperature in the Test Area: Without Heating Source

Four tests without a heating source were conducted over 24 hours on September 2, 6, 9, and 15, 2021. These tests aimed to monitor temperature changes in the experimental area and assess the impact of cyclical changes in the external environment and the duct ventilation system on the test room. Figures 4.4(a) and (b) display the data from the tests

conducted on September 2 and 6, 2021, under sunny and clear skies. Thermal data was collected at a sampling rate of 0.025 Hz, starting at 10:35 AM on the day of the test and ending at 10:35 AM the following day.

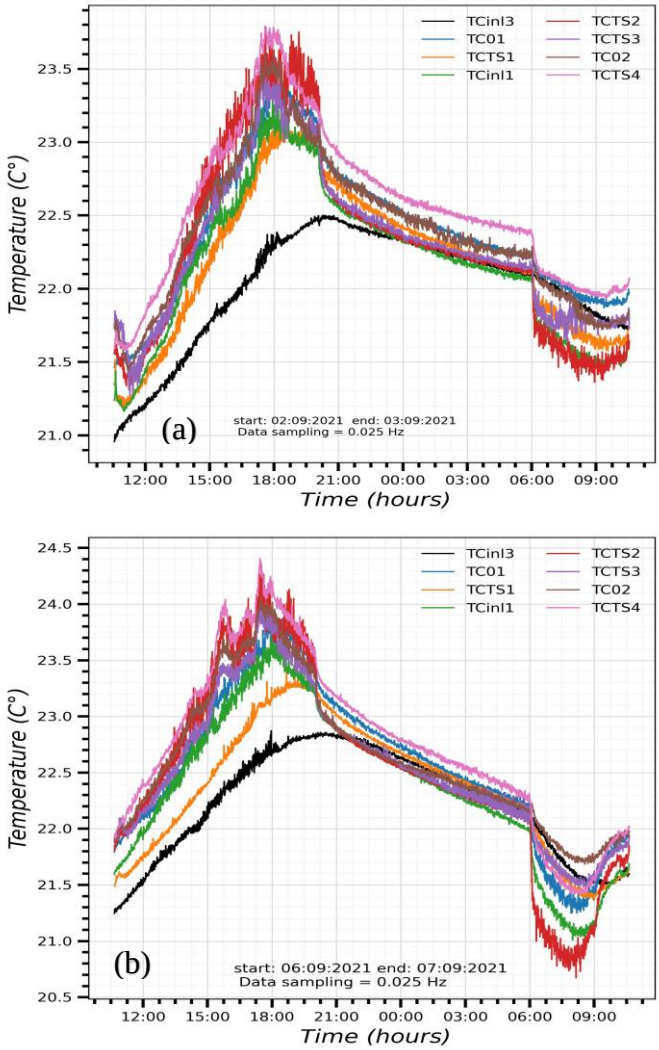


Figure 4.4: Evolution of ambient temperature in the test room close to the experimental bench (a) Test on September 2 (b) Test on September 6

The temperature in the test room starts rising from 9:00 in the morning to late in the evening, at around 19:30. Depending on the outside ambient temperature, a temperature rise is observed in the test room. Thermal stratification in this elapsed time is not more than 0.5°C from floor to ceiling of the test room throughout this time interval. And then, the air temperature in the test room starts declining from 21:30 to 6:00, and the slope of the graph becomes negative. The air temperature change in this interval of time is almost

0.2°C from the ground to the ceiling of the test room. From 6:00 to 9:00, inverse stratification in the test room is observed and can be attributed to several reasons, ranging from the cooling of the room during the night, no heat from power consumption sources in the room, and the restart of the mechanical duct ventilation system early in the morning. Two additional tests were conducted on September 9th and 15th: one on a rainy day and the other on a cloudy day. These tests have shown a significant impact on the slope of the temporal temperature plot lines in the graph, causing it to transition from a steeper slope on sunny days to a gentler slope up from 9:00 until 19:30 on rainy and cloudy days with vertical thermal stratification less than 0.3°C. Based on the tests conducted, it was determined that diurnal temperature changes and weather fluctuations affect the evolution of ambient temperature within the test room. Moreover, these experiments revealed that the ideal time for studying natural convection in the test room is between 21:30 and 6:00. However, conducting experiments during the night presents potential hazards, such as the risk of the heater causing the electrical power system to overheat. Without access to the laboratory, such overheating could pose serious risks. Consequently, a time-window for all experiments was chosen between 9:30 and 18:00. In the absence of a heat source in the test room, the temperature changes and stratification behind both the chimney wall and the window-carrying wall of the experimental bench were almost similar in magnitude. Throughout the experimental period, the temperature difference between the floor (at 1.05 m) and the ceiling (3.15 me from the floor) did not exceed 0.5°C. Additionally, the temperature difference between the chimney outlet (at 2.1 m) and the chimney inlet did not exceed 1.5°C.

### 4.3.2 Temperature in the Test Area: With Heating Source

To monitor air temperature changes in the test room with a heating source on December 16, 2022, the heater inside the active wall of the solar chimney test rig was activated. The primary goal was to observe and analyse the evolution and stratification of the ambient temperature near the chimney wall and the window carrying wall of the attached room when a heat source is introduced in the test room. The test was conducted by injecting electrical heat flux of 235 W/m² into the active wall of the chimney. This resulted in a maximum temperature increase of 67 °C on the active chimney wall. However, a similar test in August showed a temperature rise of 75 °C. Hence, to prevent overheating of the electrical power injection system, the test duration was limited to 5 hours. It was observed that the presence of a heat source reduces temperature stratification in the test room compared to when no heat source is present. The evaluation of the overall air temperature rise in the test room through comparing tests conducted with and without a heat source is considered unreliable in this study, contrary to the approach taken by [1,2]. This unreliability stems from the fact that the tests with and without heating were conducted in different months within this research work.

Figure 4.5 illustrates a test conducted on December 16, 2022, to compare the impact of a heat source in a test room. The test began around 9:52 with no heater activation on the active wall of the chimney for 22 minutes. Subsequently, the heater was activated, resulting in a temperature spike at the inlet of the chimney after approximately 30 minutes of heating. This spike is attributed to heat loss from the back side of the heater penetrating into the room wall in contact with the chimney. Additionally, the heating source has impacted the dynamic temperature changes in the test room, resulting in increased

fluctuations in temperature plots. These observations clearly indicated the influence of the heating source on the air temperature of the test room.

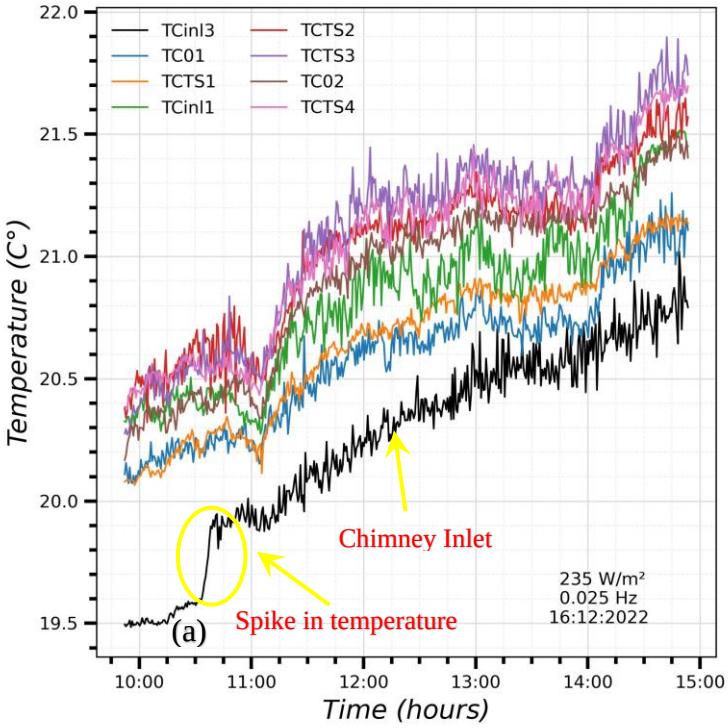


Figure 4.5: Evolution of air temperature in the test room with heating source

With the presence of heat source in the test room, the air temperature stratification between the floor (above 1.05 m) and the ceiling of the experimental room (at a height of 3.15 m from the floor) does not surpass 0.5°C. Likewise, between the height corresponding to the chimney outlet and the chimney inlet, the temperature stratification remains within 1°C. Furthermore, the temperature evolution and stratification behind the chimney wall and the window carrying wall of the attached room exhibit almost identical patterns, with negligible temperature disparities between the thermocouples at corresponding heights.

## 4.4 Dynamic Temperature Analysis of the Experimental Bench

The dynamic temperature analysis of the experimental bench had two main objectives: first, to establish the criteria for achieving a thermal quasi-steady state in the experimental setup; and second, to identify any malfunctioning thermocouples installed on the apparatus. Hence, on December 16, 2022, a thermal test was carried out by injecting an electrical heat flux of 235 W/m² into the active wall of the chimney and the low-emissive walls of the chimney for nearly 5 hours, from 9:52 to 14:54, while recording thermal data at a sampling rate of 0.025 Hz.

### 4.4.1 Temperature Variation on the Active Wall of the Chimney

Figure 4.6 depicts the temperature variation over time for all thermocouples mounted on the surface of the heater on the active wall of the chimney, subjected to a uniform heat flux of 235 W/m² at low emissive walls of chimney ($\varepsilon \sim 0.08$). The surface temperature of the heater rises sharply within the first 40 minutes after the electrical heat injection. After two hours, the surface temperature of the heater stabilizes. This stabilization occurs more slowly in the upper part of the heater compared to the lower part, as the temperature progressively increases from the leading edge to the trailing edge of the heater. At the trailing edge of the heater, an adiabatic segment of the chimney was formed by placing a glass plate on the glass heater. However, a perfect adiabatic boundary condition was not achieved. Heat energy leaked from the trailing edge of the heater into the adiabatic part of the chimney, resulting in a significant drop in temperature readings from the two thermocouples up to 5 mm below the top end of the heater compared to nearby thermocouples.

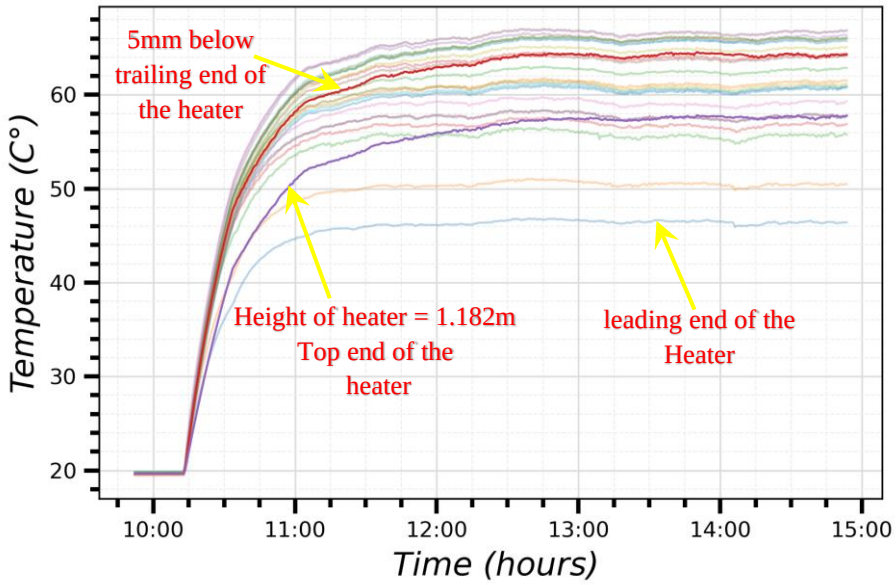


Figure 4.6: Temperature evolution on the heater surface at 235 W/m²

The temperature variation over time from the thermocouples mounted on the surface of the glass plate of the active wall of the chimney is shown in Figure 4.7. The maximum temperature is recorded at the bottom end of the glass plate, in contact with the top end of the heater, and the minimum temperature is recorded at the top end of the adiabatic part.

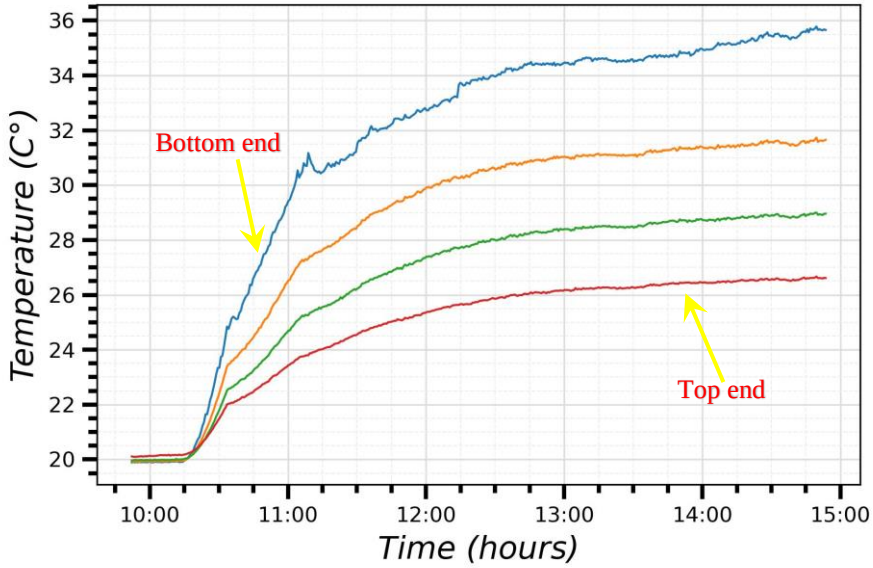


Figure 4.7: Temperature evolution on the adiabatic part of the active wall at 235 W/m²

The surface temperature rises sharply within the first 40 minutes after the test starts. After two hours, the surface temperature on the adiabatic part of the chimney stabilizes. Moreover, the temperature on the adiabatic part of the active wall of the chimney is consistently higher than the inlet air temperature, indicating conductive heat transfer from the trailing edge of the heater and natural convection heat transfer from the heated air in contact with the active wall of the chimney. As detailed in Section 3.3.1 of Chapter 3, thermocouples were installed 50 mm to the left of the mid-width active wall to measure its temperature. Additional thermocouples were placed 50 mm to the right of the mid-width active wall to ensure temperature uniformity along the x-axis of the chimney walls. The resulting time-varying temperature graphs, which utilized data from thermocouples at identical heights on both sides of the symmetry line, exhibited overlapping trends and identical average temperature readings. This confirms that the surface temperature is consistent over a 100-mm span along the x-axis.

### 4.4.2 Temperature Variation on the Passive Wall of the Chimney

Figure 4.6 depicts the temperature variation over time for all thermocouples mounted on the surface of the passive wall of the chimney. The surface temperature of the passive wall rises approximately 40 minutes after the electrical heat injection from the active wall of the chimney. Subsequently, over the course of two hours of continuous heating, the temperature changes on the passive wall surface exhibit a more gradual pattern. The time-varying temperature changes remain within the range of 0.2°C even after three hours. These fluctuation in the temperature is attributed to the evolution of the air temperature within the test room throughout the experimental time window. Figure 4.6 illustrates the temporal temperature variations for all thermocouples placed on the surface passive wall of the chimney. Around 40 minutes following the activation of the active wall, the

temperature of the passive wall starts to increase. Over the subsequent two hours of steady heating, the temperature changes on the passive wall display a slower rate of increase. Even after three hours, the fluctuation in temperature remains within ±0.2°C. These temperature fluctuations are attributed to changes in the air temperature within the experimental chamber during the test period.

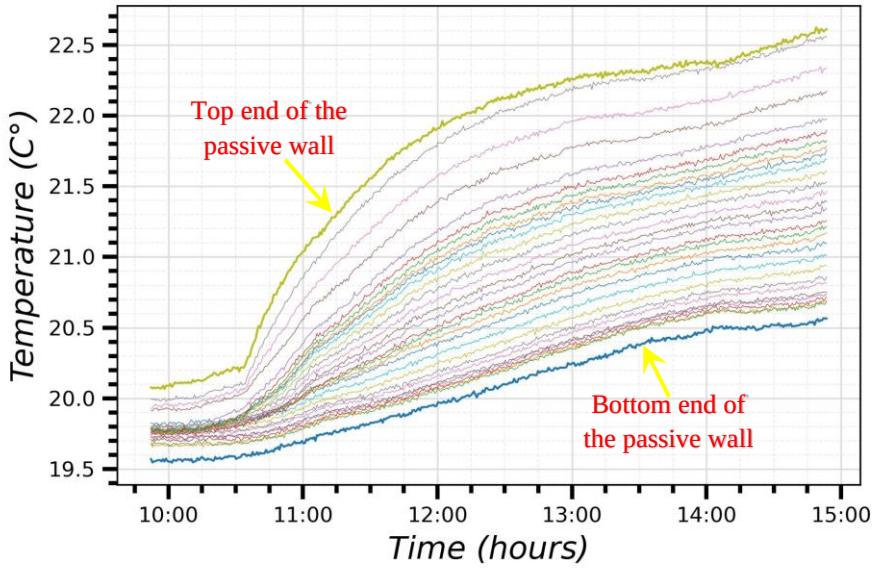


Figure 4.8: Temperature evolution on the Passive wall of the chimney at 235 W/m²

The graph illustrates that, despite the low emissivity of the chimney walls, the passive wall absorbs a small amount of radiation emitted by the active chimney wall, causing its temperature to rise. As the height of the passive increases, its temperature also rises correspondingly. This temperature elevation in relation to the height is attributed to the higher view factor of the upper portion of the passive wall towards the active wall of the chimney, resulting in a higher absorption of radiation from the active wall. Similar to the analysis carried out on the active wall of the chimney to ensure temperature uniformity along the x-axis of the passive wall, Time-varying temperature graphs were generated from thermocouples placed on the 50mm left and 50mm right sides of the mid-width of the passive wall. These graphs showed similar trends and nearly identical temperature

readings. This confirms that the surface temperature is consistent over a 100-mm span along the x-axis.

### 4.4.3 Temperature Variation inside the Room Attached with Chimney

Figure 4.9 depicts the temporal evolution of temperature changes recorded by all the thermocouples positioned within the room connected to the solar chimney. For precise sensor locations, please refer to Figure 3.15 in Chapter 3. A slight spike in room air temperature is observed approximately 20 minutes after initiating electrical heat flux injection into the active chimney wall. Throughout the test, the room temperature rises by 1°C. Due to the lower height of the attached room relative to the test room, vertical stratification in air temperature among sensors positioned near the floor, at the room centre, and near the ceiling is very subtle.

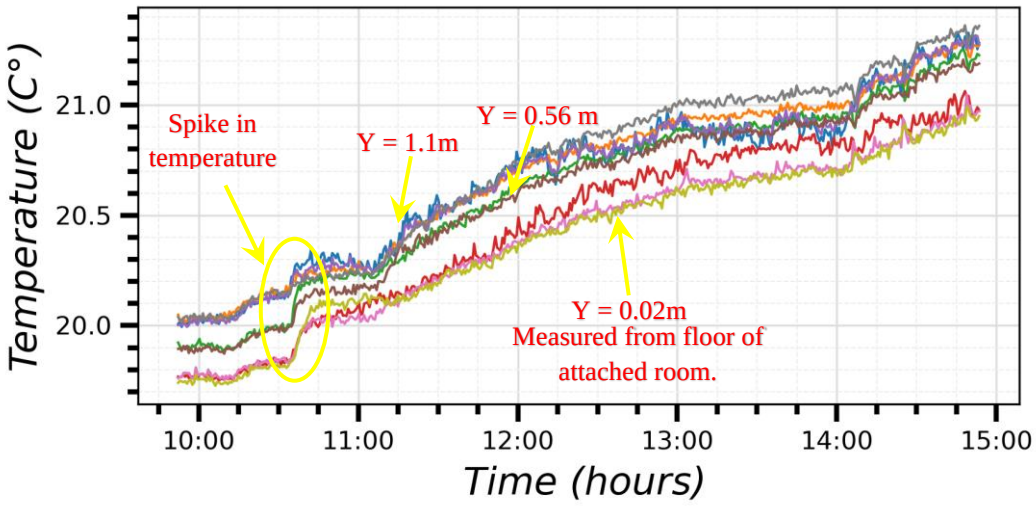


Figure 4.9: Temperature evolution on the attached room of the chimney at 235 W/m²

During experimentation involving heat flux injection at a rate of 235 W/m$^2$, a notable increase in room air temperature of up to 1.5°C was recorded. Likewise, when heat flux injection was set at 110 W/m$^2$, the temperature within the room rose by 0.8°C. This rise in air temperature within the attached room of the solar chimney during the experiments

can be attributed to diurnal temperature changes in the laboratory room and heat conduction losses from the active wall of the chimney into the attached room.

## 4.5 Criteria for Thermal Quasi-steady State

To establish the thermal quasi-steady state of the experimental setup within the laboratory environment, a test was conducted on December 16, 2022, exposing the setup to a heat flux of 235 W/m² for nearly 5 hours. Thermal data was collected at a frequency of 0.025 Hz. The test began at 9:30, the heater on the active wall was turned 0ff for 22 minutes. Following this, the heater remained activated until 14:54. Figure 4.10(a) shows the time-varying temperature graph of four thermocouples located on both the heated section of the active wall and the glass wool insulation cover behind it. Refer to Chapter 3, Figure 3.13 for the precise positioning of these thermocouples. After 2 hours and 46 minutes of heating, the temperature on the heated part of active wall stabilizes fully at 13:00. Meanwhile, thermal stabilization in the insulation cover of the active wall takes 3 hours and 18 minutes, occurring at 13:32. The same analysis is also extended to the passive wall, its insulation cover, the adiabatic part of active wall of the chimney, and the room wall adjacent to the active wall. Hence, the time required for the experimental test bench to reach a quasi-steady state in the test room environment was defined to be 3 hours and 18 minutes of heating. Once the system reached the time duration for thermal equilibrium on the experimental bench, a total of 30 data points were collected from all the thermocouples over a span of 20 minutes. These data points were then used to compute time-averaged temperature values from the experimental bench. Figure 4.10(b) illustrates the procedure for computing the time-averaged value from the thermocouple, which is positioned 1.24 m from the bottom plate of the chimney and mounted on the backside of

the heater on the active wall. The average temperature was calculated to be 65.7 °C, with a standard deviation of ±0.1 °C.

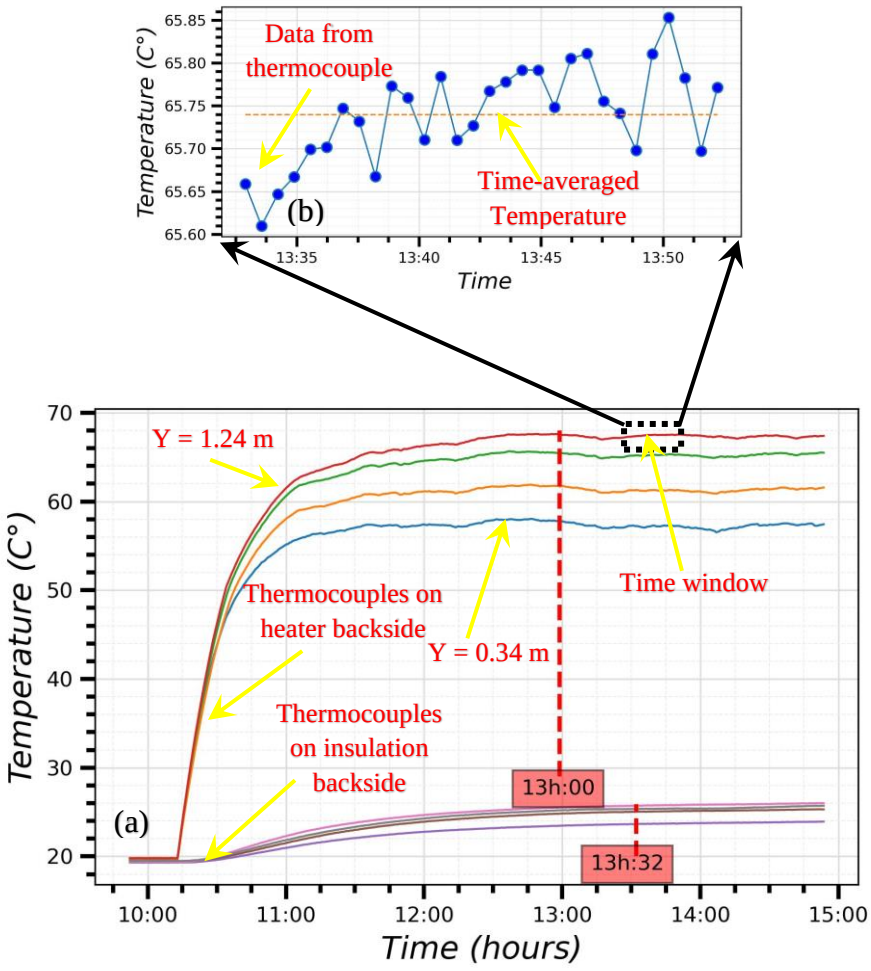


Figure 4.10: Criteria for global thermal equilibrium for test bench at 235 W/m² (a) Temperature evolution behind the heater and glass wool insulation (b) Time-averaged temperature calculation

Based on these findings, the total duration for all the tests was adjusted from 5 hours and 22 minutes to 4 hours and 10 minutes. Each test, as always, began with 22 minutes without heating. The heating duration for all tests was changed from 5 hours to 3 hours and 45 minutes. Based on the thermal equilibrium criteria for the experimental bench, after 3 hours and 18 minutes of heating, the experimental bench reached a state of global thermal equilibrium with the test room environment. At this point, a total of 30 data points were collected, and time-averaged temperature values were computed for all the tests.

## 4.6 Repeatability of Thermal Field on Chimney Walls

The repeatability of operational wall temperature field on both active and passive walls of the chimney was verified under established thermal equilibrium criteria. Two consecutive tests, conducted on December 16 and 17, 2022, were rigorously analysed. Each test was subjected to a heat flux of 235 W/m² from the active wall of the chimney. The aspect ratio of the chimney, determined by dividing the height of the heater by the chimney air gap, was maintained at 8. The air gap between the active and passive walls measured 0.146 m, with a consistent surface emissivity of 0.08. Mean temperature values were calculated from thermal data in accordance with established thermal equilibrium criteria.

Figures 4.11(a) and (b) depict how the operational wall temperature (the local wall temperature ($T_{wall}$) minus the inlet air temperature ($T_{inlet}$)) changes over time for both the Active wall and the Passive wall of the chimney. This change is observed at a quasi-steady state along the mid-width of the chimney (X/W = 0.5). The x-axis of the graph illustrates the operational wall temperature, while the y-axis represents the non-dimensional height of the chimney. In all experiments, there was a consistent maximum deviation of 0.5°C observed at the chimney inlet. However, throughout all trials, temperature variation within the test room never surpassed 0.5°C. During the phase of repeatability of tests, the maximum difference in the operational wall temperature of the heated section of the active chimney wall between the two tests was 0.2°C, while on the adiabatic section of the active wall, it did not exceed 0.9°C.

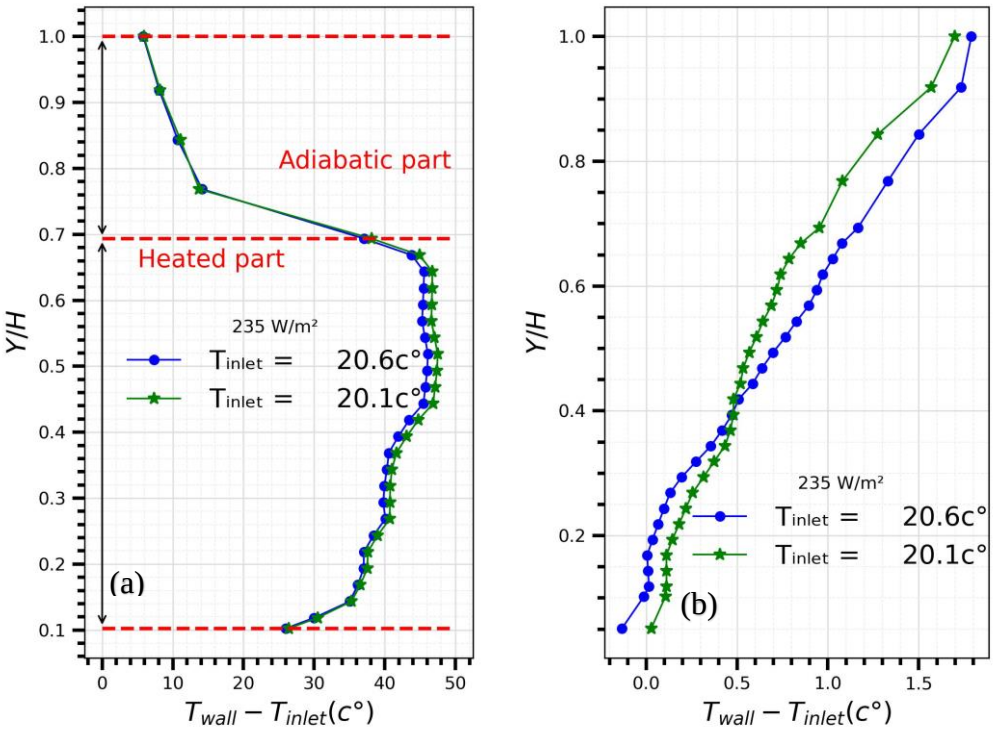


Figure 4.11: Repeatability analysis on wall thermal field at 235 W/m² (a) Operational wall temperature on the active wall (b) Operational wall temperature on the passive wall

The operational wall temperature on the passive wall was very close to the inlet air temperature, making it more influenced by the external conditions of the test room. The maximum difference in the operational wall temperature on the passive wall between the two tests was 0.09°C, while the difference in the mean operative wall temperature on the passive wall between the two tests was 0.04°C.

## 4.7 Criteria for PIV Test

To establish criteria for the PIV test, several trials were conducted to properly calibrate the CCD camera, ensuring accurate data acquisition from the flow domain at the central plane of the chimney. Additionally, a particle seeding protocol was developed to effectively capture the entire natural convection flow within the chimney. A series of preliminary trials were conducted to determine the optimal trigger rate and time intervals between laser beam pulses for acquiring reliable data on the airflow field inside the

chimney. Further trials were then performed to ascertain the number of image pairs required to capture the reliable and consistent time-averaged airflow field in the chimney. In the initial trial, a time-averaging process was performed on 50 image pairs. With each subsequent trial, an additional 50 image pairs were added to the previous set, and the time-averaging process was repeated. This progressive averaging procedure continued until reaching a total of 300 image pairs, at which point the time-averaged velocity profiles did not show any variation with the addition of more image pairs. On December 16, 2022, a test was conducted to first acquire thermal data to compute the time-averaged temperature at the quasi-steady state of the experimental bench. Once the thermal data was collected, the thermal acquisition system was deactivated. Meanwhile, the Particle Image Velocimetry (PIV) system was kept on standby. Seeding particles were injected into the chimney for 30 seconds, after which the pressure valve of the particle injection system was closed. Then, a waiting period of 3 minutes was observed to allow the seeded air in the chimney to accurately trace the airflow in the chimney. Subsequently, a series of 300 double-frame PIV images were captured, with a frequency of 4 Hz and an inter-pulse time of 1000 μs. The CCD camera underwent incremental repositioning to match the vertical field of view of the image on the traversing unit. Following a 15-minute interval, particle reinjection took place again.

For this test, with the chimney having a low surface emissivity ($\varepsilon \sim 0.08$), the entire procedure was repeated eight times, with the CCD camera moving approximately 1.3 meters away from the inlet of the chimney using the traversing unit. It took about 1 hour and 40 minutes to capture a total of 2400 PIV image pairs from 8 successive locations along the chimney. For the PIV test with high-emissive walls of the chimney ($\varepsilon \sim 0.96$), the same procedure was repeated ten times. In this case, the CCD camera traversed

approximately 1.7 m from the inlet of the chimney. It took about 2 hours to record a total of 3000 PIV images from 10 successive locations, starting from the chimney inlet.

## 4.8 Repeatability of Time-averaged Vertical velocity Profiles

This section examines the consistency and repeatability of vertical velocity profiles at different sections of the chimney through the use of the PIV technique. This method is commonly employed in studies concerning flow field analysis in natural and mixed convection [1–6], ensuring the reliability and consistency of experimental results. To this end, two PIV tests were conducted following the criteria outlined in the previous section. The first test, conducted on December 16, 2022, served as the benchmark test, while Test 2 was undertaken the subsequent day.

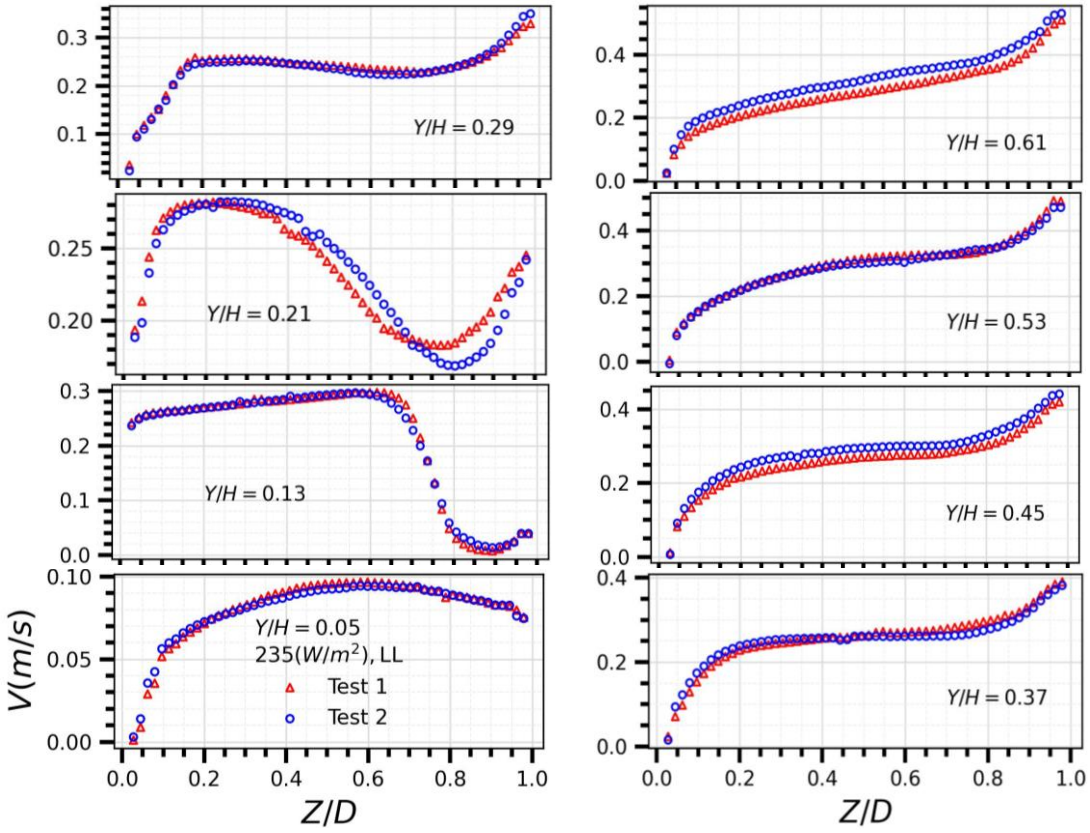


Figure 4.12: Vertical velocity profiles for tests 1 and 2 at 235 W/m²

The time-averaged vertical velocity profiles for both tests are plotted in a transformed coordinate system, where the active wall of the chimney is on the right side of each graph and the passive wall is on the left. The X-axis represents the nondimensional air cavity gap, and the Y-axis shows the distribution of time-averaged vertical velocity. Figure 4.12 illustrates the evolution of the time-averaged vertical velocity field along the height of the chimney in the upstream direction, from Y/H = 0.05 to Y/H = 0.61. The velocity profiles for both tests are plotted at fixed intervals of Y/H = 0.0805. It can be observed that all the vertical velocity profiles at the same locations within the chimney exhibit similar vertical velocity distributions and overlap with each other. This demonstrates the consistency of the time-averaged flow field obtained by adhering to the protocol developed for conducting the PIV experiments with the experimental setup.

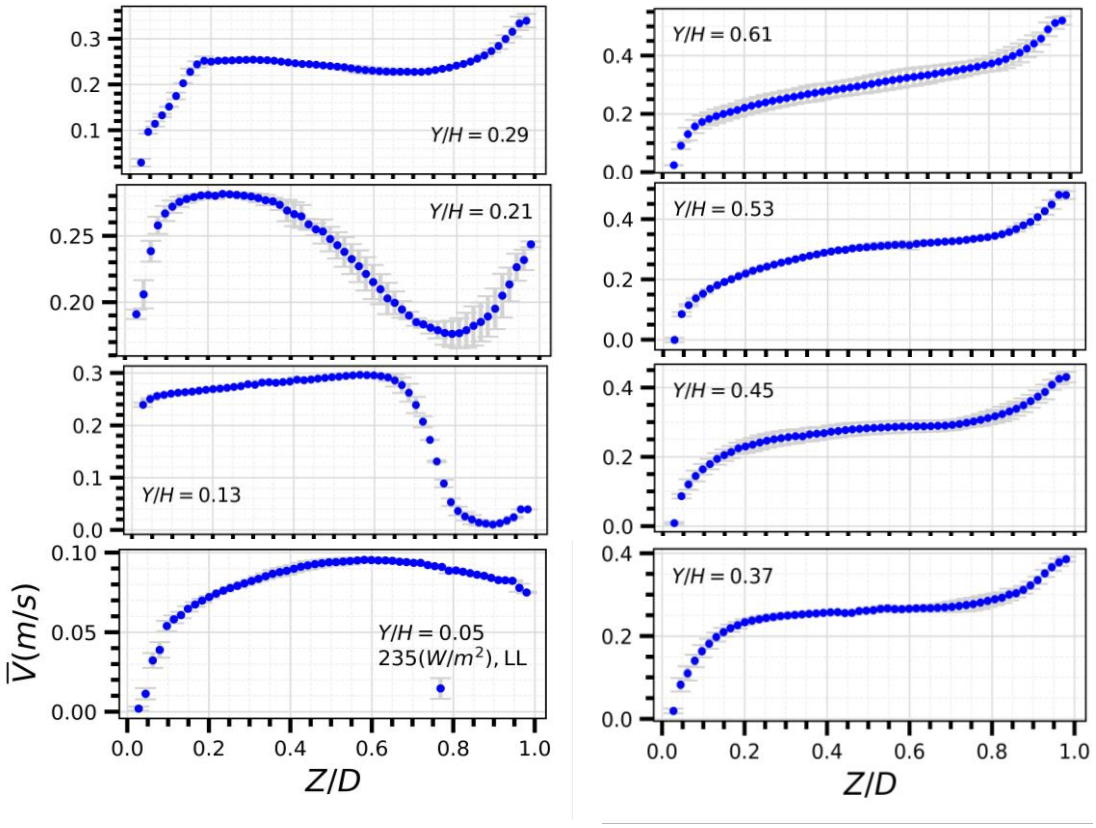


Figure 4.13: Scatterplot with error bars for tests 1 and 2 at 235 W/m²

To assess the discrepancies and uncertainty between the vertical velocity profiles of both tests, scatterplots with error bars were plotted for each of the eight locations along the height of the chimney, as illustrated in Figure 4.13. The maximum standard deviation values in the vertical velocity profiles ranged from ±0.016 m/s to ±0.031 m/s. These measurements were taken from positions spanning from Y/H = 0.05 to Y/H = 0.61 along the height of the chimney.

## 4.9 References

[1] J. Vareilles, Étude des transferts de chaleur dans un canal vertical differentiellement chauffé: application aux enveloppes photovoltaïques thermiques, 2007.

[2] S.Q. Estibaliz, Experimental investigation of thermal and fluid dynamical behavior of flows in open-ended channels. Application to Building Integrated Photovoltaic (BiPV) Systems, (n.d.).

[3] O.A. Tkachenko, V. Timchenko, S. Giroux-Julien, C. Ménézo, G.H. Yeoh, J.A. Reizes, E. Sanvicente, M. Fossa, Numerical and experimental investigation of unsteady natural convection in a non-uniformly heated vertical open-ended channel, Int. J. Therm. Sci. 99 (2016) 9–25. https://doi.org/10.1016/j.ijthermalsci.2015.07.029.

[4] F. Corvaro, M. Paroncini, An experimental study of natural convection in a differentially heated cavity through a 2D-PIV system, Int. J. Heat Mass Transf. 52 (2009) 355–365. https://doi.org/10.1016/j.ijheatmasstransfer.2008.05.039.

[5] L. Martínez-Suástegui, C. Treviño, Particle image velocimetry measurements for opposing flow in a vertical channel with a differential and asymmetric heating condition, Exp. Therm. Fluid Sci. 32 (2007) 262–275. https://doi.org/10.1016/j.expthermflusci.2007.04.003.

[6] M. Thebault, Coherent structures and impact of the external thermal stratification in a transitional natural convection vertical channel, (n.d.).

# CHAPTER 5: EXPERIMENTAL RESULTS AND DISCUSSION

## 5.1 Introduction

Most of the experimental studies reported in the literature considered boundary conditions of uniform wall temperature (UWT) and uniform heat flux (UHF) type on vertical open-ended channels having vertical inlet and outlet openings either heated asymmetrically or subjected to a one-wall uniform heat flux configuration, which have been extensively studied for the last 80 years since the pioneering work of Elenbaas in 1942 [1]. Given that configurations of open-ended vertical heated channels are pertinent to various engineering applications at different scales, ranging from the scale of electronic circuit boards to that of buildings.

But for the direct application of the solar-heated ventilation cavities like the wall solar chimney connected to the living space through a horizontal inlet air opening and a vertical outlet opening for removing the heated air inside the channel, few indoor experimental studies have been conducted in a laboratory setting on the wall solar chimney attached to the room and are reported in the literature, either symmetrically heated UWT or asymmetrically heated UHF boundary types [2–4] . None of these studies mentioned have measured the detailed thermal behaviour of the walls of chimneys for heat transfer analysis. Additionally, none of these experimental studies have quantitatively measured the two-dimensional velocity field and the associated flow structures within the entire wall solar chimney configuration along its centre plane. Furthermore, there is a lack of research linking the thermal field of the wall with the time-averaged kinematic field resulting from natural convection flow inside the L-shaped cavity. Few research works are available on a vertical channel with vertically configurated inlet and outlet openings on linking the wall thermal behaviour and kinematical distribution along the centre-plane

of the channel at low surface emissivity of walls (ε = 0.092) were carried out by [5–9] using the PIV technique, but none of these studies have completely determined the flow field in the whole channel during the experimentation. The current study aims to provide new insights into the natural convection flow and thermal fields along the walls that develop in a quasi-steady state within an L-shaped cavity. This cavity is connected to a small-scale model of a room, featuring a horizontal inlet opening duct designed for air admission from the room to the chimney cavity.

The study initially examines the impact of room position of the room air inlet on the thermal field of a chimney with low-emissive walls (ε = 0.08) under two heat flux conditions (110 W/m$^2$ and 235 W/m$^2$). It then analyses the 2D kinematic airfield within the chimney cavity along the centre plane (X/W = 0.5) for the top window (TW) and all window (AW) room air inlet configurations to evaluate their influence on solar chimney performance. Additionally, qualitative flow patterns and average temperature rise relative to incoming air stream temperature are assessed for four different room air inlet configurations to gauge their impact on room thermal comfort. The study investigates the impact of varying surface emissivity, ranging from 0.08 to 0.96, on both the active and passive walls of the chimney. Additionally, it analyses the effect of ohmic heat flux, which ranges from 110 W/m$^2$ to 235 W/m$^2$, while taking into account the (TW) opening in the reduced-scale model of the room. It examines how these factors affect the thermal fields on the chimney walls and the kinematic flow fields within the chimney air gap.

In this research work, all the results plotted have first undergone repeatability test analysis. In this regard, two tests were conducted with the same test variables to ensure accuracy and consistency. During the phase of repeatability of tests, the maximum difference in the operational wall temperature of the heated section of the active chimney

wall between the two tests was 0.2°C, while on the adiabatic section of the active wall, it did not exceed 0.9°C. Additionally, the maximum standard deviation values in the vertical velocity profiles ranged from ±0.016 to ±0.031 m/s from Y/H = 0.05 to 0.61 nondimensional height of the chimney. Therefore, the results presented in this research are the averages of thermal and kinematic data obtained from two tests under identical testing conditions. Moreover, analyses have been conducted to assess how the emissivity of wall surfaces and the ohmic heat flux influence the volume flow rate of the chimney. This also entails evaluating the mean and maximum operational wall temperature on both the active and passive walls of the chimney.

The equations (1) and (2) have been used to determine the range of modified Rayleigh number (Ra*) and global Rayleigh number (Ra) for all the cases studied:

$$Ra^* = \frac{g\,\boldsymbol{\beta}\,q''_{in}\,D^5}{VK\,\boldsymbol{\alpha}\,Y_H} \qquad (1)$$

$$Ra = \frac{g\,\boldsymbol{\beta}\,q''_{in}\,Y_H^4}{VK\boldsymbol{\alpha}} \qquad (2)$$

$$T_{film} = {}^1\!/_2\ (T_{wall,avg} + T_{inlet}) \qquad (3)$$

The Ra* values have been calculated based on the characteristic air cavity gap (D) and the inverse aspect ratio of the chimney ($D/Y_H$), The Ra values have been calculated based on the characteristic height of the heater ($Y_H$) for both non-dimensional numbers. Spatially averaged ohmic uniform heat flux entering into the chimney ($q''_{in}$) was used in the respected formulas and thermal-physical properties of the heated air in the channel, like dynamic viscosity (V), thermal conductivity (K), thermal diffusion (α), and thermal volumetric expansion coefficient (β), calculated at the film temperature ($T_{film}$) by employing equation (3). The film temperature ($T_{film}$) has been calculated for all cases

studied by utilizing the average wall temperature ($T_{wall,avg}$) obtained from the heated section of the active wall, along with the temperature of the air at the inlet of the chimney during the quasi-steady state of the test rig. The calculated value of the ($T_{film}$) have been used to find all the required thermophysical properties by using the same correlations adopted by [5–7].

Table 5.1: Electrical power, average thermal fluxes, and average Rayliegh numbers for all the tested configurations.

| $\varepsilon$ | $P_{elec}$ (W) | $q''_{elec}$ (W/m$^2$) | $q''_{loss}$ (W/m$^2$) | $q''_{in}$ (W/m$^2$) | $Ra$ | $Ra^*$ |
|---|---|---|---|---|---|---|
| LL= 0.08 | 49.3 ±2.3 | 110 ± 6 | 9.89 | 100.11 | 6.59 x10$^{11}$ | 1.89 x10$^7$ |
| LL = 0.08 | 105 ±3.3 | 235 ±10 | 17.59 | 217.41 | 1.22 x10$^{12}$ | 3.5 x10$^7$ |
| HH = 0.96 | 49.3 ±2.3 | 110 ± 6 | 6.35 | 103.65 | 7.47 x10$^{11}$ | 2.15 x10$^7$ |
| HH = 0.96 | 105 ±3.3 | 235 ±10 | 12.02 | 222.98 | 1.41 x10$^{12}$ | 4.04 x10$^7$ |

Table 5.1 presents the summary of the tested range of Rayleigh numbers: electrical power and electrical flux ($q''_{elec}$) injected into the test rig: heat flux due to the ohmic dissipation (assumed to be uniform and calculated by measuring a voltage drop and current in the circuit), conductive heat flux ($q''_{loss}$) from behind the active wall of the chimney, and thermal flux ($q''_{in}$) reaching on the heated part of the active wall of the chimney. As the emissivity of both active and passive wall chimneys increases from LL = 0.08 to HH = 0.96, the thermal flux ($q''_{in}$) reaching the active wall of the chimney rises while the conductive heat flux ($q''_{loss}$) behind the active wall decreases, at the same ohmic heat flux ($q''_{elec}$) injected into the test rig. Consequently, the magnitudes of Ra* and Ra increased with the high emissivity of the chimney walls.

The scheme of the nondimensional heights of the chimney (Y/H), where the time-averaged vertical velocity profiles and flow characteristics are examined during PIV

experiments for each tested configuration, is illustrated in Figure 5.1. For all PIV tests at low-emissive walls of chimneys (LL = 0.08), nondimensional heights of the channel marked from Y/H = 0.05 to Y/H = 0.61 are exploited for plotting velocity profiles. During the PIV data post-processing of tests at low-emissive chimney walls, in order to cope with unwanted high reflections generated by the pluses of the laser and the low definition of the flow in the boundary sub-layer near walls, 4 mm masking was applied to the passive wall of the chimney along the z-axis and 3 mm masking was applied to the active wall of the chimney. Hence, time-averaged velocity profiles and flow fields are plotted between the nondimensional chimney air gap (Z/D) from 0.03 to 0.98.

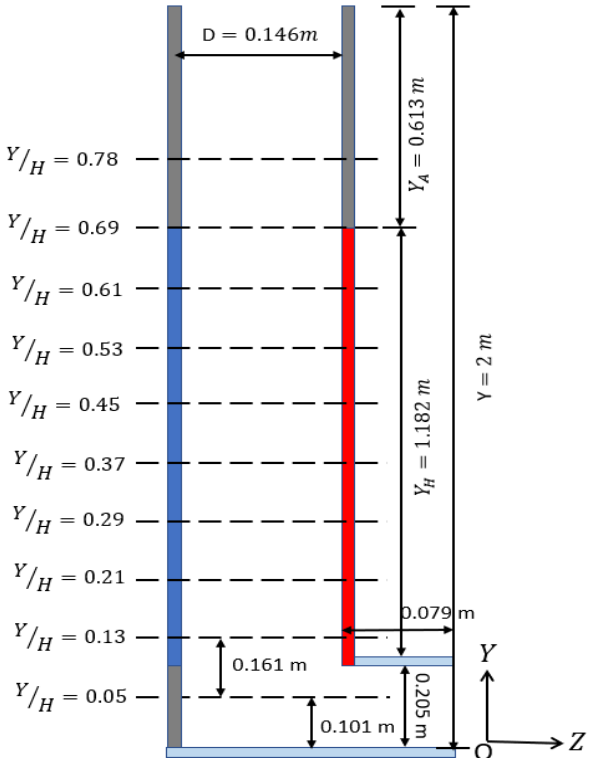


Figure 5.1: Schematics of the Streamwise PIV measurements for vertical velocity profiles.

Similarly, for all PIV tests at high emissive walls of chimney, nondimensional heights of the channel marked from Y/H = 0.05 to Y/H = 0.78 are exploited for plotting time-averaged velocity profiles. PIV data post-processing of tests at high-emissive walls of chimneys (HH = 0.96). A 7-mm mask was applied to the passive wall of the chimney

along the z-axis, and a 4 mm mask was applied to the active wall of the chimney. Hence, velocity profiles and flow fields are in the range of the nondimensional chimney air gap (Z/D) from 0.048 to 0.97.

## 5.2 Effect of Room Air Inlet

Room air inlet can play a crucial role in the effectiveness of a solar chimney, influencing both its performance, impact air temperature, and indoor air quality in a living space. In this regard, several factors of the room window can play, for instance, the type of window, its size, and its location. In this section, as illustrated in the schematic of Figure 3.2, four configurations (TW, MD, BW, and AW) of rectangular-shaped room air inlet openings equally spaced, each with a fixed area of 0.205 m x 0.375 m, are tested to study the effect of their location in the (1.48 m x 1.48 m x 1.12 m) room in terms of room air temperature and airflow movement from the room air inlet opening to the inlet of the chimney of area (0.205 m x 0.38 m) using an air smoke generator. Moreover, the effect of room air inlet placement and its aperture size on the performance of a solar chimney is analysed in terms of measuring the thermal behaviour of the walls of the chimney, time-averaged vertical velocity profiles developed inside the chimney, and lastly, the volumetric flow rate of the chimney for room air ventilation.

### 5.2.1 Thermal field on Active Wall of chimney

Operational Temperature profiles were measured along the Active wall of the chimney for four distinct room air inlet opening configurations (TW, MD, BW, and AW). These measurements were conducted at a fixed chimney aspect ratio of $Y_H/D = 8$ and a surface emissivity of $\varepsilon = 0.08$. Several tests were conducted with electrical flux injection rates of 110 W/m² and 235 W/m² for different room air inlet configurations at modified Rayleigh

numbers of 1.89 x $10^7$ and 3.5 x $10^7$. Throughout all sixteen experiments, there was a consistent maximum fluctuation of 5.5°C in the air temperature at the chimney inlet ($T_{inlet}$).

Table 5.2: Room air inlet configurations, Ohmic flux and Modified Rayliegh numbers for all the tested cases

| **No: tests** | **Cases** | **Air inlet** | $q''_{elec}$(W/**m²**) | **Ra*** |
|---|---|---|---|---|
| 2 | 1 | TW | 110± 6 | 1.89 x$10^7$ |
| 2 | 2 | MD | 110± 6 | 1.89 x$10^7$ |
| 2 | 3 | BW | 110± 6 | 1.89 x$10^7$ |
| 2 | 4 | AW | 110± 6 | 1.89 x$10^7$ |
| 2 | 1 | TW | 235± 10 | 3.5 x$10^7$ |
| 2 | 2 | MW | 235± 10 | 3.5 x$10^7$ |
| 2 | 3 | BW | 235± 10 | 3.5 x$10^7$ |
| 2 | 4 | AW | 235± 10 | 3.5 x$10^7$ |

Table 5.2 details the specifics of each case, including room air inlet configuration, associated ohmic heat flux values, and corresponding modified Rayleigh numbers for every experimental instance. Results from two tests per case, conducted at respective values of injected ohmic flux, were averaged before graphical representation in this research.

The evolution of the mean wall temperature relative to the inlet temperature is depicted in Figures 5.2(a) and (b) for all four cases of room air inlet placement on the active wall of the chimney at heat fluxes of 110 W/m² and 235 W/m². The X-axis denotes the temperature in degrees Celsius, while the Y-axis represents the nondimensional height of the chimney. These temperatures illustrate the quasi-steady state wall temperature field at the mid-width of the Active wall of the chimney (X/L = 0.5).

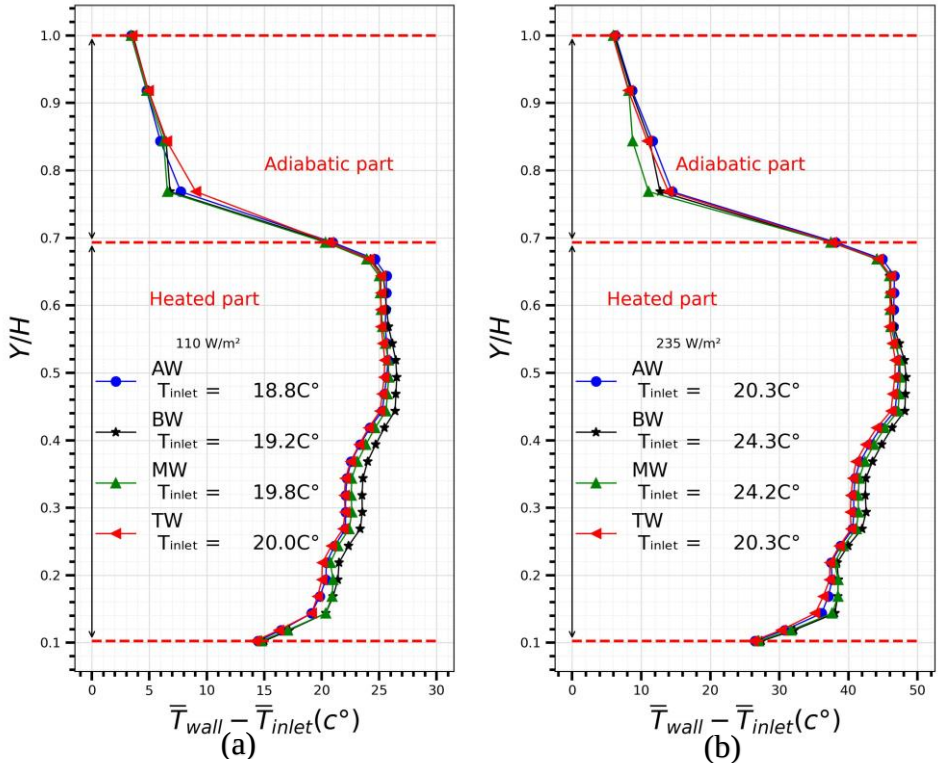


Figure 5.2: Room air inlet effect on the thermal field of the Active Wall (a) ohmic heat flux 110 W/m$^2$ and (b) 235 W/m$^2$

Figure 5.2 reveals that position of the room air inlet has no significant effect on the temperature evolution on the active wall of the chimney. Tests conducted at 110 W/m$^2$ and 235 W/m$^2$ ohmic heat fluxes exhibited consistent thermal trends in both heated and adiabatic sections. Minor variations between tests can be attributed to differences in the inlet air temperature ($T_{inlet}$) during each test. Table 5.3 outlines the mean temperature values of the local thermal field in the heated and adiabatic sections across all room air inlet configurations and heat flux levels. The average thermal field in both the heated and adiabatic sections of the chimney consistently remained at a mean value of 22.8 ± 0.18 °C and 5.51 ± 0.24 °C, respectively, across all tested cases at a heat flux of 110 W/m².

Table 5.3: Comparison of mean Active wall temperature fields at all room air inlet configurations.

| $q''_{elec}$(W/m²) | Air inlet | Mean wall thermal field (°C) (Heated part) | Mean wall thermal field (°C) (Adiabatic part) |
|---|---|---|---|
| 110 | TW | 22.7 | 5.9 |
| 110 | MW | 22.85 | 5.25 |
| 110 | BW | 23.1 | 5.43 |
| 110 | AW | 22.6 | 5.46 |
| 235 | TW | 41.7 | 9.7 |
| 235 | MW | 41.9 | 9.5 |
| 235 | BW | 42.1 | 9.6 |
| 235 | AW | 41.6 | 10.2 |

Similarly, at a heat flux of 235 W/m², the average thermal field in these sections maintained a mean value of 41.8 ± 0.19 °C and 9.75 ± 0.27 °C, respectively. Thus, it can be inferred that the placement of the room air inlet does not significantly impact the thermal performance of the chimney.

### 5.2.2 Vertical Velocity Profiles inside Chimney

To investigate the impact of the placement of the room air inlet and its aperture size on the evolution of the time-averaged kinematic field within the air cavity gap of the solar chimney. Two PIV tests were exclusively undertaken for two specific configurations of room air inlet openings, namely, AW and TW, at 235 W/m$^2$. The ohmic heat flux and surface emissivity of chimney walls were at $\varepsilon = 0.08$. This selection was made subsequent to establishing the negligible influence of room air inlet position and size on the local thermal filed on the active wall. In Figure 5.3, the time-averaged vertical velocity profiles are plotted within a transformed coordinate system for both tests at 235 W/m$^2$ ohmic heat flux, wherein the active wall of the chimney is positioned on the right side and the passive wall is situated on the left side of each graph. It is evident that the shapes of the time-

averaged vertical profiles in both tests exhibit substantial overlap across all locations along the chimney, ranging from Y/H = 0.05 to Y/H = 0.61 in the streamwise direction. The time-averaged vertical velocity profiles in the chimney illustrate one-wall heating conditions in the L-shaped cavity.

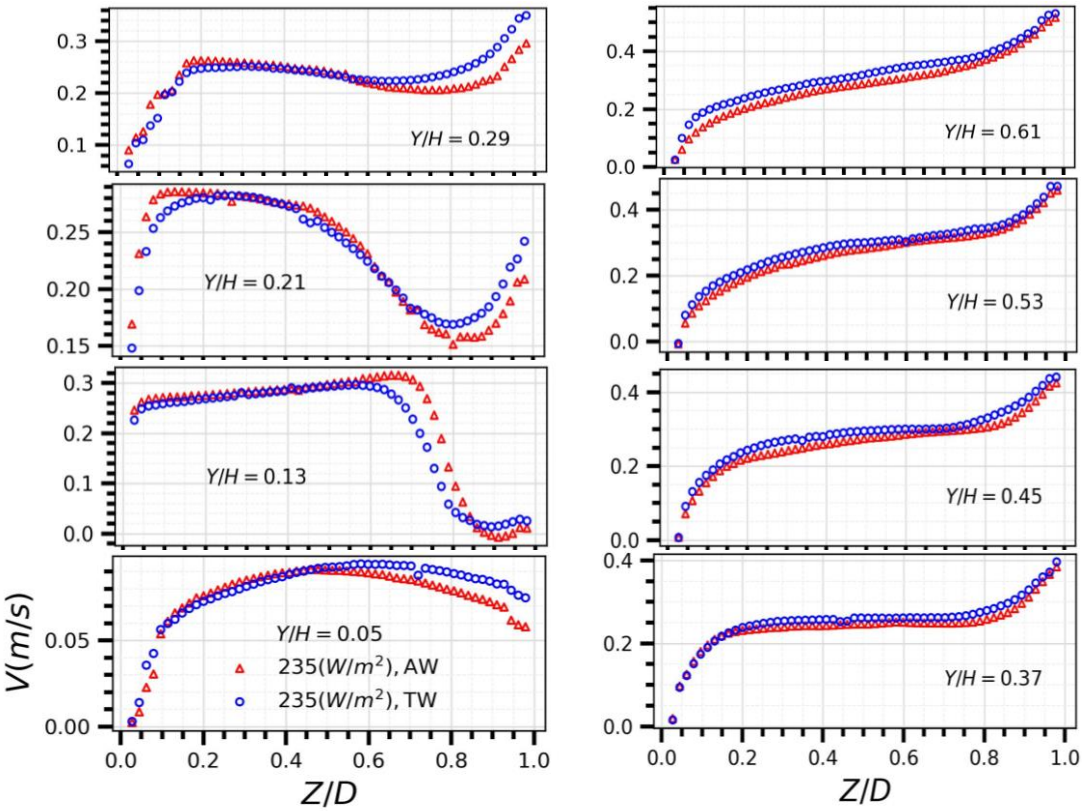


Figure 5.3:Room air inlet effect on streamwise time-averaged velocity profiles in the upwards direction of the chimney at 235 W/m$^2$ ohmic heat flux

This observation clearly indicates that the room air inlet configuration of the test rig does not exert any discernible influence on the alteration of the kinematic characteristics of the flow within the solar chimney. To quantify the impact of room air inlet configuration, Table 5.4 displays the mean values of time-averaged vertical velocity profiles for both tests. Table 5.4 clearly shows a progressive rise in average velocity profile values along the streamwise direction, increasing from Y/H = 0.05 to 0.61.

Table 5.4: Streamwise mean values of vertical velocity profiles for room air inlet configurations.

| Cases | $V_{avg}$(m/s) at (Y/H ) | | | | | | | |
|---|---|---|---|---|---|---|---|---|
| | **0.05** | **0.13** | **0.21** | **0.29** | **0.37** | **0.45** | **0.53** | **0.61** |
| AW | 0.075 | 0.229 | 0.233 | 0.228 | 0.243 | 0.264 | 0.268 | 0.268 |
| TW | 0.079 | 0.212 | 0.232 | 0.234 | 0.245 | 0.284 | 0.286 | 0.291 |

Calculations indicate a 257.3% increase for AW air inlet configuration and 268.3% for TW air inlet configuration. Thus, it can be inferred that room air inlet configurations do not impact the kinematic performance of the wall solar chimney, as evidenced by the consistent thermal fields along the chimney walls regardless of the position of room air inlet.

### 5.2.3 Chimney Airflow Rate

To calculate the mean volume flow rate out of the chimney for AW and TW room air inlet configurations, numerical integration was performed on the time-averaged vertical velocity profiles obtained from the PIV test at chimney heights (from Y/H = 0.37 to 0.61) on the chimney cavity area of (D x W) to determine the volume flow rate along the chimney sections. Subsequently, the mean volume flow rate for each respective test was calculated by averaging the volume flow rate values computed at four locations of the chimney height. Finally, a bar plot in Figure 5.4 visually presents the mean volume flow rate out of the chimney at AW and TW air inlet configurations at low emissive walls of the chimney (LL = 0.08) injected with 235 W/m$^2$ ohmic heat flux.

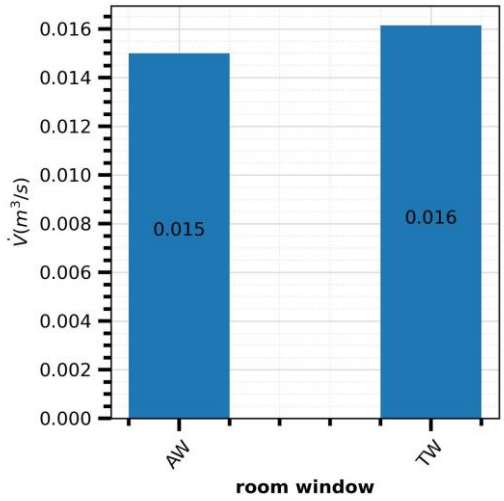


Figure 5.4: Room air inlet effect on volume flow rate.

The mean volume flow rates computed for AW and TW air inlet configurations does not show any significant difference. This suggests that the placement and the size of the room air inlet opening has no discernible impact on the ventilation performance of the wall-mounted solar chimney, given the geometric and thermal parameters used in this study. Additionally, the literature review yielded no experimental or numerical investigations comparing volume flow rates under similar conditions. However, the results of this experiment align with those of a numerical study referenced in [10], which examined a full-scale model of a wall solar chimney and similarly found no significant effect of position room air inlet on the volume flow rate out of the chimney.

### 5.2.4 Airflow Pattern and Average Room Temperature

To visualize the flow pattern in the room attached to the wall solar chimney measuring (1.48 m x 1.48 m x 1.12 m), a dense white smoke generator was utilized. The white smoke was introduced into the airflow through the room air inlet openings once the test rig attained a quasi-steady state for each of the four room air inlet configurations (TW, MW, BW, and AW). A single test was carried out for each configuration under conditions of 235 W/m$^2$ ohmic heat flux, with the surface emissivity of chimney walls at $\varepsilon = 0.08$. The

resulting smoke patterns were observed visually and are schematically depicted in Figure 5.5. The smoke tests revealed that the airflow followed a streamlined path from all the room inlet configurations to the chimney inlet. These observations clearly indicate that the airflow did not disperse entirely within the room, which is consistent with the findings of [2] regarding full-scale experimental work on wall solar chimneys. No peeling off in the smoke streamlines near the chimney inlet, as mentioned in reference [3], was observed in this research work.

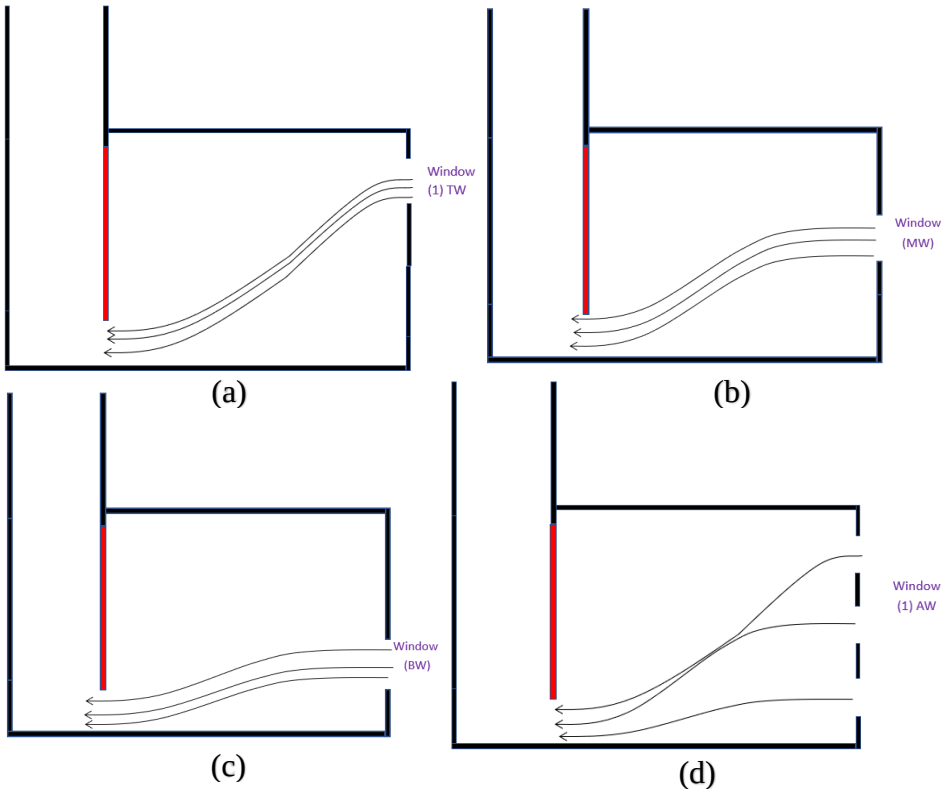


Figure 5.5: Schematic of the observed airflow patterns in the room: (a) Top window (TW) open (b) middle window (MW) open (c) bottom window (BW) open (d) and all window (AW) open.

Except for AW, the air jet consistently travelled at the same speed from the room air inlet to the chimney inlet. The decreased air speed for AW resulted from a threefold increase in the size of the room air inlet opening, allowing more air intake. This decrease in room air speed maintains mass flow rate conservation, balancing air entering the room through

air inlets and leaving via the chimney outlet. Consequently, chimney volume flow rates for both AW and TW cases remain unchanged.

Additionally, the impact of four room air inlet configurations (TW, MW, BW, and AW) on the air temperature variation within the attached room of a wall chimney at an ohmic heat flux of 235 W/m$^2$, with the chimney wall surface emissivity (ε) at 0.08, was also examined. Detailed information regarding the precise placement of the thermocouples used for air temperature measurement within the attached room can be found in Figure 3.15, presented in Chapter 3. After analysing the thermal data from all tests, it was observed that the air temperature, as measured by the thermocouples positioned in the attached room, exhibited an increase from floor to ceiling, and room air inlet openings affected this air temperature distribution inside the room. The path of the stream of air entering from the room air inlet to the inlet of the chimney showed minimum temperature values compared to readings from the adjacent thermocouples.

Table 5.5: Average room air, room air inlet and difference in air temperature for all room air inlet configurations at electrical heat flux of 235 W/m$^2$

| Air inlet | $T_{r,avg}$ (°C) | $T_{win,avg}$ (°C) | $T_{r,avg} - T_{win,avg}$ (°C) |
|---|---|---|---|
| TW | 20.91 | 20.47 | 0.44 |
| MW | 24.47 | 23.96 | 0.51 |
| BW | 24.77 | 23.98 | 0.78 |
| AW | 20.58 | 19.86 | 0.72 |

Table 5.5 presents data on average room temperature, mean air temperature at room air inlet openings, and the temperature difference between the room and air inlet openings across four room air inlet configurations. The TW and MW configurations demonstrated superior ventilation compared to others. Furthermore, upon scrutinizing the existing

literature, it is noteworthy that there is an absence of experimental or numerical data pertaining to the distribution of room air temperature during the operation of a wall solar chimney under conditions that match exactly with both the geometric and thermal parameters employed in the present experimental study. The findings of this study imply that the positioning of the room air inlet and the size of its opening may not significantly impact the performance of the wall solar chimney. However, it is observed that these factors could exert an influence on the distribution of room temperatures, consequently affecting the average air temperature within the room. This, in turn, has the potential to enhance the overall thermal comfort experienced by the inhabitants. In light of this section, the TW room air inlet position has been employed for all the tests to investigate the effect of modified Rayleigh number (Ra*) and surface emissivity in an L-shaped vertical channel.

### 5.3 Effect of the Uniform Heat Flux Injection

In this section, the wall temperature fields $\overline{\boldsymbol{T_{wall}}} - \overline{\boldsymbol{T_{inlet}}}$ on the active and passive walls of the chimney and the time-averaged velocity fields in the air cavity gap of the chimney have been investigated to examine the influence of electrical heat flux injected ($q''_{elec}$) and modified Rayleigh numbers (Ra*). The experiment involves ohmic heat flux values of 100 and 235 W/m² tested at surface emissivity of chimney walls at 0.08 and 0.96. The thermal and kinematic data were collected at the centre plane of the chimney (X/W = 0.5), with a fixed chimney aspect ratio of 8 and an extension ratio of 0.52. Throughout all experiments, the top room air inlet (TW) of the attached room was open. The study includes modified Rayleigh numbers (Ra*) of $1.89 \times 10^7$ and $3.5 \times 10^7$ for cases with low-emissivity walls in the chimney (LL = 0.08). Similarly, for cases with high-emissivity walls in the chimney (HH = 0.96), the modified Rayleigh numbers (Ra*) are $2.15 \times 10^7$

and 4.04 x $10^7$. It is noteworthy that across all tests, the temperature of the air at the inlet of the chimney ($T_{inlet}$) exhibited a maximum variation of 0.6°C.

Table 5.6: Surface emissivity, Ohmic flux, and Modified Rayliegh numbers for all the tested cases

| No: tests | Cases | $\varepsilon$ | $q''_{elec}$(W/$m^2$) | Ra* |
|---|---|---|---|---|
| 2 | 1 | LL = 0.08 | 110± 6 | 1.89 x$10^7$ |
| 2 | 2 | LL = 0.08 | 235± 10 | 3.5 x$10^7$ |
| 2 | 3 | HH = 0.96 | 110± 6 | 2.15 x$10^7$ |
| 2 | 4 | HH = 0.96 | 235± 10 | 4.04 x$10^7$ |

Table 5.6 provides a summary of the four cases, each subjected to two experimental tests. It includes the values of ohmic heat flux, the wall surface emissivity of both the active and passive walls of the chimney, and the corresponding modified Rayleigh numbers for each case. It is interesting to note that for the same magnitude of ohmic flux injected into the chimney, the modified Rayleigh number increases with higher emissive walls compared to lower emissive walls.

### 5.3.1 Thermal Behaviour of Chimney Walls

The evolution of the average wall temperature ($\overline{T_{wall}}$) minus the inlet temperature ($\overline{T_{inlet}}$) along the height of the chimney is plotted for all four cases show mentioned in Table 5.6. These temperatures represent the thermal field developed on the heated wall (active wall) of the chimney at mid-width (X/L = 0.5). To analyse the effect of ohmic heat flux ($q''_{elec}$) and modified Rayleigh number (Ra*) on the evolution of the wall thermal field, cases 1 and 2 are plotted in Figure 5.6(a), and cases 3 and 4 are plotted in Figure 5.6(b). In plots, X-axis represents the temperature difference measured in °C and Y-axis represents the nondimensional height of the chimney. The plots clearly demonstrate that the temperature of the active wall of the chimney increases with the rise in the magnitude

of ($q^{"}_{elec}$) from 110 W/m$^2$ to 235 W/m$^2$. Moreover, the plots depict similar five characteristic trends in wall thermal field for all the cases, developing along the chimney height.

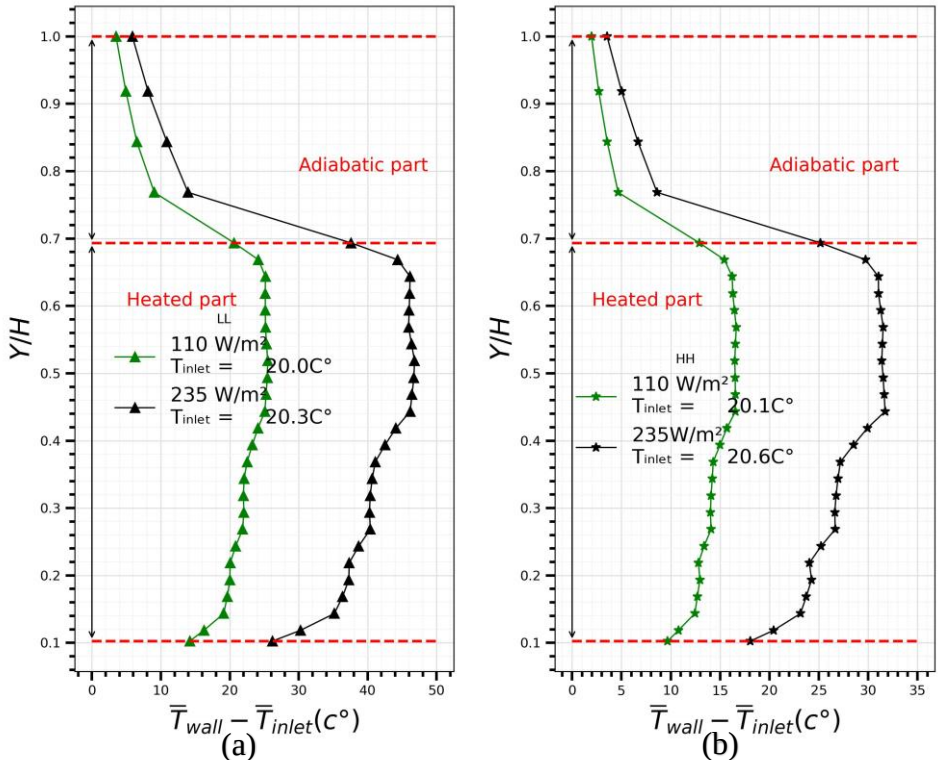


Figure 5.6: Comparison of the evolution of operational wall surface temperature with height for Active wall, between cases: (a) 1 and 2 (b) 3 and 4

Starting from the leading edge of the active wall at Y/H=0.1 to Y/H=0.14, the wall temperature field exhibits a sharp increase in all cases. Moving from Y/H=0.14 to Y/H=0.44, the wall temperature field on the active wall gradually rises with two distinct local sections alternately displaying gradual and sharp increases. Between Y/H=0.44 and Y/H=0.64, the temperature on the active wall experiences a slight decrease attributed to increased radiative transfer. From Y/H=0.64 to Y/H=0.69, the temperature on the active wall sharply decreases at the trailing edge of the heater adjacent to the adiabatic section of the chimney. In the adiabatic segment of the active wall of the chimney, spanning from Y/H=0.77 to Y/H=1, the wall thermal field decreases rapidly, although the temperature remains significantly higher than the air inlet temperature. To explain the characteristics

of the wall thermal field developed on the active wall of the chimney in a quasi-steady state, an analysis was conducted on the time-averaged flow field data obtained from Particle Image Velocimetry (PIV) tests for all four cases.

It was observed that the maximum temperature gradient localized at the leading edge of the active wall from Y/H=0.1 to Y/H=0.14 was attributed to the development of an airflow separation region caused by the interaction of airflow with the sharp corners of the active wall and bending of the airflow from the inlet of the chimney. Immediately following the separation region, spanning from Y/H=0.14 to Y/H=0.44, the airflow adjacent to the active chimney wall experiences multiple instances of attachment, detachment, and reattachment. This phenomenon leads to a consequential loss of X-momentum. Simultaneously, the air gains Y-momentum due to the heating of the air stream in contact with the active wall. This intricate interplay is identified as the root cause behind the successive localized and abrupt increases in wall temperature within this region. After the flow separation region at Y/H=0.14, the airflow stream reattaches and collides with the active wall, leading to a gradual rise in the temperature of the active wall in this local region. then at Y/H=0.22, the airflow stream, in contact with the active wall, deflects away due to a change in the X-momentum caused by the previous collision of air streams and the push of the air stream behind, resulting in a sudden increase in wall temperature in this local region. Similarly, at Y/H=0.27, the flow stream next to the active wall reattaches, causing another collision and further loss of X-momentum in the air stream, leading to a local, gradual change in wall temperature. Continuing at Y/H=0.37, the flow stream adjacent to the active wall again deflects due to the change in X-momentum caused by the previous collision of air, once again causing a sudden increase in wall temperature in this region. Finally, at Y/H=0.44, the flow stream next to the active wall reattaches, resulting in a final collision that decreases the strength of the X-

momentum in the air stream and its capacity to deflect the airflow next to the active wall of the chimney further downstream. From Y/H=0.44 to Y/H=0.64, a marginal decrease in active wall temperature is evident in all the examined cases. The velocity flow field, as observed through particle image velocity (PIV), is determined to be laminar within the chimney height. Consequently, this slight temperature reduction is solely ascribed to increased radiative heat transfer and an increased view factor of the heated part of the active wall on to the adiabatic top part of the passive wall of the chimney. From Y/H=0.64 to Y/H=0.69, a sharp drop in the active wall temperature is observed in all tested cases. This drop is primarily attributed to conductive heat losses in the Y-direction, originating from the trailing edge of the heater into the adjacent adiabatic top on the active wall of the chimney. Additionally, it is partly due to increased radiative heat loss to the adiabatic top part on the passive wall of the chimney. Lastly, in the section ranging from Y/H=0.77 to Y/H=1, the temperature of the active wall in the adiabatic part sharply decreases with respect to the height. However, it is observed that the temperature of the wall in this section is significantly higher than the ambient air temperature. The pattern and magnitude of the temperature rise in the adiabatic part of the active wall provide a clear indication of conductive heating along the Y-axis from the trailing edge of the heater, partly due to natural convection heat transfer from the heated air of the chimney in contact with the adiabatic part of the active wall.

To quantify the effect of ohmic heat flux ($q''_{elec}$) on the development of characteristic trends and evolution of wall thermal field, the difference in operational wall temperature has been calculated between the start to end of each characteristic trend observed in the evolution of wall surface thermal field, and the results are presented in Table 5.7.

Table 5.7: Summary of evolution of operational active wall surface temperature in between five distinctive trends for all cases

| Cases | $\Delta(\overline{T_{wall}} - \overline{T_{inlet}})$ | | | | |
|---|---|---|---|---|---|
| | **Y/H=0.1 & 0.14** | **Y/H=0.14 & 0.44** | **Y/H=0.44 & 0.64** | **Y/H=0.64 & 0.69** | **Y/H=0.77 & 1** |
| 1 | 5.5°C | 6.3°C | -0.03°C | -4.8 °C | -17.5°C |
| 2 | 9°C | 10.4°C | -0.12°C | -8.5°C | -31.2°C |
| 3 | 2.7°C | 4.2°C | -0.31°C | -3.3°C | -10.8°C |
| 4 | 5°C | 8.5°C | -0.62°C | -5.8°C | -21.8°C |

The magnitude of Ohmic heat flux and emissivity of the surface walls, significantly influence the characteristic trends and the development of the wall thermal field. The wall temperature field between the 1st and 2nd trends on the active wall shows an increase of 63.6% and 65% from Case 1 to 2, and an 85.1% and 102.3% increase from Case 3 to 4. In contrast, the wall thermal field between the 3rd and 4th trends experiences a decrease of 300% and 77% from Case 1 to 2, and a decrease of 100% and 75.7% from Case 3 to 4. Similarly, the wall thermal field between the 5th trend on the adiabatic part of the active wall shows a decrease of 78% from Case 1 to 2 and a decrease of 101.8% from Case 3 to 4. Additionally, the average and maximum operational wall temperatures were analysed across all cases. This investigation included the heated and adiabatic sections of the active chimney wall. The relevant data is summarized in Table 5.8.

From Case 1 to Case 2, the average operational wall temperature on the heated section of the active wall increased by 19°C, marking an 84% rise due to the increased heat flux. Likewise, in Cases 3 to 4, the average operational wall temperature on the heated part of the active wall rose by 13°C, representing an 89.6% increase. Moreover, the maximum operational wall temperature surged by 21.4°C from Case 1 to Case 2, reflecting an 84.2% increase, and by 15.1°C from Case 3 to Case 4, indicating a 90.6% rise.

Table 5.8: Summary of average, maximum, inlet, and outlet operational wall temperature on active wall for all cases

| Cases | $\overline{\overline{T_{wall}}} - \overline{T_{inlet}}$ (°C) heated part ( Y/H=0.1 to 0.69 ) | $\overline{T_{wall,max}} - \overline{T_{inlet}}$ (°C) heated part ( Y/H=0.1 to 0.69 ) | $\overline{\overline{T_{wall}}} - \overline{T_{inlet}}$ (°C) Adiabatic part ( Y/H=0.77 to 1) | $\overline{T_{wall,inlet}} - \overline{T_{inlet}}$ (°C) at ( Y/H=0.1 ) | $\overline{T_{wall,outlet}} - \overline{T_{inlet}}$ (°C) at ( Y/H=1 ) |
|---|---|---|---|---|---|
| 1 | 22.4°C | 25.4°C | 5.9°C | 14.7°C | 3.4°C |
| 2 | 41.2°C | 46.8°C | 9.7°C | 26.2°C | 5.8°C |
| 3 | 14.5°C | 16.6°C | 3.2°C | 9.7°C | 1.9°C |
| 4 | 27.5°C | 31.7°C | 5.9°C | 18°C | 3.5°C |

Additionally, the average operational wall temperature on the adiabatic part of the active wall rose by 3.8°C, demonstrating a 64% increase from Case 1 to Case 2, and by 2.7°C from Case 3 to Case 4, signifying an 84.3% rise. Similarly, operational inlet and outlet wall temperatures on the active wall increased by 11.5°C (78.2%) and 2.4°C (70.6%), respectively, from Case 1 to Case 2. These values increased by 8.3°C (85.6%) and 1.6°C (84.2%), respectively, from Case 3 to Case 4.

The evolution of the average wall temperature ($\overline{\overline{T_{wall}}}$) minus the inlet temperature ($\overline{T_{inlet}}$) along the non-heated wall (passive wall) of the chimney is also plotted for all four cases. These temperatures represent the thermal field of the wall in °C developed at the mid-width of the chimney (X/L = 0.5) along the non-dimensional height of the chimney. To assess the influence of ($q''_{elec}$) and (Ra*) on the progression of the thermal field along the height of the passive wall of the chimney, cases 1 and 2 are plotted in Figure 5.7(a), while cases 3 and 4 are plotted in Figure 5.7(b). In plots, X-axis represents the temperature difference measured in °C and Y-axis represents the nondimensional height of the chimney. The plots illustrate that as the modified Rayleigh number increases in all cases, the temperature on the passive wall also rises. A unique characteristic pattern

for operational wall temperature is developed for both low-emissive and high-emissive wall cases.

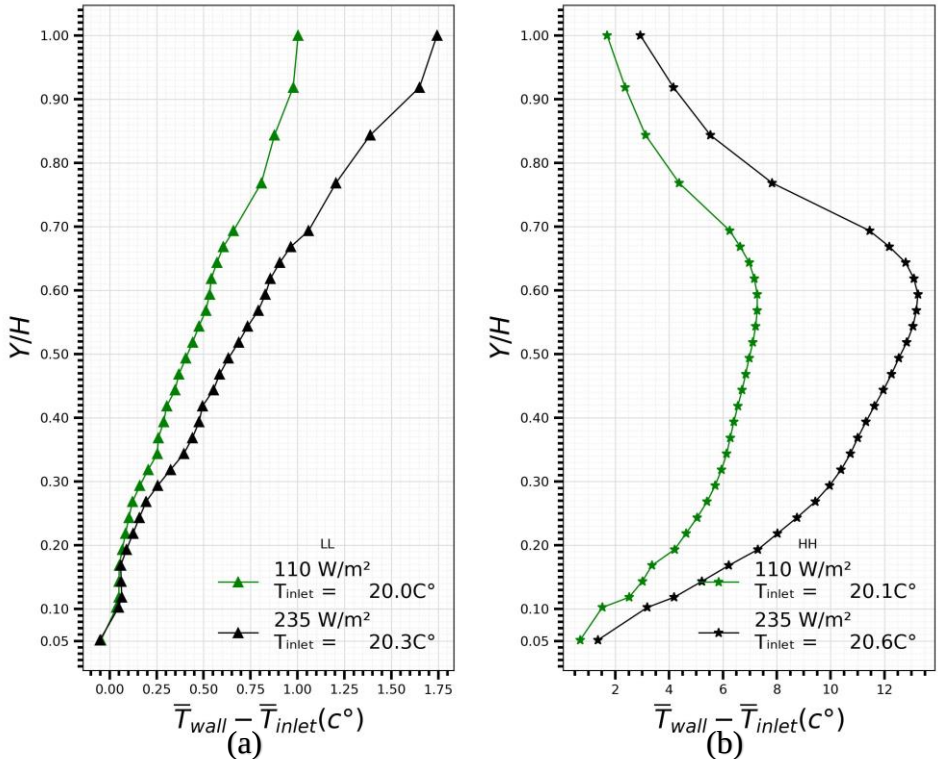


Figure 5.7: Comparison of the evolution of operational wall surface temperature with height for passive wall, between cases: (a)1 and 2 (b) 3 and 4

Despite the low surface emissivity of the chimney walls in cases 1 and 2, radiation remains the only mode of heat transfer to the passive chimney wall within the tested range of ohmic heat flux. The thermal field starts to develop at nearly the operational wall temperature of 0 °C, from Y/H = 0.05 to 0.1. Subsequently, it gradually rises, reaching the maximum operational wall temperatures of 0.5°C and 1.64°C for cases 1 and 2, respectively, at Y/H = 1. The results show a gradual evolution of surface temperature along the height of the passive chimney wall, even at low-emissive walls of the chimney. The rate of increase in the temperature of the passive wall is also found to be dependent on the modified Rayleigh number. In Case 1, the average operational wall temperature rises by 0.3°C, with a maximum increase of 1°C. In Case 2, the average operational wall temperature increases by 0.5°C, reaching a maximum rise of 1.64°C.

For cases 3 and 4, the operational surface temperature field on the passive wall shows characteristics typical of a heated wall. Consequently, radiation exchanges result in a shift in the thermal conditions of the chimney from one-wall heating to asymmetric heating. The operational wall temperature on the passive wall for cases 3 and 4 evolves from 0.7°C and 1.4°C, respectively, at Y/H = 0.05. The operational wall temperature varies significantly with both increased chimney height and electrical heat flux ($q''_{elec}$). The highest operational wall temperatures for Cases 3 and 4 reached 7.3°C and 13.3°C, respectively, at Y/H = 0.59. Subsequently, temperatures gradually decrease from Y/H = 0.59 to Y/H = 0.69 due to the reduced view factor between the heated part of the active wall on the passive wall of the chimney. Beyond Y/H = 0.69, there was a sharp decline in temperature on the passive wall due to a drop in temperature in the adiabatic part of the active wall and less radiation reaching the passive wall of the chimney. Consequently, for Cases 3 and 4, at Y/H = 1, the operational wall surface temperature dropped to 1.7°C and 2.9°C, respectively.

During the repeatability analysis of Cases 1 and 2, it was observed that the evolution of wall temperature on the passive wall was influenced by ambient room temperature, given the proximity of the passive wall temperature to the ambient temperature. Conversely, in Cases 3 and 4, changes in ambient temperature had no significant impact, as the temperature of the passive wall was notably higher.

Furthermore, the mean and maximum operational temperatures of the passive wall are calculated to evaluate the effect of injected ohmic heat flux ($q''_{elec}$) on both low-emissive and high-emissive wall scenarios. These results are presented in Table 5.9.

Table 5.9: Summary of average, maximum and outlet surface temperature on passive wall for all cases

| Cases | $\overline{\overline{T_{wall}} - \overline{T_{inlet}}}$ (°C) | $\overline{T_{wall,max}} - \overline{T_{inlet}}$ (°C) | $\overline{T_{wall,inlet}} - \overline{T_{inlet}}$ (°C) | $\overline{T_{wall,outlet}} - \overline{T_{inlet}}$ (°C) |
|---|---|---|---|---|
| | Passive wall ( Y/H=0.05 to 1 ) | | at ( Y/H=0.05 ) | at ( Y/H=1 ) |
| 1 | 0.3°C | 1°C | 0°C | 1°C |
| 2 | 0.5°C | 1.64°C | 0°C | 1.64°C |
| 3 | 5.2°C | 7.3°C | 0.7°C | 1.7°C |
| 4 | 9.2°C | 13.2°C | 1.4°C | 2.9°C |

By comparing cases 1 and 2, the average and maximum operational wall temperatures on the passive wall increased by 0.2°C (66.6%) and 0.64°C (64%), respectively, with the rise in ($q^{"}_{elec}$) from 110 W/m$^2$ to 235 W/m$^2$. Similarly, for cases 3 and 4, the average and maximum wall temperatures on the passive wall increased by 3.7°C (67.2%) and 5.5°C (80.8%), respectively. The operational inlet wall temperature on the passive wall for cases 1 and 2 remains zero and remains at zero up to Y/H = 0.1 within the tested range of ($q^{"}_{elec}$). In contrast, from cases 3 to 4, the inlet operational wall temperature increased by 0.7°C (100% rise). The value of the operational outlet wall temperature on the passive wall increased by 0.64 °C (64%), from cases 1 to 2, and by 1.2 °C (70.6%), from cases 3 to 4.

### 5.3.2 Analysis of Vertical velocity Profiles

To investigate the impact of electrical heat flux and modified Rayleigh number on the time-averaged kinematic airflow field within a chimney with low-emissive walls, 2D PIV flow field data were gathered for cases 1 and 2 at the mid-width of the chimney (X/L = 0.5) along the central plane of the air cavity gap (from Z/D = 0.027 to 0.98). Subsequently, the time-averaged vertical velocity profiles are plotted within a transformed coordinate system for both cases, wherein the active wall of the chimney is

positioned on the right side of each graph and the passive wall is situated on the left side of each graph. The X-axis in the plots represents the nondimensional chimney air cavity gap, and the Y-axis represents the time-averaged vertical velocity distribution. Figure 5.8 depicts the evolution of the vertical velocity field along the height of the chimney in the streamwise direction, ranging from Y/H = 0.05 to Y/H = 0.61 at consistent intervals of Y/H = 0.0805.

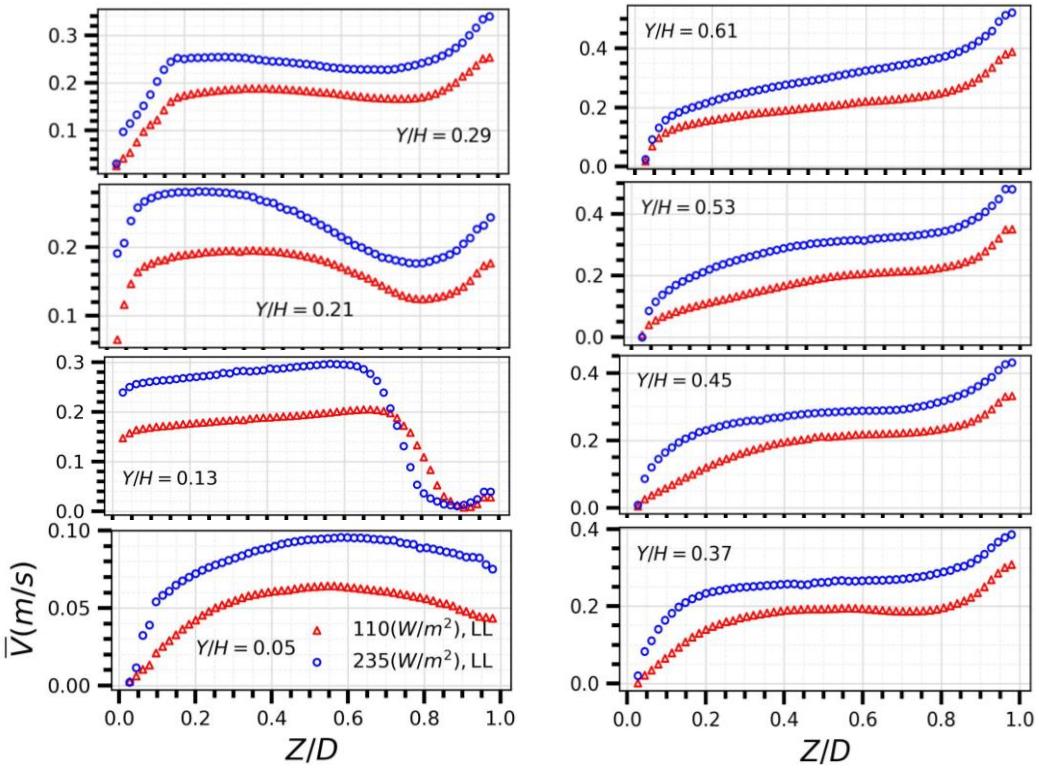


Figure 5.8: Streamwise time averaged vertical velocity profiles in the upwards direction of the chimney for Case1 and 2.

The time-averaged vertical velocity profiles illustrate the conditions of one-wall heating in the vertical channel. Furthermore, the effect of the horizontal inlet opening of the channel on the development of the time-averaged vertical velocity profiles can be observed from a height of Y/H = 0.05 to 0.29 in the channel. As the modified Rayleigh numbers (Ra*) escalate from 2.1.89 x $10^7$ to 4.04 x 3.5 x $10^7$ due to an increase in ohmic heat injection from 110 W/$m^2$ to 235 W/$m^2$, the magnitude of the time-averaged vertical

velocity field increases. Meanwhile, the profiles maintain a consistent shape at the corresponding location across all graphs.

At a height of Y/H = 0.05, air enters the chimney through the inlet opening, resulting in a non-zero velocity on the right side of the graph. At a height of Y/H = 0.1, a flow separation region forms upstream, causing a slight drop in vertical velocity on the right side of the graph at Y/H = 0.05. Additionally, an air recirculation zone forms at the corner of the passive wall, leading to a sharp decrease in vertical velocity, which reaches zero before reaching the passive wall. Consequently, the vertical velocity profile resembles a broken parabolic shape.

At a height of Y/H = 0.13, the vertical velocity increases as flow develops within the chimney. Near the active wall, velocity remains stagnant due to the formation of a flow detachment region from Y/H = 0.1 to 0.14. At Y/H = 0.13, some airflow glides over the separation region, while most is directed towards the passive wall. Consequently, no obvious signs of heating of the air in contact with the active wall are observed in this region. Vertical velocity is lowest on the right side due to the flow separation region. As air moves away from this region, velocity increases uniformly but decreases near the passive wall, reaching zero due to the no-slip boundary condition.

At a height of Y/H = 0.21, the air stream attaches to the active wall of the chimney, resulting in a velocity peak close to the wall due to the heating of the air in contact with it. Velocity drops thereafter up to an air cavity gap of Z/D = 0.8, due to a decrease in the temperature of the air. Between the air cavity gap from Z/D = 0.4 to 0.8, the downstream flow separation region on the active wall causes a drop in velocity upstream. However, the velocity increases again near the passive wall of the chimney due to some unimpeded

airflow being deflected towards the passive wall, and then airflow decreases again due to the wall shear effect of the passive wall.

At the height of Y/H = 0.29, the peak velocity near the active wall continues to rise as the air density decreases in contact with the active wall, promoting a more dominant flow from the active wall of the chimney. The effects of the downstream flow separation region and the horizontal inlet opening are still noticeable in this region. Beyond this height, the flow stream nearly loses x-momentum, and the velocity profiles start to resemble those of a one-wall heated vertical channel. Finally, from Y/H = 0.37 to 0.61, velocity profiles undergo evolution in the streamwise direction, with the peak velocity near the active wall increasing in magnitude.

Similarly, to investigate the impact of electrical heat flux and modified Rayleigh number on the time-averaged kinematic airflow field within a chimney with high-emissive walls, PIV flow field data were gathered for cases 3 and 4 at the mid-width of the chimney (X/L = 0.5) along the central plane of the air cavity gap (from Z/D = 0.048 to 0.97). Subsequently, the time-averaged vertical velocity profiles are plotted within a transformed coordinate system for both cases, wherein the active wall of the chimney is positioned on the right side of each graph and the passive wall is situated on the left side of each graph. The X-axis in the plots represents the nondimensional chimney air cavity gap, and the Y-axis represents the time-averaged vertical velocity distribution. Figure 5.9 depicts the evolution of the vertical velocity field along the height of the chimney in the streamwise direction, ranging from Y/H = 0.05 to Y/H = 0.78 at consistent intervals of Y/H = 0.0805.

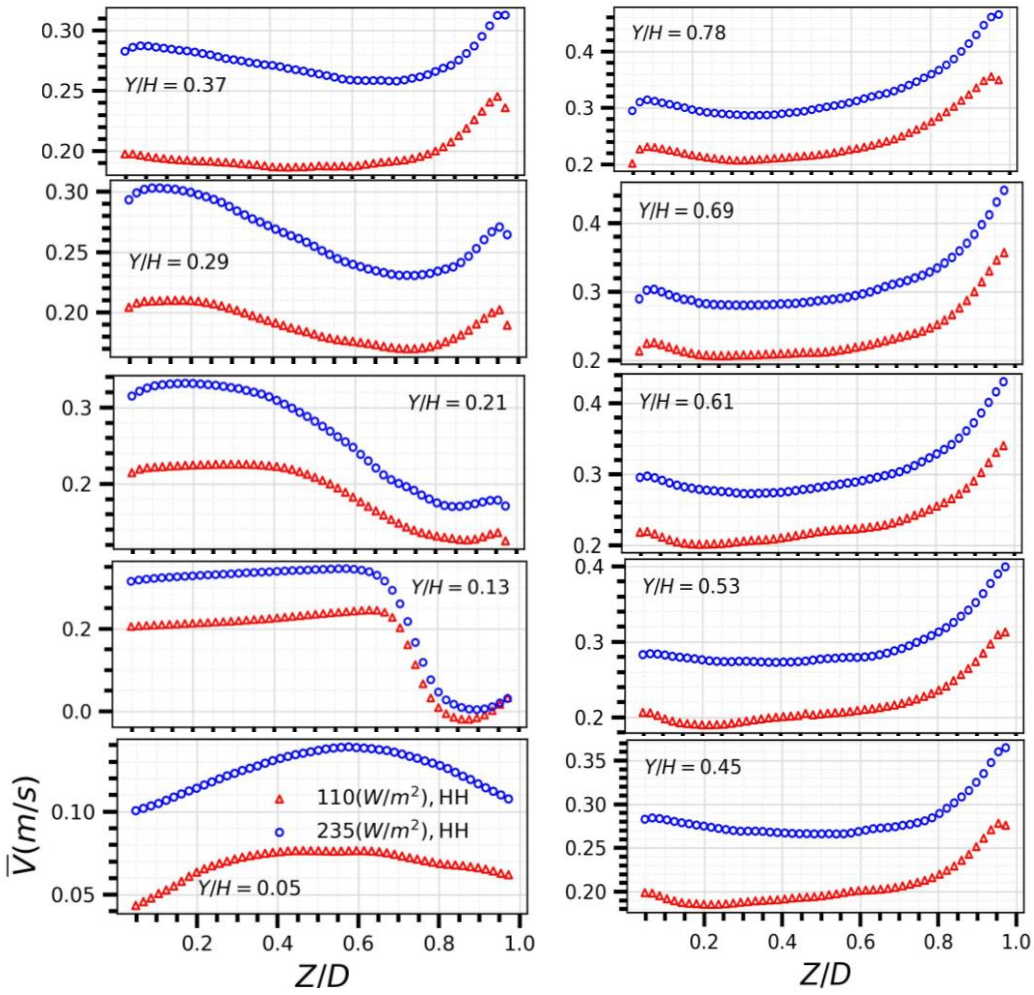


Figure 5.9: Streamwise time averaged vertical velocity profiles in the upwards direction of the chimney for Case 3 and 4.

The time-averaged vertical velocity in the chimney reveals asymmetrical heating conditions between the active and passive walls. As the ($q''_{elec}$) increases from 110 W/m$^2$ to 235 W/m$^2$, the time-averaged vertical velocity field rises, while the shape of the profiles remains unchanged at the same location in each graph. Similar to Cases 1 and 2, the influence of the horizontal inlet opening of the chimney on the development of vertical velocity profiles is evident in the chimney height, ranging from Y/H 0.05 to 0.29.

At a height of Y/H = 0.05, air enters the chimney through the inlet opening, resulting in a non-zero velocity on the right side of the graph. At a height of Y/H = 0.1, a flow separation region forms upstream, and the wall shear effect on the leading edge of the

active wall causes a slight drop in vertical velocity on the right side of the graph at Y/H = 0.05. In contrast to cases 1 and 2, the size of the air recirculation region at the corner of the passive wall decreases in velocity profile for cases 3 and 4. Hence, the velocity gradually diminishes to zero at the passive wall of the chimney due to the wall shear effect. Consequently, the vertical velocity profile resembles a parabolic shape.

At a height of Y/H = 0.13, the vertical velocity increases as flow develops within the chimney. Near the active wall, velocity remains stagnant due to the formation of a flow detachment region from Y/H = 0.1 to 0.14. At Y/H = 0.13, some airflow glides over the separation region, while most is directed towards the passive wall. As a result, no obvious signs of air heating are observed from the active wall of the chimney in this region, but the passive wall indicates signs of air heating upon contact. Hence, the vertical velocity is lowest on the right side due to the flow separation region. As air moves away from this region, the velocity remains uniform but decreases near the passive wall, eventually reaching zero due to the wall shear effect.

At a height of Y/H = 0.21, the air stream attaches to the active wall of the chimney, resulting in a velocity peak close to the wall due to the heating of the air in contact with it. The velocity drops thereafter up to an air cavity gap of Z/D = 0.8, due to a decrease in the temperature of the air. Between the air cavity gap from Z/D = 0.4 to 0.8, the downstream flow separation region on the active wall causes a drop in velocity upstream. However, the velocity increases again near the passive wall of the chimney due to some unimpeded airflow being deflected towards the passive wall as well as the heating of air from the passive wall of the chimney. The velocity eventually decreases again due to the wall shear effect of the passive wall.

At the height of Y/H = 0.29, the peak velocities near the active and passive walls continue to rise as the air density decreases in contact with the active and passive walls of the chimney, indicating fully developed flow. The effects of the downstream flow separation region and the horizontal inlet opening are still noticeable in this region. Beyond this height, the flow stream nearly loses x-momentum, and the velocity profiles start to resemble those of an asymmetrically heated vertical channel. From Y/H = 0.37 to 0.69, velocity profiles undergo evolution in the streamwise direction, with the peak velocities near the active and passive walls increasing in magnitude. Lastly, at the height of Y/H = 0.78 in the adiabatic part of the chimney, the peak velocities near the active and passive walls show a slight increase, and the vertical velocity profile continues to evolve in the chimney.

To further analyse the effect of the ohmic heat flux ($q''_{elec}$) injected from the active wall of the chimney on the low and high emissive walls of the chimney, the mean vertical velocities have been calculated from vertical velocity profiles for all tested cases along the height of the chimney. The results are highlighted in Table 5.10 to showcase the average flow development.

Table 5.10: Streamwise mean values of vertical velocity profiles for all cases.

| | $\overline{V_{avg}}$ (m/s) at (Y/H ) | | | | | | | | | |
|---|---|---|---|---|---|---|---|---|---|---|
| **Cases** | **0.05** | **0.13** | **0.21** | **0.29** | **0.37** | **0.45** | **0.53** | **0.61** | **0.69** | **0.78** |
| 1 | 0.05 | 0.15 | 0.165 | 0.169 | 0.174 | 0.188 | 0.18 | 0.2 | - | - |
| 2 | 0.08 | 0.213 | 0.234 | 0.234 | 0.255 | 0.272 | 0.29 | 0.299 | - | - |
| 3 | 0.068 | 0.168 | 0.186 | 0.190 | 0.197 | 0.206 | 0.217 | 0.231 | 0.234 | 0.242 |
| 4 | 0.124 | 0.252 | 0.261 | 0.264 | 0.274 | 0.283 | 0.294 | 0.303 | 0.311 | 0.326 |

The mean vertical velocity profile increases from Y/H = 0.05 to 0.61 by 300% for case 1, 237.8% for case 2, 239% for case 3, and 144.3% for case 4. Specifically, at Y/H = 0.05,

there is a 60% increase from case 1 to case 2, and an 82% increase from case 3 to case 4. Conversely, at Y/H = 0.61, the mean vertical velocity profile shows a 49.5% rise from cases 1 to 2 and a 31.16% rise from cases 3 to 4.

Moreover, to further analyse the effect of the ohmic heat flux ($q''_{elec}$) injected from the active wall of the chimney on the low and high emissive walls of the chimney, the increase in peak vertical velocity along the height of the active wall of the chimney across all tested cases is presented in Table 5.11.

Table 5.11: Streamwise Peak values of vertical velocity profiles on active wall for all cases

| | $\overline{V_{peak}}$ (m/s) at (Y/H ) | | | | | | | | | |
|---|---|---|---|---|---|---|---|---|---|---|
| **Cases** | **0.05** | **0.13** | **0.21** | **0.29** | **0.37** | **0.45** | **0.53** | **0.61** | **0.69** | **0.78** |
| 1 | - | - | 0.176 | 0.252 | 0.308 | 0.331 | 0.35 | 0.387 | - | - |
| 2 | - | - | 0.234 | 0.339 | 0.385 | 0.43 | 0.48 | 0.52 | - | - |
| 3 | - | - | 0.136 | 0.2 | 0.245 | 0.278 | 0.312 | 0.34 | 0.357 | 0.355 |
| 4 | - | - | 0.178 | 0.27 | 0.312 | 0.364 | 0.399 | 0.43 | 0.447 | 0.465 |

The percentage increase in the peak velocity value near the active wall is calculated from Y/H = 0.21 to 0.61 for all cases. For Case 1, the increase in the peak value of the vertical velocity was calculated at 54.5%. In Case 2, this value rose to 114%, while in Case 3, it reached 150%, and in Case 4, it was 141.5%. From Case 1 to Case 2, there was a 38% increase in the peak value of the vertical velocity profile at Y/H = 0.21. Similarly, for Case 3 to Case 4, this increase was 30.8%. At Y/H = 0.61, the peak value of the vertical velocity profile increased by 34.3% from Case 1 to Case 2 and by 26% from Case 3 to Case 4.

## 5.4 Effect of Surface Emissivity of Chimney Walls

In this section, an experimental investigation is carried out to examine the influence of surface emissivity on natural convection flow within a one-wall heated L-shaped vertical channel with a fixed aspect ratio of 8. During the experiment, the emissivity of both the active and passive walls of the chimney was tested at values of 0.08 and 0.96 under ohmic heat fluxes of 110 W/m² and 235 W/m². The operational wall temperature was measured on both the active and passive walls of the chimney, and time-averaged vertical velocity profiles were measured at the mid-width (X/W = 0.5) of the chimney. To visualize the effect of changing wall surface emissivity under similar heat flux, Case 1 was compared to Case 3, and Case 2 was compared to Case 4. The experimental details for each case are provided in Table 5.6.

### 5.4.1 Thermal Behaviour of Chimney Walls

To analyse the impact of the surface emissivity of the chimney walls on the evolution of the wall thermal field ($\overline{\boldsymbol{T_{wall}}} - \overline{\boldsymbol{T_{inlet}}}$ ) along the height of the active wall. Case 1 is plotted against Case 3 in Figure 5.10(a), and Case 2 and 4 are plotted in Figure 5.10(b). In these plots, the X-axis represents the temperature difference measured in °C, while the Y-axis represents the nondimensional height of the chimney. The results clearly demonstrate that the temperature of the active wall of the chimney decreases as the surface emissivity of the chimney walls increases.

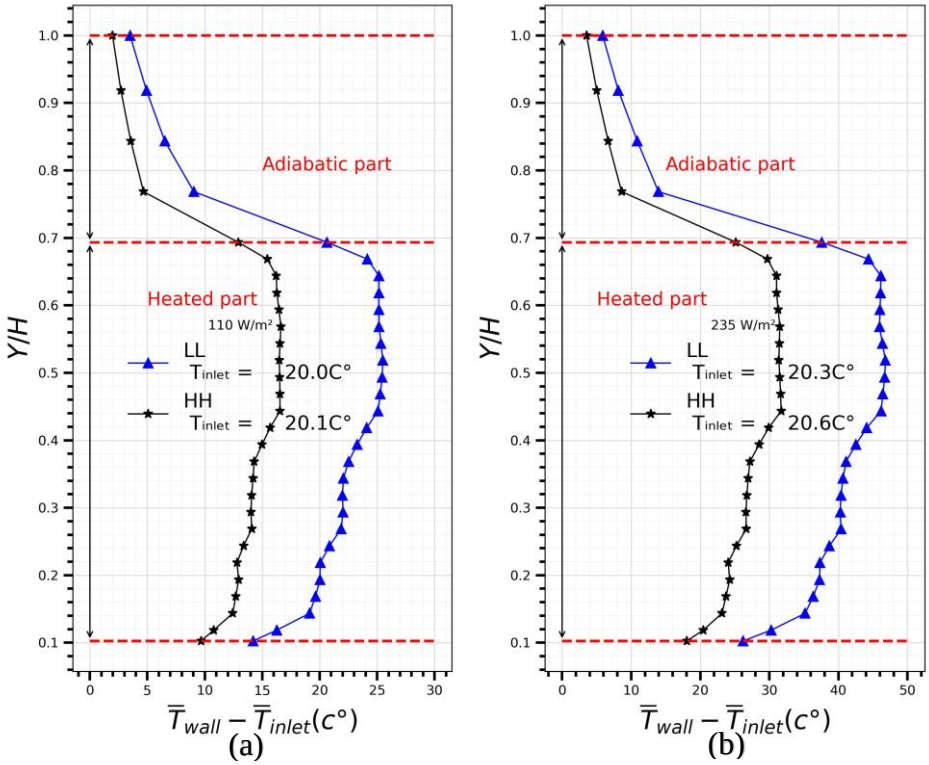


Figure 5.10: Comparison of the evolution of operational wall surface temperature with chimney height for Active wall, between cases: (a) 1 and 3 (b) 2 and 4

To assess the impact of variations in the surface emissivity of the chimney wall at ohmic heat fluxes of 110 W/m² and 235 W/m², the differences between the average and maximum wall temperatures and the inlet air temperature were calculated. These calculations were performed for both the heated and adiabatic sections of the active wall. Additionally, the operational temperatures of the active wall at the inlet of the chimney and outlet were determined for all cases, as shown in Table 5.8. From Case 1 to Case 3, the operational wall temperature on the heated section of the active wall decreased by 8.2°C, representing a 36.6% drop. Similarly, in Cases 2 to 4, the average operational wall temperature on the heated part of the active wall decreased by 13.7°C, constituting a 33.2% drop. Furthermore, the maximum operational wall temperature decreased by 8.8°C (34.6%) from Case 1 to Case 3 and by 15.1°C (32.3%) from Case 2 to Case 4. The average operational wall temperature on the adiabatic part of the active wall (from Y/H = 0.77 to 1) decreased by 2.7°C (45.7%) from Case 1 to Case 3. From Case 2 to Case 4, it decreased

by 3.8°C (39.1%). Similarly, the operational inlet and outlet wall temperatures on the active wall decreased by 5°C (34%) and 1.5°C (44.1%), respectively, from Case 1 to Case 3. From Case 2 to Case 4, these values decreased by 8.2°C (31.2%) and 2.3°C (39.6%), respectively.

To analyse the impact of surface emissivity on the thermal field evolution along the height of the passive chimney wall, Case 1 and Case 3 are plotted together as shown in Figure 5.11(a). Additionally, Cases 2 and 4 are plotted together, as illustrated in Figure 5.11(b). In these plots, the X-axis represents the temperature difference in °C, and the Y-axis represents the nondimensional height of the chimney. The results clearly demonstrate that the temperature of the passive chimney wall increases significantly with higher surface emissivity. At high surface emissivity (HH = 0.96), the passive wall becomes thermally active and enhances wall-to-wall radiative heat transfer. Consequently, both convection and radiation become the dominant modes of heat transfer to the air. In contrast, at low emissivity, the passive wall does not participate in wall-to-wall radiative heat transfer, making convection the only dominant mode of heat transfer to the air in the chimney.

To assess the effect of changing the surface emissivity of the chimney wall under ohmic heat fluxes of 110 $W/m^2$ and 235 $W/m^2$, the average, maximum, inlet, and outlet operational wall temperatures are computed for each case and are presented in Table 5.9. From Case 1 to Case 3, there was a 4.9°C increase in the average operational wall temperature on the passive wall, representing a 1633% rise. Similarly, from Cases 2 to 4, the average operational wall temperature on the passive wall increased by 8.7 °C, constituting a 1740% increase. Furthermore, the maximum operational wall temperature increased by 6.3°C (630%) from Case 1 to Case 3 and by 11.56°C (704.8%) from Case 2 to Case 4.

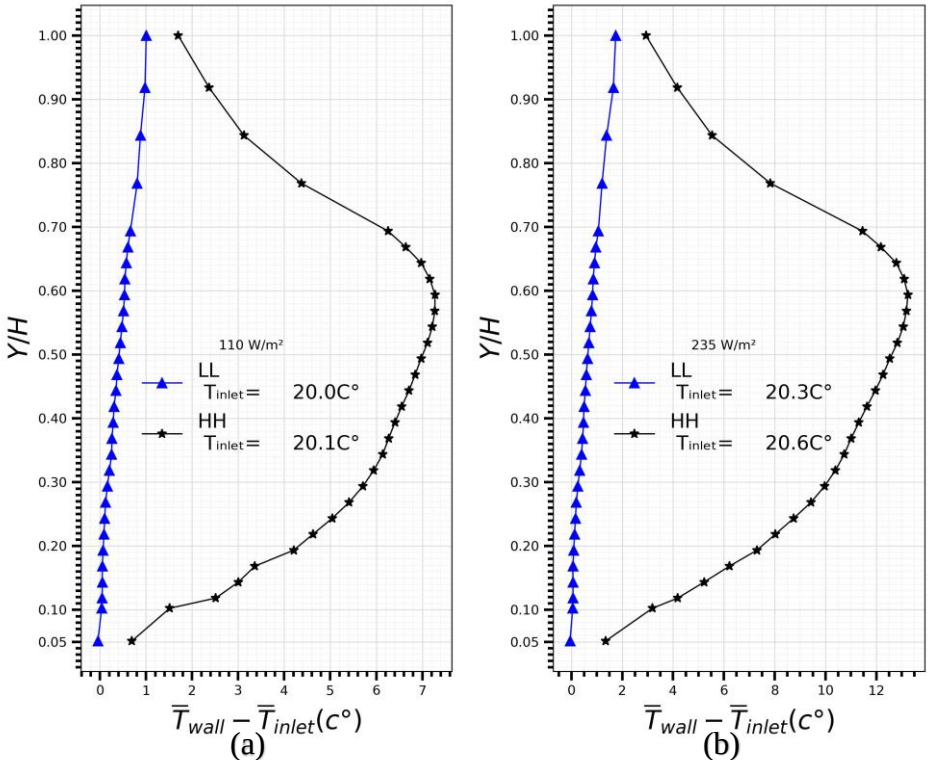


Figure 5.11: Comparison of the evolution of operational wall surface temperature with chimney height for passive wall, between cases: (a)1 and 3 (b) 2 and 4

Similarly, the outlet wall temperatures on the active wall increased by 0.7°C (70%) from Case 1 to Case 3. For Case 2 to Case 4, these values increased by 1.2 °C (70.5%). The operational inlet wall temperature on the passive wall for Cases 1 and 3 remains 0°C, and it increased to 0.7°C and 1.4°C for Cases 3 and 4, respectively.

### 5.4.2 Analysis of Vertical Velocity Profiles

To assess the effect of varying chimney wall surface emissivity under ohmic heat fluxes of 110 W/m² and 235 W/m² on the development of the time-averaged vertical velocity field along the chimney height, Cases 1 and 3 are plotted together in Figure 5.12, while Cases 2 and 4 are shown in Figure 5.13. The transformed coordinate system is used to illustrate the time-averaged vertical velocity profiles for all cases. In each graph, the right side represents the active wall of the chimney, while the left side corresponds to the

passive wall. In these plots, the X-axis represents the nondimensional air cavity gap in the chimney, and the Y-axis shows the time-averaged distribution of vertical velocity.

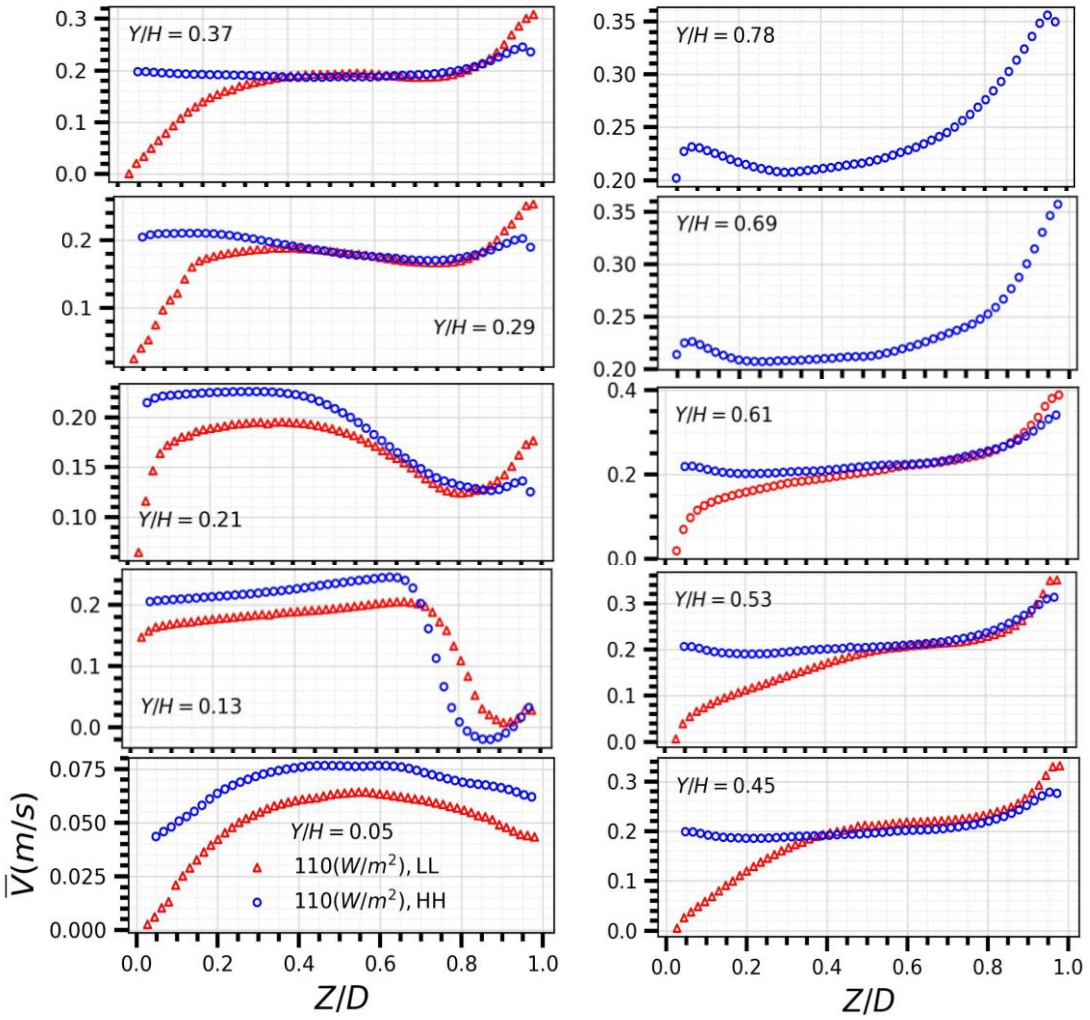


Figure 5.12: Streamwise time averaged vertical velocity profiles in the upwards direction of the chimney for Case 1 and 3.

Graphs clearly illustrate significant changes in the evolution of time-averaged velocity profiles inside the chimney due to surface radiative heat transfer from low-emissive (LL = 0.08) to high-emissive (HH = 0.96) walls, with ohmic heat fluxes of 110 W/m$^2$ and 235 W/m$^2$ injected from the active wall. The vertical velocity profiles and their evolution along the streamwise direction (Y-axis) indicate that radiation exchanges between the active and passive walls modify thermal conditions, transitioning from one-wall heating to asymmetrical heating within the chimney. Additionally, the design of the horizontal

inlet opening significantly influences the flow topology in the Y/H = 0.05 to 0.29 region for both low and high emissive wall cases.

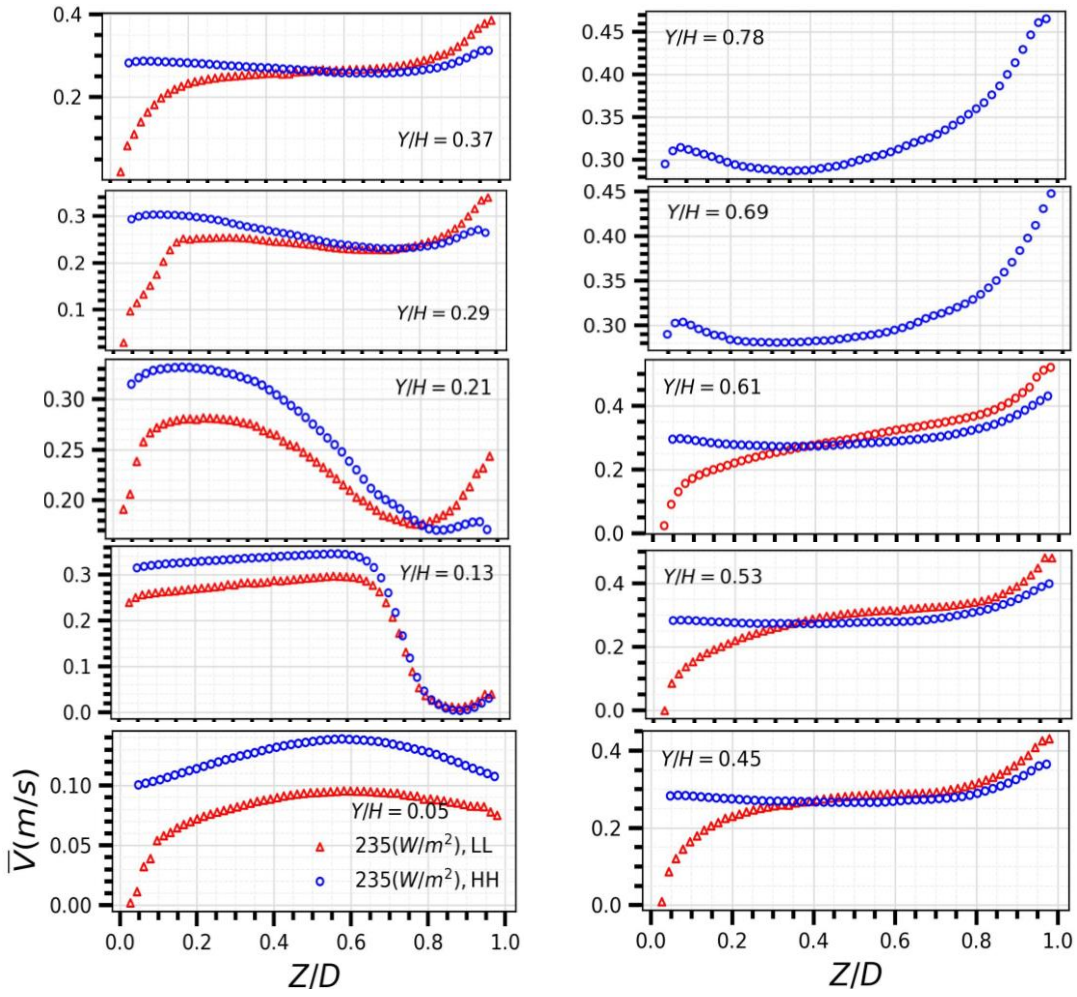


Figure 5.13: Streamwise time averaged vertical velocity profiles in the upwards direction of the chimney for Case 2 and 4.

The impact of radiation on vertical velocity from a chimney height ratio (Y/H) of 0.05 to 0.78 is shown in Figures 5.12 and 5.13. The velocities increase significantly as the wall emissivity changes from LL = 0.08 to HH = 0.96. This increase is due to the passive wall of the chimney becoming thermally active, which happens due to increased radiation heat transfer from the active wall of the chimney. Moreover, the air recirculation region along the corner of the passive wall also decreases in size with high-emissive walls. This reduction is due to the thermal activation of the passive wall, which causes the vertical

velocity profiles on the left side of the graph to be fully developed from the chimney inlet, unlike the low-emissive wall cases. In low-emissive wall cases, the air remains mostly still near the passive wall, and the thickness of this quiescent layer is observed to decrease as the ohmic flux increases from 110 W/m² to 235 W/m². This indicates that the flow is not fully developed in the chimney, but no reverse flow is observed near the passive wall of the chimney. In high-emissive wall cases, velocities are evenly distributed in the air cavity gap due to the asymmetric heating of the chimney. As the air in the velocity profiles evolves upstream from a height of Y/H = 0.37 to Y/H = 0.78, the effects of flow separation and the horizontal inlet configuration decrease in all cases, resulting in velocity profiles that reflect the flow within the vertical channel.

At a chimney height of Y/H = 0.05, there is a 55% increase in the mean of the vertical velocity profile from case 1 to case 3 and a 36% increase from case 2 to case 4. Similarly, at Y/H = 0.61, the mean of the vertical velocity profile showed a 15.5% increase from case 1 to case 3 and a 1.33% increase from case 2 to case 4. At Y/H = 0.21, comparing Case 1 to Case 3 resulted in a decrease of 22.7% in the peak value of the velocity profile on the active wall, while the reduction in the peak velocity value from Case 2 to Case 4 is 31.4%. Similarly, at Y/H = 0.61, there is a 12.1% decrease in the peak vertical from Case 1 to Case 3 and a 17.3% reduction from Case 2 to Case 4.

## 5.5 Analysis on Chimney Airflow Field

To determine the time-averaged airflow topology on the entire vertical centre plane of the L-shaped channel at mid-width (X/W = 0.5), experiments were conducted using a 2D PIV technique on a 2 m high chimney with a cavity gap of 0.164 m. The geometric parameters were consistently maintained across all cases. These included an aspect ratio ($Y_H/D = 8$), an extension ratio of the adiabatic cavity top ($Y_A/Y_H = 0.52$), chimney width (0.38

meters), aperture height of the inlet opening (0.205 m), and length of the inlet opening duct (0.079 m). Detailed information on the experimental variables for each case is provided in Table 5.6. The experiments aimed to visualize the evolving airflow pattern within the L-shaped channel. Additionally, the study explored the impact of variations in the magnitude of ohmic flux and wall surface emissivity on the airflow field and flow structures within the chimney.

### 5.5.1 Airflow Field at Low Emissive Walls

The air flow fields for Case 1 and Case 2 were recorded using the PIV technique along the central plane of the chimney. This plane, with dimensions ($Y_{PIV} \approx 1.288$ m) and ($D_{PIV} = 0.139$ m), represents the PIV flow domain. Figure 5.14 depicts the structural dimensions of the chimney alongside the PIV computational flow area under investigation. Starting from a chimney height of Y = 0.021 m, the airflow field was captured within a flow domain extending 0.161 m along both the Z-axis and the Y-axis of the chimney. To mitigate unwanted reflections from laser pulses and low flow definition within the boundary sub-layer near the walls of the chimney, a 4 mm masking was applied to the passive wall along the Z-axis and a 3 mm masking to the active wall. This resulted in a PIV computational flow domain of 0.139 m along the Z-axis of the chimney. Additionally, to ensure complete coverage without overlap or missing areas, the camera was incrementally repositioned along the Y-axis by 0.161 m eight times. This process achieved a computational flow domain of $Y_{PIV} \approx 1.288$ m in the Y-axis direction, with an error of ± 2 mm between two tests for each case.

To measure the airflow field and flow patterns within the chimney, time-averaged values of the resultant velocity vectors were computed across the entire captured PIV flow domain. These values were then plotted on a nondimensional space grid covering

nondimensional chimney height (Y/H) from 0.0105 to 0.6545 and air gap (Z/D) from 0.027 to 0.98 using contour plots.

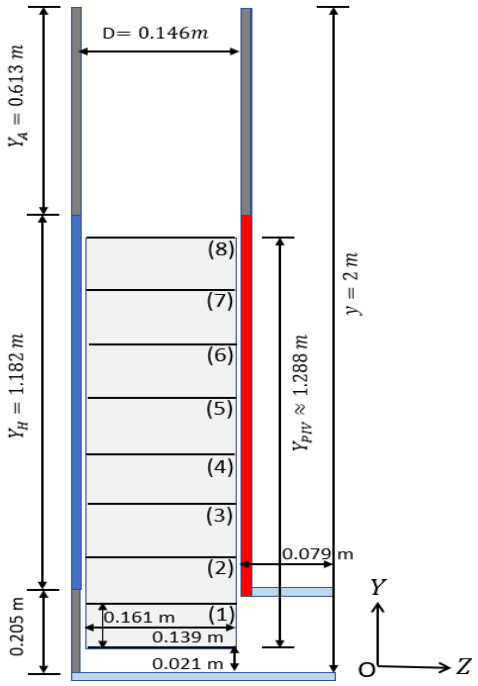


Figure 5.14: Schematic view of the Streamwise PIV measurements for air flow field measurement for low emissive wall cases (1 & 2).

Figure 5.15 depicts the magnitude of the time-averaged resultant velocity ($\overline{V_{mag}}$) variable across combinations of Z/D and Y/H nondimensional space variables for Cases 1 and 2. The X and Y axes display Z/D and Y/H values, respectively, while contour lines and bands of the same colour between them represent regions with similar ($\overline{V_{mag}}$) values. The magnitude of ($\overline{V_{mag}}$) can be interpreted from the colour bar on the right side of the plots. These contour lines connect Z/D and Y/H variable combinations, allowing for the identification of regions with equal ($\overline{V_{mag}}$) values. The contour plots facilitated the quantification of the time-averaged airflow field and flow structures within the chimney, showcasing their unique characteristics in the form of colour patterns. The time-averaged flow pattern and structures resemble those observed in a one-wall heated vertically oriented channel, featuring a horizontal inlet opening. There is a noticeable increase in

the magnitude of ($\overline{V_{mag}}$) with rising ohmic heat flux and modified Rayleigh number. The impact of this inlet configuration on flow modification, notably in the height of the chimney between Y/H = 0.05 and 0.29, is highly evident.

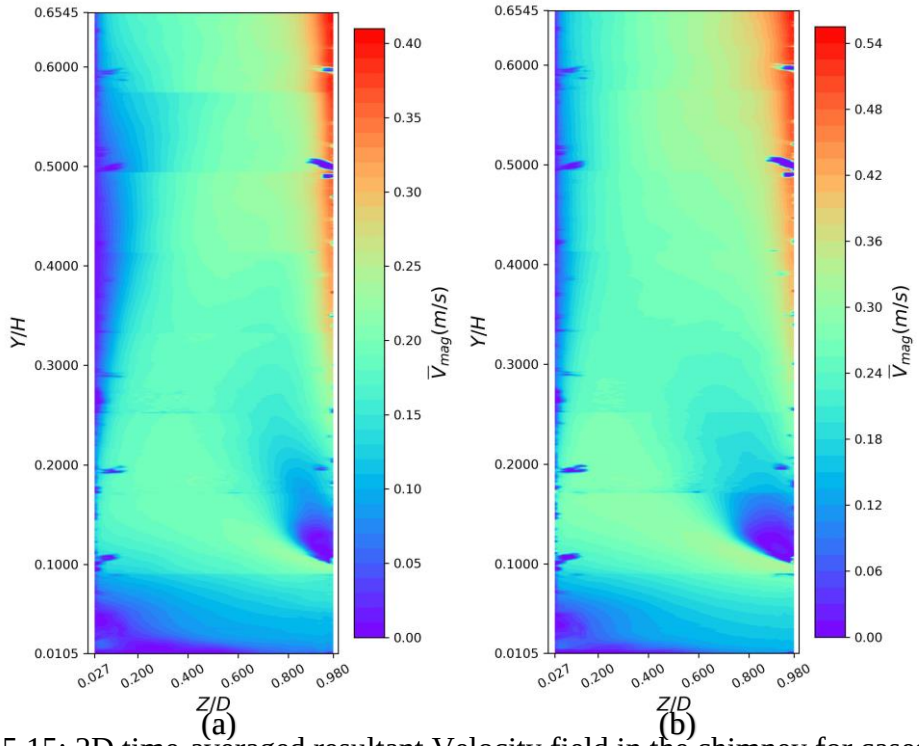


(a) (b)

Figure 5.15: 2D time-averaged resultant Velocity field in the chimney for cases: (a) 1 and (b) 2.

Because of the horizontal inlet of the chimney, it creates two distinct areas where air recirculates. The first one, a larger recirculation area, forms in the corner of the passive wall, while the second, smaller one, forms at the leading edge of the active wall. As depicted in Figure 5.16, when both the ohmic heat flux and the modified Rayleigh number rise, the larger recirculation zone diminishes in size while the smaller one above the chimney entrance expands in the in the Z-direction, albeit maintaining a constant height (from Y/H = 0.1 to 0.15). The rise in ohmic heat flux leads to increased air velocities propelled by an augmented pressure gradient between the chimney inlet and outlet. Additionally, the area of flow separation at the leading edge of the active wall expands due to the heightened air velocities at the chimney inlet. This enlargement in the flow

separation region and air velocities encourages greater air diversion towards the passive wall, aiding in diminishing both the height and depth of the stationary fluid layer formed along the passive wall of the chimney.

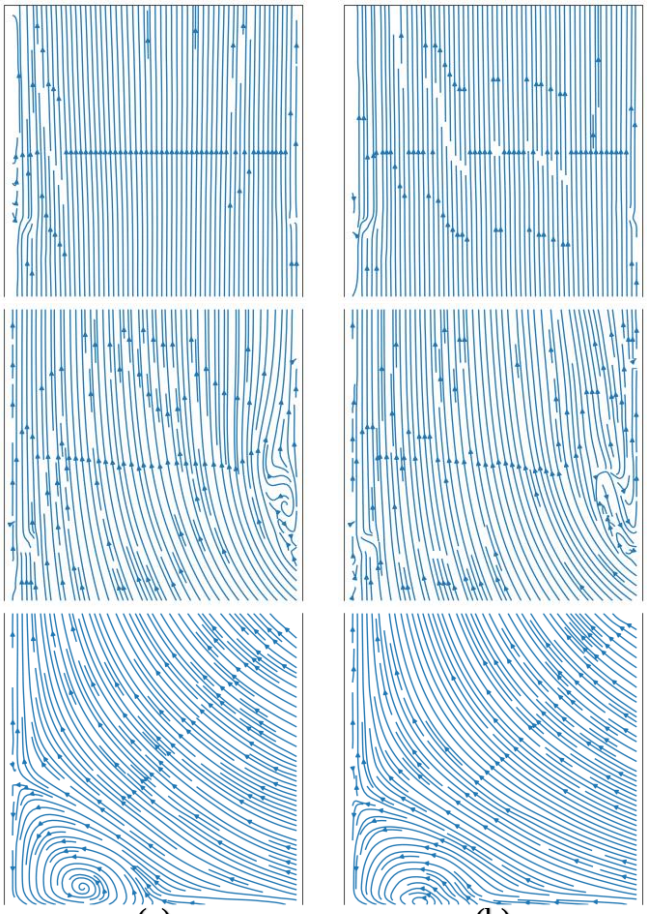


Figure 5.16: Streamline plots at Y/H = 0.01 to 0.09, 0.09 to 0.17 & 0.57 to 0.65 for (a) Case 1 and (b) Case 2

Following the flow separation region, the airflow reattaches to the active wall, leading to significantly higher velocities near the active wall of the chimney as more fluid is propelled by the heating of the air in the region close to the active wall in the streamwise direction. Consequently, the width of the velocity boundary layer also expands near the active wall. Beyond the thermal boundary layer, air is primarily driven by the pressure gradient developed between the inlet and outlet of the chimney due to the heating of air

inside the chimney. The increase in the ohmic heat flux further contributes to the thickening of the velocity boundary layer near the active wall of the chimney.

No reverse flow is observed near the passive wall from the height of the chimney (Y/H = 0.57 to 0.65) in both Cases 1 and 2, as illustrated in the streamline plots in Figure 5.16. The absence of reverse flow can be partly attributed to the diversion of most incoming airflow from the chimney inlet toward the passive wall. Additionally, due to radiative heat transfer, even with a low emissivity (LL=0.08) of the chimney wall, the operational temperature of the passive wall at the chimney outlet increased by 1°C and 1.64°C for Case 1 and Case 2, respectively. Consequently, this contributed to suppressing the downward flow from the chimney outlet.

### 5.5.2 Air Flow Field at High Emissive Walls

Similarly, the PIV technique was used to measure the airflow field for Case 3 and Case 2 along the central plane, defined by dimensions $Y_{PIV} \approx 1.96$ m and $D_{PIV} = 0.135$ m, representing the PIV flow domain. Figure 5.17 shows the structural dimensions of the chimney along with the PIV computational flow domain under investigation. Starting from a chimney height of Y = 0.015 m, the airflow field was captured within a flow domain extending 0.169 m along both the Z-axis and the Y-axis of the chimney. A 7 mm masking was applied to the passive wall along the Z-axis and a 4 mm masking to the active wall of the chimney to avoid wall effect. This resulted in a PIV computational flow domain of 0.135 m along the Z-axis of the chimney. Additionally, to ensure complete coverage without overlap or missing areas, the camera was incrementally repositioned along the Y-axis by 0.169 ten times. This process achieved a computational flow domain of $Y_{PIV} \approx 1.96$ m in the Y-axis direction, with an error of ± 2 mm between two tests for each case. To analyse the airflow within the chimney, time-averaged resultant velocity

vectors were computed across the entire PIV flow domain. These values were plotted on a nondimensional space grid covering chimney height (Y/H) from 0.0075 to 0.852 and air gap (Z/D) from 0.048 to 0.97 using contour plots for Case 3 and Case 4.

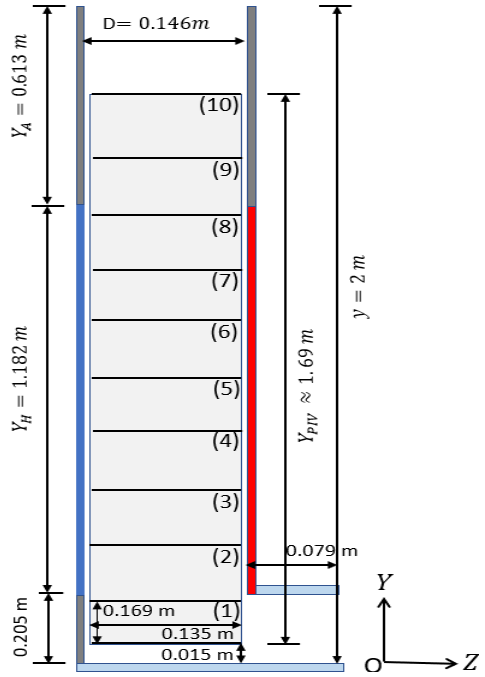


Figure 5.17: Schematic view of the Streamwise PIV measurements for whole field measurements for Case 3 & 4

Figure 5.18 illustrates the variable ($\overline{V_{mag}}$) across combinations of Z/D and Y/H nondimensional space variables. The magnitude of ($\overline{V_{mag}}$) inside the L-shaped vertical channel increases in the PIV flow domain as the ohmic heat flux increases from 110 W/m² to 235 W/m². The airflow patterns and flow structures indicate that radiation exchanges have modified the thermal conditions, shifting from one-wall heating to asymmetric heating of the air from the active and passive walls of the chimney. It has been observed that, with the same ohmic flux injected into the chimney, the inlet air flow is stronger with high-emissive walls (HH = 0.96) of the chimney compared to low-emissivity walls (LL = 0.08). There is a noticeable increase in the magnitude of ($\overline{V_{mag}}$) with rising ohmic heat flux and modified Rayleigh number.

Similar to Cases 1 and 2, both Cases 3 and 4 demonstrate the impact of the horizontal inlet opening on flow modification, particularly notable in the region from Y/H = 0.05 to 0.29. The presence of the horizontal inlet in the chimney leads to the formation of two distinct air recirculation zones. However, as the emissivity of the walls increases, the size of the air recirculation at the corner of the passive wall diminishes due to the intensified inlet airflow, as depicted in streamline plots in Figure 5.19. Conversely, the airflow separation region above the leading edge of the active wall widened owing to the heightened strength of the inlet flow. With the increase in ohmic heat flux from Case 3 to Case 4, the recirculation region at the corner of the passive wall further reduces in size with the escalating inlet air flow. Meanwhile, the air recirculation region at the leading edge of the active wall remains unaffected by the increase in modified Rayleigh number.

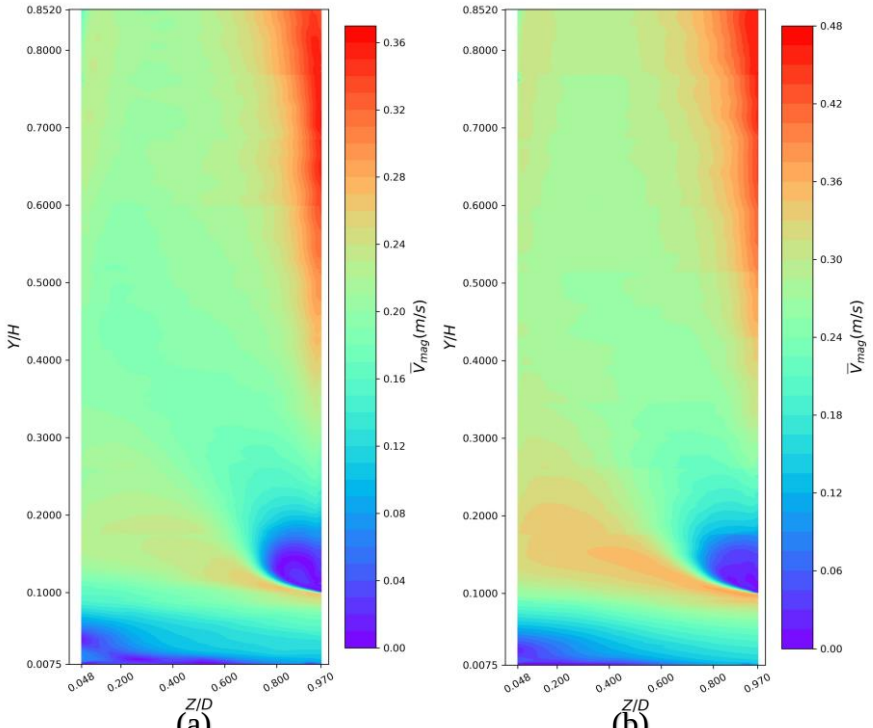


Figure 5.18: 2D time-averaged resultant Velocity field in the chimney for cases: (a) 3 and (b) 4.

The consistent width of the air separation region at the leading edge of the active wall, despite an increase in the ohmic heat flux, may be attributed to heightened radiative heat

transfer to the passive wall. This intensifies the thermal and velocity boundary layers on the passive wall, directing more airflow towards it. As a result, the buoyancy force on the passive wall increases while decreasing on the active wall due to its lower operational temperature. This balance in buoyancy forces maintains a constant size of the flow separation region at the leading edge of the active wall despite the rise in ohmic heat flux. Remarkably, the height of the air circulation region (from Y/H = 0.1 to 0.15) at the leading edge of the active wall remains consistent across all tested cases of low and high emissive walls.

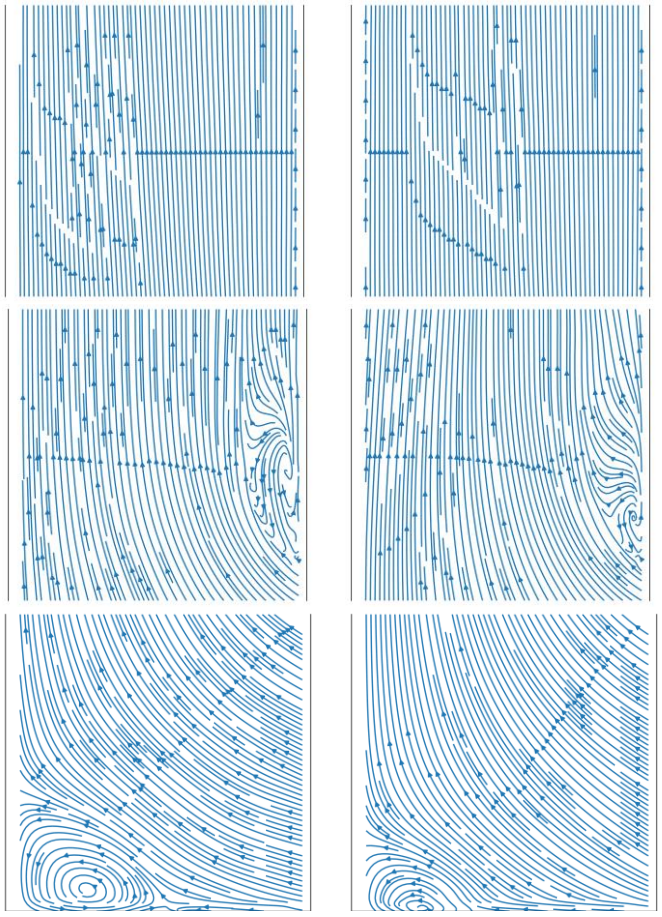


Figure 5.19: Streamline plots at Y/H = 0.0075 to 0.092, 0.092 to 0.176 & 0.59 to 0.68 for (a) Case 3 and (b) Case 4

Following the flow separation region, the airflow reattaches to the active wall of the chimney. The fluid within the chimney is propelled by the heating of air near both the

active and passive walls, resulting in significantly higher velocities in the streamwise direction. Consequently, the width of the velocity boundary layers expands near these walls due to the asymmetrical heating within the channel. The wall-to wall radiation heat transfer causes variations in temperature gradients on active and passive walls of the chimney which, in turn, affect the time-averaged air flow field. Additionally, the increase in ohmic heat flux further contributes to the thickening of the velocity boundary layers near the active and passive walls of the chimney. This thickening occurs because the increased heat flux enhances the thermal energy available, intensifying the natural convection and leading to a more pronounced development of the boundary layers. No reverse flow is observed from Y/H = 0.57 to 0.65 due to the development of the thermal boundary layer on the passive wall from the chimney height in both Cases 3 and 4, as illustrated in the streamline plots in Figure 5.19. Radiative heat transfer increased the operational temperature of the passive wall at the chimney outlet by 1.7°C in Case 3 and 2.9°C in Case 4. This temperature rise suppressed the downward flow from the chimney outlet.

## 5.6 Analysis on Chimney Airflow Rate

To boost the volume of airflow from the solar chimney, aiming to improve both occupant comfort and the temperature of the active wall of the chimney, the global average airflow rates for all four cases were calculated. Table 5.6 presents the experimental specifics for each Case. These calculations involve performing numerical integration on the time-averaged vertical velocity profiles obtained from PIV experiments across the entire cross-sectional area (D x W) of the chimney. This analysis was carried out at heights of the chimney from Y/H = 0.37 to 0.61 for low-emissive wall Cases and from Y/H = 0.53 to 0.78 for high-emissive wall cases.

Firstly, the mean volume flow rate was determined by integrating the vertical velocity profiles across the cross-sectional area at various heights of the chimney for each case. Then, an average value was calculated from the mean values of the volume flow rate, accompanied by the standard deviation calculated between the values of the two tests for each case. Finally, the globally averaged volume flow rate is visually represented for all cases in Figure 5.20 through bar plots with error bars.

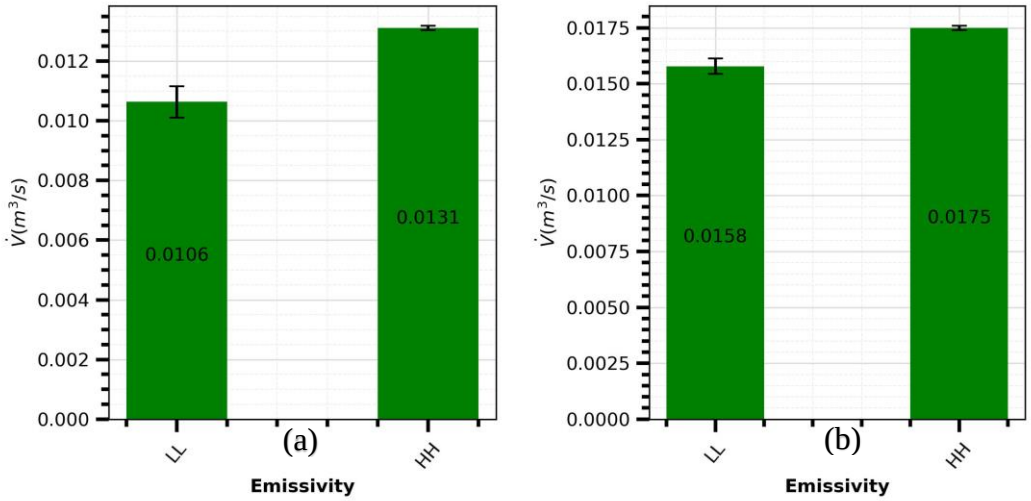


Figure 5.20: Global-averaged Volume flow rate of the chimney between cases: (a) 1 and 3 (b) 2 and 4.

Figure 5.20 demonstrates a strong positive correlation between the global-average volume flow rate of the chimney and the rise in surface emissivity of the chimney walls from LL = 0.08 to HH = 0.96 at ohmic heat fluxes of 110 W/m² and 235 W/m², respectively. To assess the impact of varying chimney surface emissivity on the global averaged volume flow rate, an increase of 23.6% in the global averaged volume flow rate out of the chimney is observed from Case 1 to Case 3. Similarly, a 10.8% increase is observed from Case 2 to Case 4. To evaluate the impact of an increase in ohmic flux on the globally averaged volume flow rate, a comparison between Case 1 and Case 2 shows a 49% increase in the globally averaged volume flow rate out of the chimney. Similarly, 33.6% increase is observed from Case 3 to Case 4.

## 5.7 Conclusions

In this study, the influence of position of room air inlet was evaluated by analysing air temperature distribution and airflow patterns in a scaled-down model room (1.48 m x 1.48 m x 1.12 m) connected to a wall chimney. Additionally, the effect of the room air inlet on the performance of the wall chimney was assessed by measuring the wall thermal field on the active side of the chimney and the kinematic flow field along the centre plane (X/W = 0.5) of the chimney. The experiments involved the injection of uniform heat fluxes of 110 W/m² and 235 W/m² from the active wall to the chimney. The surface emissivity of chimney walls was kept at ($\varepsilon \sim 0.08$). Throughout the experiments, modified Rayleigh numbers (Ra*) of $1.89 \times 10^7$ and $3.5 \times 10^7$ were tested while maintaining a constant aspect ratio of 8 and the extension ratio of the chimney top at 0.52. Across all tested room air inlet configurations, the mean operational wall temperatures were measured at 22.8 ± 0.18°C and 41.8 ± 0.19°C for heat fluxes of 110 W/m² and 235 W/m², respectively. Furthermore, the mean volume flow rate, measured with both AW and TW configurations, was 0.0155 m³/s, with a standard deviation of ± 0.005. These findings indicate that the position of the room air inlet did not affect the performance of the wall chimney. Smoke tests demonstrated that all room air inlet configurations facilitated a streamline flow of air from the room air inlet to the inlet of the chimney, reducing the spread of air within the room. Moreover, the TW configuration exhibited a lower average room temperature of 0.4°C than the rest of the configuration when subjected to a heat flux of 235 W/m$^2$. These findings underscore the importance of room air inlet placement in solar wall chimney ventilated living spaces.

The effect of surface emissivity on the performance of an L-shaped vertical channel was studied by maintaining the active and passive walls of the chimney at $\varepsilon \sim 0.08$ and $\varepsilon \sim 0.96$,

respectively, and testing at uniform heat fluxes of 110 W/m² and 235 W/m². For the low-emissivity experiments, modified Rayleigh numbers (Ra*) of $1.89 \times 10^7$ and $3.5 \times 10^7$ were tested. In the high-emissivity experiments, Ra* values of $2.15 \times 10^7$ and $4.04 \times 10^7$ were examined. Both sets of experiments maintained a constant aspect ratio of 8 and a

chimney top extension ratio of 0.52. To examine the impact of wall surface emissivity, the temperature fields on both active and passive walls were recorded, as well as the time-averaged velocity fields across the entire centre plane (X/W = 0.5) of the chimney. The study connected the thermal characteristics trends observed in the wall temperature evolution on both the active and passive walls of the chimney with the time-averaged flow structures identified in the natural convection air flow developed within the L-shaped vertical channel.

The evolution of the time-averaged flow and thermal fields on the chimney walls was influenced by both the horizontal inlet design of the chimney, particularly from Y/H = 0.05 to 0.29. Beyond this height, the flow stream nearly loses x-momentum, and the velocity profiles start to resemble those of a one-wall heated vertical channel. The results show that higher emissive walls led to increased velocity at the chimney inlet at heat fluxes of 110 W/m² and 235 W/m². Additionally, the velocity field gradually rises upstream with high-emissive walls compared to low-emissive walls at the same heat flux. At low surface emissivity ($\varepsilon \sim 0.08$) of walls, the kinematic and wall thermal fields in the chimney depict one-wall heating conditions within the L-shaped cavity. Increasing surface emissivity ($\varepsilon \sim 0.96$) induced wall-to-wall radiation exchanges, altering the thermal conditions within the chimney and causing asymmetric heating of the air between its active and passive walls.

At a heat flux of 110 W/m², with a change in surface emissivity of chimney walls from 0.08 to 0.96, the operational temperature of the passive wall increased by 4.9°C (1633%). Similarly, at 235 W/m², this temperature rose by 8.7°C (1740%). Conversely, the average operational temperature on the heated part of the active wall decreased by 8.2°C (36.6%) and 13.7°C (33.2%) at 110 W/m² and 235 W/m², respectively.

No reverse flow phenomenon is observed at the low-emissive walls of the chimney under tested ohmic heat fluxes. Thus, the airflow rate out of the chimney remains unaffected by descending cold air from the chimney outlet, as investigated by [11–13]. The suppression of bidirectional flow at the chimney outlet is likely due to the deflection of incoming airflow towards the passive wall via the horizontal inlet. Increased heat flux leads to higher inlet air velocities caused by the vena-contracta effect at the chimney inlet, further deflecting air towards the passive wall and reducing the height and depth of the stationary fluid layer along the passive wall. Additionally, the operational wall temperature at the outlet was higher than the ambient temperature due to radiative heat transfer, further suppressing the potential for downward airflow [14].

The horizontal inlet design of the wall chimney creates two sharp corners, leading to distinct air recirculation zones at the inlet of the chimney, as numerically investigated by [12,13,15,16]. The first occurs at the corner of the passive wall, while the second forms just above the chimney inlet at the sharp corner of the active wall due to the vena-contracta effect. These air recirculation regions dissipate the kinetic energy of the flow within the chimney, reducing the mass flow rate [12,13], and affecting the evolution of wall thermal and kinematic fields. The size of these flow structures is also found to be influenced by the ohmic heat flux and surface emissivity of the chimney walls [15], while the height of the flow separation region on the leading edge of the active wall remains consistent

between Y/H = 0.1 and 0.15. As a result, the maximum localized gradient of operational wall temperature on active walls occurs in this region across all cases studied.

Between chimney heights of Y/H = 0.44 and Y/H = 0.64, a decline in the operational wall temperature field is noted on the active wall of the chimney. For low-emissive walls subjected to 110 W/m² and 235 W/m², reductions of 0.03°C and 0.12°C, respectively, are observed. Similarly, high emissive walls, tested under the same wattages, experienced decreases of 0.31°C and 0.66°C, respectively. This decrease in the thermal field is solely attributed to heightened radiative heat transfer due to an increased view factor, with no indication of flow transition as the flow within the L-shaped cavity remains laminar in all studied cases, contrasting the findings of studies[5,6,9].

The volume flow rate of the chimney experienced a 23.6% increase when the surface emissivity of the chimney walls changed from 0.08 to 0.96 at 110 W/m², and a 10.8% increase at 235 W/m². Moreover, with the rise in ohmic heat fluxes from 110 W/m² to 235 W/m², the volume flow rate increased by 49% for low-emissive walls of the chimney, whereas high-emissive walls exhibited a 33.6% increase.

The results of this study highlight the considerable impact of radiation heat transfer on the ventilation efficacy of L-shaped solar-heated ventilation channels, affecting both the volume flow rate and reducing the active wall temperature of the chimney. Thus, it is a factor that cannot be ignored. Predictions of flow patterns reveal that the sharp corners at the chimney inlet positively alter the flow field, mitigating reverse flow at the outlet of the chimney, yet also result in energy dissipation. Consequently, redesigning the chimney inlet holds promise for further improvement in L-shaped solar ventilation systems.

## 5.8 References

[1] W. Elenbaas, Heat dissipation of parallel plates by free convection, Physica 9 (1942) 1–28. https://doi.org/10.1016/S0031-8914(42)90053-3.

[2] A. Bouchair, Solar chimney for promoting cooling ventilation in southern Algeria, (n.d.).

[3] S. Spencer, An experimental investigation of a solar chimney natural ventilation system, masters, Concordia University, 2001. https://spectrum.library.concordia.ca/id/eprint/1378/ (accessed September 26, 2023).

[4] R. Khanal, C. Lei, An experimental investigation of an inclined passive wall solar chimney for natural ventilation, Solar Energy 107 (2014) 461–474. https://doi.org/10.1016/j.solener.2014.05.032.

[5] J. Vareilles, Étude des transferts de chaleur dans un canal vertical differentiellement chauffé: application aux enveloppes photovoltaïques thermiques, 2007.

[6] S.Q. Estibaliz, Experimental investigation of thermal and fluid dynamical behavior of flows in open-ended channels. Application to Building Integrated Photovoltaic (BiPV) Systems, (n.d.).

[7] M. Fossa, C. Ménézo, E. Leonardi, Experimental natural convection on vertical surfaces for building integrated photovoltaic (BIPV) applications, Experimental Thermal and Fluid Science 32 (2008) 980–990. https://doi.org/10.1016/j.expthermflusci.2007.11.004.

[8] M. Thebault, S. Giroux-Julien, V. Timchenko, C. Ménézo, J. Reizes, Detailed flow development and indicators of transition in a natural convection flow in a vertical channel, International Journal of Heat and Mass Transfer 143 (2019) 118502. https://doi.org/10.1016/j.ijheatmasstransfer.2019.118502.

[9] M. Thebault, Coherent structures and impact of the external thermal stratification in a transitional natural convection vertical channel, (n.d.).

[10] L. Shi, G. Zhang, An empirical model to predict the performance of typical solar chimneys considering both room and cavity configurations, Building and Environment 103 (2016) 250–261. https://doi.org/10.1016/j.buildenv.2016.04.024.

[11] R. Khanal, C. Lei, Flow reversal effects on buoyancy induced air flow in a solar chimney, Solar Energy 86 (2012) 2783–2794. https://doi.org/10.1016/j.solener.2012.06.015.

[12] G. Gan, Prediction of heat transfer and air flow in solar heated ventilation cavities, Computational Fluid Dynamics: Theory, Analysis and Applications (2013) 137–178.

[13] G. Gan, General expressions for the calculation of air flow and heat transfer rates in tall ventilation cavities, Building and Environment 46 (2011) 2069–2080. https://doi.org/10.1016/j.buildenv.2011.04.014.

[14] R. Li, M. Bousetta, E. Chénier, G. Lauriat, Effect of surface radiation on natural convective flows and onset of flow reversal in asymmetrically heated vertical channels, International Journal of Thermal Sciences 65 (2013) 9–27. https://doi.org/10.1016/j.ijthermalsci.2012.10.023.

[15] R. Khanal, C. Lei, Numerical investigation of the ventilation performance of a solar chimney, ANZIAM Journal 52 (2010) C899–C913. https://doi.org/10.21914/anziamj.v52i0.3947.

[16] R. Bassiouny, N.S.A. Koura, An analytical and numerical study of solar chimney use for room natural ventilation, Energy and Buildings 40 (2008) 865–873. https://doi.org/10.1016/j.enbuild.2007.06.005.

# CHAPTER 6: THEORETICAL MODELLING OF INDOOR SOLAR CHIMNEY

## 6.1 Purpose of Theoretical Modelling

The solar chimney functions as a thermosiphon with a solar collector, absorbing and retaining solar heat along its absorber wall and consequently heating the air inside the chimney. This heat-induced buoyancy generates a natural updraft, drawing room air into the chimney channel to compensate for the pressure drop from the upward flow. Solar chimneys have garnered considerable research attention for their ability to enhance natural ventilation. Researchers have dedicated significant effort to optimizing solar chimney configurations under various conditions.

The typical factors considered for enhancing the performance of a solar chimney encompass a range of actions, such as: (1) modifying the width of the air gap (refer to works [1–3]); (2) altering the height of the chimney (consult studies [4–6]); (3) adjusting the angle of inclination (see research [2,7–9]); (4) adding the adiabatic extension on the Trombe wall and vertical channel (refer to works [10–15]); and (5) altering the surface emissivity of the vertical channel (see, for example, [7,9,16]).

Numerous studies have been carried out to predict the ventilation performance of solar chimneys and the mean temperature values of the walls and air within the chimney, while also investigating the impact of geometric parameters on the ventilation rate and mean temperatures of the wall of the chimney [17–21]. All these studies are based on the global energy balance model approach developed by [22,23] as their basis. The mathematical models formulated in these investigations underwent validation using data obtained from outdoor experimental setups. However, conducting studies using outdoor models introduces challenges in controlling environmental factors, such as fluctuations in solar

radiation, ambient temperature, and wind velocity, which are pivotal for maintaining the system in a steady state [17]. Consequently, certain studies anticipate higher ventilation performance and mean temperatures for both the chimney air and walls than what is projected by the mathematical model. Conversely, some studies foresee results lower than the experimental findings.

In order to overcome the drawbacks of the conventional method for validation of the theoretical model, a novel reduced-scale model of an indoor solar chimney attached to a single room has been fabricated by the present author, and the first indoor steady-state global energy balance model of a solar chimney with an adiabatic top downstream of the chimney, in line with the research work of [22,23], has been formulated for validation. Not only the mean temperature of the air in the chimney and its walls and ventilation rate are computed and validated with the experimental results, but also the efficacy of the model has been tested with the results obtained by changing the surface emissivity of the chimney walls. In the present study, a steady heat balance model (SHBM) is established to further study the thermal performance of the combined system. A series of SHBM calculations is performed to exploit the impacts of the air gap between the walls of the chimney and the surface emissivity of the wall of the chimney. It is worth noting that the present investigation focuses on the validation of the theoretical model developed for indoor solar chimney and the efficacy of this model in predicting the performance of the chimney at low and high surface emissivity.

### 6.1.1 Physical Model

The schematic of the proposed system, which encompasses the wall solar chimney attached to the room, is depicted in Figure 3.1(a). The dimensions of the reduced-scale model of room are 1.48 m × 1.48 m × 1.12 m, resulting in a total volume of 2.45 $m^3$. The

air inlet in the room has a cross-sectional area of 0.375 m × 0.205 m and is positioned at a height of 0.639 m above the floor. Figure 6.1 displays the cross-sectional perspective of the indoor solar chimney.

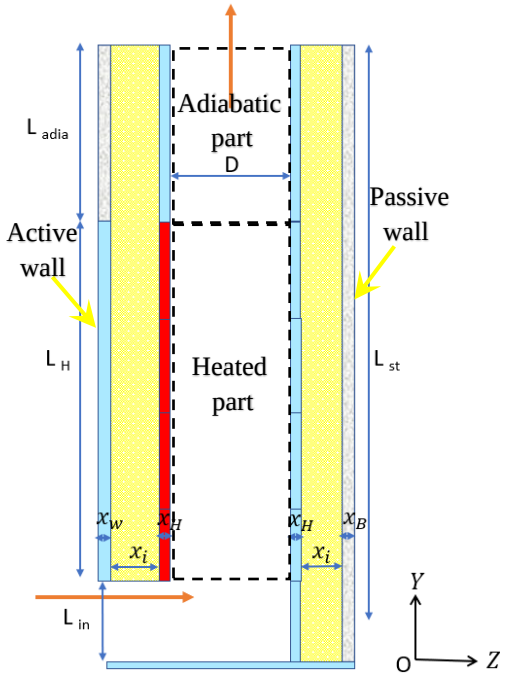


Figure 6.1: Cross-sectional view of the chimney at the plane of symmetry along y-z plane.

The inlet cross-sectional area of the chimney is 0.38 m × 0.205 m, while the outlet has a cross-sectional area of 0.38 m × 0.146 m. The overall height of the chimney is 2 m, with the inlet opening situated at a height of 0.205 m from the floor and the heater providing heating surface up to a height of 1.182 m. Additionally, 0.613 m of adiabatic height is added to the chimney wall at the downstream end of the heated part of the chimney walls. The stack height of the chimney is measured to be 1.9 m from the midpoint of the inlet opening [17]. Additionally, Table 6.1 below provides details on the thickness and thermal conductivities of the material layers that make up both the active and passive walls of the chimney.

Table 6.1: Thickness and thermal conductivities of the material on active and Passive wall of the chimney

| Material | Symbol | Unit | Value |
|---|---|---|---|
| Glass heater thickness | $X_H$ | m | 0.004 |
| Glass wool insulation thickness | $X_i$ | m | 0.065 & 0.06 |
| Plexiglass room wall thickness | $X_w$ | m | 0.01 |
| Gypsum board thickness | $X_B$ | m | 0.01 |
| Glass heater conductivity | $K_H$ | W/mK | 1 |
| Glass wool insultion conductivity | $K_H$ | W/mK | 0.042 |
| Plexiglass room wall | $K_H$ | W/mK | 0.17 |
| Gypsum board | $K_H$ | W/mK | 0.01 |

A typical outdoor solar chimney consists mainly of a black wall, known as the absorber wall, and a transparent cover, referred to as the glazing. It also features two side walls, an opening at the bottom as well as another at the top, establishing one-wall heated open-ended channel. The glass cover, being semitransparent, permits sunlight to penetrate and warm the channel. As solar energy is incident upon it, the air inside the chimney is heated, prompting an upward flow due to the stack effect. The operation of the solar chimney relies on distinct mechanisms of heat transfer. The glass cover receives solar radiation in the form of both diffuse and direct solar radiation. While the glass pane reflects and absorbs these radiations, a portion of the direct solar radiation and diffuse radiation is transmitted through the glazing. Furthermore, a segment of the transmitted energy is absorbed by the black wall, subsequently heating up the air within the chimney. This heat is then transferred through radiation to the inner surface of the glass wall, further contributing to the heating of the air inside the chimney.

In the case of a reduced-scale model of an indoor solar chimney developed at LOCIE for this research work, both heated walls of the chimney are constructed as opaque. The

measured electrical heat flux is introduced into the chimney by activating the heater mounted on the active wall of the chimney. This is done to simulate the impact of sunlight striking the opaque wall of an outdoor solar chimney. Additionally, to maintain a low surface emissivity for both the active and passive walls, the wall surfaces were covered with a thin layer of aluminium scotch tape with a known emissivity of 0.08. To adjust the wall emissivity from low to high values, the walls were coated with matte black paint, which has a known emissivity of 0.96. Please refer to Appendix A of this thesis for the surface emissivity measurement procedure.

### 6.1.2 Assumption for 1-D SHBM of Indoor Solar Chimney

The assumptions for the development of the steady heat balance model (SHBM) are presented as follows:

- There is no heat transfer due to conduction in the system along the y-axis.
- Air in the channel is acting as a non-participatory medium for radiation heat transfer between the channel walls.
- Heat transfer throughout the system is modelled at the plane of symmetry, and heat transfer is taking place in a steady-state condition.
- A uniform heat flux is supplied to the system from the active wall of the chimney.
- The heater is generating a uniform heat flux on the heated section of the active wall of the chimney.
- Linear empirical correlations, as suggested by Incropera in his book, will be used to measure the thermo-physical properties of air in the temperature range of 300 K to 350 K.
- The temperature of the air is modelled to vary linearly along the height of the chimney and is assumed to be constant along the cross section of the channel.

- The properties of the air in the channel are measured at the mean fluid temperature inside the chimney.
- A linearized radiative heat transfer coefficient will be used to maintain the linearity of the system of steady-state energy balance equations.
- Existing correlations between the Nusselt number and the Rayleigh number available in the literature will be used to measure natural convection heat transfer coefficients.
- The air mass flow rate in the chimney for a room with two openings and a uniform room air temperature will be calculated according to Bansal et al. (1993) and Andersen (1995).
- The temperature of the room will be considered equal to the ambient temperature.
- During the operation of the indoor solar chimney test rig inside the laboratory room, the ambient temperature of the air remains constant.

### 6.1.3 Formulation of 1-D SHBM

In order to evaluate the thermal performance of the indoor solar chimney, a one-dimensional (1-D) steady heat balance model (SHBM) is developed. A heat transfer diagram is shown at the plane of symmetry along the Y-Z plane in Figure 6.2 to illustrate the heat transfer between different components of the system as well as between the system and the ambient environment. Each node represents the temperature of a single participating element in the SHBM, either in the building envelope or in the ambient. It is assumed that at all nodes in the active and passive walls of the chimney, the room wall, and the air in the channel of the cavity gap are in thermal equilibrium with the ambient temperature.

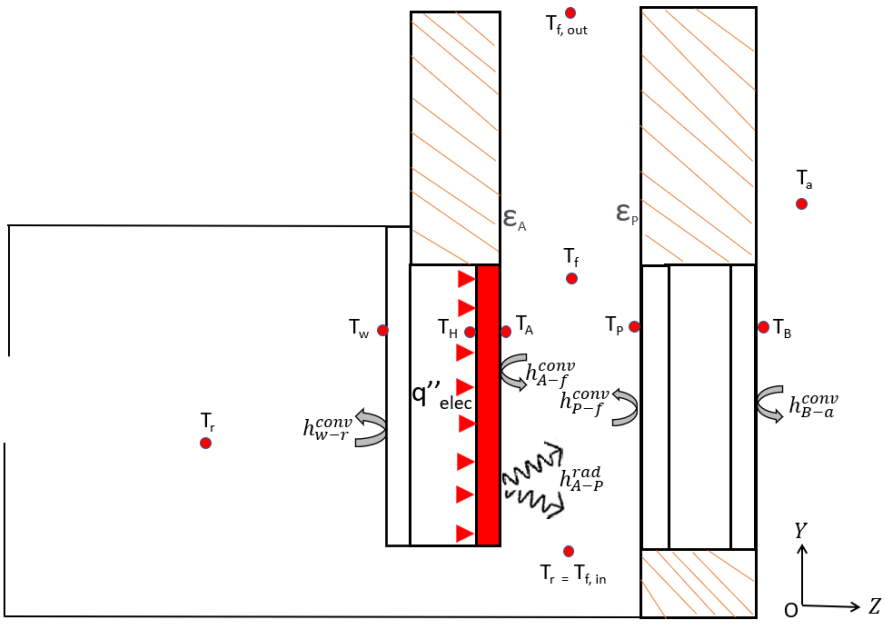


Figure 6.2: Heat transfer diagram of the solar chimney

The active wall of the chimney attached to the room is being evenly heated by an electrical flux density ($q''_{elec}$) from the heater mounted on the wall. The majority of the heat flux from the heater is transferred towards the chimney as the back side of the heated wall is insulated. A portion of this heat is conducted through the wall of the attached room and into the room. On the other hand, the heat flux conducted from the heater to the surface of the active wall, which is in contact with the air in the chimney, gets convected to the air. Some of the heat emitted from this surface of the active wall is radiated towards the passive wall of the chimney. Part of this radiated heat is convected to the air in contact with the passive wall, while the minute amount is lost to the surroundings through the outer surface of the gypsum board on the passive wall, which is in contact with the ambient air. Because of all the three modes of heat transfer processes inside the chimney, the air entering the chimney at the initial temperature ($T_{f,\,in}$) undergoes an increase in air temperature ($T_f$) as well as a reduction in air density. This causes the heated fluid to become buoyant and rise upwards, eventually exiting through the outlet opening at a temperature ($T_{f,\,out}$). As a result, an equivalent volume of outside air at room temperature ($T_a$) enters to replace the same volume of air that previously occupied the attached room.

The fresh air enters through a window carrying the wall of the room. The heat transfer diagram illustrates the average temperatures and heat fluxes of each element of the solar chimney at every node. The temperature at the backside of the heater is denoted as ($T_H$), the temperature on the active wall of the channel in contact with the air in the chimney as ($T_A$), the temperature of the room wall as ($T_r$), the temperature on the passive wall of the channel in contact with the air in the chimney as ($T_P$), the temperature on the gypsum board of the passive wall of the channel as ($T_B$), and the temperature of the air in the room as ($T_r$).

### 6.1.4 Global Energy balance equations of indoor solar chimney

A detailed thermal resistance network for the SHBM for indoor solar chimney is depicted in Figure 6.3(a). In this network diagram, all system nodes are denoted by red circles, each labelled with its corresponding temperature. Arrows indicate the direction of heat transfer within the thermal system. Thermal resistances within the system are illustrated using electrical resistor symbols placed between consecutive nodal points in the thermal circuit. The vertical red dotted arrow signifies the electrical heat flux density acting on the rear side of the heater mounted on the active chimney wall. On the other hand, the black vertical arrow represents the heat flux transferred to the air inside the chimney. The Thermal Heat Balance Model (THBM) considers the thermal coupling between the air in the chimney and the chimney structure. It is capable of estimating the thermal performance of the proposed system by solving the energy conservation equation at all thermal nodes. Moreover, the airflow rate through the solar chimney is computed using the formula proposed by [24,25]. This formula is derived from the vertical momentum and mass balance, as well as the energy conservation equations for the air within the chimney domain.

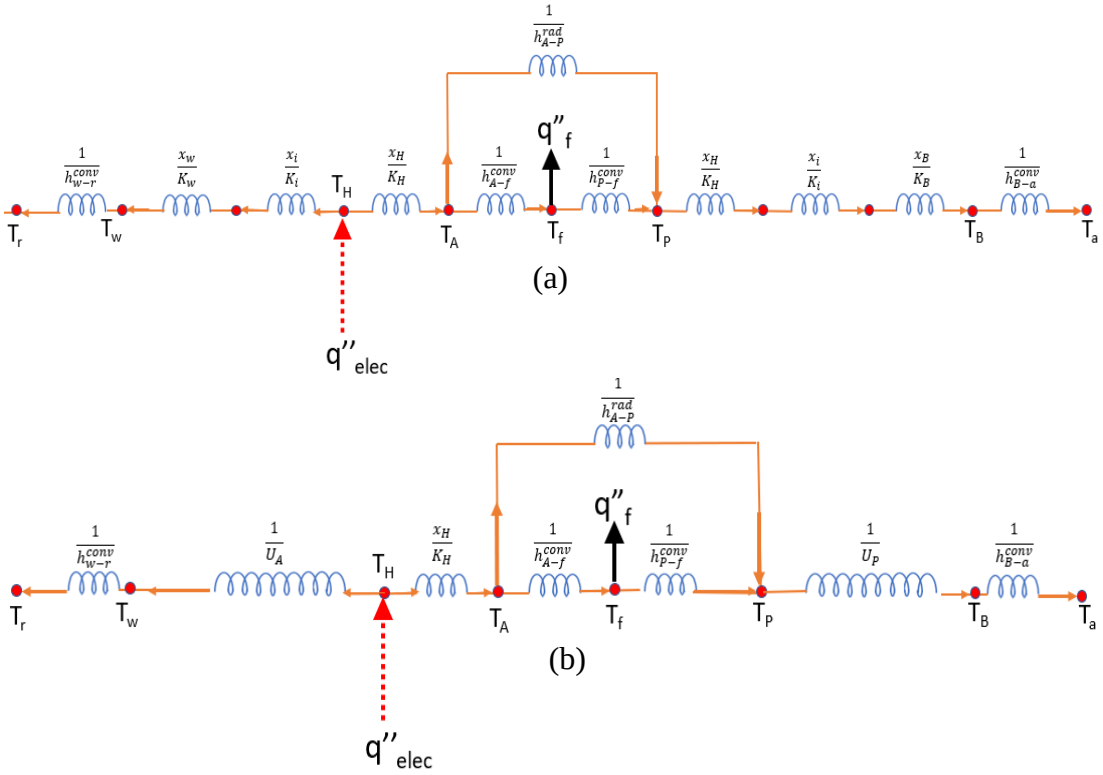


Figure 6.3: Thermal resistance network for the indoor solar chimney (a) Detailed thermal resistance diagram (b) Equivalent thermal resistance diagram.

The equivalent thermal resistance network for the indoor solar chimney is illustrated in Figure 6.3(b). In this network diagram, certain thermal resistances have been consolidated to decrease the node count and, consequently, the number of equations needed for unknown temperatures. By employing a global energy balance approach to each node in the equivalent thermal network diagram of the solar chimney, the energy balance for each node corresponding to the average values of glass cover temperature ($T_H$), fluid temperature ($T_w$), ambient temperature ($T_A$), fluid temperature ($T_f$), absorber metallic plate temperature ($T_P$), and back surface temperature ($T_B$) is described by the following equations:

Heat energy balance equation derived at node $T_H$

$$q''_{elec} = \frac{K_H}{x_H}(T_H - T_A) + U_A(T_H - T_w) \qquad (1)$$

Heat energy balance equation derived at node $T_w$

$$U_A(T_h - T_w) = h_{w-r}^{conv}(T_w - T_r) \quad (2)$$

Heat energy balance equation derived at node $T_A$

$$\frac{K_H}{x_H}(T_h - T_A) = h_{A-f}^{conv}\left(T_A - T_f\right) + h_{A-P}^{rad}\left(T_A - T_P\right) \quad (3)$$

Heat energy balance equation derived at node $T_f$

$$h_{A-f}^{conv}\left(T_A - T_f\right) = q_f^{"} + h_{P-f}^{conv}\left(T_f - T_P\right) \quad (4)$$

Heat energy balance equation derived at node $T_P$

$$h_{A-P}^{rad}\left(T_A - T_P\right) + h_{P-f}^{conv}\left(T_f - T_P\right) = U_P(T_P - T_b) \quad (5)$$

Heat energy balance equation derived at node $T_B$

$$U_P(T_P - T_b) = h_{B-a}^{conv}(T_B - T_a) \quad (6)$$

#### 6.1.4.1 Calculation of Heat collected by Air Inside Chimney

Figure 6.4 illustrates the heat transferred to the air stream flowing upward within the heated section of the chimney, where natural convection occurs from the active wall. For deriving the steady-state heat transfer equation for fluid inside the chimney, we will apply the energy balance approach to an infinitesimally small control volume of air inside the chimney at an arbitrary location.

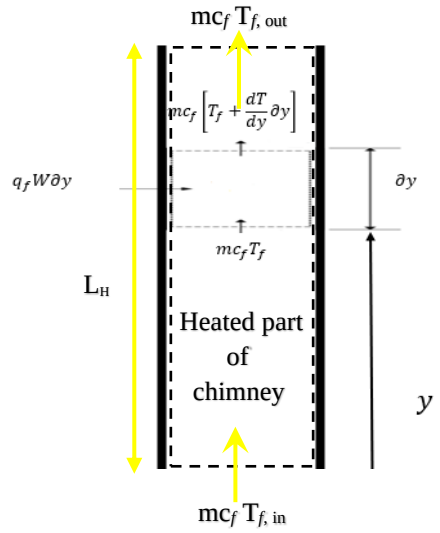


Figure 6.4: Heat balance to air stream in direction of flow in the heated part of the chimney

Consider the heat flows into and out of this element of thickness ($\partial$y) in the air stream at a distance y measured from the start of the heated section of the chimney. The temperature of the air stream at a distance y from the collector inlet is assumed to be at ($T_f$). It is assumed that the temperature remains constant along the height of the heated section of the chimney on both the active and passive walls. The heat balance for the element can thus be expressed as

$$\dot{m}\, c_f T_f + q_f W \partial y = \dot{m}\, c_f \left[T_f + \frac{dT_f}{dy}\partial y\right] \qquad (7)$$

Simplifying and dividing the equation (7) by $\partial y$ will result in the following expression.

$$\frac{dT_f}{dy} = \frac{q_f W}{\dot{m}\, c_f} \qquad (8)$$

Integrating the equation (8) from both sides will result in following expression.

$$\int dT_f = \frac{q_f W}{\dot{m}\, c_f} \int dy \qquad (9)$$

After solving the integral in the above we yield the expression as under

$$T_{f,out} - T_{f,in} = \frac{q_f W L_H}{\dot{m}\, c_f} \qquad (10)$$

The mean air temperature inside the chimney is modelled by the following linear equation as proposed by [23] in their experimental and empirical study.

$$T_f = \gamma T_{f,out} + (1-\gamma) T_{f,in} \qquad (11)$$

In the above equation, γ represents the mean temperature weighting factor, which is taken as 0.74 in this model, a value determined experimentally by sources , [17,19,20,26]. However, source [23] reported a value of γ = 0.75. To proceed, rearrange equation (11) to solve for ($T_{f,out}$) , and then substitute this value into equation (10). This allows the expression for the useful heat transferred to the moving air stream to be reformulated in terms of the mean fluid temperature and the inlet air temperature.

$$\frac{T_f - T_{f,in}}{\gamma} = \frac{q_f'' W L_H}{\dot{m}\, c_f} \qquad (12)$$

Rearranging equation (12) yields the algebraic expression for the heat flux absorbed by the fluid, as shown in the following equation.

$$q_f'' = \frac{\dot{m}\, c_f}{\gamma W L_i}(T_f - T_{f,in}) = m(T_f - T_{f,in}) \qquad (13)$$

In the above equation, M represents heat transfer to the fluid that exits the chimney and is defined as

$$M = \frac{\dot{m}\, c_f}{\gamma W L_i} \qquad (14)$$

#### 6.1.4.2 Rearranging System of Algebraic Equations

Now, all six equations corresponding to the six nodes of the equivalent thermal network diagram of a solar chimney will be rearranged in a way that combines all coefficients of the same variables together and moves the constants to the right side of the equations.

The following expression results from rearranging Equation (1)

$$\left(\frac{K_H}{x_H} + U_A\right) T_H - U_A T_w - \frac{K_H}{x_H} T_A = q''_{elec} \quad (15)$$

Rearranging Equation (2) yields the following expression:

$$(U_A + h_{w-r}^{conv}) T_w - U_A T_H = h_{w-r}^{conv} T_r \quad (16)$$

Rearranging Equation (3) yields the following expression:

$$\left(\frac{K_H}{x_H} + h_{A-f}^{conv} + h_{A-P}^{rad}\right) T_A - \frac{K_H}{x_H} T_H - h_{A-f}^{conv} T_f - h_{A-P}^{rad} T_P = 0 \quad (17)$$

Substituting equation (13) and then Rearranging equation (4) yields the following expression:

$$\left(h_{A-f}^{conv} + h_{P-f}^{conv} + M\right) T_f - h_{A-f}^{conv} T_A - h_{P-f}^{conv} T_P = G T_{f,in} \quad (18)$$

Equation (5) can be rearranged to provide the following expression.

$$\left(h_{A-P}^{rad} + h_{P-f}^{conv} + U_P\right) T_P - h_{A-P}^{rad} T_A - h_{P-f}^{conv} T_f - U_P T_B = 0 \quad (19)$$

Finally, rearranging Equation (6) results in the expression shown below.

$$(U_P + h_{B-a}^{conv}) T_B - U_P T_P = h_{B-a}^{conv} T_a \quad (20)$$

The provided set of algebraic equations has been expressed using a matrix structure [A] with dimensions of 6 by 6. This matrix form serves as an organized representation of the coefficients, variables, and constants within the equations. In this arrangement, each column of the matrix corresponds to coefficients associated with the unknown temperatures, whereas each row corresponds to an individual equation. The unknown temperatures are collectively organized into the variable vector [T], and the constants of the equations are appropriately placed within the vector [B].

$$A = \begin{bmatrix} \left(\frac{K_H}{x_H} + U_A\right) & -U_A & -\frac{K_H}{x_H} & 0 & 0 & 0 \\ -U_A & (U_A + h_{w-r}^{conv}) & 0 & 0 & 0 & 0 \\ -\frac{K_H}{x_H} & 0 & \left(\frac{K_H}{x_H} + h_{A-f}^{conv} + h_{A-P}^{rad}\right) & -h_{A-f}^{conv} & -h_{A-P}^{rad} & 0 \\ 0 & 0 & -h_{A-f}^{conv} & \left(h_{A-f}^{conv} + h_{P-f}^{conv} + M\right) & -h_{P-f}^{conv} & 0 \\ 0 & 0 & -h_{A-P}^{rad} & -h_{P-f}^{conv} & \left(h_{A-P}^{rad} + h_{P-f}^{conv} + U_P\right) & -U_P \\ 0 & 0 & 0 & 0 & -U_P & (U_P + h_{B-a}^{conv}) \end{bmatrix}$$

$$T = \begin{bmatrix} T_H \\ T_w \\ T_A \\ T_f \\ T_P \\ T_B \end{bmatrix} \quad B = \begin{bmatrix} q_{elec}^{"} \\ h_{w-r}^{conv} T_r \\ 0 \\ M\, T_{f,in} \\ o \\ h_{B-a}^{conv} T_a \end{bmatrix} \qquad (21)$$

In general, the above matrix and vectors may be displayed as [A] [T] = [B]. The average temperature vector [T] is calculated by inverting the matrix [T] = $[A]^{-1}$ [B]. It is simpler to use various matrix operations and strategies to solve the system of equations when the equations are organized in this way.

### 6.1.4.3 Determination of Unknown Terms in Matrix [A] and Vector [B]

The heat transfer coefficients within the matrix denoted as [A], encompassing both heat transfer coefficients and overall heat loss coefficients, along with supplementary terms in [B], are computed by using the established correlations in the literature.

To calculate the radiation heat transfer coefficient from the active to the passive wall of the chimney, the correlation established by [27] in their book is employed. This correlation applies to a configuration involving two infinitely parallel plates.

$$h_{A-P}^{rad} = \frac{\sigma\left(T_A{}^2+T_P{}^2\right)(T_A+T_P)}{\left(\frac{1}{\varepsilon_A}+\frac{1}{\varepsilon_P}-1\right)} \quad (22)$$

The heat transfer coefficient for convection from the active wall to the fluid is defined as follows:

$$h_{A-f}^{conv} = \frac{Nu_A \kappa_f}{L_H} \quad (23)$$

The empirical correlations were developed by [22] using the data compiled by [28] in their book. These correlations are used to calculate various key thermophysical properties of air at the average temperature inside the chimney. It is important to note that within the lower temperature range pertinent to the solar chimney's operation (300–350 K), the physical properties of air are assumed to vary linearly with the fluid temperature.

$$K_f = \left[0{,}0263 + 0{,}000074\left(T_f - 300\right)\right] \quad (25)$$

$$\mu_f = \left[1{,}846 + 0{,}00472\left(T_f - 300\right)\right] \times 10^{-5} \quad (26)$$

$$c_f = \left[1.007 + 0.00004\left(T_f - 300\right)\right] \times 10^3 \quad (27)$$

$$\rho_f = \left[1{,}1614 - 0{,}00353\left(T_f - 300\right)\right] \quad (28)$$

$$\nu_f = \frac{\mu_f}{\rho_f} \quad (29)$$

$$\beta = \frac{1}{f} \quad (30)$$

The correlations referenced in [28], and cited by [29] in their book are used to calculate the average natural convection coefficient for air near an active wall. The following correlation applies to a laminar flow situation when Ra < $10^9$.

$$Nu_A = 0.68 + \frac{0.67Ra_A^{\frac{1}{4}}}{\left[1+(0.492/Pr)^{\frac{9}{16}}\right]^{\frac{4}{9}}} \quad (31)$$

For turbulent flow (when Ra > 109) the following correlation is employed:

$$Nu_A = \left[0.825 + \frac{0.387Ra_A^{\frac{1}{6}}}{\{1+(0.492/Pr)^{\frac{9}{16}}\}^{\frac{8}{27}}}\right]^2 \quad (32)$$

The Prandtl number for air in contact with active wall is defined as

$$Pr = \frac{c_f \mu_f}{K_f} \quad (33)$$

The Grashof number for air in contact with active wall is defined as

$$Gr_A = \frac{g\beta(T_A+T_f)L_H^3}{\nu_{f1}{}^2} \quad (34)$$

The expression to determine the Rayleigh number for air in contact with an active wall is derived as follows.

$$Ra_A = Gr_A\, Pr \quad (35)$$

Similarly, the heat transfer coefficient for convection from the passive wall to the fluid is defined as follows:

$$h_{P-f}^{conv} = \frac{Nu_P\, \kappa_f}{L_H} \quad (36)$$

The same correlations are utilized to determine the mean natural convection coefficient for air adjacent to a passive wall during laminar flow conditions (Ra < $10^9$).

$$Nu_P = 0.68 + \frac{0.67Ra_P^{\frac{1}{4}}}{\left[1+(0.492/Pr)^{\frac{9}{16}}\right]^{\frac{4}{9}}} \quad (37)$$

And for turbulent flow (Ra > $10^9$) the following correlation are used:

$$Nu_P = \left[0.825 + \frac{0.387 Ra_P^{\frac{1}{6}}}{\{1+(0.492/Pr)^{\frac{9}{16}}\}^{\frac{8}{27}}}\right]^2 \quad (38)$$

The Grashof number for air in contact with passive wall is defined as

$$Gr_P = \frac{g\beta(T_P+T_f)L_H^3}{\nu_{f2}{}^2} \quad (39)$$

The Rayleigh number for air in contact with passive wall is expressed as

$$Ra_P = Gr_P\, Pr \quad (40)$$

This modelling approach utilizes the procedure detailed in references [25] and [24] to calculate the mass flow rate within a chimney linked to a room with a uniform temperature.

$$\dot{m} = C_d \frac{\rho_{f,out} A_{out}}{\sqrt{1+(\frac{A_{out}}{A_{in}})^2}} \sqrt{\frac{2gl_{st}(T_f-T_r)}{T_r}} \quad (41)$$

Several references, such as [3,8,24], advocate for a discharge coefficient of 0.57, while an alternative viewpoint presented in reference [30] suggests a value of 0.6. However, results from an experimental investigation outlined in reference [19] indicate that an optimal discharge coefficient (Cd) is around 0.52, which is also taken into account within this model.

The volume flow rate exiting the chimney is determined by dividing equation (41) by the fluid density on both sides, yielding the subsequent equation.

$$\dot{V} = C_d \frac{A_{out}}{\sqrt{1+\frac{A_{out}}{A_{in}}}} \sqrt{\frac{2gl_{st}(T_f-T_r)}{T_r}} \quad (42)$$

Air Changes per Hour (ACH) is a measure of how many times the air volume within a room will be replaced, removed, or exchanged with filtered clean air. The (ACH) is also calculated using the following expression:

$$ACH = \frac{3600\,\dot{V}}{V} \tag{43}$$

Calculation of over all the conduction coefficient on active wall $U_A$, passive wall $U_P$ are evaluated by the following respective equations.

$$U_A = \frac{1}{\left(\frac{x_i}{K_i}+\frac{x_w}{K_w}\right)} \tag{44}$$

$$U_P = \frac{1}{\left(\frac{x_H}{K_H}+\frac{x_i}{K_i}+\frac{x_b}{K_b}\right)} \tag{45}$$

The convection heat transfer coefficient on the wall of the room attached to the solar chimney is assumed to be 10 W/m²K for the full-scale model of the attached room [17,31]. In this indoor model of the solar chimney, the convection heat transfer coefficients on the outer surface of the gypsum board on the passive wall ($h_{B-a}^{conv}$) and on the room wall in contact with the active wall ($h_{w-r}^{conv}$) are both assumed to be 2.8 W/m²K, consistent with the values used by [3] in their reduced-scale experimental model of an outer solar chimney attached to a room. Furthermore, the model does not account for radiative heat transfer with a sky temperature gradient or convection heat transfer due to wind, as these factors are not relevant for an indoor solar chimney model.

### 6.1.5 Description of Algorithm Steps for SHBM of Solar Chimney

Python, being a versatile programming language with an extensive standard library and a wide range of third-party libraries, offers functions that can significantly streamline the implementation of the required algorithmic functionalities. Hence, as illustrated in Figure

6.5, codes are written in Python to implement the algorithm for solving the mathematical model developed for the indoor solar chimney.

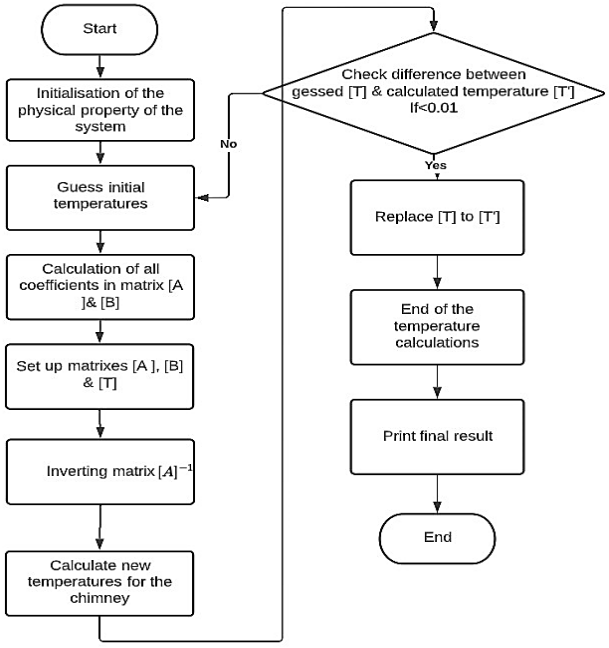


Figure 6.5: Flow chart for algorithm steps for indoor solar chimney code

The following are descriptions of the algorithmic steps of the solution:

- All relevant known data is provided.
- Initially, guessed values are assigned for the temperatures of the fluid, glass cover, metallic plate, and back surface wall. A recommended value for these temperatures ($T_A$, $T_P$, $T_H$, $T_f$, $T_w$, and $T_B$) is the ambient temperature.
- The heat transfer coefficient and the overall heat loss coefficients are then calculated.
- A matrix is constructed along with coefficient vectors.
- The matrix is inverted, and preliminary temperature values are calculated.
- These calculated temperatures are compared with the guessed temperatures. If the differences are smaller than a convergence criterion (less than 0.01°C), the

process concludes. If the differences exceed the criterion, the process returns to the second step for further iterations.

### 6.1.6 Validation of SHBM

In order to assess the predictive accuracy of the Steady Heat Balance Model (SHBM) in predicting the thermal and kinematic behaviour of the indoor solar chimney experimental setup, a validation procedure is conducted.

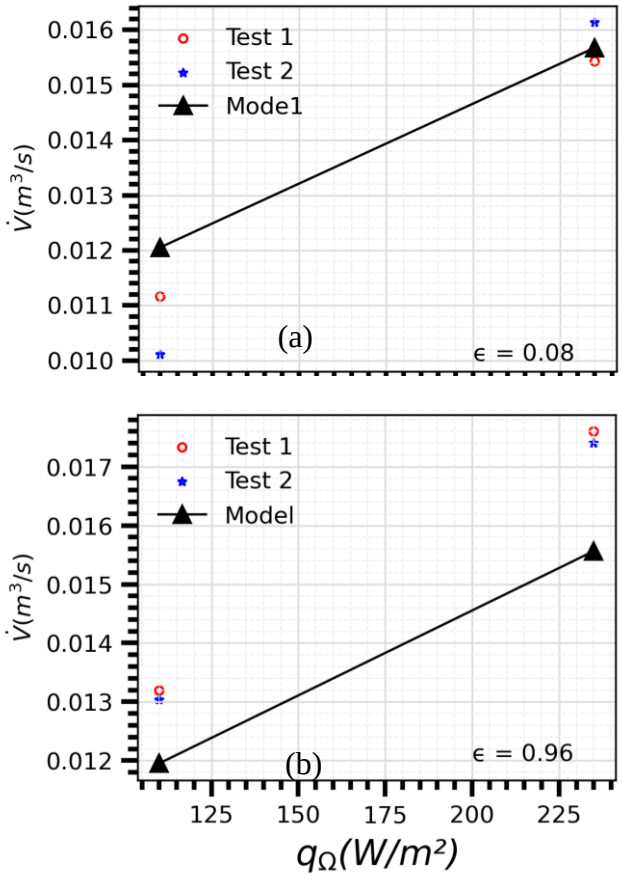


Figure 6.6: Validation of the results predicted by the SHBM for (a) volume flow rate at low surface emissivity (b) volume flow rate at high surface emissivity

This procedure entails a thorough comparison between the simulated results generated by the mathematical model and the empirical data gathered during experimentation under similar conditions, as detailed in Chapter 5 of this thesis. To conduct the validation, the volume flow rate exiting the chimney and the average temperatures of both the active and

passive chimney walls, as measured during the experiments, are plotted against the model results obtained under comparable testing conditions. Figure 6.6(a) illustrates the measurement results of volume flow rate alongside the results of the theoretical model for the low emissivity walls ($\epsilon = 0.08$) of the chimney. for comparing the experimental results with the model. Two tests (1 and 2) were conducted at an electrical flux injection of 110 W/m², and another two tests (1 and 2) were conducted at 235 W/m². Similarly, Figure 6.6(b) depicts the volume flow rate alongside the theoretical model results for the high emissivity walls ($\epsilon = 0.96$) of the chimney. For chimney walls with $\epsilon = 0.08$, the percentage error in volume rate prediction ranges from 11.7% to 0.6% higher, based on experimental results obtained at 110 and 235 W/m². The high emissivity walls ($\epsilon = 0.96$) exhibit slightly lower percentage errors, at around 9.6% and 12.4%, respectively, for the same heat flux conditions, with model predictions consistently lower than experimental results.

To validate the average active wall temperature predictions of the mathematical model for the chimney, experimental results obtained under both low and high emissivity conditions of the chimney walls are compared with the simulation results under similar conditions. Figure 6.7(a) shows the mean wall temperature minus the inlet air temperature and the theoretical model results for low emissivity walls ($\epsilon = 0.08$) of the chimney, based on two tests at 110 W/m² and two at 235 W/m². Similarly, Figure 6.7(b) presents the same comparison for high emissivity walls ($\epsilon = 0.96$).

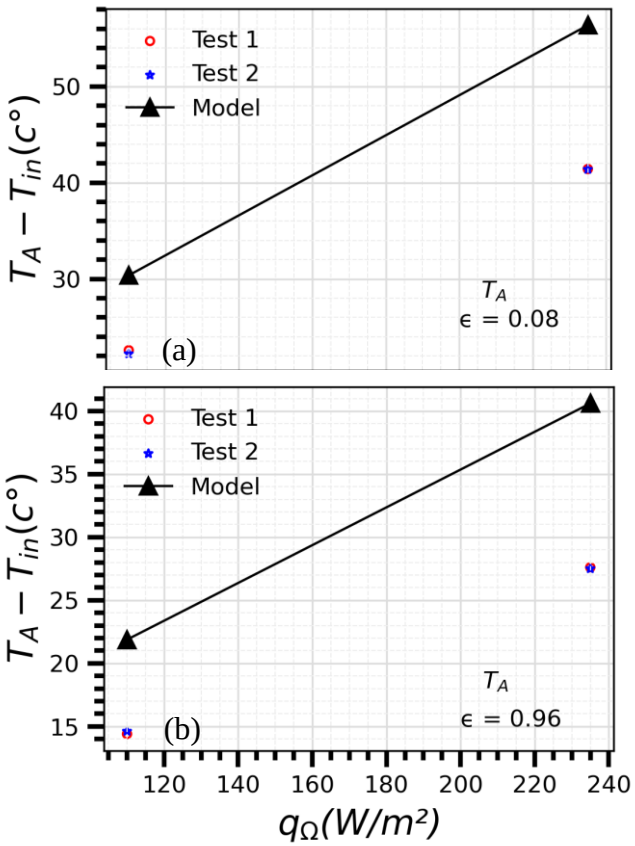


Figure 6.7: Validation of the results predicted by the SHBM for (a) Temperature difference between active wall mean and inlet air at low emissive walls (b) Temperature difference between active wall and inlet air at high emissive walls

Experimental results indicate that low-emissive walls have a mean temperature prediction error of approximately 11.7% higher than the active wall at heat fluxes of 110 and 235 W/m². High-emissive walls show slightly higher errors, around 32%, under the same heat flux conditions, consistently exceeding experimental results.

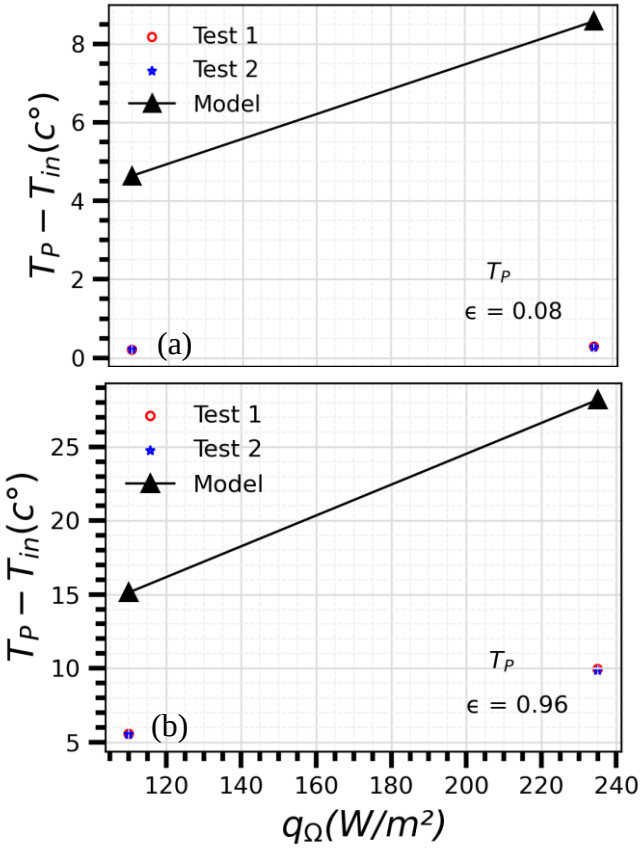


Figure 6.8: Validation of the results predicted by the SHBM for (a) temperature difference between passive wall mean and inlet air at low emissive walls (b) temperature difference between passive wall and inlet air at high emissive walls

To validate the average passive wall temperature predictions of the mathematical model for the chimney, experimental results obtained under both low and high emissivity conditions of the chimney walls are plotted against the simulation results obtained under similar conditions. Figure 6.8(a) shows the mean wall temperature minus the inlet air temperature and the theoretical model results for low emissivity walls ($\epsilon = 0.08$) of the chimney, based on two tests at 110 W/m² and two at 235 W/m². Similarly, Figure 6.8(b) presents the same comparison for high emissivity walls ($\epsilon = 0.96$). The mean passive wall temperature predictions show significantly higher percent errors for low-emissivity walls (approximately 95% higher) compared to high-emissivity walls (around 63% higher) under heat flux conditions of 110 and 235 W/m². Model predictions consistently surpass experimental results.

## 6.2 Simulation Results

The primary objective of this modelling approach is to create a simplified model for rapid parametric analysis of an experimental bench. This model aims to assess its ability to predict the impact of wall surface emissivity and the air cavity gap on the performance of a solar chimney. This comprehensive analysis reveals insights into system behaviour, explains overpredictions and prediction failures, and offers recommendations for improving the accuracy of the model in predicting indoor solar chimney performance.

### 6.2.1 Effect of Surface Emissivity of Chimney Walls

To investigate the impact of surface emissivity, the air cavity gap between the walls was maintained at 0.146 m, and all other known thermal and geometric parameters of the model were kept constant. The surface emissivity of the chimney walls varied from 0.08 to 0.96 in each simulation, across a heat flux range of 200 to 400 W/m $^2$. Furthermore, the ambient air temperature surrounding the solar chimney in the laboratory test rig was set at 20°C. Before commencing the simulation, all system components were assumed to be at this ambient temperature. The iterative model was subsequently executed for simulation. Figure 6.9(a), (b), and (c) show average values for the active wall temperature ($T_A$), passive wall temperature ($T_P$), and air temperature in the chimney ($T_f$) plotted against the electrical heat flux at low and high surface emissivity of the chimney walls.

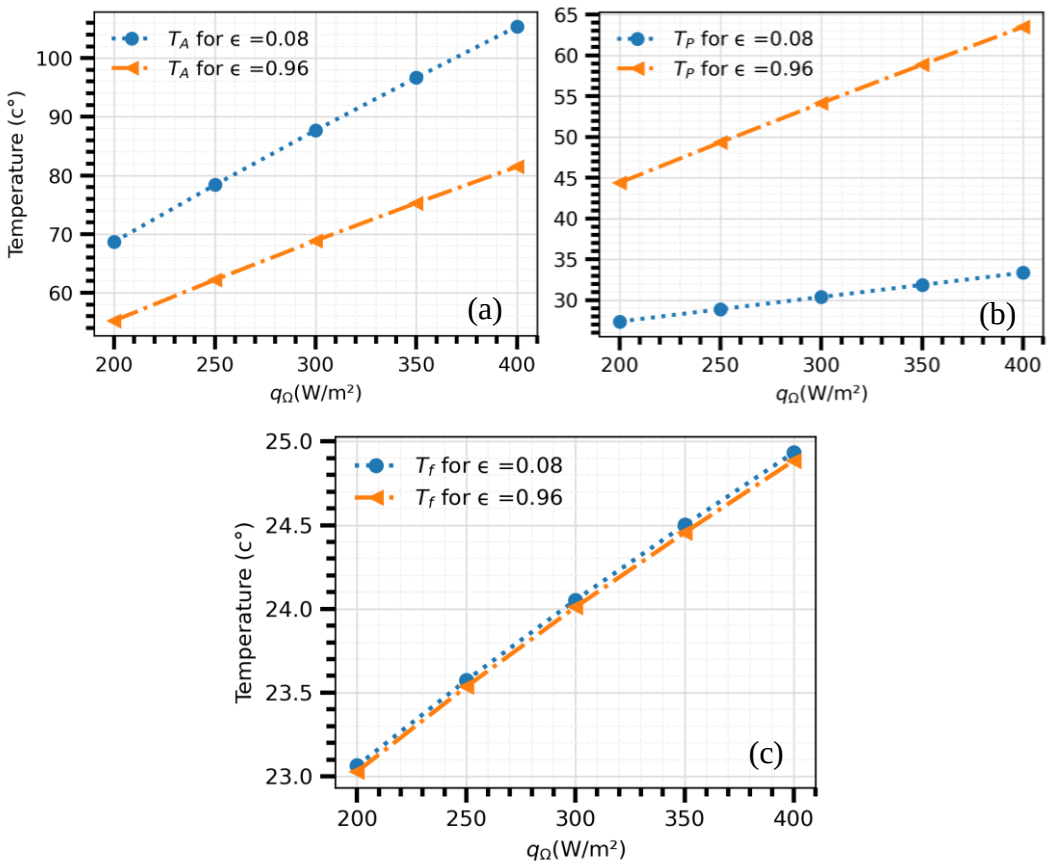


Figure 6.9: Mean temperature profiles versus electrical heat flux at varying surface emissivity (a) mean temperature variation on heated active wall section (b) mean temperature variation on heated passive wall section. (c) mean air temperature variation on the heated section of the chimney

As shown in Figure 6.9, the simulations show a linear increase in mean temperatures across system components as heat flux rises from 100 to 400 W/m². Increasing chimney wall emissivity reduces ($T_A$) magnitude at the same flux due to enhanced radiative heat transfer from the active wall, with a 13°C drop at 200 W/m² and a 23°C drop at 400 W/m$^2$. Conversely, higher emissivity boosts ($T_P$) magnitude on the passive wall, raising surface temperatures by 17°C at 200 W/m$^2$ and approximately 30°C at 400 W/m². Notably, ($T_f$) inside the chimney remains largely unaffected by wall emissivity variations.

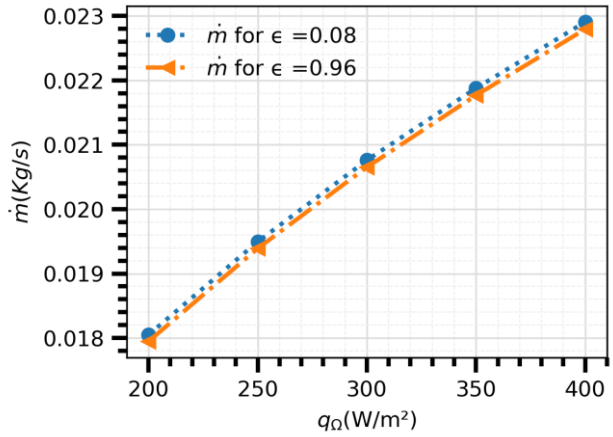


Figure 6.10: Mass flow rate versus electrical heat flux at varying surface Emissivity

The data depicted in Figure 6.10 illustrates the correlation between mass flow rate, heat flux variations, and surface emissivity. As the heat flux ranges between 200 and 400 W/m$^2$, the mass flow rate rises from 0.018 kg/s to 0.022 kg/s, indicating that higher heat flux levels correspond to increased flow rates. However, the model fails to predict changes in mass flow rate with an increase in wall surface emissivity, likely due to the mass flow rate formula used in the model, which only considers the temperature difference between the active wall and the fluid in the chimney. Interestingly, experimental data reveals that mass flow rates are higher on surfaces with low emissivity within the chimney, contrary to the expected trend of higher flow rates with higher emissivity.

### 6.2.2 Effect of Air Gap between Walls of the Chimney

To investigate the impact of air cavity gap, the emissivity of between the walls was maintained at 0.08, and all other known thermal and geometric parameters of the model were kept constant. The air cavity gap of the chimney walls adjusted, ranging from 0.146 m to 0.175 m to 0.205 m in in each simulation, across a heat flux range of 200 to 400 W/m ². Furthermore, the ambient air temperature surrounding the solar chimney in the

laboratory test rig was set at 20°C. Before commencing the simulation, all system components were

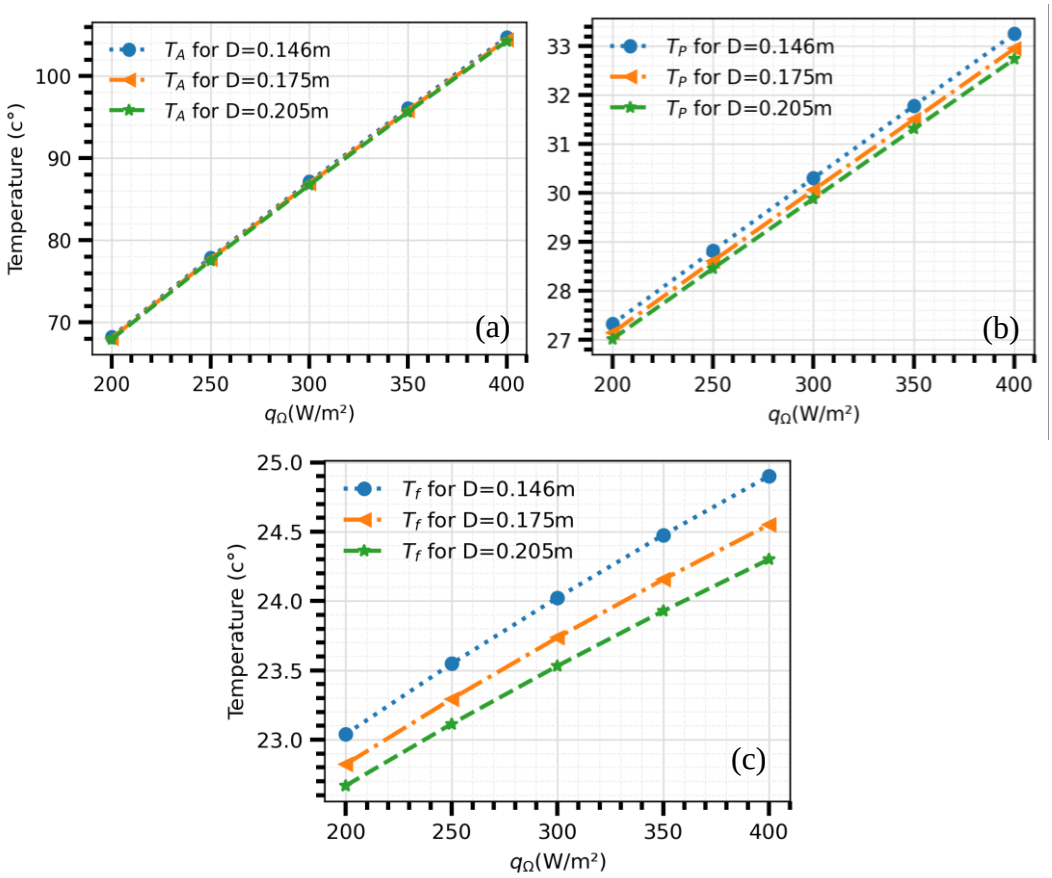


Figure 6.11: (a) Mean temperature profiles versus electrical heat flux at varying air gap emissivity (a) mean temperature variation on heated active wall section (b) mean temperature variation on heated passive wall section. (c) mean air temperature variation on the heated section of the chimney

As depicted in Figure 6.11, the model demonstrates a consistent increase in average temperatures among system elements over a heat flux range of 100 to 400 W/m$^2$. The change in air gap between chimney walls has negligible effects on the temperature of the active wall ($T_A$). Nonetheless, widening this gap decreases the temperature of the passive wall ($T_P$) under equivalent heat flux conditions, as it facilitates greater mass flow within the chimney, leading to a cooling effect. Moreover, enlarging the air gap in the chimney walls reduces the temperature ($T_f$) at the same heat flux due to a shorter duration of contact with heated walls, a consequence of the increased mass flow rate within the chimney.

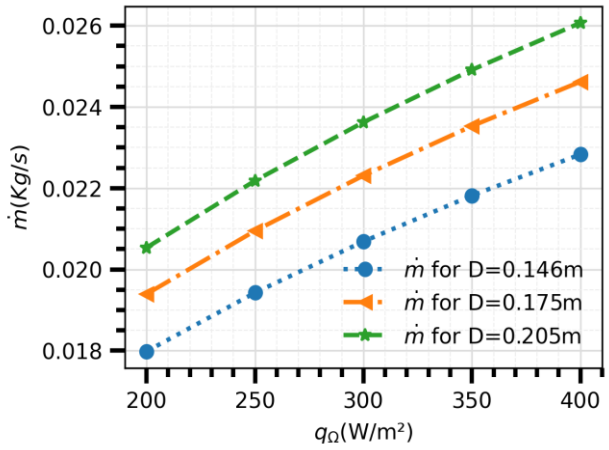


Figure 6.12: Mass flow rate versus electrical heat flux at varying air gap

Figure 6.12 depicts a rise in mass flow rate corresponding to increased heat flux and widening of the air cavity gap in the chimney, with higher heat flux (200 to 400 W/m²) and wider air gaps leading to higher mass flow rates. For instance, at a heat flux of 200 W/m², changing the air gap from 0.146 m to 0.205 m predicts a mass flow rate increase of about 0.003 kg/s, rising to approximately 0.04 kg/s at 400 W/m².

### 6.2.3 Prediction of ACH

Air changes per hour (ACH) measures the frequency with which the entire volume of air in a room is replaced by fresh air through the stack effect induced by the indoor solar chimney. Therefore, simulations of the model have been run to predict changes in surface emissivity and the air cavity gap affecting the ACH. As depicted in Figure 6.13(a). The higher heat flux and air gap lead to increased ACH, showing a direct correlation. For instance, at 200 W/m², a change in the air gap from 0.146 m to 0.205 m results in a 3 ACH increase, while at 400 W/m², the increase is 4 ACH.

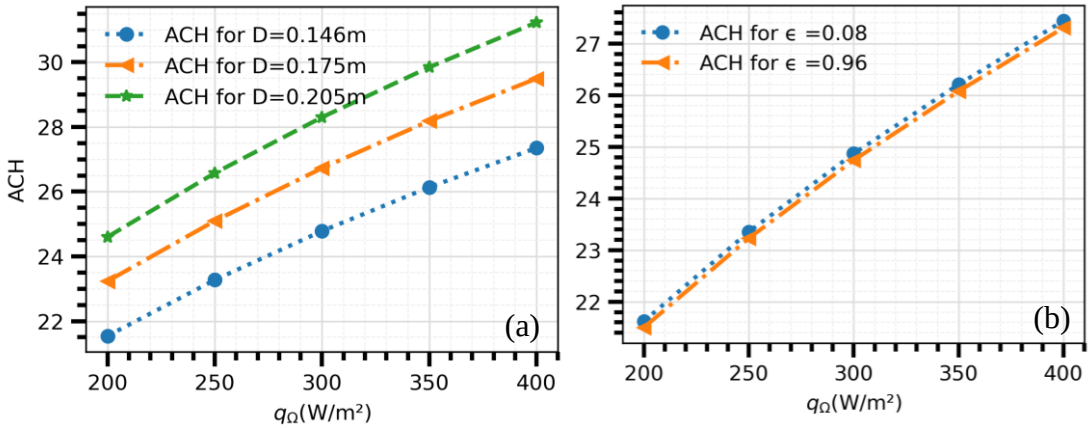


Figure 6.13: Air change per hour for solar chimney attached to room (a) ACH versus electrical heat flux at varying air gap (b) ACH versus electrical heat flux at varying surface wall emissivity

As shown in Figure 6.13(b), there is a rise in air change rate (ACH) as the heat flux varies between 200 and 400 W/m². Specifically, ACH increases from 21.6 to 27.3 while maintaining a constant air cavity of 0.146 m. The model could not predict ACH changes from surface emissivity adjustments due to its formula for calculating flow rate, which only relies on the temperature difference between the Active wall and air in the chimney.

## 6.3 Discussions and Conclusions

The mathematical model for this indoor solar chimney has been developed by following the approach proposed in [22,23]. This approach has been experimentally validated and supported by various publications [8,17,18,20,26,31]. Consequently, for the indoor solar chimney, modifications have been made to the thermal resistance network diagram to incorporate all the relevant thermal resistances and heat transfer coefficients that interact with the model and the ambient environment of the laboratory room. In all of the previous studies, the outdoor solar chimney has been modelled either as a vertical wall chimney or an inclined rooftop chimney. In each case, the stack height of the chimney has been assumed to be the same as the height of the absorber wall. However, in this indoor model of wall-mounted solar chimney, the adiabatic height of the solar chimney is also included

in the stack height of the chimney. Unlike outdoor solar chimneys that have a glass wall exposed to sky temperature and wind-related heat losses, the glass wall of the indoor solar chimney, modelled as the passive wall of the chimney, is made from opaque material, similar to the active wall of the chimney, which is modelled as the absorber wall of the outdoor chimney. In contrast to the outdoor model, which considers the emissivity, absorptivity, and transmissivity of the glass and absorber walls of the chimney, the indoor model considers only the emissivity on the surface of active and passive chimneys. Furthermore, in all of the previous studies, the emissivity of the absorber wall and glass has been assumed to be equal to or greater than 0.9. However, in this particular model, the surface emissivity was first set to 0.08 and then to 0.96 for simulations in order to also verify the performance of the model under conditions of low and high surface wall emissivity of the chimney.

The developed modelling approach for this innovative indoor solar chimney design has found to be predict the ventilation rate of the experimental model, especially at the low-emissive walls of the chimney but fails to predict the increase in the ventilation rate of the experimental bench at high-emissive walls of the chimney. Moreover, the temperature prediction of the chimney walls, particularly the passive wall, was significantly higher than the experimental results. The model can also predict changes in parameters such as air gap and surface emissivity on temperature variations at thermal nodes. It also estimates changes in mass flow rate, volumetric flow rate, and ACH, but further experimental results are needed to validate these numerical predictions.

To address the limitations of the current modelling approach, a new transient model for an indoor solar chimney can be developed based on the methodology proposed by [32]. This model determines the mass flow rate within the solar chimney channel and through

the room by utilizing momentum and mass conservation equations for the air entering the room and subsequently entering and exiting the chimney.

## 6.4 References

[1] H.B. Awbi, Design considerations for naturally ventilated buildings, Renew. Energy 5 (1994) 1081–1090. https://doi.org/10.1016/0960-1481(94)90135-X.

[2] Z.D. Chen, P. Bandopadhayay, J. Halldorsson, C. Byrjalsen, P. Heiselberg, Y. Li, An experimental investigation of a solar chimney model with uniform wall heat flux, Build. Environ. 38 (2003) 893–906. https://doi.org/10.1016/S0360-1323(03)00057-X.

[3] J. Mathur, N.K. Bansal, S. Mathur, M. Jain, Anupma, Experimental investigations on solar chimney for room ventilation, Sol. Energy 80 (2006) 927–935. https://doi.org/10.1016/j.solener.2005.08.008.

[4] M.M. AboulNaga, S.N. Abdrabboh, Improving night ventilation into low-rise buildings in hot-arid climates exploring a combined wall–roof solar chimney, Renew. Energy 19 (2000) 47–54. https://doi.org/10.1016/S0960-1481(99)00014-2.

[5] C. Afonso, A. Oliveira, Solar chimneys: simulation and experiment, (2000) 9.

[6] K.H. Lee, R.K. Strand, Enhancement of natural ventilation in buildings using a thermal chimney, Energy Build. 41 (2009) 615–621. https://doi.org/10.1016/j.enbuild.2008.12.006.

[7] D.J. Harris, N. Helwig, Solar chimney and building ventilation, Appl. Energy 84 (2007) 135–146. https://doi.org/10.1016/j.apenergy.2006.07.001.

[8] R. Bassiouny, N.S.A. Koura, An analytical and numerical study of solar chimney use for room natural ventilation, Energy Build. 40 (2008) 865–873. https://doi.org/10.1016/j.enbuild.2007.06.005.

[9] Q. Lin, S.J. Harrison, Experimental Study on Natural Convection in an Asymmetrically Heated Inclined Channel With Radiation Exchange, in: Heat Transf. Vol. 1, ASME, Las Vegas, Nevada, USA, 2003: pp. 41–45. https://doi.org/10.1115/HT2003-47202.

[10] A. Auletta, O. Manca, B. Morrone, V. Naso, Heat transfer enhancement by the chimney effect in a vertical isoflux channel, Int. J. Heat Mass Transf. 44 (2001) 4345–4357. https://doi.org/10.1016/S0017-9310(01)00064-3.

[11] A. Auletta, O. Manca, M. Musto, S. Nardini, Thermal design of symmetrically and asymmetrically heated channel–chimney systems in natural convection, Appl. Therm. Eng. 23 (2003) 605–621. https://doi.org/10.1016/S1359-4311(02)00241-7.

[12] Z. Nasri, A.H. Laatar, J. Balti, Natural convection enhancement in an asymmetrically heated channel-chimney system, Int. J. Therm. Sci. 90 (2015) 122–134. https://doi.org/10.1016/j.ijthermalsci.2014.11.033.

[13] Y. Cherif, E. Sassine, S. Lassue, L. Zalewski, Experimental and numerical natural convection in an asymmetrically heated double vertical facade, Int. J. Therm. Sci. 152 (2020) 106288. https://doi.org/10.1016/j.ijthermalsci.2020.106288.

[14] M. Rabani, V. Kalantar, A.A. Dehghan, A.K. Faghih, Empirical investigation of the cooling performance of a new designed Trombe wall in combination with solar chimney and water spraying system, Energy Build. 102 (2015) 45–57. https://doi.org/10.1016/j.enbuild.2015.05.010.

[15] M. Rabani, V. Kalantar, M. Rabani, Passive cooling performance of a test room equipped with normal and new designed Trombe walls: A numerical approach, Sustain. Energy Technol. Assess. 33 (2019) 69–82. https://doi.org/10.1016/j.seta.2019.03.005.

[16] B. Moshfegh, M. Sandberg, Flow and heat transfer in the air gap behind photovoltaic panels, Renew. Sustain. Energy Rev. 2 (1998) 287–301. https://doi.org/10.1016/S1364-0321(98)00005-7.

[17] K.S. Ong, C.C. Chow, Performance of a solar chimney, Sol. Energy (2003) 17.

[18] H.H. Al-Kayiem, S. K.V., S.I.U.-H. Gilani, Mathematical analysis of the influence of the chimney height and collector area on the performance of a roof top solar chimney, Energy Build. 68 (2014) 305–311. https://doi.org/10.1016/j.enbuild.2013.09.021.

[19] J. Arce, M.J. Jiménez, J.D. Guzmán, M.R. Heras, G. Alvarez, J. Xamán, Experimental study for natural ventilation on a solar chimney, Renew. Energy 34 (2009) 2928–2934. https://doi.org/10.1016/j.renene.2009.04.026.

[20] R. Vargas-López, J. Xamán, I. Hernández-Pérez, J. Arce, I. Zavala-Guillén, M.J. Jiménez, M.R. Heras, Mathematical models of solar chimneys with a phase change material for ventilation of buildings: A review using global energy balance, Energy 170 (2019) 683–708. https://doi.org/10.1016/j.energy.2018.12.148.

[21] N.K. Bansal, J. Mathur, S. Mathur, M. Jain, Modeling of window-sized solar chimneys for ventilation, Build. Environ. 40 (2005) 1302–1308. https://doi.org/10.1016/j.buildenv.2004.10.011.

[22] K.S. Ong, A mathematical model of a solar chimney, Renew. Energy (2003) 14.

[23] J. Hirunlabh, W. Kongduang, P. Namprakai, J. Khedari, Study of natural ventilation of houses by a metallic solar wall under tropical climate, Renew. Energy 18 (1999) 109–119. https://doi.org/10.1016/S0960-1481(98)00783-6.

[24] K.T. Andersen, DESIGN OF NATURAL VENTILATION BY THERMAL BUOYANCY WITH TEMPERATURE STRATIFICATION, (n.d.) 8.

[25] N.K. Bansal, R. Mathur, M.S. Bhandari, Solar chimney for enhanced stack ventilation, Build. Environ. 28 (1993) 373–377. https://doi.org/10.1016/0360-1323(93)90042-2.

[26] J. Martı´-Herrero, M.R. Heras-Celemin, Dynamic physical model for a solar chimney, Sol. Energy 81 (2007) 614–622. https://doi.org/10.1016/j.solener.2006.09.003.

[27] J.A. Duffie, W.A. Beckman, Solar Engineering of Thermal Processes, (n.d.).

[28] S.W. Churchill, H.H.S. Chu, Correlating equations for laminar and turbulent free convection from a vertical plate, Int. J. Heat Mass Transf. 18 (1975) 1323–1329. https://doi.org/10.1016/0017-9310(75)90243-4.

[29] D. Incropera, ed., Introduction to heat transfer, 6th ed, Wiley, Hoboken, NJ, 2011.

[30] F. Flourentzou, J. Van der Maas, C.-A. Roulet, Natural ventilation for passive cooling: measurement of discharge coefficients, Energy Build. 27 (1998) 283–292. https://doi.org/10.1016/S0378-7788(97)00043-1.

[31] J. Arce, J.P. Xamán, G. Álvarez, M.J. Jiménez, R. Enríquez, M.R. Heras, A Simulation of the Thermal Performance of a Small Solar Chimney Already Installed in a Building, J. Sol. Energy Eng. 135 (2013) 011005. https://doi.org/10.1115/1.4007088.

[32] H. Wang, Combined Solar Chimney and Water Wall for Enhancing Building Ventilation and Thermal Comfort, (n.d.).

# CHAPTER 7: CONCLUSIONS AND FUTURE RECOMMENDATIONS

## 7.1 Summary of the Research Work

Experimental investigations were conducted by fabricating an indoor model of a wall solar chimney attached to a reduced-scale model of a room. These experiments were carried out in a controlled laboratory setting with the aim of generating high-quality thermal and kinematic data under quasi-steady-state conditions. The data obtained from these experiments are intended for direct application in L-shaped solar-heated natural ventilation cavities and solar building facades that are connected to living spaces via horizontal inlet air openings. Solar flux enters the chimney through the heated section of the active wall, where a heater is installed. The active wall also includes a horizontal inlet opening for admitting air from the attached room. To maintain adiabatic conditions for the passive wall and manipulate surface emissivity, both walls were constructed from similar opaque materials. Additionally, an adiabatic chimney top was extended on the chimney to ensure adiabatic conditions at the trailing edge of the heated part of the active wall and to enhance the stack height of the wall chimney.

To assess the impact of changing the surface emissivity of the active and passive walls from 0.08 to 0.96 in the L-shaped vertical channel attached to a reduced-scale model of room, the study examines the thermal and kinematic fields developed at heat fluxes of 110 W/m$^2$ and 235 W/m$^2$. In this regard, the evolution of the operative wall temperature on both the active and passive walls of the chimney, as well as the 2D time-averaged velocity field along the centre plane (X/W = 0.5), is measured. For all the experiments, the aspect ratio ($Y_H$/D) is maintained constant at 8, and the extension ratio of the adiabatic chimney top ($Y_A/Y_H$) is set at 0.52. The spanwise width of the chimney is W = 0.38 m. Additionally, the chimney is connected to the room via a horizontal inlet duct with an

inlet aperture height of 0.205 m and a length of 0.079 m. The study also correlated the wall thermal field developed on the active and passive walls of L-shaped vertical channel with the time-averaged natural convection flow between the channel walls. Moreover, mean volume flow rates are computed from the time-averaged vertical velocity flow field to assess the ventilation performance of the wall solar chimney at low and high surface emissivity of the walls of the chimney at electrical fluxes of 110 W/m$^2$ and 235 W/m$^2$.

Furthermore, qualitative airflow patterns within the attached room (1.48 m x 1.48 m x 1.12 m), from room air inlet to chimney inlet (0.205 m x 0.38 m), are visualized via three equally spaced and same-size air inlet openings (0.205 m x 0.375 m) on the room. Quantitative measurements, including volumetric flow rate, wall thermal field on the active wall, and mean temperature difference between room air and room air inlet opening, are measured to analyse the effects of room air inlet placement and size on the thermal and kinematical performance of solar chimneys and room ventilation.

A simplified 1-D steady heat energy balance model (SHBM) was developed for the indoor wall chimney test rig and validated using experimental data. The model was validated at different heat flux levels (110 W/m$^2$ and 235 W/m$^2$) for both low- and high-emissive walls of the chimney. After validation, the model was used to predict the effect of changes in surface emissivity of chimney walls and chimney air gap on mean temperatures of the chimney walls and air, as well as on mass flow rate out of the chimney and air changes per hour (ACH) of the wall chimney from the attached room.

### 7.1.1 Thermal and Kinematical Investigation on L-shaped Vertical Channel

The kinematic and wall thermal fields in the chimney, at low surface emissivity ($\varepsilon \sim 0.08$) of active and passive walls, depict one-wall heating conditions within the L-shaped

cavity. Increasing surface emissivity of walls (ε ~ 0.96) triggers wall-to-wall radiation exchanges between the active and passive walls of the chimney, altering the thermal conditions within the chimney and causing asymmetric heating of the air in the L-shaped vertical channel. Moreover, As the heat flux increased from 110 W/m² to 235 W/m², both the time-averaged vertical velocity field and the wall thermal fields increased in magnitude and maintained consistent evolution patterns for tests at similar values of surface emissivity.

The results show that higher emissive walls led to increased velocity at the chimney inlet at heat fluxes of 110 W/m² and 235 W/m². Additionally, the velocity field gradually rises upstream with high-emissive walls compared to low-emissive walls at the same heat flux. The difference in average velocity field between low-emissive and high-emissive walls equalizes as flow develops upstream. The evolution of the time-averaged flow and thermal fields on the chimney walls was influenced by both the horizontal inlet of chimney and the surface emissivity of the walls.

The increase in the mean of vertical velocity profiles from Y/H = 0.05 to 0.61 at low emissive walls (ε ~ 0.08) of the chimney indicated a 300% increase at a heat flux of 110 W/m$^2$ and a 237.8% increase at 235 W/m². Similarly, at high emissive walls of the chimney (ε ~ 0.96), there was a 239% increase at a heat flux of 110 W/m², and a 144.3% increase at 235 W/m². Increasing wall surface emissivity from 0.08 to 0.96 led to mean vertical velocity profile increases of 36% and 55% at 110 W/m² and 235 W/m², respectively, at Y/H = 0.05. Similarly, the same change in surface emissivity showed increases of 15.5% and 1.33%, respectively, from 110 W/m² to 235 W/m² at Y/H = 0.61. With the increase in heat flux from 110 W/m² to 235 W/m², there were mean vertical velocity profile increases of 36% and 60% at ε = 0.08 and ε = 0.96, respectively, at Y/H

= 0.05. Furthermore, the increase in heat flux led to mean vertical velocity profile increases of 49.5% at 110 W/m² and 31.16% at 235 W/m², respectively, at Y/H = 0.61.

The operational temperature of the passive wall increased by 4.9°C (1633%) when the heat flux was 110 W/m² and the surface emissivity of chimney walls increased from 0.08 to 0.96. At 235 W/m², this temperature rose by 8.7°C (1740%). Conversely, the average operational temperature on the heated part of the active wall decreased by 8.2°C (36.6%) and 13.7°C (33.2%) at 110 W/m² and 235 W/m², respectively, with the same heat flux and emissivity range. For the passive and heated parts of the active wall, at a surface emissivity of 0.08, the operational temperature increased by 0.2°C (66.6%) and 19°C (84%), respectively, with an increase in heat flux from 110 to 235 W/m². Similarly, at a surface emissivity of 0.96, the operational temperature for the passive and heated parts of the active wall increased by 3.7°C (67.2%) and 13°C (89.6%) with the same increase in heat flux.

No reverse flow phenomenon occurs at low-emissive walls of the chimney ($\varepsilon \sim 0.08$) under tested ohmic heat fluxes of 110 W/m$^2$ and 235 W/m². The airflow rate out of the chimney remains unaffected by descending cold air from the outlet due to incoming airflow deflection towards the passive wall via the horizontal inlet. This deflection increases as heat flux rises from 110 W/m² to 235 W/m², resulting in a reduction in the height and depth of the stationary fluid layer along the passive wall. Minimal radiative heat transfer to the passive wall raises the operative wall temperature at the outlet by 1°C at 110 W/m² and 1.64°C at 235 W/m² above ambient temperature, further suppressing the potential for bidirectional flow at the outlet of the L-shaped vertical channel.

The horizontal inlet design of the wall chimney creates two distinct air recirculation zones. The first occurs between the passive wall and the bottom wall, while the second

forms above the chimney inlet due to the vena-contracta effect at the sharp corner of the active wall. These flow patterns dissipate kinetic energy within the chimney, reducing the mass flow rate and influencing the development of wall thermal and kinematic fields. The size of these flow structures is found to be affected by the ohmic heat flux and surface emissivity of the chimney walls. However, the height of the flow separation region on the leading edge of the active wall remains consistent between Y/H = 0.1 and 0.15. Consequently, the maximum localized gradient of operative wall temperature on the active wall occurs in this region across all cases studied.

In all cases examined, an inflection point in the operative wall temperature occurs between chimney heights of Y/H = 0.44 and Y/H = 0.64. Low-emissive walls ($\varepsilon \sim 0.08$) subjected to 110 W/m$^2$ and 235 W/m$^2$ show decreases of 0.03°C and 0.12°C, respectively. Similarly, high-emissive walls ($\varepsilon \sim 0.96$) experience decreases of 0.31°C and 0.66°C under the same wattages. This inflection is solely attributed to increased radiative heat transfer due to an increased view factor, with no indication of flow transition as laminar flow persists within the L-shaped vertical channel in all cases studied.

Surface emissivity and ohmic heat flux have been observed to have a positive impact on volume flow rate in an L-shaped vertical channel. Increasing surface emissivity from 0.08 to 0.96 resulted in a 23.6% increase in chimney volume flow rate at 110 W/m² and a 10.8% increase at 235 W/m². For low-emissive walls ($\varepsilon \sim 0.08$), increasing ohmic heat fluxes from 110 W/m² to 235 W/m² resulted in a 49% increase in volume flow rate, while high-emissive walls ($\varepsilon \sim 0.96$) showed a 33.6% increase.

The results of this experimental study show that radiation heat transfer plays a significant role in modifying the flow field within L-shaped solar-heated ventilation cavities. This increases the airflow rate and modifies the temperature of the active and passive walls of

the chimney. Therefore, it should not be overlooked. Moreover, air flow patterns reveal that the sharp corners of the horizontal inlet of the chimney have affected the flow field development upstream in the chimney. The horizontal inlet design of the chimney had a beneficial effect on the flow dynamics by reducing the occurrence of reverse flow at the chimney outlet when the chimney walls had low surface emissivity. However, this horizontal inlet design also resulted in a loss of flow kinetic energy at the entrance for both high and low surface emissivity of chimney walls. Hence, reengineering the design of the horizontal inlet could further enhance the ventilation performance of the L-shaped solar-ventilated channel by reducing flow energy dissipation.

### 7.1.2 Room Air Inlet Investigation on Chimney Performance and Room ventilation

The research investigated the link between the position and size of a room air inlet on the thermal performance of a wall chimney. This was accomplished by analysing the evolution of the operative wall temperature on the active wall at four different configurations of room air inlet placement opposite to the chimney inlet on the room wall. In this regard, the low-emissivity walls of the chimney were tested with heat flux levels of 110 $W/m^2$ and 235 $W/m^2$. It is concluded that the temperature field remained consistent across all configurations, with minor variations attributed to fluctuations in air temperatures at the chimney inlet. The average operative wall temperature at the heated part of the active wall was 22.8 ± 0.18 °C at 110 W/m² and 41.8 ± 0.19 °C at 235 W/m².

Experimental investigations were also undertaken to study the effect of position and size of the room air inlet on the development of airflow patterns and the kinematical performance of a chimney. In this regard, two room air inlet positions, AW and TW, were analysed under an ohmic heat flux of 235 W/m² with low-emissive walls. The results showed that vertical velocity profiles at the same heights overlapped between two tests,

indicating a consistent trend in the development flow field in the streamwise direction. Therefore, the mean values of vertical velocity profiles at identical chimney heights were similar in magnitude. Consequently, the mean volume flow rate out of the chimney with both room air inlet configurations was calculated to be 0.0155 $m^3/s$, with a standard deviation of ±0.005.

The experiments were also carried out to determine how the placement of air inlets in a room affects the thermal comfort and ventilation of the room. This was done by measuring the distribution of room air temperature and the movement of air within the room, starting from the room air inlet and extending to the chimney inlet. In this regard, the experiments were conducted using low-emissivity ($\varepsilon$ ~0.08) walls of the chimney exposed to a heat flux of 235 $W/m^2$ on the heated part of the active wall. Smoke tests revealed that air flows in a streamlined manner from all the tested room air inlet positions into the chimney inlet, with minimal dispersion in the room. In the TW configuration, the average temperature difference between the air inside the room and the room air inlet opening is measured to be 0.4°C, which is lower than in all other tested cases. Additionally, thermal stratification inside the room is also found to be minimal compared to other configurations.

The findings of this study suggest that the placement and size of the room air inlet have no significant impact on the performance of the wall solar chimney. However, it is noted that these factors do influence the distribution of room temperatures, thus affecting the average air temperature within the room. Consequently, this has the potential to improve the overall thermal comfort of the occupants. Therefore, the room air inlet should be kept at the top of the room wall, opposite the wall that forms the inlet opening of the chimney.

### 7.1.3 Theoretical Modelling of Indoor Solar Chimney

A simplified one-dimensional theoretical model, known as the Steady Heat Balance Model (SHBM), has been built to predict the thermal and ventilation performance of an indoor experimental model. This novel model consists of a vertical wall chimney fabricated with well-insulated opaque walls and an adiabatic chimney top, with the inlet connected to a scaled-down model of the room. In the SHBM, all essential components of the experimental test rig, whether in the structure or in the ambient environment, are treated as individual thermal nodes. These nodes form a thermal network by exchanging heat with neighbouring nodes. The SHBM model has been validated using experimental data collected from both low-emissive and high-emissive walls of the chimney, where heat fluxes of 110 and 235 W/m² were applied. The developed modelling approach for this innovative indoor solar chimney design has proven to be an effective tool for quickly predicting the ventilation rate of the experimental model, especially at the low-emissive walls of the chimney. However, the temperature prediction of the chimney walls, particularly the passive wall, was significantly higher than the experimental results. The major findings of the theoretical modelling are summarized below.

- For low-emissive walls of the chimney, the percent error in volume rate prediction ranges from 0.6% to 11.7% lower, based on experimental results obtained at 110 and 235 W/m². High-emissive walls show slightly higher percent errors, at around 9.6% and 12.4%, respectively, for the same heat flux conditions, with model predictions consistently lower than experimental results.
- For low-emissive walls, the mean temperature prediction of the heated part of the active wall shows a percent error of approximately 11.7% higher, based on experimental results obtained at heat fluxes of 110 and 235 W/m². High-emissive

walls exhibit slightly higher percent errors, around 32%, respectively, for the same heat flux conditions, with model predictions consistently exceeding experimental results.

- For low-emissivity walls, the percent error in predicting the mean passive wall temperature is approximately 95% higher, based on experimental results obtained at 110 and 235 W/m². High-emissivity walls exhibit slightly lower percent errors, at around 63% for the same heat flux conditions, with model predictions consistently exceeding experimental results.

## 7.2 Scope for Future Work

The potential for advancing this experimental study is substantial, as evidenced by the results of this experimental research. There are two perspectives for future experimental endeavours. The first perspective involves refining the experimental apparatus, which includes improving the existing setup, instrumentation, and experimental procedures. The second perspective entails conducting heat transfer analysis on thermal data and conducting further investigations into the spatial-temporal evolution of the flow field and flow structures within the L-shaped vertical channel. Furthermore, there is ample room for initiating new experiments using the built experimental bench to investigate the impact of various uniform heating modes and aspect ratios while also taking into account both low-emissive and high-emissive walls of the channel. Additionally, the instrumentation for the background oriented Schlieren technique can also be integrated with relative ease into the experimental bench to obtain the thermal field of the air in the chimney air cavity gap. Finally, a theoretical modelling approach is required to accurately simulate the effect of wall surface emissivity on predicting the performance of the experimental bench.

### 7.2.1 Thermal Measurements

To determine the average temperature of the air at the inlet and outlet of the chimney, three thermocouples were immersed in the air at both the inlet and outlet points. These thermocouples were placed at equal distances from each other and positioned at the center plane of the chimney openings. However, three thermocouples and their configuration are insufficient for accurately measuring the average temperature of the air at the outlet chimney. Therefore, for future research, it is recommended to densely mount thermocouples in a line configuration close to the walls of the chimney outlet. This will provide more precise readings of the average air temperature at the chimney outlet.

Similarly, for the estimation of mass flow rate calculations, the density of the air needs to be measured. Therefore, a set of thermocouples must be immersed in the channel for future work, particularly in the near-wall regions where temperature gradients are most significant. In such cases, the wire diameter of the thermocouples could be reduced to 0.1 mm in order to minimize disturbance of the airflow.

### 7.2.2 Flow Field Measurements

Regarding velocity measurements, the PIV system has exhibited a primary limitation near the walls, attributable to its low definition in the near-wall regions. Consequently, masking was implemented for walls with high emissivity. A 7 mm mask was applied to the passive wall and a 4 mm mask to the active wall of the chimney. Similarly, for walls with low emissivity, a 4 mm mask was applied to the passive wall and a 3 mm mask to the active wall. The strong velocity gradients present in these zones tend to decrease the probability of detecting the displacement peak, resulting in greater uncertainty in these regions. This uncertainty arises from the uniformly applied interrogation areas across the

image section of the flow. Therefore, in future work, selecting rectangular interrogation windows extending parallel to the wall can enhance measurements in the near-wall regions and also help in reducing the size of the masking operation on the PIV images.

### 7.2.3 Characterization of Laboratory Room

A primary necessity for accurately obtaining the wall thermal and kinematical fields developed due to pure natural convection is to control the environmental conditions in the laboratory room while an experiment is in progress. This requires assessing the influence of external conditions such as thermal stratification and air movement in the laboratory room and their effects on the development of natural convection air flow inside the chimney. To achieve this, several steps were taken to modify the mechanical duct ventilation system in the laboratory room, aiming to create a quiescent state of air surrounding the experimental bench. Thermocouples were suspended at different heights in the room adjacent to the experimental bench to monitor temperature evolution and stratification in the vicinity of the test rig during the experiments. Throughout all experiments, the thermal stratification of the air near the experimental bench did not exceed 0.5°C, and the temperature difference in the air close to the test rig, between the height equivalent to the chimney inlet and outlet, did not exceed 1°C. Additionally, without activating the heater in the experimental bench, the air speed at the chimney outlet and air inlet opening of the room were measured using an omnidirectional anemometer, registering approximately 0.05 m/s and 0.074 m/s, respectively. For future work, it is imperative to conduct a more comprehensive analysis of the evolution of environmental conditions within the laboratory room during tests to ascertain their influence on experimental results. In this regard, dedicated anemometer probes are required adjacent to the chimney outlet, room air inlet, and various points near the test rig during each

experiment. Furthermore, pressure sensors are also required near the test rig to measure instantaneous static pressures and evaluate pressure gradients during each test. All these measurements will help in correlating with velocities inside the chimney and accurately evaluating the impact of the room environment on the results.

### 7.2.4 Data Reduction and Post-processing

Energy balance analysis is required to measure the various modes of heat transfer occurring within walls and air inside the chimney and to assess the influence of surface emissivity on these heat exchanges. Through this analysis, it will be possible to compute both local and overall heat transfer coefficients as well as Nusselt numbers. Subsequently, all the findings can then be condensed into compact nondimensional correlations between the Nusselt number and Rayleigh number for an L-shaped vertical channel uniformly heated from one wall, both with low and high emissivity of the channel walls.

The spatial-temporal evolution of the flow field and flow structures inside chimneys can also be analysed from the PIV data collected in this thesis. Additionally, the 2D distribution of turbulent intensity in both the spanwise and streamwise directions of the chimney can be computed to gain a comprehensive understanding of the impact of variations in the surface emissivity of the chimney wall and injection heat flux. These analyses will aid in linking the operative temperature fields developed on the chimney walls with both low- and high-emissive chimney walls.

Furthermore, post-processing utilizing proper orthogonal decomposition (POD) could be applied to the acquired PIV velocity field data in this thesis. This method will assist in extracting the primary dominant spatial and temporal features of the flow inside the L-shaped vertical channel, as well as evaluating the impact of variations in surface

emissivity on the chimney wall and heat flux on the evolution of these dominant flow structures.

### 7.2.5 New Experimentation

Three additional heating modes in the L-shaped vertical channel can also be studied with this constructed experimental bench: Mode I involves one-wall uniform heating from the wall opposite to the wall forming the inlet of the chimney; Mode II involves both the wall forming the inlet of the chimney and its opposite wall being either symmetrically or asymmetrically heated; and Mode III, non-uniform (periodic and alternate heating) between both walls of the chimney can also be studied.

The design optimization analysis of the L-shaped solar ventilated vertical channel connected to a room can also be studied by varying the aspect ratio ($Y_H/D$) of the chimney from 8 to 5.8 for all four potential heating modes of the chimney.

The background-oriented Schlieren (BOS) technique can be integrated into the constructed test rig to measure the 2D temporal and spatial evolution of the thermal field and thermal structures within the chimney air cavity gap. Furthermore, this instrumentation will also facilitate quantitative measurements of the 2D density field inside the chimney.

### 7.2.6 Theoretical Modelling of Test rig

After analysing the theoretical model simulations and identifying its shortcomings, it is necessary to improve its predictive capabilities. Several investigations can be pursued to enhance the accuracy and robustness of the theoretical modelling approach for the indoor wall solar chimney test rig.

indoor solar chimney model can be improved by using the thermal nodal network modelling approach outlined in [1]. This approach calculates the mass flow rate within the solar chimney and across the room by applying momentum and mass conservation equations to the air entering and leaving the chimney. This refinement can enhance the accuracy of air flow rate predictions.

In this modelling approach, the correlation between Nusselt and Rayleigh numbers is employed to calculate the convection heat transfer coefficients on the walls of a vertical channel heated with a uniform wall temperature, considering both low and high emissivity wall scenarios within the chimney. To enhance the accuracy of the model in predicting the mean temperature of chimney walls, it is crucial to utilize correlations derived for standalone wall solar chimney setups or, more specifically, L-shaped vertical channels connected to rooms that are uniformly heated from a single wall, tailored to low and high wall emissivity scenarios. This approach ensures a more precise estimation of temperature variations across both low and high emissivity walls within the channel.

Finally, it is advisable to compute the thermophysical characteristics of air based on the average film temperature of air, as opposed to relying on the average air temperature as done in this modelling approach.

## 7.3 References

[1] H. Wang, C. Lei, Theoretical modeling of combined solar chimney and water wall for buildings, Energy and Buildings 187 (2019) 186–200. https://doi.org/10.1016/j.enbuild.2019.01.025.

## APPENDIX A: Surface Emissivity Measurement

This section outlines the development of the experimental setup, the design of protocols, and the experiments aimed at determining the bulk emissivity of low-emissive aluminium Scotch and matte black painted aluminium Scotch through the utilization of infrared radiation (IR) thermography.

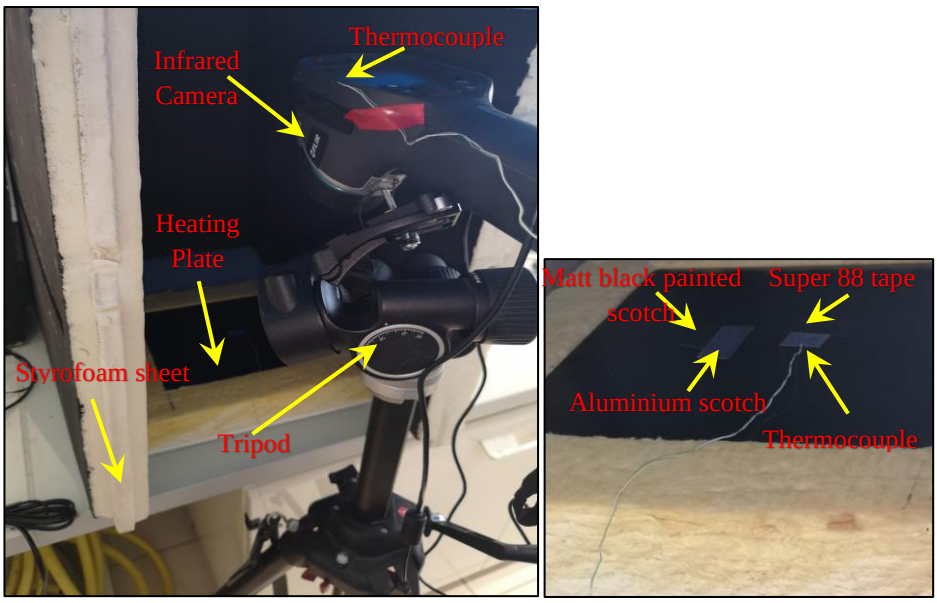


Figure A.1: The experimental setup for surface emissivity measurement; (a) view of whole setup (b) heating plate attached testing samples and reference temperature measurements.

The equipment required for the experiments includes an infrared camera for recording radiometric thermograms, a tripod stand to hold the IR camera firmly at an angle of 20° from vertical, and a heating unit. Figure A.1 illustrates the typical experimental setup, wherein the thermal imager camera is appropriately positioned in front of the samples, which are situated on a heating plate enclosed within a frame constructed from glass wool insulation cover sheets. The temperature range and uniformity on the heating plate are controlled using an Arduino microcontroller. A dedicated LabVIEW program is developed to regulate the voltage and current for heating the plate to specific temperatures and to monitor the heating plate temperature continuously. Pieces of aluminium foil and

matte black painted aluminium foil are affixed at the centre of the heating plate to facilitate emissivity measurements. Moreover, K-type thermocouples and a piece of Super 88 electrical tape are affixed to the heating plate for precise temperature monitoring. Styrofoam sheets are strategically placed on all sides, excluding the front side facing the IR camera, as well as on the top of the heating plate, to mitigate unwanted background effects during IR measurements and to aid in maintaining a steady-state temperature of the heating plate.

The experiments utilized the FLIR E60bx thermal imager, with technical specifications provided in Table A.1. Radiometric thermograms, captured by the thermal camera, enable retrospective adjustment of parameters such as emissivity, distance from the object, reflected temperature, and ambient temperature. Each pixel in the image contains information about measured values, allowing temperature measurement for every single point in the thermogram.

Table A.1: Specifications of infrared camera

| Specifications | |
|---|---|
| IR resolution | 320 x 240 pixels |
| Spatial resolution (IFOV) | 1.36 mrad |
| Thermal sensitivity | < 0.045°C, +30C / (45 mK) |
| Field of view (FOV) | 25° x 19° |
| Object temperature range | - 20 to +120°C |
| Accuracy | ±2°C, ±2% of reading, for ambient temperature 10°C to 35°C |
| Spectral range | 7.5 – 13 µm |

The apparent reflection temperature, sometimes referred to as the background temperature, is a crucial parameter influencing emissivity measurements. To determine this value, a crumpled sheet of aluminium foil was placed atop the target area of the heating plate. The emissivity value was manually set to 1, and the camera distance was adjusted to 0 in the IR camera settings. Subsequently, the average temperature of the region of interest on the aluminium foil was measured to ascertain the effect of the reflective source in the laboratory room, serving as a proxy for the background temperature. Concurrently, ambient temperature was monitored using thermocouples positioned at the left corner of the IR camera during the experiments. Additionally, the camera distance between the target and the camera was measured. These parameters were inputted into the camera's object settings, as illustrated in Table A.2, to calculate the surface emissivity.

Table A.2: Camera setting for Emissivity measurement

| **Object parameters in Camera setting** | |
|---|---|
| Ambient Temp | 25 |
| Camera Distance | 0.5 m |
| Reflected Temperature | 23 C° |

To accurately measure the apparent temperature of a heating plate using a thermal imager (TI), a piece of Super 88 electric tape with an unknown emissivity of 0.95 is affixed to the heating plate. This emissivity value was then set in the camera. Additionally, the apparent temperature of the heating plate was simultaneously compared with the actual temperature measured using a thermocouple attached to the heating plate.

During experiments to determine the bulk emissivity of the samples affixed to the heating plate, the heating plate is initially heated for two hours at a temperature of 35°C using a dedicated LabVIEW program until thermal equilibrium is reached between the heating plate and the attached samples. Once thermal equilibrium is achieved, surface temperature measurements of the heating plate are recorded using a K-type thermocouple and stored in the computer at a sampling rate of 0.1. Simultaneously, infrared (IR) videos are recorded at a rate of 1 frame per second for approximately 5 minutes using a thermal imager (TI) and stored on the personal computer via a USB cable in real-time for later post-processing of the thermal imagery in FLIR TOOLS+ software. Figure A.2 displays a thermogram from one frame of the recorded IR video.

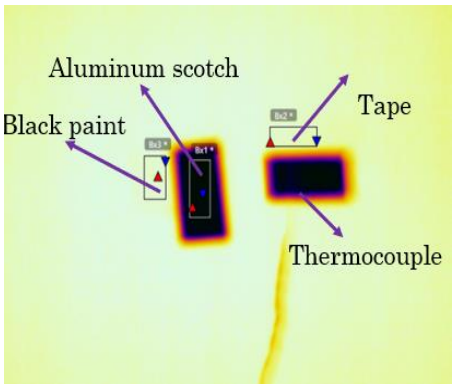


Figure A.2: Thermogram of uniformly heated plate during experimentation.

The bulk surface emissivity of the matte black painted Scotch and aluminium Scotch is measured by initially highlighting the respective target areas on the samples in the infrared imagery. Subsequently, the emissivity values of these target areas are manually adjusted using FLIR TOOLS+ software until the time and spatially averaged surface temperature measurements match those of the target area of the Super 88 electrical tape. Table A.3 presents the time and spatially averaged surface temperatures of the tested samples, also known as the apparent temperature, along with their corresponding target areas.

Table A.3:Apparent temperature and surface area of the samples in IR camera

| | **Matt Black paint** | **Super 88 scotch** | **Aluminum Scotch** |
|---|---|---|---|
| Aparent Temperature | 33.47 C° | 33.49 C° | 33.37 C° |
| Surface area | 390 pixels | 384 pixels | 429 pixels |

The bulk emissivity of aluminium Scotch and matte black painted Scotch is computed to be 0.08 and 0.96, respectively. At these computed values of emissivity, as shown in Figure A.3, the temporal variation of the average surface temperature of aluminium Scotch and matte black painted Scotch is plotted against the temporal variation of the temperature of Super 88 electrical tape and the thermocouple affixed to the heating plate.

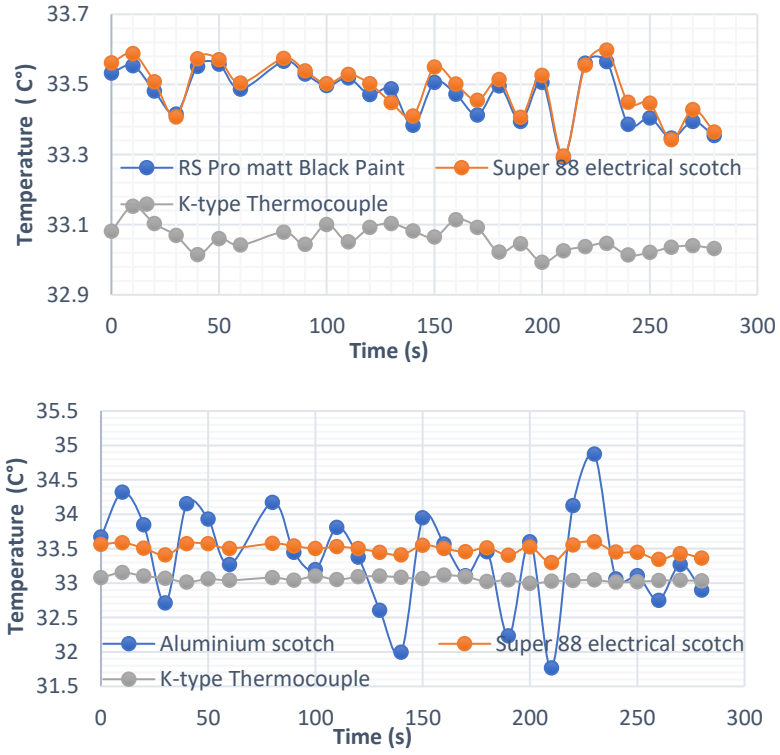


Figure A.3: Temporal temperature evolution of the samples and thermocouple attached to the heating plate.

The plot demonstrates a clear correlation between the matte black painted Scotch and Super 88 electrical tape and the apparent temporal temperature trend, which can be

attributed to their high emissivity. In contrast, the aluminium Scotch tape, characterized by its low emissivity, exhibited a noticeable level of noise in temperature detection by the IR camera, which caused a deviation from the temperature plot of the Super 88 electrical tape.